

# Laser Powder Bed Fusion of AlSi10Mg for Fabrication of Fluid Power Components

by

Lisa Brock

A thesis

presented to the University Of Waterloo

in fulfilment of the

thesis requirement for the degree of

Master of Applied Science

in

Mechanical and Mechatronics Engineering

Waterloo, Ontario, Canada, 2019

© Lisa Brock 2019

## **Author's Declaration**

I hereby declare that I am the sole author of this thesis. This is a true copy of the thesis, including any required final revisions, as accepted by my examiners.

I understand that my thesis may be made electronically available to the public.

## Abstract

Laser powder bed fusion (LPBF) is an additive manufacturing (AM) process that produces 3D objects in a layer-by-layer fashion by using a laser to selectively melt powdered material. Some of the advantages of LPBF include the potential for more design freedom, reduced waste, and flexible production strategies. It is possible to produce parts with complex geometries that cannot be created through traditional methods without great expense in terms of time, money, and resources. There is no need for expensive tooling, thus enabling fast production of unique designs. To implement LPBF in industry, adopters must develop personalized plans for product qualification, quality assurance, manufacturing, and post-processing requirements. The manufacturing strategy is particularly important, as the machine, material, and process parameters that are used have a large impact on the resulting microstructure and mechanical properties, ultimately controlling the quality of the end-product.

The generation, control, and transmission of fluid power is critical for many engineering applications, such as the automotive transmission pump. Energy losses within the pump reduce the transmission's ability to convert torque from the engine, so a more efficient, lightweight pump would reduce the fuel consumption of the vehicle. If LPBF is found suitable for the manufacture of aluminum fluid power components, design improvements could be implemented, and custom solutions could be offered to individual customers. This thesis aims to add to the body of knowledge for process development in LPBF of AlSi10Mg in order to improve the resulting part density, surface roughness, and material performance for fluid power applications. The material performance is evaluated through a comparison with an existing product: the cast aluminum pump housing for use in automotive transmissions.

Process parameters were selected for the LPBF of AlSi10Mg on a modulated laser system to minimize porosity and surface roughness, and maximize production efficiency. This was accomplished through the use of initial process mapping, prediction of melt pool dimensions using a thermophysical model, and fine-tune adjustment of parameters. AlSi10Mg powder from two suppliers was characterized for morphology and particle size distribution. The density or solid fraction of manufactured artifacts was evaluated by optical microscopy and x-ray computed tomography (CT), and the surface roughness by laser confocal microscopy. Two process parameter sets were identified for manufacturing fluid power components. A relative density of 99.95% and surface roughness (Sa) of 11.39  $\mu\text{m}$  were achieved.

These process parameters were used to manufacture LPBF artifacts of various geometries for characterization of the relative density, surface roughness, and durability in terms of hardness, wear resistance, and corrosion resistance. The results were compared with benchmark values for a cast aluminum pump housing, which was also characterized for chemical composition and microstructure.

The AM artifacts had a lower hardness (54.3 to 69.3 HRB) than the cast pump housing (72.8 to 81.5 HRB). The specific wear rate was determined through the dry sliding wear test, and the AM artifacts ( $3.92 \times 10^{-13}$  to  $6.04 \times 10^{-13} \text{ m}^2\text{N}^{-1}$ ) had a lower wear resistance than the cast pump housing ( $2.50 \times 10^{-13}$  to  $2.55 \times 10^{-13} \text{ m}^2\text{N}^{-1}$ ). Cyclic polarization testing revealed that the corrosion resistance and pitting potential were better for the AM artifacts (-0.57 to 0.48 V vs SCE in 0.001M Cl<sup>-</sup>) than the cast pump housing, which exhibited general corrosion. Linear polarization resistance tests also suggested a better corrosion resistance for the AM artifacts, as the corrosion current density was lower. The surface roughness and durability of three different surface types for the AM artifacts (upskin, sideskin, and polished) and cast pump housing (as-cast, horizontal; as-cast, vertical; and machined) were also compared.

The manufacturability of design features was investigated. Thin walls were printed with thicknesses of 1.0 to 3.0 mm. The wall thickness did not have a significant effect on the part density. Slot artifacts were printed with varying gap widths of 0.5 to 4.5 mm. The interior vertical walls were characterized for surface roughness, which was marginally lower for the smallest and largest gap widths. Straight circular channels were printed with hole diameters of 0.2 to 1.2 mm, and with a height of 10 or 20 mm. Powder was successfully removed from channels with a minimum diameter of 0.5 mm.

Recommendations for future work include performing further in-depth study on the relationship between process parameters and the microstructure of LPBF-processed material in order to better understand and control the resulting mechanical properties. Further development of design constraints, especially those related to non-uniform channels, would also be of use to designers of fluid power components as it would provide more design freedom and ultimately enable innovation.

## Acknowledgements

Before anything else, I would like to thank my supervisor, Dr. Mihaela Vlasea. Your knowledge and enthusiasm are inspiring and I am so grateful to have had your guidance and support.

I would like to thank all of my friends and colleagues at the Multi-Scale Additive Manufacturing Laboratory (MSAM) and the Advanced Manufacturing Consortium (AMC).

I would like to acknowledge Dr. Allan Rogalsky, who provided the theoretical development and documentation for the thermophysical model appearing in Sections 5.2.3.1 and 5.2.3.2, and implemented the model within software. Thank you for your contributions and advice. I would also like to acknowledge Dr. Hamed Asgari for performing the metallographic examinations and SEM/EDX analysis, except that which appears in Section 6.2.5, and for sharing his experience and technical expertise throughout the project. I sincerely appreciate all of the time you spent helping me! Thank you to Henry Ma and Dr. Mehrnaz Salarian for performing the CT scans, Jakob Staines and Gibril Bachouchi for performing the powder particle size analysis, and our lab technicians Jerry Ratthapakdee, Karl Rautenberg, and Grace Kurosad for supporting the additive manufacturing process. Special thanks to Sagar Patel for sharing your knowledge about the LPBF process, and for all of your advice and encouragement. Pablo Enrique, thank you for the training and support for the wear testing. I would also like to thank Ibrahim Ogunsanya for performing the electrochemical testing. Thank you for your assistance and guidance.

This research was made possible through the generous funding support received from Federal Economic Development Agency for Southern Ontario (FedDev Ontario), grant number 809104, as well as the Ontario Centres of Excellence, Voucher for Innovation and Productivity (VIP), grant number 31402.

I would like to express gratitude to my industry partner, Advanced Test and Automation, Milton, ON for their financial support, engineering guidance, and vested interest in the success of this project. In addition, Burloak Technologies have generously contributed to this project through donating powder materials for the metal additive manufacturing process, which directly contributed towards the success of this project. I would also like to thank Carlo Bottoni from Mister Transmission, Orangeville, ON for the gracious donation of the automotive transmission pump.

Finally, I want to thank my family for their support, especially my parents, grandma, Lindsay, Mark, Eric, C.B., and Elsie. Your love sustains me.

## **Dedication**

*To my parents, Sonja and Gary Brock.*

# Table of Contents

Author's Declaration .....	ii
Abstract.....	iii
Acknowledgements.....	v
Dedication.....	vi
Table of Contents.....	vii
List of Figures.....	x
List of Tables .....	xv
1 Introduction.....	1
1.1 Motivation.....	1
1.2 Objectives .....	2
1.3 Thesis Outline.....	3
2 Background and Literature Review .....	5
2.1 Laser Powder Bed Fusion (LPBF) Technology.....	5
2.1.1 Advantages and Challenges in LPBF .....	6
2.1.2 Process Parameters in LPBF.....	8
2.2 Laser Powder Bed Fusion of AlSi10Mg.....	12
2.2.1 Al-Si Alloys.....	12
2.2.2 Parameter Optimization for Al-alloys.....	15
2.2.3 Design Considerations for LPBF and Applications.....	19
2.3 Research Contributions.....	23
3 General Experimental Procedures for Material and Performance Characterization.....	24
3.1 Powder Material Characterization .....	24
3.1.1 Scanning Electron Microscopy .....	24
3.1.2 Particle Size Distribution.....	24
3.2 Printing Process .....	25
3.2.1 Full Build Environment .....	25
3.2.2 Reduced Build Volume Environment.....	26
3.3 Material Performance Characterization.....	27
3.3.1 X-Ray Fluorescence Spectroscopy .....	27
3.3.2 Optical Microscopy and Image Processing.....	27
3.3.3 X-Ray Computed Tomography .....	28
3.3.3.1 CT Image Processing in MATLAB.....	29
3.3.4 Surface Roughness.....	30

3.3.5	Hardness .....	32
3.3.6	Wear.....	32
3.3.6.1	Data Processing of Material Volume Loss .....	33
3.3.7	Scanning Electron Microscopy and Energy Dispersive X-Ray Spectroscopy.....	35
3.3.8	Corrosion .....	36
4	Benchmarking Performance in LPBF by Characterization of Cast Aluminum Pump Housing.....	39
4.1	Pump Housing Product Description .....	39
4.2	Methods for Cast Pump Housing Characterization .....	39
4.2.1	Material Characterization .....	39
4.2.2	Geometric Feature Characterization .....	40
4.2.3	Pump Housing Sample Extraction.....	41
4.3	Results for Cast Pump Housing Characterization.....	42
4.3.1	Chemical Composition .....	42
4.3.2	Microstructure.....	43
4.3.3	Density.....	46
4.3.4	Surface Roughness.....	47
4.3.5	Geometric Features.....	49
4.3.6	Hardness .....	49
4.3.7	Wear.....	50
4.3.8	Corrosion .....	54
4.4	Summary of Cast Pump Housing Characterization .....	58
5	LPBF Process Parameter Mapping and Ideal Parameter Selection for Density and Surface Roughness.....	59
5.1	Powder Material Characterization .....	59
5.1.1	Powder Type Selected for Experiments.....	59
5.1.2	Scanning Electron Microscopy .....	59
5.1.3	Particle Size Distribution.....	60
5.2	Process Parameter Selection for Core.....	61
5.2.1	Methods for Initial Process Mapping for Density.....	61
5.2.2	Results for Initial Process Mapping for Density.....	63
5.2.3	Methods for Parameter Selection Using Thermophysical Modelling Tool .....	69
5.2.3.1	Thermophysical Model Suite .....	70
5.2.3.2	Combined Parameters for Experiment Planning .....	71
5.2.3.3	Model Calibration of Absorptivity .....	72
5.2.3.4	Manufacturing Strategy and Process Parameter Selection.....	75



5.2.4	Results for Thermophysical Model Parameters .....	78
5.2.5	Selection of Ideal Recipes for Dense Core .....	81
5.2.6	Outcomes for Ideal Core Recipes .....	84
5.3	Process Parameter Selection for Border .....	91
5.3.1	Initial Process Mapping for Surface Roughness .....	91
5.3.2	Selection of Ideal Recipes for Surface Quality .....	92
5.3.3	Outcomes for Ideal Border Recipes .....	94
5.4	Summary of Selected Processing Parameters for AM Part Production .....	98
6	Performance of LPBF-Manufactured Components for Fluid Power Applications .....	99
6.1	Methods for AM Part Characterization .....	99
6.1.1	Characterization Approach .....	99
6.1.2	Geometric Feature Characterization .....	99
6.1.3	Manufacturing Strategy .....	102
6.2	Results for AM Part Characterization .....	104
6.2.1	Density .....	104
6.2.2	Surface Roughness .....	106
6.2.3	Geometric Features .....	108
6.2.3.1	Thin Walls .....	108
6.2.3.2	Slots .....	110
6.2.3.3	Channels .....	111
6.2.4	Hardness .....	113
6.2.5	Wear .....	115
6.2.6	Corrosion .....	121
7	Summary, Conclusions, and Future Work .....	126
	References .....	129
	Appendix A – LPBF Process Parameters .....	138
	Appendix B – MATLAB Code for CT Scan Data Processing .....	140
	Appendix C – Selection of Threshold for Image Segmentation .....	146
	Appendix D – MATLAB Code for Wear Rate Calculation .....	150
	Appendix E – Powder Particle Size Distribution .....	152
	Appendix F – LPBF Manufacturing Parameters .....	153
	Appendix G – Micrographs .....	155
	Appendix H – LPBF Design Artifacts .....	156
	Appendix I – Electrochemical Results .....	158

# List of Figures

Figure 1-1: Selected fluid power application – aluminum transmission pump housing.....	2
Figure 2-1: Schematic diagram of Laser Powder Bed Fusion equipment [2].....	6
Figure 2-2: Top view of laser scan path on a square cross-section of a part .....	10
Figure 2-3: Upskin and downskin surfaces.....	11
Figure 2-4: Aluminum-Silicon phase diagram [46].....	13
Figure 2-5: Optical micrograph of AlSi10Mg processed by LPBF, side cross-section.....	14
Figure 2-6: SEM images of the microstructure of LPBF-processed AlSi10Mg, from [15] .....	15
Figure 2-7: Recommended ranges of volumetric energy density for LPBF of Al-alloys [21], [36]–[39]16	
Figure 2-8: Volumetric energy density for LPBF of Al-alloys using a modulated laser system [21], [54], [76]–[78] .....	16
Figure 2-9: Applications for LPBF of AlSi10Mg: a) Optimized model of the pedal crank and relevant design guidelines [97]; b) Stages of AM repair of aluminum beams, from cast parts (left) to final model (right) [98]; c) Foam built by LPBF of AlSi10Mg [99]; d) AlSi10Mg periodic lattice structures with a volume fraction of 10% and a unit cell size of 4 mm (left) and 5 mm (right) [10] e) AlSi10Mg gyroid lattice structure with varying volume fraction [11] .....	22
Figure 2-10: LPBF applications in fluid power: a) IN625 pump impeller on the build plate (left) and after post-processing (right) [100]; b) Hydraulic safety valve original design (left) and optimized design with 20% weight (right) [101] .....	23
Figure 3-1: Renishaw AM400 laser powder bed fusion machine [103].....	25
Figure 3-2: a) Renishaw AM400 full build environment; and b) top view of the build plate when viewed in QuantAM software .....	26
Figure 3-3: a) Renishaw AM400 reduced build volume environment; and b) top view of the RBV build plate when viewed in QuantAM software .....	26
Figure 3-4: a) Original micrograph; b) greyscale micrograph with pores highlighted in red; and c) ImageJ greyscale intensity histogram with threshold indicated in red .....	28
Figure 3-5: Image types generated during MATLAB processing of CT scan data .....	30
Figure 3-6: Surface types on cast pump housing.....	31
Figure 3-7: Surface types on cube manufactured by LPBF .....	32
Figure 3-8: a) Linear wear test apparatus; and b) close-up view of the sample stage .....	33
Figure 3-9: Top view of wear track and surrounding surface height data (a), with corners used for best-fit plane highlighted (b) .....	34
Figure 3-10: Isometric view of height data (a), with surface best-fit plane overlaid (b).....	34
Figure 3-11: a) As-cast vertical surface height data (left) and plane fit (right) before surface shape correction; and b) after surface shape correction for the curved surface .....	35
Figure 3-12: a) E/pH diagram, and b) Pourbaix diagram for pure aluminum in DI water [106].....	37
Figure 4-1: Cast aluminum pump product: a) pump cover; b) pump body; c) assembly .....	39

Figure 4-2: Measurement locations on the cast pump housing assembly:.....	40
Figure 4-3: Locations of surface roughness (S), density (D), and hardness (H) measurements on the cast pump housing .....	41
Figure 4-4: Locations of sample extraction for three surface types on the cast pump housing: a) machined; b) as-cast, horizontal; and c) as-cast, vertical.....	42
Figure 4-5: Optical micrographs of the cast pump housing at low magnifications (a and b) and high magnification (c and d).....	44
Figure 4-6: SEM images of the cast pump housing at various magnifications: a) 100x; b) 300 x; c) 891x; d) 2.09kx; e) 929x; f) 1.32kx .....	45
Figure 4-7: EDX element mapping of the cast pump housing microstructure .....	46
Figure 4-8: Cast pump housing sample D1: a) Density vs. distance graph; b) minimum intensity projection across 2.56 mm; c) binary image of single slice # 208/640 (0.832/2.56 mm).....	47
Figure 4-9: Cast pump housing sample D2: a) Density vs. distance graph; b) minimum intensity projection across 3.51 mm; c) binary image of single slice # 595/878 (2.38/3.51 mm).....	47
Figure 4-10: Surface roughness measurement locations, optical micrographs, and height images for four surface types: a) as-cast, horizontal; b) as-cast, outside; c) as-cast, vertical; d) machined .....	48
Figure 4-11: Average surface roughness for cast pump housing.....	48
Figure 4-12: Rockwell B Hardness for cast pump housing .....	50
Figure 4-13: Average specific wear rate ( $k_w$ ) for cast pump housing surfaces .....	50
Figure 4-14: SEM images of the wear track for the cast surface types: a) as-cast, horizontal; b) as-cast, vertical; and c) machined, at low magnification (left) and high magnification (right).....	51
Figure 4-15: SEM images showing a) flaking of wear surface, b) crater containing wear debris, and c) transverse microcracks.....	52
Figure 4-16: EDX measurement locations within the wear track for a) the as-cast, vertical surface; and b) the machined surface .....	52
Figure 4-17: EDX measurement areas inside (location 1) and outside (location 2) the wear track, for a) the as-cast, vertical surface; and b) the machined surface .....	53
Figure 4-18: Cyclic potentiodynamic polarization curves for three replicates of the cast pump housing surfaces .....	54
Figure 4-19: Effect of increasing chloride concentration on cyclic polarization curves for the cast pump housing.....	55
Figure 4-20: Open circuit potential (OCP) and corrosion current density ( $i_{corr}$ ) determined by LPR for the cast pump housing .....	57
Figure 5-1: SEM micrographs of the AlSi10Mg powder from Supplier 1: a) low magnification; b) high magnification .....	60
Figure 5-2: SEM micrographs of the AlSi10Mg powder from Supplier 2: a) low magnification; b) high magnification .....	60
Figure 5-3: Top view of the build plate layouts shown in QuantAM software for: a) DOE 2-1; b) DOE 2-2; c) DOE 2-3; d) DOE 2-4, where the label corresponds with the recipe number used for that sample. ....	62

Figure 5-4: Optical micrographs for selected samples from DOE 2-1 and 2-4 .....	64
Figure 5-5: Optical micrographs for samples from DOE 2-2 .....	64
Figure 5-6: Optical micrographs for samples from DOE 2-3 .....	65
Figure 5-7: Bubble plot showing estimated porosity versus the process parameters for DOE 2-1 to 2-4 .....	65
Figure 5-8: a) Main effects and b) interaction plot for porosity .....	66
Figure 5-9: Optical micrographs for samples from DOE 3-1 .....	67
Figure 5-10: Mean pore fraction for 5 micrographs from each sample, which were manufactured with the same processing parameters but different powder suppliers .....	68
Figure 5-11: Optical micrographs for samples from DOE 3-2 .....	68
Figure 5-12: Bubble plot showing estimated porosity versus process parameters for DOE 2-1 to 3-2... ..	69
Figure 5-13: Melt pool dimensional measurement locations.....	73
Figure 5-14: Average percent difference between the theoretical and experimental melt pool dimensions. Inset: optimal absorptivity value was selected at the point of intersection .....	74
Figure 5-15: Comparison between experimental melt pool dimensions (for image 1 and image 2) and theoretical dimensions predicted using the calibrated absorptivity value ( $\beta = 0.2473$ ).....	75
Figure 5-16: Schematic diagram showing a melt depth ratio = 2 .....	76
Figure 5-17: Non-dimensionalized power ( $P^*$ ) and speed ( $v^*$ ) for DOE 3-3 (black) superimposed on porosity results for previous experiments and recipes from literature [21], [54], [76], [77] .....	77
Figure 5-18: Build plate layout for DOE 3-3, where the labels from 1 – 15 correspond with the recipe number used for that sample, and 17 – 31 correspond with the replicates .....	78
Figure 5-19: Optical micrographs for samples from DOE 3-3 .....	79
Figure 5-20: Optical micrographs of top layer for recipe 9, 10, 12, and 13 from DOE 3-3 .....	79
Figure 5-21: Melt pool temperature ratio ( $\Delta T_{max}/\Delta T_m$ ) vs. melt depth ratio for samples from DOE 3-3 .....	80
Figure 5-22: Bubble plot showing estimated porosity versus process parameters for DOE 3-3 .....	80
Figure 5-23: Melt pool size ratio vs. $T/T_m$ (left) or $v^*$ (right) for DOE 3-3, Recipes 7 to 15 .....	82
Figure 5-24: Non-dimensionalized power ( $P^*$ ) and speed ( $v^*$ ) for DOE 3-5 core recipes (red) superimposed on previous porosity results for DOE 3-3 .....	83
Figure 5-25: Optical micrographs for samples from DOE 3-5 .....	85
Figure 5-26: Optical micrographs for samples from DOE 3-6, manufactured using: a) recipe 1, powder supplier 2; b) recipe 3, powder supplier 2; c) recipe 1, powder supplier 1; d) recipe 3, powder supplier 1 .....	86
Figure 5-27: Density vs. distance graph for samples from DOE 3-6 (Slice density in x-direction), manufactured using: a) recipe 1, powder supplier 2; b) recipe 3, powder supplier 2; c) recipe 1, powder supplier 1; d) recipe 3, powder supplier 1 .....	87
Figure 5-28: Minimum intensity projections for samples from DOE 3-6, manufactured using: a) recipe 1, powder supplier 2; b) recipe 3, powder supplier 2; c) recipe 1, powder supplier 1; d) recipe 3, powder supplier 1 .....	88

Figure 5-29: Binary image for single slice of samples from DOE 3-6, manufactured using: a) recipe 1, powder supplier 2 (slice # 583/646); b) recipe 3, powder supplier 2 (slice # 317/705); c) recipe 1, powder supplier 1 (slice # 434/647); d) recipe 3, powder supplier 1 (slice # 241/670).....	88
Figure 5-30: Optical micrographs for samples from DOE 4-2, manufactured using: a) recipe 1; b) recipe 3.....	89
Figure 5-31: Density vs. distance graph for samples from DOE 4-2 (Slice density in x-direction), manufactured using: a) recipe 1; b) recipe 3.....	90
Figure 5-32: Minimum intensity projections for samples from DOE 4-2, manufactured using: a) recipe 1; b) recipe 3 .....	90
Figure 5-33: Binary image for single slice of samples from DOE 4-2, manufactured using: a) recipe 1 (slice # 419/750); b) recipe 3 (slice # 333/742).....	90
Figure 5-34: Bubble plot showing surface roughness versus process parameters for DOE 3-3.....	92
Figure 5-35: Non-dimensionalized power ( $P^*$ ) and speed ( $v^*$ ) for DOE 3-5 border recipes (red) superimposed on previous surface roughness results for DOE 3-3 .....	93
Figure 5-36: Surface roughness results for samples from DOE 3-5 .....	94
Figure 5-37: Optical micrographs taken at the edges of samples manufactured using border recipe I and III from DOE 3-5.....	95
Figure 5-38: Optical micrographs taken at the border of samples from DOE 3-6, manufactured using border recipe I and: a) powder supplier 2, core recipe 1; b) powder supplier 2, core recipe 3; c) powder supplier 1, core recipe 1; d) powder supplier 1, core recipe 3 .....	96
Figure 5-39: Surface roughness results for samples from DOE4-2 (border recipe V), shown with DOE 3-5 results for comparison .....	97
Figure 5-40: Optical micrographs taken at the edges of samples manufactured using border recipe V from DOE 4-2. The labels indicate the average Sa value. ....	97
Figure 6-1: Thin wall artifact; all dimensions in mm. ....	100
Figure 6-2: Largest (left) and smallest (right) slot artifacts; all dimensions in mm. ....	100
Figure 6-3: Circular channel artifact; all dimensions in mm. ....	101
Figure 6-4: a) Top view and b) isometric view of the build plate layout shown in QuantAM.....	103
Figure 6-5: Density measurements for AM artifacts and cast pump housing.....	104
Figure 6-6: Minimum intensity projections of pores for samples: a) cast pump housing, location 1; b) cast pump housing, location 2; c) AM artifact manufactured with Recipe 1; and d) AM artifact manufactured using Recipe 3.....	105
Figure 6-7: Binary image for single slice of samples from: a) cast pump housing, location 1 (slice # 208/640); b) cast pump housing, location 2 (slice # 595/878); c) AM artifact manufactured with Recipe 1 (slice # 419/750); and d) AM artifact manufactured using Recipe 3 (slice # 333/742).....	106
Figure 6-8: Surface roughness measurement locations, optical micrographs, and height images for AM Recipe 1 (left-hand columns) and Recipe 3 (right-hand columns).....	107
Figure 6-9: Average surface roughness for AM artifacts and cast pump housing.....	107
Figure 6-10: Example of thin wall artifact printed using Recipe 1.....	108
Figure 6-11: Density for AM thin wall artifacts of varying thicknesses and cast pump housing.....	109

Figure 6-12: Minimum intensity projections across 4mm in Z-direction showing porosity for thin wall artifacts of varying thickness, manufactured using a) Recipe 1, high density option; or b) Recipe 3, high productivity option.....	109
Figure 6-13: Examples of slot artifacts printed using Recipe 1 .....	110
Figure 6-14: Average surface roughness for AM slot artifacts with varying gap width and cast pump housing.....	111
Figure 6-15: Examples of circular channel artifacts printed using Recipe 1 .....	111
Figure 6-16: Examples of circular channels printed with a) Recipe 1 and b) Recipe 3, viewed through optical microscope for the visible light test.....	112
Figure 6-17: Cross sectional image of circular channels printed with a) Recipe 1 and b) Recipe 3, examined through CT scanning .....	113
Figure 6-18: Average hardness (HRB) for AM artifacts and cast pump housing.....	114
Figure 6-19: Average specific wear rate ( $k_w$ ) for AM artifacts and cast pump housing .....	115
Figure 6-20: Specific wear rate ( $k_w$ ) versus hardness for AM artifacts and cast pump housing .....	116
Figure 6-21: Low and high magnification SEM images of the wear track for the AM samples manufactured with Recipe 1 (a and b) and Recipe 3 (c and d).....	117
Figure 6-22: SEM images from three surface types showing a) and b) ridges; and c) craters with flaky wear debris.....	118
Figure 6-23: EDX measurement locations within the wear track for a) the upskin surface; b) the sideskin surface; and c) the machined surface, for samples manufactured using recipe 1, and d) the machined surface for sample manufactured using recipe 2 .....	119
Figure 6-24: EDX measurement areas outside (location 1) and inside (location 2) the wear track, for the upskin (a), sideskin (b), and machined surfaces (c and d).....	120
Figure 6-25: Cyclic polarization curves for one replicate of the cast and AM surfaces.....	121
Figure 6-26: Effect of increasing chloride concentration on cyclic polarization curves for the AM artifacts manufactured using a) Recipe 1 and b) Recipe 3.....	122
Figure 6-27: Open circuit potential (OCP) and corrosion current density ( $i_{corr}$ ) determined by LPR for the cast pump housing and AM artifacts .....	124

## List of Tables

Table 2-1: Process parameters for the Renishaw AM400 [31].....	9
Table 3-1: Chemical composition of AlSi10Mg powder [45], [102] .....	24
Table 3-2: Scout-and-scan settings used for CT scanning.....	28
Table 3-3: Electrochemical reactions for pure aluminum.....	36
Table 3-4: Schedule of LPR measurements.....	38
Table 4-1: XRF and EDX measurements compared with specifications (elemental weight %) .....	43
Table 4-2: Density measurements for cast pump housing .....	46
Table 4-3: Feature size measurements for cast pump housing; all dimensions in mm.....	49
Table 4-4: Minimum feature size requirements for cast pump housing; all dimensions in mm.....	49
Table 4-5: Specific wear rate ( $k_w$ ) for cast pump housing surfaces, in units of $m^2N^{-1}$ .....	50
Table 4-6: EDX results for chemical composition at various locations within the wear track.....	53
Table 4-7: EDX results for chemical composition inside and outside the wear track .....	54
Table 4-8: Results for cyclic polarization testing of the cast pump housing .....	56
Table 4-9: Average results for three replicates tested in the 0.001 M chloride solution .....	56
Table 4-10: Corrosion properties for pump housing, from replicate 1 of cyclic polarization test.....	56
Table 5-1: Powder type selected for each experiment .....	59
Table 5-2: Particle size values corresponding with 10%, 50%, and 90% cumulative passing .....	61
Table 5-3: Controlled parameters for DOE 2-1 to 2-4.....	61
Table 5-4: Levels used for $3^3$ full factorial experiment – DOE 2-1 to 2-4 .....	62
Table 5-5: Processing parameters for DOE 3-1 .....	63
Table 5-6: Processing parameters for DOE 3-2.....	63
Table 5-7: Material properties used as inputs for thermal model .....	71
Table 5-8: Processing parameters used as inputs for thermal model.....	73
Table 5-9: Processing parameters for DOE 3-3 .....	76
Table 5-10: Controlled parameters for DOE 3-3 .....	77
Table 5-11: DOE 3-3 data used for linear regression to generate each recipe for DOE 3-5 .....	81
Table 5-12: DOE 3-5 core recipes .....	83
Table 5-13: DOE 3-6 core recipes .....	84
Table 5-14: Average density measurements for each core recipe used in DOE 3-5, estimated using optical microscopy method.....	85
Table 5-15: Average density measurements for DOE 3-6 samples estimated using optical microscopy and CT scan methods.....	86
Table 5-16: Average density measurements for DOE 4-2 samples estimated using optical microscopy and CT scan methods.....	89

Table 5-17: Surface roughness results for samples from DOE 3-3 .....	91
Table 5-18: DOE 3-5 border recipes.....	92
Table 5-19: DOE 3-6 border recipe .....	93
Table 5-20: DOE 4-2 border recipe .....	94
Table 5-21: Average surface roughness measurements for each border recipe used in DOE 3-5.....	95
Table 5-22: Average surface roughness measurements for DOE 3-6.....	96
Table 5-23: Average surface roughness measurement for DOE 4-2 (border recipe V), shown with DOE 3-5 results for comparison .....	97
Table 5-24: Ideal processing parameters and resulting density and surface roughness.....	98
Table 5-25: Additional parameters for ideal manufacturing recipes .....	98
Table 6-1: Processing parameters for LPBF part production .....	102
Table 6-2: Additional parameters for LPBF part production.....	102
Table 6-3: Artifact type and quantity.....	103
Table 6-4: Relative density (%) results for thin wall artifacts.....	108
Table 6-5: Average surface roughness ( $\mu\text{m}$ ) results for slot artifacts .....	111
Table 6-6: Visible light test results for channels of varying length and diameter .....	112
Table 6-7: Average hardness (HRB) for AM artifacts and cast pump housing.....	114
Table 6-8: Specific wear rate ( $k_w$ ) for AM artifacts and cast pump housing, in units of $\text{m}^2\text{N}^{-1}$ .....	116
Table 6-9: EDX results for chemical composition at various locations within the wear track on the AM artifacts .....	119
Table 6-10: EDX results for chemical composition inside and outside the wear track on the AM artifacts .....	120
Table 6-11: Average results for three replicates of cyclic polarization testing of the cast pump housing and AM artifacts .....	121
Table 6-12: Results for cyclic polarization testing of the cast pump housing and AM artifacts at varying chloride concentrations.....	123



# 1 Introduction

In the modern industrial landscape, it is of the utmost importance to deploy engineering solutions that are highly functional, efficient, affordable, and sustainable. Additive manufacturing technologies provide a great opportunity to achieve these objectives by supplementing traditional manufacturing methods.

Additive manufacturing (AM) refers to fabrication processes that produce objects by joining material according to computerized 3D model data, usually in a layer-by-layer fashion. Alternative titles for this class of technologies include “3D printing”, “direct digital manufacturing”, and “solid freeform fabrication”, so named for the ability to produce 3D geometries without the need for part-specific tooling or direct artisan involvement. AM technologies are classified by the technique used to join the material, which is in the form of filament, powder, or liquid resin. Examples include material extrusion, material jetting, binder jetting, direct energy deposition, vat photopolymerization, and powder bed fusion, which is the type of technology investigated in this thesis.

Laser powder bed fusion (LPBF), sometimes referred to as direct metal laser sintering (DMLS) or selective laser melting (SLM), is an AM process that uses a laser to selectively melt powder into the shape of a part, layer-by-layer. Some of the advantages of LPBF include the high level of design freedom, reduced material waste, and adaptability to changes in the type and quantity of products for manufacture. It is possible to produce parts with complex geometries that cannot be created through traditional manufacturing methods without great expense in terms of time, money, and resources. With AM, there is no need for expensive tooling, thus enabling the creation and fast production of individualized, innovative designs. The challenges of implementing LPBF in industry include the need for extensive development prior to adoption, such as the creation of personalized plans for product qualification, quality assurance, manufacturing strategies, and post-processing requirements. The manufacturing strategy is particularly important, as the specific machine, material, and processing parameters that are used have a large impact on the resulting microstructure and mechanical properties, ultimately controlling the quality of the end-product.

## 1.1 Motivation

A fluid power system uses a pump driven by mechanical energy to generate pressurized fluid that is controlled by valves and used to transmit power through the use of actuation devices. The generation,

control, and transmission of fluid power is critical for many engineering applications, such as hydraulic lifts or components for automotive engines.

This thesis aims to add to the body of knowledge for process development in LPBF of AlSi10Mg in order to improve the resulting part density, surface roughness, and material performance for fluid power applications. The durability of the LPBF-processed material is investigated in terms of hardness, wear resistance, and corrosion resistance. The performance is evaluated through a comparison with an existing product: the cast aluminum pump housing for use in automotive transmissions, as shown in Figure 1-1.



**Figure 1-1: Selected fluid power application – aluminum transmission pump housing**

When selecting an application area for AM, it is important to determine both the feasibility of printing that product, and its potential for advancement through the unique capabilities of AM. Energy losses within the oil pump reduce the automatic transmission’s ability to convert torque from the engine, so a more efficient, lightweight transmission pump would lead to an overall reduced fuel consumption by the vehicle. If LPBF is found suitable for the manufacture of aluminum fluid power components, design improvements could be iterated, tested, and implemented, and custom solutions could be offered to individual customers.

## **1.2 Objectives**

There are inherent differences between cast and AM microstructures because of the layer-wise processing and high cooling rates of LPBF. The differences in microstructure will have an impact on the mechanical properties of the material, and will ultimately affect the material performance of the end-product. The purpose of this work is to test the material properties to see if the product

specifications required for fluid power applications can be met through LPBF. In order to do so, the following objectives are addressed:

1. Identify ideal process parameters for LPBF of AlSi10Mg in order to achieve an improved density and surface roughness.
2. Characterize the cast aluminum pump housing in order to provide benchmark values for the material requirements for fluid power applications.
3. Produce AlSi10Mg artifacts using the ideal LPBF process parameters, characterize the material properties to compare with the cast pump housing benchmark, and provide recommendations for implementation of LPBF in fluid power application space.

### **1.3 Thesis Outline**

The thesis is structured into seven chapters. Chapters 1 and 2 contain the introduction and background information. Chapter 3 describes the general characterization methods that will be used throughout the thesis, where applicable, in the subsequent chapters. Chapter 4 discusses the characterization of the cast pump housing for benchmarking the performance of LPBF for fluid power applications. Chapter 5 selects ideal LPBF process parameters for use in manufacturing parts with a dense core and good surface quality, with process productivity considered. Chapter 6 uses those selected parameters to manufacture LPBF parts for performance testing, and directly compares the results with the cast pump housing benchmarks. Chapter 7 provides the conclusions and recommendations.

In Chapter 2, background information is presented for the LPBF technology and the processing of aluminum alloys. The working principle, main process parameter inputs, advantages, and challenges of the technology are introduced. A brief overview of the relevant aluminum alloy is provided, including a description of the microstructure, effect of alloying elements, common applications, and key differences between the cast and LPBF-processed microstructures. The literature review includes previous works investigating the relationship between LPBF processing parameters, microstructure, and resulting part properties for AlSi10Mg and other aluminum alloys, as well as design constraints for manufacturability of AlSi10Mg and several examples of applications for LPBF in fluid power and other areas.

In Chapter 3, general experimental procedures for material and performance characterization are described. These include powder material characterization through scanning electron microscopy and particle size analysis, a description of the additive manufacturing system used for printing and the two options for build environments, and material performance characterization through x-ray fluorescence spectroscopy, optical microscopy and image processing, x-ray computed tomography, laser confocal

microscopy, Rockwell hardness, linear dry sliding wear, scanning electron microscopy, energy dispersive x-ray spectroscopy, and electrochemical measurements.

In Chapter 4, a cast aluminum pump housing is characterized in order to provide benchmark values for evaluating the performance of LPBF for fluid power applications. First, the chemical composition and microstructure of the cast pump housing are investigated. The product is then characterized for performance based on its relative density, surface roughness, hardness, wear resistance, and corrosion resistance. The geometric features of the cast pump housing are also evaluated to provide minimum feature size requirements for the manufacturability constraint.

In Chapter 5, process parameters are identified for the LPBF of AlSi10Mg on a modulated laser system through iterations of manufacturing recipes and selection of final parameters based on three objectives: to minimize porosity, minimize surface roughness, and maximize production efficiency. This is accomplished through the use of initial process mapping using a full factorial design of experiment, prediction of melt pool dimensions and calculation of parameters using a thermophysical model, and fine-tune adjustment of the parameters to meet the desired objectives. Two parameter sets are identified for use in Chapter 6 – a high density option, and a high productivity option.

In Chapter 6, the selected process parameters are used to manufacture LPBF artifacts of various geometries for characterization in order to evaluate the performance of LPBF for fluid power applications. The artifacts are analyzed for relative density, surface roughness, hardness, wear resistance, corrosion resistance, and quality of geometric features such as thin walls, slots, and channels. The results are compared with the cast pump housing characterized in Chapter 4.

Finally, Chapter 7 provides the conclusions and recommendations that arise from this work.

## 2 Background and Literature Review

### 2.1 Laser Powder Bed Fusion (LPBF) Technology

Laser powder bed fusion (LPBF) is an additive manufacturing (AM) process that uses a laser to selectively melt powder into the shape of a part, layer-by-layer. The process begins with a digital part file generated by 3D CAD software and converted to a compatible file format such as an STL file, which describes the geometry of the 3D part. The STL file is imported into a preprocessing software, such as QuantAM (Renishaw, UK), to prepare it for the execution of the AM process or “printing”. For LPBF, this preparation includes selecting the print orientation for the part, generating support structures, and choosing the desired machine settings and process parameters. The ideal print orientation depends on the geometry of the part and the presence of design features such as cutouts and overhangs, which may require support structures. Support structures are extraneous geometry features attached to the part in order to provide anchoring of the part to a substrate and stability for gravity, as well as heat dissipation during the LPBF process to avoid part curling, distortion and over-heating. The support structures are printed as-one with the part, and must be removed during post-processing. The support structures are often a simple geometry such as cylindrical or X-shaped posts, however for highly complex parts, customized supports may be created in the 3D CAD software. When the part is ready to be printed, the preprocessing software segments or “slices” the part perpendicular to the build direction, such that the slice data may be used to print the part’s cross section, one layer at a time.

Figure 2-1 shows a schematic diagram of a general LPBF system. The working chamber is filled with an inert gas to minimize oxidation of the metal powder [1]. To print a single layer, first a thin layer of powder is spread across the so-called build plate (for the first layer) or build bed (for subsequent layers) in the working chamber using a tool to distribute and smooth the material. This tool may be a roller or a recoating blade. The laser is then delivered and focused to a fine spot size via optics used to direct the laser beam trajectory onto the powder bed. Finally, the build plate is incrementally lowered by one layer thickness using a piston mechanism to allow room for the next layer of powder to be spread on top and selectively melted using the focused laser beam. Additional powder is delivered to the build bed by using either a piston-based powder feed bed supply or a hopper-doser system. The process is then repeated until the part is complete. After printing, post-processing steps include and are not limited to powder removal, heat treatment, separating parts from the build plate, removal of support structures, and surface finishing.

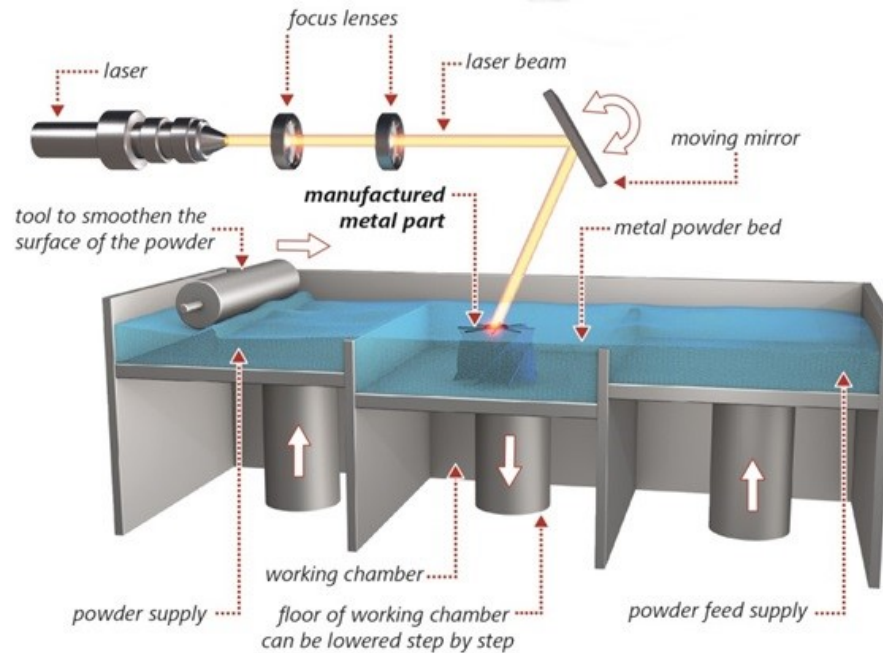


Figure 2-1: Schematic diagram of Laser Powder Bed Fusion equipment [2]

### 2.1.1 Advantages and Challenges in LPBF

In recent years, AM has been viewed as a mature technology ready for industrial uses, beyond research and development. Industry trends have shown that there is a high level of interest in AM technologies, with the level of adoption ranging from the preliminary evaluation of its capabilities, to full-scale production [3]. While there is still a wealth of opportunity for advancement in terms of machine development, material capabilities, and process optimization, the current technology is able to meet industrial manufacturing standards. Early adopters are now more informed about both the advantages and the challenges of the technology. Some of the main benefits of AM include the potential for more design freedom, reduced waste, and flexible production strategies. The challenges include product qualification, quality assurance, the development of manufacturing plans including process parameter selection and post-processing, and determining the relationship between processing parameters, part microstructures, and mechanical properties [4].

AM unlocks design potentials that cannot be achieved through traditional manufacturing methods. LPBF is well-suited for the manufacturing of internal features [5], passageways [6], and organic or complex geometries [7], therefore enabling specialized designs with reduced weight and enhanced performance. This includes designs created with topology optimization [8], functionally graded features [9], or integrated lattice structures [10], [11]. These design features support the development of innovative, intricate parts that can stand alone, or reduce the complexity of assemblies through

consolidation – thus propelling designers toward more elegant, practical solutions to complex engineering problems.

In addition, AM has the potential to reduce resource consumption and produce less waste when the full product manufacturing lifecycle is compared to other manufacturing methods, provided that sustainable design practices are employed [12], [13]. While laser-based processes have a high energy consumption during production, reductions in raw material usage and improvements in product functionality through lightweighting and optimized design may result in an overall positive environmental impact [13]. Because the part is built up layer-by-layer instead of machined out of a larger block of material or formed using molds and dies, less raw material is required to enter the supply chain through energy-intensive extraction and processing [14]. Unmelted powder material can be re-used in subsequent laser powder bed fusion processes, with little to no impact on the resulting part properties [15]–[17]. Additionally, LPBF does not directly require metalworking fluids such as coolant or lubricant, which may be toxic to the environment [14].

Another benefit is that AM provides the ability to pivot from concept to prototype quickly, resulting in accelerated design cycles. On-demand printing is made possible for the manufacture of legacy parts that have been stored digitally, which otherwise may be unobtainable due to the limitations of physical storage for discontinued parts or tooling. Additionally, manufacturers can offer a general design with different customizations available for each customer without making significant changes to the manufacturing process chain.

Despite the advantages, there are challenges inherent to the LPBF technology that may result in a failure to achieve the expected potentials of using this process. Because of the layer-by-layer melting and highly concentrated heat input introduced by a quickly moving, focused laser beam, LPBF parts experience cyclic thermal loading and very high solidification rates during production [18], [19]. The maximum cooling rate has been estimated to be 3 – 4 orders of magnitude higher than that attained during conventional casting processes [18]. As a result, parts manufactured by LPBF have a different microstructure and unique types of defects that may occur. These include geometric distortions caused by residual stress from inadequate heat dissipation, poor surface finish due to unstable dynamics in the liquid melt pool or the adherence of powder to the outside of the part, porous voids, and anisotropic properties that change the quality of the part depending on its build orientation [20]–[24]. Each material that can be used in LPBF has its own set of thermal and physical properties that may affect the outcome of the print, and therefore optimization of the printing parameters is required in order to ensure that the engineering requirements for the end-product can be met. Undesirable microstructures and defects such

as internal porosity may occur if the processing parameters fall outside of the range suitable for that material [25]. It is highly desirable to find a balance between part quality and productivity, which can be increased by using higher powers and faster laser scanning speeds, pushing process stability to the limits [4]. The mechanical properties are also impacted by the LPBF processing parameters and resulting microstructure, so therefore quality assurance is required to ensure part consistency and suitability for functional use. To aid in this respect, there are several established standards that provide guidelines for the production and testing of LPBF parts, however the specific requirements and processing parameters must be agreed upon between the manufacturer and the customer [26].

Pre- and post-processing of LPBF parts may present another challenge in achieving high production efficiency and low costs for high quality parts. During the pre-processing steps, the optimal build orientation, size, shape and number of support structures must be selected. Emerging software tools can help to automatically generate support structures and simulate the residual stresses that will occur during processing; however this is typically done manually based on the prior experience of the designer. The location of the part (or parts) on the build plate can also impact the final part quality because of variations in powder layer delivery [27], material ejection from the process zone [28], [29], direction of gas flow [30], and contributions from the laser optics. In order to mitigate the effect of AM production defects (pore defects, surface roughness, distortion, etc.), post-processing techniques such as surface polishing or sand-blasting, hot-isostatic pressure treatments, and heat treatments may be employed [25]. Even without these optional treatments, post-processing is always required for LPBF to remove parts from the build plate, and to remove support structures and unmelted powder from the parts, and therefore efficient post-processing methods must be developed [4]. There may be some opportunity for automation in the LPBF pre- and post-processing steps.

### **2.1.2 Process Parameters in LPBF**

There are numerous process inputs that can be modified in a laser powder bed fusion system in order to optimize the process performance and minimize defects. In the Renishaw AM400 machine, which was used for this work, there are over 100 such customizable process parameters. These parameters are divided into categories, as shown in Table 2-1. The full list of editable parameters can be found in Appendix A.

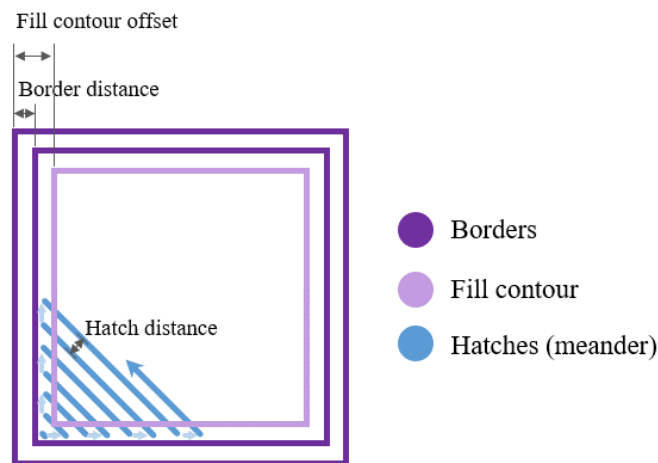


**Table 2-1: Process parameters for the Renishaw AM400 [31]**

Category	Description	Examples
General	Spatial information for part(s) that will be printed	Layer thickness, number of layers, position (X, Y)
Strategy	Hatch pattern strategy for how the laser scan will fill in the part's cross-section	Hatch pattern, size, offset, block sort/optimized sort
Control	Control (on/off setting) if hatches are used for the interior part volume, and if unique settings for the fill contours, upskin, or downskin of the part are used	Total fill, volume fill contours, volume hatch, upskin, downskin
Order	The order that the different hatch types will be scanned	Scan order (1 to 9), volume border in/out, volume fill contour in/out
Volume / Upskin / Downskin	Spatial information for how the hatch pattern, border(s), and fill contour(s) will be implemented	Beam compensation, number of borders, border distance, number of fill contours, fill contour distance, hatch distance, hatch increment angle, upskin/downskin number of exposures and number of layers
Scan Volume / Scan Upskin / Scan Downskin	The laser power and exposure settings for the border(s), hatches, fill contour(s), upskin, and downskin	Power, focus, point distance, exposure time

The “general parameters” listed in Table 2-1 are used to specify the location of the part(s) on the build plate in order to determine the geometric requirements of the build in 3-dimensional space. After choosing the best orientation for each part, its position is set using X-Y coordinates. The Z-coordinate can also be changed to modify the height of the support structures under the part. If multiple parts are being printed, they should be placed at a reasonable distance (at least 2 mm) from one another in order to minimize interference and allow for easy removal from the build plate. If possible, parts should also be placed near the center of the build plate in order to avoid failure if the powder bed becomes unstable or non-uniform near the edges of the plate, however this is highly dependent on the system utilized and on the mechanism for powder spreading. It is also beneficial to avoid placing long, flat edges perpendicular to the direction of powder spread or delivery, because the part edges may become slightly raised, and the recoating blade could collide with them and cause defects such as layer shifting. The layer thickness should be selected based on the powder particle size distribution and laser beam characteristics. The number of layers corresponds with the number of slices that will be generated with the part's cross-sectional geometric data, and is automatically calculated based on the layer thickness and the part height (including support structures) in the z-direction.

The “strategy” category of parameters are also listed in Table 2-1. The hatch pattern strategy refers to the pattern the laser scan will use to fill in the volume of the part. Three commonly used patterns are “meander”, which is a straight-line vector path that zigzags between the borders, “stripe”, which splits the part into strips of a specified length such that meander is then used within a strip, and “chessboard”, which is similar to stripe but splits the part into squares. In this work, the meander strategy is used. In addition to the hatches used to fill in the volume of the part, each layer of the build requires the laser scan path to trace the borders along the outside of the part. It is optional to also have additional borders and fill contours offset inward from the part’s edge, as illustrated in Figure 2-2. The scan order, distance between borders, distance between fill contours, and hatch spacing can all be specified. When a new layer is printed, the hatch pattern is rotated in the X-Y plane to avoid propagation of defects along the laser scan path. By default, the laser scan path skips directly over holes and continues in a straight line until a border is reached. Alternatively, optimized jumping can be enabled to reduce the scan time, but this may result in cold welds when the laser eventually jumps to the other side of the gap.



**Figure 2-2: Top view of laser scan path on a square cross-section of a part**

The scan strategy and the laser exposure settings can be changed for different locations of the part, depending on the part orientation. Portions of the part that are angled downward (facing the build plate) would be in contact with the powder bed rather than the previous layer of melted material. These surfaces are called the “downskin” and may require reduced energy input to avoid a poor surface finish caused by penetrating too deeply into the powder bed. Portions of the part that are angled upward (away from the build plate) and will not have subsequent layers build on top (hence they are an outside surface of the final part) are called the “upskin” and may require optimized parameters in order to eliminate visible laser scan tracks and improve the surface quality. Figure 2-3 shows an example of the upskin and downskin surfaces on a cube.

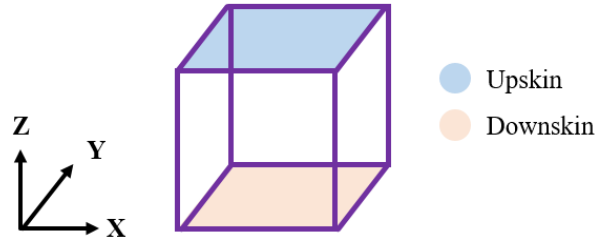


Figure 2-3: Upskin and downskin surfaces

The scan settings are used to specify the intensity and duration of the laser exposures by changing the laser power and the scan speed. The Renishaw AM400 utilizes a modulated laser system, meaning that the laser output is a discrete, point-by-point exposure rather than continuous. Each exposure results in a melt pool of metal that partially re-melts previously solidified layers as well. For a modulated laser system, the effective scan speed ( $v$ ) depends on two factors: the exposure time ( $t_e$ ) and the point distance ( $p_d$ ) between exposures, as shown in Equation 1. The drill time ( $t_d$ ) is a constant value that is used to correct for the delay that occurs when the laser is turned off and repositioned at the next exposure point. The point distance and exposure time are typically measured in  $\mu\text{m}$  and  $\mu\text{s}$ , while the effective scan speed is on the order of  $\text{mm/s}$  or  $\text{m/s}$ .

$$v = \frac{p_d}{t_e + t_d} \quad \text{Equation 1}$$

The Renishaw AM400 laser spot diameter can vary from  $66 - 75 \mu\text{m}$ , depending on the machine calibration. The spot size can also be modified by moving the focal point above or below the powder bed.

During the LPBF process, it is highly important to control the amount of energy input from the laser to the material, as too much heat can cause excessive material boiling and the formation of keyhole porosity, while too little will result in a lack of fusion between hatch lines or layers [32]–[34]. The volumetric energy density (VED), measured in  $\text{J}/\text{mm}^3$ , is a metric often used to describe the energy input to the system, which combines the power input ( $P$ ) with the geometric factors of layer thickness ( $l$ ), laser spot diameter, ( $d$ ), and scan speed, ( $v$ ), as shown in Equation 2. In some cases, the hatch spacing is used instead of the laser spot diameter [35]. For the modulated laser system, the equation can be rewritten with point distance and exposure time, as shown in Equation 3. The VED has been used in literature to develop processing windows for different materials [21], [36]–[39]; however, its use is limited in explaining quality outcomes because the VED fails to capture the complex laser-material interaction phenomena in the melt pool region [40], [41]. For instance, the same VED can be achieved

based on multiple combinations of process parameters, and some parameters constituting a sufficient VED may still result in unfavourable process outcomes. In this thesis work, in addition to the VED method, a process window identification strategy based on modeling theory (developed elsewhere) was deployed and will be discussed in Chapter 5.

$$VED = \frac{P}{v d l} \quad \text{Equation 2}$$

$$VED = \frac{P}{\frac{p_d}{t_e} d l} \quad \text{Equation 3}$$

In addition to the process parameters that can be modified on the Renishaw AM400 machine and LPBF machines in general, there are many other considerations which will affect the outcome of the build. These include but are not limited to the type of powder recoater, type of powder feed system, build plate material and thickness, powder collection and recycling method, build chamber atmospheric conditions, and powder characteristics including material, morphology, size, and rheology [42]. In addition, the design features play a role in the quality outcomes and are discussed in Chapter 6.

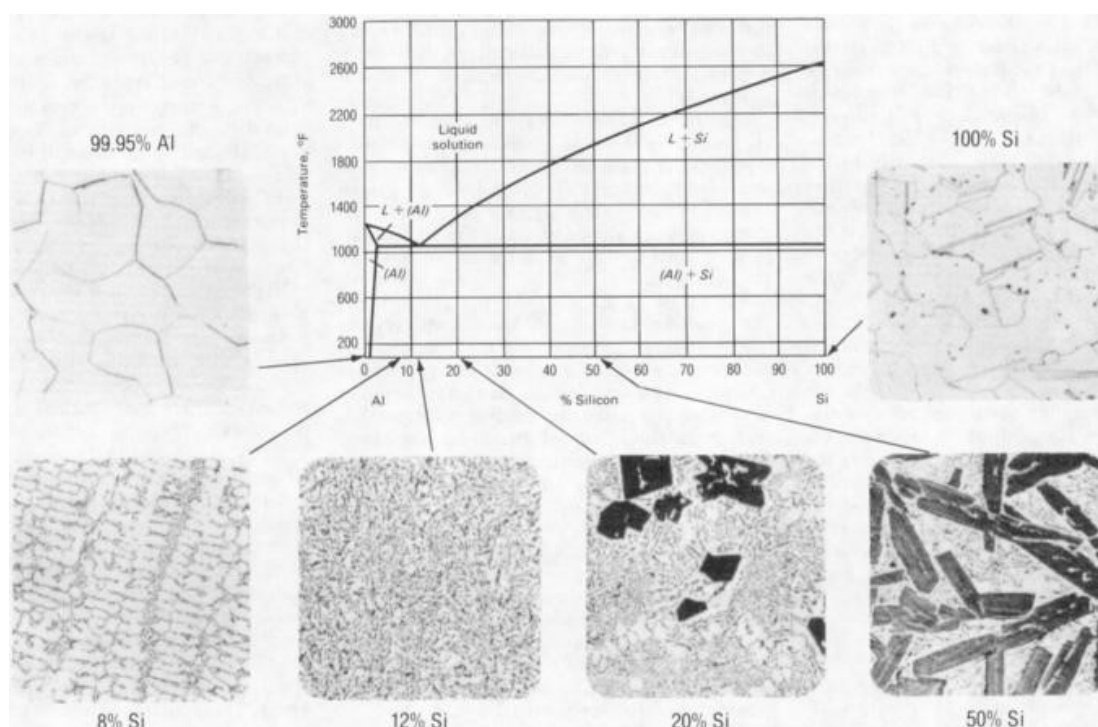
## 2.2 Laser Powder Bed Fusion of AlSi10Mg

### 2.2.1 Al-Si Alloys

Some of the most extensively used aluminum casting alloys are in the Aluminum-Silicon + Copper and/or Magnesium family of alloys (3xx.x) [43]. Such alloys are readily welded and have excellent fluidity, high strength, and high toughness. Conversely, commercially pure aluminum has low strength, so it is primarily only used in electronic applications due to its high conductivity. The addition of silicon results in high fluidity, which is important for casting because improved feeding into the mold can reduce defects such as cracking and shrinkage porosity. Higher silicon content also decreases the thermal expansion coefficient, which is useful for engine applications such as pistons and cylinder blocks [44]. The addition of magnesium renders the alloy harder and stronger by providing solid solution hardening, or precipitation strengthening through the formation of the  $Mg_2Si$  phase [45]. The addition of copper can also increase the strength of the material system by facilitating hardening or the formation of precipitates, however it reduces the ductility and corrosion resistance of the alloy [43].

The Aluminum-Silicon family (4xx.x) has excellent fluidity and the alloys can be used to create intricate castings with moderate strength and high ductility and impact resistance; however, without a small addition of Cu or Mg, they are not heat-treatable. The aluminum-silicon phase diagram is shown

in Figure 2-4. The eutectic composition occurs at approximately 12 wt% Si, and commonly used alloys range from 9.0 – 13 wt% Si because the freezing range is small and helps avoid casting defects such as coring [43]. The hypoeutectic microstructure, such as that pictured for 8% Si, consists of long dendrites of primary aluminum surrounded by the eutectic composition. When the primary phase is silicon, as it is in the hypereutectic microstructures (20 and 50% Si), the primary crystals take the form of geometric shapes or coarse particles. This results in a higher wear resistance, but may also cause poor machinability and casting defects such as gravity segregation. The deleterious effects may be mitigated by using a modifier that encourages nucleation of primary silicon, or by rapid cooling during solidification in order to refine the microstructure. The coarseness of shrinkage porosity is proportional to the grain size, which is typically 0.13 – 13 mm for casting [43]. Large grains are also more susceptible to shrinkage and hot cracking, and have worse tensile strength and ductility.



**Figure 2-4: Aluminum-Silicon phase diagram [46]**

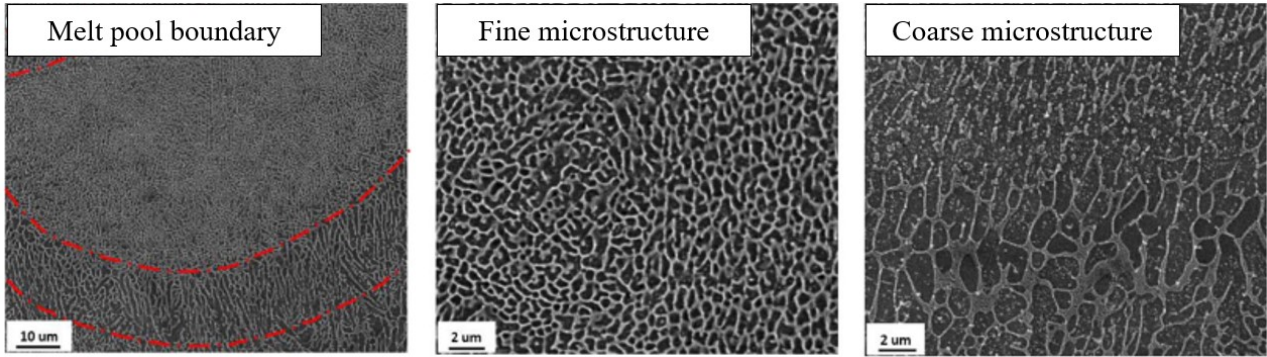
The AlSi10Mg alloy is the AM equivalent to the A360.0 casting alloy. The low density and relatively high strength of aluminum make it an ideal choice for applications requiring a high specific strength. Al-Si-Mg alloys are often used in the automotive and aerospace industry because lightweighting of parts results in reduced fuel costs [34]. A360.0 is a popular choice for cover plates, housings, production tools, engine parts, and hinges [44], [47]. AlSi10Mg has a high reflectivity and thermal conductivity, which affects the material interaction with the laser and the melt pool formation during

LPBF processing [48]. This means that the AlSi10Mg material may require a higher initial energy input to compensate for the rapid heat dissipation and low absorptivity of the incident laser beam [19], [34]. However, the absorptivity also abruptly increases as the material undergoes melting, thus the melt pools can quickly become unstable and transition from conduction mode melting to keyhole [49]. This renders AlSi10Mg a challenging material system to work with in LPBF. In addition, the low-density, lightweight nature of the powder material can result in poor flowability, which would impact the ability to spread a uniform layer of powder onto the build bed [34].

The macrostructure of AlSi10Mg parts manufactured by LPBF typically features a fish scale morphology with the melt pools and melt pool boundaries clearly visible, as shown in Figure 2-5. It has been noted that the microstructure consists of three zones: the fine, coarse, and heat affected zone [18], [19], [23]. Figure 2-6 shows low and high magnification SEM images of the fine and coarse microstructures. The fine microstructure is located in the interior of the melt pool and consists of a very fine, submicron-sized cellular dendritic structure of  $\alpha$ -aluminum with a silicon-rich intercellular phase [15], [18], [19], [23]. Because there is a thermal gradient within the melt pool, the variation in solidification rate results in a coarse microstructure with larger dendritic  $\alpha$ -Al cells located in the vicinity of the melt pool boundaries [15], [18], [19], [23], [24]. The lamellar Al-Si eutectic is also present in the Si-rich network between cells [18], [19], and nano-sized Si-rich precipitates have been observed within the  $\alpha$ -Al phase [18]. A narrow heat affected zone is present near the edges of the melt pool boundaries, where an increased diffusion rate of Si results a coarsening of the Si-rich phase into distinct particles, breaking up the intercellular network [15], [19], [23]. The presence of magnesium in the alloy could induce  $Mg_2Si$  precipitate formation upon heat treatment; however, depending on the processing parameters and build plate temperature, the  $Mg_2Si$  phase may or may not be observed in the as-printed samples [19], [50].



**Figure 2-5: Optical micrograph of AlSi10Mg processed by LPBF, side cross-section**



**Figure 2-6: SEM images of the microstructure of LPBF-processed AlSi10Mg, from [15]**

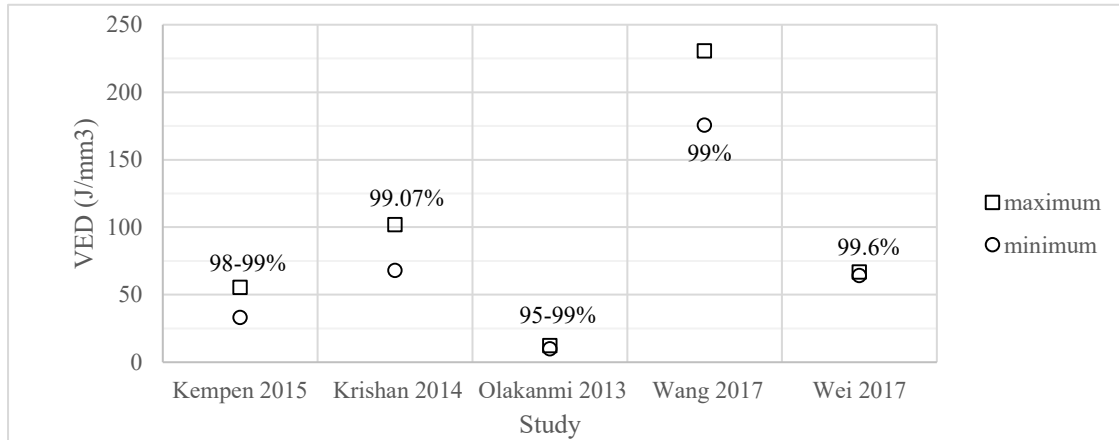
LPBF processing of AlSi10Mg using continuous laser beams has been extensively studied in order to investigate the relationship between processing parameters, microstructure and resulting properties, including density [1], [14], [21], [24], [36]–[39], [51]–[54], surface roughness [21], [48], [55], [56], hardness [19], [22], [36], [39], [57]–[60], wear properties [35], [60]–[65], and corrosion behaviour [66]–[75]. The modulated laser beam LPBF has not received similar attention in literature and is the focus of this work.

### **2.2.2 Parameter Optimization for Al-alloys**

#### ***Bulk Density Studies:***

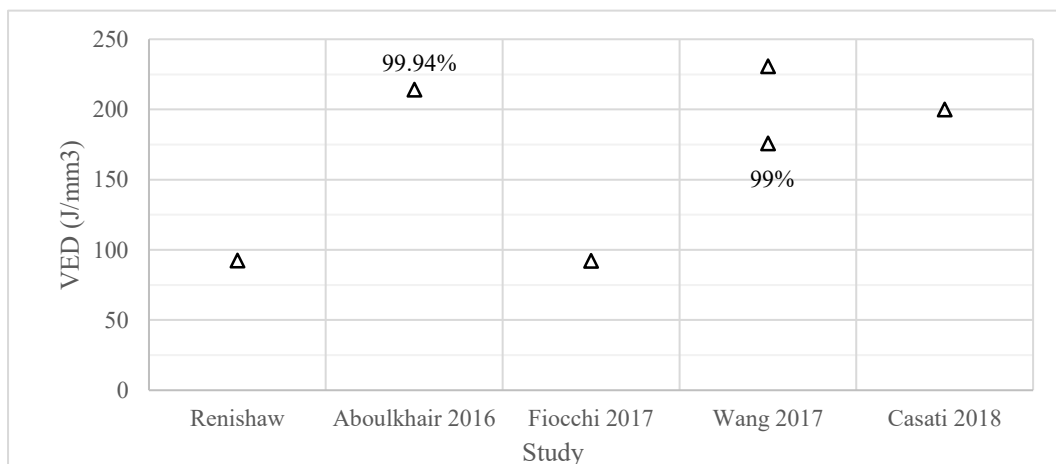
There have been numerous studies on achieving near-fully dense parts through the LPBF of AlSi10Mg [1], [14], [21], [24], [36]–[38], [48], [51]–[53]. Several research groups have recommended an ideal processing window, which is displayed in Figure 2-7 in terms of the volumetric energy density ( $J/mm^3$ ), for specific LPBF systems. Kempen et al. defined a processing window in which a stable melt pool is formed, and within that window, an optimized range for achieving a high relative density of around 98–99% [36]. Krishan et al. performed a full factorial experiment in order to determine which processing parameters had a significant effect on the resulting properties [37]. They identified a range of energy densities in which the changes in scanning speed and hatching distance had little effect, and so these parameters could be changed within that range to optimize the core properties up to a maximum relative density of 99.07%. Olakanmi et al. examined a variety of Al, Al-Si, and Al-Mg powders and found a range of energy densities beyond which there was no benefit toward further increase in the part's relative density, which were around 95–99% [38]. Wang et al. investigated the effect of energy density on resulting part density and surface roughness for parts manufactured by the Renishaw AM 250, which is a modulated laser system [21]. They suggested a range of laser point distances and exposure times resulting in high densities, and a maximum of 99% relative density was achieved. Wei et al.

investigated the influence of the laser power, scanning speed, and hatch spacing on the part density and identified two sets of processing parameters that resulted in a high relative density of around 99.6% [39].



**Figure 2-7: Recommended ranges of volumetric energy density for LPBF of Al-alloys [21], [36]–[39]**

Because the interaction between the laser and the material is different for continuous and modulated LPBF systems, the exact processing parameters required for a high density part may not be directly transferrable between laser types. Figure 2-8 shows the volumetric energy density calculated from processing parameters that were optimized specifically for a modulated laser system. The default manufacturing recipe for AlSi10Mg provided by Renishaw plc. is also provided as a point of reference [76]. Alboukhair et al. achieved a maximum relative density of 99.94% [54]. Fiocchi et al. and Casati et al. used previously optimized parameters from separate studies to investigate the effect of heat treatment on the microstructure [77], [78].



**Figure 2-8: Volumetric energy density for LPBF of Al-alloys using a modulated laser system [21], [54], [76]–[78]**



### ***Surface Roughness Studies:***

The surface roughness is also influenced by the LPBF processing parameters, and will vary depending on the build orientation of the part. The side surface roughness can be improved by optimizing the manufacturing parameters used at the part border. Likewise, the top and bottom surfaces can be optimized through the upskin and downskin scan parameters. Kempen et al. observed that the surface quality will improve with an increasing energy density as long as the melt pool remains stable [48]. After optimizing process parameters for a high relative density, they measured a corresponding top-surface roughness (Ra) of around 20  $\mu\text{m}$ . Melt pool instabilities may result in surface defects such as balling, which occurs when the molten track forms large droplets due to high surface tension or insufficient wetting, and satellites, which are distinct particles that adhere to the surface due to splattering and do not experience sufficient energy input to re-melt [56], [59]. Boschetto et al. investigated the balling defect for the development of a model for LPBF of AlSi10Mg that can predict surface roughness based on part geometry [56]. Using the “original EOS parameter set for AlSi10Mg”, which was provided by the LPBF system manufacturer (EOS GmbH, Munich, Germany), they observed a side surface roughness (Ra) of 6.52  $\mu\text{m}$  and a top surface roughness (Ra) of 23.9  $\mu\text{m}$ . Calignano et al. used a Taguchi orthogonal array design of experiment to determine optimized parameters for reducing the top surface roughness (Ra) and achieved a minimum value of 14.35  $\mu\text{m}$  on the as-built surface, and 2.50  $\mu\text{m}$  after shot-peening [55]. Wang et al. determined optimized parameters for reducing top surface roughness (Ra) using a modulated laser system and measured values ranging from 4.1 to 8.1  $\mu\text{m}$  [21].

### ***Hardness Studies:***

Hardness values of the as-built AlSi10Mg alloy are reported in literature as ranging from 127 to 145 HV (71 – 78 HRB) [19], [22], [36], [57]. An increase in hardness has been observed after post-processing treatments such as media blasting of the surface or aging heat treatments [36], [58]. Nano-hardness measurements have ranged from 2.25 to 2.71 GPa, exceeding the nano-hardness of the cast counterpart, which was around 1.1 to 1.52 GPa if the measurements taken directly on a coarse Si-flake are excluded [39], [59]. The nano-hardness at melt pool borders was observed to be higher than that at the core [39].

### ***Hardness and Wear Resistance Studies:***

The tribological properties of AlSi10Mg are impacted by LPBF processing, as the wear resistance is correlated to the hardness of the material [35], [60], [61]. Higher hardness and a lower coefficient of friction typically result in better wear resistance. Kang et al. investigated the effect of laser power on

the hardness and dry sliding wear properties of a hypereutectic Al-Si alloy (18 wt% Si) [61]. They found that the as-built samples had the same coefficient of friction; however, the softer materials exhibited a longer period of fluctuation caused by cyclic cold-welding and fracture before a stable surface was established. The sample obtained at a power of 210 W had the highest relative density (96%), hardness (105 HV), and the lowest wear rate of about  $7.0 \times 10^{-4} \text{ mm}^3 \text{ N}^{-1} \text{ m}^{-1}$ . It was also found that higher Si content resulted in a better wear resistance (50 wt% Si resulted in a minimum wear rate of  $5.5 \times 10^{-4} \text{ mm}^3 \text{ N}^{-1} \text{ m}^{-1}$ ) [62]. The wear tracks exhibited deep parallel grooves of local deformation, delamination cracks, debris, and a selective oxide region. Similar observations have been made in other studies of Al-alloys, and are indicative of types of abrasive and oxidative wear [61], [63]–[65]. Prashanth et al. found that the as-printed AlSi12 had better wear resistance in sliding and fretting when compared to its cast counterpart and printed samples that had undergone an annealing heat treatment [63]. Liu et al. tested the dry sliding wear properties of AlSi10Mg sampled from the top surface and the core of a part produced by LPBF [60]. Both the hardness and the wear resistance of the surface were better than the core, demonstrating a gradient in mechanical properties due to the variable cooling rate in LPBF. Islam and Farhat found that the size, shape and amount of pores in Al-Si alloys processed by power metallurgy impacted the material removal mechanism during dry sliding wear [64]. The primary wear mechanism was delamination due to subsurface cracks initiating at the pores. The wear rate increased with surface porosity, then decreased when the pore size reached a critical value relative to the size of the probe tip, despite the reduction in hardness that accompanied the increased porosity.

### ***Corrosion Resistance Studies:***

With proper process control, AM parts can have improved corrosion resistance. Leon et al. compared the corrosion behaviour of AlSi10Mg manufactured by LPBF with that of its counterpart cast alloy in an electrolyte of 3.5% NaCl solution with naturally dissolved oxygen [66]. The additively manufactured alloy showed a better corrosion resistance than the cast alloy, as the higher solidification rate during LPBF had resulted in a more homogenous microstructure with fewer precipitates and defects. The AM alloy also had a higher low cycle corrosion fatigue lifespan than the cast alloy, which exhibited accelerated cracking due to gravity casting defects such as irregular pores. Leon and Aghion also compared polished and unpolished AlSi10Mg samples evaluated in air and in 3.5% NaCl solution and found that surface roughness had a detrimental effect on the low cycle corrosion fatigue life, possibly due to the higher amount of cavities and surface defects [67]. Studies by Cabrini et al. examined the effect of build orientation, heat treatment, and surface finish on the corrosion resistance of AlSi10Mg manufactured by LPBF through potentiodynamic testing [68]–[71]. It was found that the transverse plane (perpendicular to the build platform) had a slightly lower corrosion resistance when compared

with surfaces oriented parallel to the build platform, when evaluated in aerated diluted Harrison solution (3.5 g/L of  $(\text{NH}_4)_2\text{SO}_4$ , 0.5 g/L di NaCl, pH 5.5) [68]. A low temperature stress relief heat treatment did not reduce penetrating localized corrosion in aerated diluted Harrison solution, while an annealing treatment promoted the coalescence of Si particles which formed a galvanic couple with the Al matrix and resulted in localized corrosion without penetrating attack [69]. The shot-peened or polished surface finishes showed an increased pitting potential and decreased corrosion rate when compared with the as-built surface, when evaluated in aerated diluted Harrison solution [70]. Two surface types were tested in aerated NaCl solutions, with a concentration ranging from 0.01 to 0.6 mol/L [71]. It was found that at low chloride levels ( $<0.05$  M), the corrosion behaviour of the as-built and polished surfaces was significantly different, with the as-built surfaces showing lower pitting potentials. Both surface types experienced selective attack at the melt pool borders due to the potential difference between the Si-particles and the  $\alpha$ -Al matrix. Duchardt et al. used a custom test apparatus to investigate the effect of thermal loading and local boiling of water-based coolant on the corrosion behaviour of AlSi10Mg [72]. Various coolants containing silicium and/or organic acid were tested, and depending on the composition it was found that an increase in flow coolant temperature resulted in either an increase in general corrosion or an increase in the formation of a protective layer, which may or may not be stable depending on the thermal loading. Cavitation erosion has also been studied for AlSi10Mg fabricated by LPBF, using the apparatus and methods from the ASTM G32 and G134 standards [73]–[75].

### ***Further Studies:***

Several other mechanical properties have been studied in the context of LPBF parameter optimization for aluminum alloys, including tensile strength and elongation [14], [23], [36], [52], [54], [79]–[83], fatigue [1], [84]–[87], impact toughness [88], electrical properties [89], and creep [52]. Such studies are considered beyond the scope of the present thesis.

### **2.2.3 Design Considerations for LPBF and Applications**

Additive manufacturing can provide design freedoms that are not possible with traditional manufacturing methods; however, there are limitations that must be considered to ensure manufacturability. For LPBF, these constraints may include the types of materials available, the type of machine and its processing parameters, and the types of geometric features that can successfully be produced. The challenge for designers is identifying those limitations with enough accuracy to add value to their designs. There are several design frameworks that exist to help document design

guidelines and rules, aiding designers by limiting design features depending on the context [90], [91]. One example is the modularity method proposed by Jee et al., wherein logic statements are written for each design feature by breaking it down into its essential “primitives” or measurable feature parameters, and linking those primitives to limiting thresholds for known outcomes, thus allowing for the creation of quantitative design rules [90]. For LPBF, the primitives for any design feature may fall under three different categories: geometric (feature dimensions, locations, orientations, angles), process-related (machine type, layer thickness, scan strategy, scan speed, power, build orientation), or material-related (chemical composition, density, powder size distribution, particle morphology). Other design considerations may include the product requirements such as functionality, operating environment, 3D shape criteria including creation of mating surfaces for integration into assemblies, selection of quality assurance metrics for evaluating the design, life cycle and durability, sustainability including carbon footprint and recyclability, and total costs.

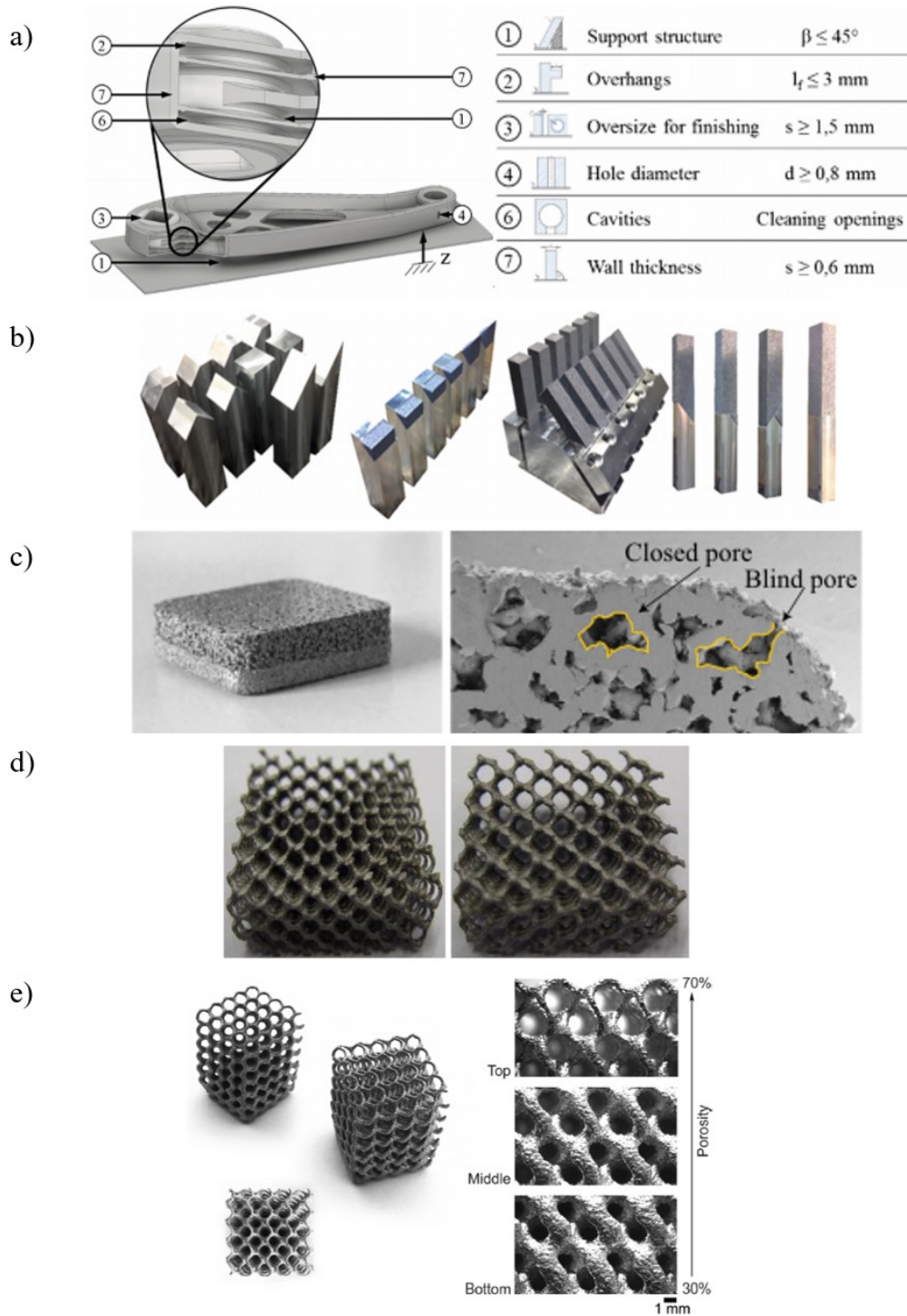
While many machine manufacturers will provide estimates for the typical feature resolution that can be obtained, it is not possible to generalize the quality that can be obtained for varying geometries of different shape and complexity. For example, the article entitled “Design for Metal AM – A Beginner’s Guide” published by Renishaw recommends avoiding lateral holes with a diameter less than 0.4 mm, using support structures for lateral holes with a diameter greater than 10 mm and for horizontal overhangs longer than 1 mm, and avoiding overhangs at less than 45° from the build plate [92]. However, these values may vary depending on the processing parameters, material, and the exact dimensional accuracy and surface quality required for the application. Overhang structures, otherwise known as downward-facing surfaces, can experience manufacturing defects such as poor surface quality due to the staircase effect and dross formation, or sagging and warpage that occurs due to thermal stress exceeding the material yield stress [93], [94]. These issues may be mitigated through the use of support structures, however, there is a need to balance the improvements in structural integrity and geometric accuracy with the additional resources consumed through time-limiting post-processing and material waste [93].

In research studying the LPBF processing of AlSi10Mg, efforts have been made to determine geometric parameters of overhangs based on overhang ratio (height change/distance), angle, and curvature for which support structures are not required [95], and to evaluate different support structure types to determine the corresponding part structural performance [93] or select the optimal support structures [94]. The use of support structures was found to reduce dross defects and improve the compressive strength of circular and half-circle overhangs [93]. It has been noted that generally overhangs at angles less than 30° from the build platform will always require support, while angles greater than 45° are self-

supporting. Angles ranging from  $30^\circ - 45^\circ$  were found to be self-supporting but had high surface roughness and distortion in the flatness of the bottom face [94].

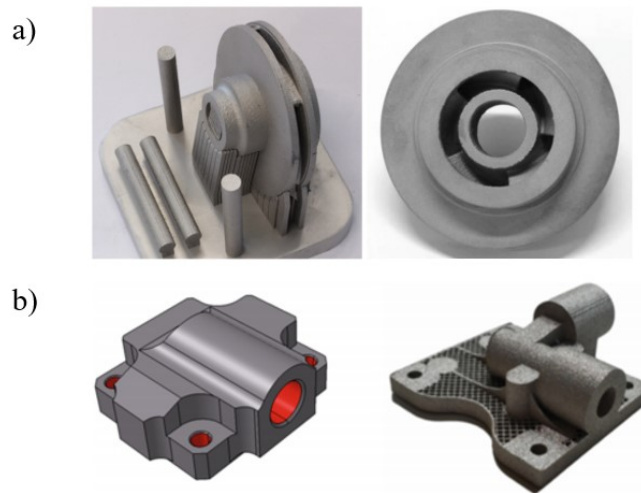
The limits of dimensional accuracy have also been investigated for LPBF of AlSi10Mg. The exact minimum feature size that can be produced is dependent on several factors including the processing parameters and resulting melt pool size, the laser spot size, and the powder particle size distribution. A minimum wall thickness of 0.140 mm ( $\pm 0.040$  mm) has been achieved, while the 0.200 mm thick wall from the same study had near-zero dimensional error between the CAD and the as-built wall [41]. Parallelepiped-based pins have been produced down to a minimum side length of 0.8 mm, below which the sharp edges were no longer discernable [11]. The parameters used to generate the STL geometry from the CAD file can affect the geometric tolerance and surface roughness of the final part, and by choosing good parameters for the angle tolerance and deviation control, researchers were able to successfully print a gyroid lattice structure with a minimum strut diameter of 0.48 mm [11]. The manufacture of internal channels is dependent on factors such as diameter, cross-sectional geometry, length, pathway / curves, and build orientation. It is necessary to determine boundary conditions for designers to maintain good dimensional accuracy and to reliably clear the powder from channels after manufacturing. For AlSi10Mg, a dependency on length was observed and a minimum channel diameter of 0.75 mm was recommended [96].

LPBF has been used to create parts made from AlSi10Mg for both structural and non-structural applications, with notable case study examples illustrated here. Lippert et al. created a lightweight pedal crank using topology optimization, resulting in a part featuring cavities and internal structures [97]. Figure 2-9-a shows the pedal crank CAD and detail view alongside the selected design guidelines that were used to constrain the geometry. Yousif et al. developed an AM approach to repairing structural beams under transverse loading using LPBF of AlSi10Mg to build-over cast aluminum alloys, as shown in Figure 2-9-b [98]. Calignano et al. created metal foams with controlled porosity, shown in Figure 2-9-c, for use in applications such as heat exchangers, water purification, or biomedical devices [99]. Lightweight, periodic lattice structures have been manufactured with varying unit cell sizes and volume fractions by Yan et al. (Figure 2-9-d) and Calignano et al. (Figure 2-9-e) [10], [11].



**Figure 2-9: Applications for LPBF of AlSi10Mg: a) Optimized model of the pedal crank and relevant design guidelines [97]; b) Stages of AM repair of aluminum beams, from cast parts (left) to final model (right) [98]; c) Foam built by LPBF of AlSi10Mg [99]; d) AlSi10Mg periodic lattice structures with a volume fraction of 10% and a unit cell size of 4 mm (left) and 5 mm (right) [10] e) AlSi10Mg gyroid lattice structure with varying volume fraction [11]**

LPBF has been used for fluid power applications such as a pump impeller and a hydraulic safety valve [100], [101]. The pump impeller, shown in Figure 2-10–a, was a traditionally cast part that had design features at the lower limit of castability, and was investigated to determine the optimal print orientation and support structure design [100]. Figure 2-10–b shows a hydraulic safety valve for use in aerospace applications, before and after weight optimization and manufacture by LPBF [101].



**Figure 2-10: LPBF applications in fluid power: a) IN625 pump impeller on the build plate (left) and after post-processing (right) [100]; b) Hydraulic safety valve original design (left) and optimized design with 20% weight (right) [101]**

## 2.3 Research Contributions

While the current literature casts a wide net exploring the general properties of LPBF-processed AlSi10Mg, this thesis will use a structured approach to explore the properties in the context of tailoring the process for fluid power applications. The work will focus firstly on benchmarking the properties of a general aluminium pump housing for fluid power applications (Chapter 4), followed by LPBF parameter optimization for increased density in the core, with process speed as an important consideration, and surface roughness parameter optimization (Chapter 5). The best selected recipes for the core and skin will then be used to manufacture LPBF artifacts for performance characterization and comparison with the cast benchmarks in terms of density, surface roughness, hardness, wear resistance, corrosion resistance, and manufacturability of geometric features (Chapter 6).

# 3 General Experimental Procedures for Material and Performance Characterization

## 3.1 Powder Material Characterization

Pre-alloyed AlSi10Mg powder was obtained from two different suppliers. According to the supplier specifications, the AlSi10Mg powder particle size ranged from 20 to 63  $\mu\text{m}$  and had a chemical composition as shown in Table 3-1.

**Table 3-1: Chemical composition of AlSi10Mg powder [45], [102]**

Element	Supplier 1 (wt%)	Supplier 2 (wt%)
Aluminum	Balance	Balance
Silicon	9.00 to 11.00	9.0 to 11.0
Magnesium	0.25 to 0.45	0.2 to 0.45
Iron	< 0.25	< 0.55
Nitrogen	< 0.20	-
Oxygen	< 0.20	-
Titanium	< 0.15	< 0.15
Zinc	< 0.10	< 0.10
Manganese	< 0.10	< 0.45
Nickel	< 0.05	< 0.05
Copper	< 0.05	< 0.05
Lead	< 0.02	< 0.05
Tin	< 0.02	< 0.05

### 3.1.1 Scanning Electron Microscopy

The surface morphology of the powder was examined using scanning electron microscopy (Zeiss LEO FE-SEM 1530, Waterloo Advanced Technology Laboratory). A small sample of powder was adhered to carbon tape and placed in the SEM chamber. The equipment was set to secondary electron mode, the operating voltage was 15 kV, and the working distance ranged from 9.7 to 13.3 mm. Several micrographs were taken at randomized locations and at magnifications of 50x, 100x, 150x, and 200x.

### 3.1.2 Particle Size Distribution

The powder particle size distribution was measured using a dynamic image particle size / shape analyzer (Camsizer X2, Retsch Technology). The X-Jet module was used to eject the particles with a nozzle gap width of 4.0 mm and a dispersion pressure of 30 kPa. The dispersed particles pass in front of pulsed LEDs and the shadows are captured with two digital cameras optimized for high resolution or large field of view. Digital image processing software is then used to analyze each particle. The size



was quantified using the  $X_{c,min}$  measurement, which is the minimum chord length across an irregular-shaped particle. The measurement was repeated 5 times for each powder type using samples of approximately 690 mg, and the samples were taken after mixing the powder on a tumbler for 10 minutes.

## 3.2 Printing Process

The Renishaw AM400 laser powder bed fusion printer, shown in Figure 3-1, was used for the production of all AM parts. It features a 400W yttrium fibre laser (1064 nm wavelength) with a focus diameter of 70  $\mu\text{m}$ . It has a build rate of up to 20  $\text{cm}^3/\text{hr}$  and a maximum laser scan speed of 2 m/s. The powder layer thickness can typically range from 20  $\mu\text{m}$  to 100  $\mu\text{m}$ . The printing process takes place under an inert atmosphere, generated by drawing a vacuum and filling with argon gas to reach a concentration of less than 0.1% oxygen gas in the chamber. The gas is recirculated to reduce overall consumption, and there is a secondary gas flow diverted past the laser window in order to protect it from contamination.



Figure 3-1: Renishaw AM400 laser powder bed fusion machine [103]

### 3.2.1 Full Build Environment

The Renishaw AM400 full build environment has a build volume (W x D x H) of 250 mm x 250 mm x 300 mm and a typical maximum build envelope of 248 mm x 248 mm x 285 mm. Powder delivery occurs through the use of a hopper-doser system that deposits material along the edge of the build area by gravity-induced powder flow. The powder recoater then spreads the material over the build plate in a thin layer. Figure 3-2 shows a photograph of a print in progress in the full build environment (left) and a screenshot of the build plate in the QuantAM preprocessing software (right). The direction of powder spreading and gas flow is indicated.

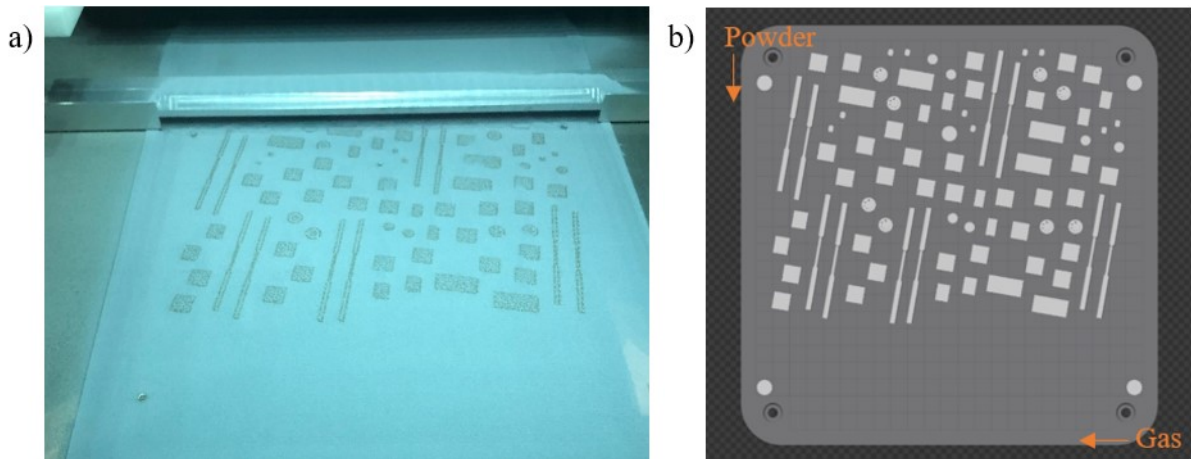


Figure 3-2: a) Renishaw AM400 full build environment; and b) top view of the build plate when viewed in QuantAM software

### 3.2.2 Reduced Build Volume Environment

The Renishaw AM400 Reduced Build Volume (RBV) is a retrofit insert that allows for reduced material usage and rapid development cycles for experimental materials or process parameters. The RBV environment has a build volume (W x D x H) of 80 mm x 80 mm x 64 mm and a typical maximum build envelope of 78 mm x 78 mm x 55 mm. Powder delivery occurs through the use of a dosing piston that moves incrementally upwards after each layer so that when the powder recoater passes over it, a thin layer of material is spread across the build plate. Figure 3-3 shows a photograph of a print in progress in the reduced build volume environment (left) and a screenshot of the build plate in the QuantAM preprocessing software (right). The direction of powder spreading and gas flow is indicated.

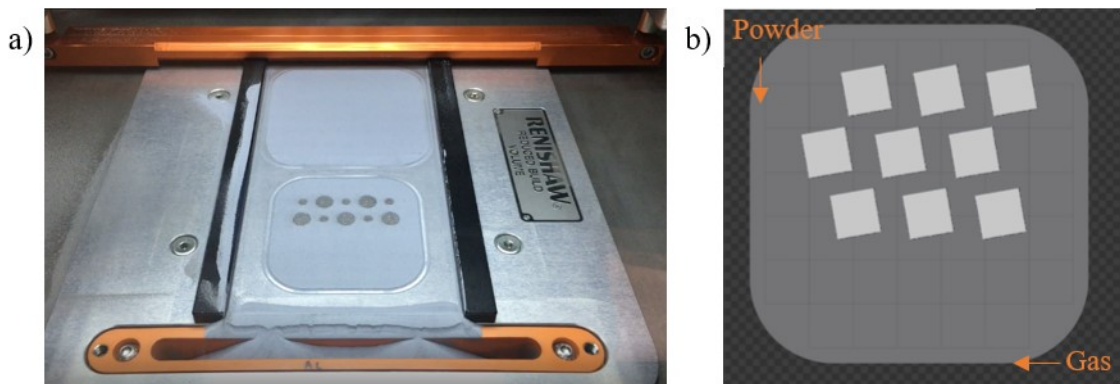


Figure 3-3: a) Renishaw AM400 reduced build volume environment; and b) top view of the RBV build plate when viewed in QuantAM software

### **3.3 Material Performance Characterization**

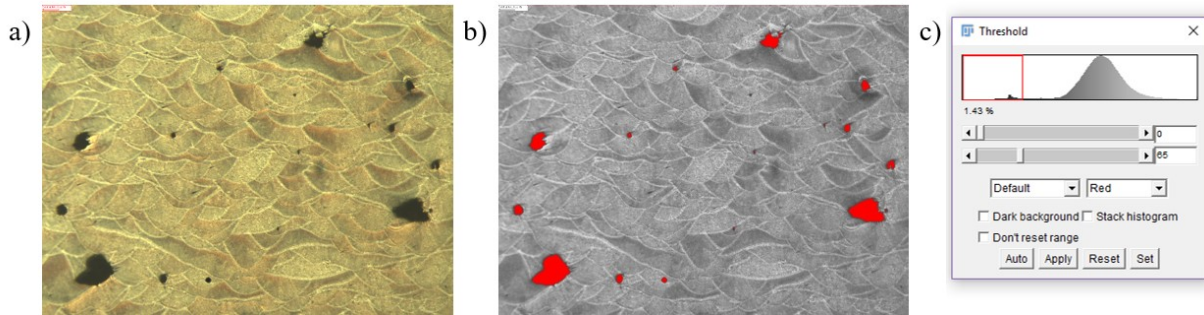
#### **3.3.1 X-Ray Fluorescence Spectroscopy**

A handheld X-ray fluorescence (XRF) analyzer (Thermo Scientific Niton XL3t XRF Analyzer) was used to provide nondestructive bulk chemical analysis of the cast pump housing. The XRF analyzer uses a low-wattage X-ray tube, and detection is limited to magnesium and heavier elements. XRF is a surface measurement technique, so the sample surface was cleaned with isopropanol prior to analysis, and it was assumed that the surface chemistry was representative of the bulk material. The instrument face was placed in direct contact with or as close as possible to the sample. Two different locations were measured for each part. After irradiation, X-rays emitted from the sample were measured by the detector and the data was automatically processed to identify the composition and alloy grade, if applicable.

#### **3.3.2 Optical Microscopy and Image Processing**

Samples were prepared for optical microscopy (Olympus BX Series optical microscope) using standard metallographic techniques. The samples were sectioned using a precision cutoff saw (Buehler Isomet 1000), and then hot-mounted by conductive powder, as needed. Mounted samples were then ground using SiC papers, beginning with 500 grit and subsequently grinding with finer abrasives up to 4000 grit. The samples were then polished using 6, 3 and 1 micron diamond suspension to a mirror-like surface. The polished samples were etched using Keller's etchant (190 mL Distilled water, 5 mL Nitric acid + 3 mL Hydrochloric acid + 2 mL Hydrofluoric acid) in order to reveal the laser melt pools created due to melting and solidification of the material during the printing process. Micrographs were taken at various locations including the top edge and the core of the sample.

LPBF parts produced for Section 5.2 were analyzed for porosity based on optical micrographs. Image processing was performed using ImageJ software (Version 1.52i) in order to obtain an estimate for the percent area of porosity in each micrograph. First, the RGB image was converted to 16-bit greyscale. Then an intensity threshold was manually selected for differentiating the pores in the image from the solid part, so that only the pores were highlighted based on the greyscale value of each pixel, as shown in Figure 3-4. The area fraction of the pores was then calculated, thus providing an estimate for the density of the part. A minimum of 5 micrographs with a field of view of approximately 1290  $\mu\text{m}$  x 1720  $\mu\text{m}$  were analyzed for each part.



**Figure 3-4: a) Original micrograph; b) greyscale micrograph with pores highlighted in red; and c) ImageJ greyscale intensity histogram with threshold indicated in red**

### 3.3.3 X-Ray Computed Tomography

X-ray computed tomography (CT) scanning (Zeiss Xradia 520 Versa) was used to measure the internal pore fraction and relative density of the samples and to provide visualization of the pore size and distribution within the sample. The density measurements determined through CT scanning were necessary to provide an estimate of the bulk part density, as the Optical Microscopy and Image Processing method described in Section 3.3.2 was limited to only a small cross-sectional area of the part and was used in order to reduce the time and expense of analysis. CT scanning was performed for benchmarking the density of the cast sample, and to verify the density of several of the LPBF parts: thin wall artifacts (refer to Section 6.1.2) and cylindrical artifacts (Section 5.2). Circular channel artifacts (Section 6.1.2) were also CT scanned to check for the presence of powder within each channel.

Table 3-2 shows the scout-and-scan settings that were used. The detection was limited to pores with a diameter that was at least 3x larger than the voxel size. Image processing was performed using MATLAB in order to determine the density of the part.

**Table 3-2: Scout-and-scan settings used for CT scanning**

	Cast Samples	LPBF cylinders – recipe development	LPBF cylinders – final recipes	LPBF thin walls	LPBF circular channels
Source power	7 W	7 W	7 W	7 W	7 W
X-ray energy	80 kV	80 kV	80 kV	80 kV	80 kV
X-ray optic	0.4x lens	0.4x lens	0.4x lens	0.4x lens	0.4x lens
Exposure time	1 s	0.5 s	0.5 s	0.5 s	0.5 s
Number of projections	1201	1601	801	1001	801
Binning level	2	2	2	2	2
Voxel size (approximate)	4 $\mu\text{m}$	12 $\mu\text{m}$	12 $\mu\text{m}$	7.9 $\mu\text{m}$	12 $\mu\text{m}$

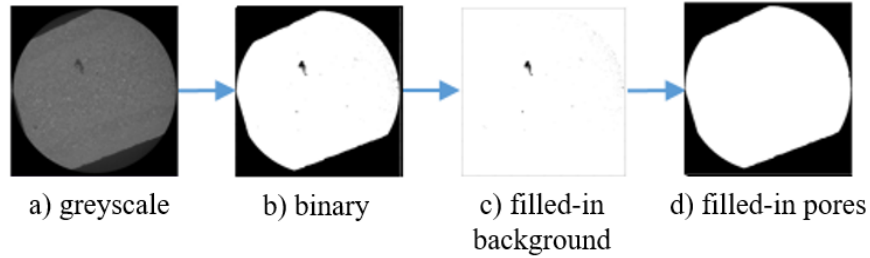
### 3.3.3.1 CT Image Processing in MATLAB

The CT scan data was processed using the built-in image analysis capabilities in MATLAB (Version R2018b). Refer to Appendix B for the MATLAB code. The CT scan data were imported into MATLAB in the form of 16-bit TIFF images, which are a greyscale representation of the x-ray intensity detected after passing through the sample. This intensity varies depending on the density of the material, so the presence of different materials or a lack of material (i.e. pores) appears as different greyscale values. The goal of the image processing was to identify the pores and provide an estimate of the relative density of the sample.

To reduce noise, an edge-preserving Gaussian bilateral filter was applied. The default spatial sigma (1) and degree of smoothing were used (1% of the square data range, which was 65535 for a 16-bit greyscale), and when kept small, the filter smooths areas with small variance but preserves areas with large variance such as strong edges.

Image segmentation was performed using a calculated threshold value. The greyscale image was converted to binary where values above the threshold were assigned zero and represented pores, and values below were assigned one and represented solid part, as pictured in Figure 3-5 a) and b). The threshold was found using Otsu's multi-threshold method [104]. For each image, a global threshold was calculated by iterating through all possible threshold values (integers from 1 to 65535), and selecting the one that minimizes the within-class variance for the greyscale values included in the foreground (solid) and background (pores) spreads. For the cast parts, 10 levels of binning were used and the threshold between pores and solid was the 4<sup>th</sup> of 9. For the AM parts, 4 levels of binning were used and the threshold between pores and solid was the 3<sup>rd</sup> of 3. For comparison, an alternative method of image segmentation using a locally adaptive threshold was performed for the cast parts only, and is described in Appendix C.

Next, the area outside the part was filled using the MATLAB *imfill* function, which changed the interconnected pixels of the background from black to white, as shown in Figure 3-5 c). This resulted in a "filled-in background" image with the pores isolated. The pores were then subtracted from the original binary image, leaving only the solid part with "filled-in pores", as shown in Figure 3-5 d).



**Figure 3-5: Image types generated during MATLAB processing of CT scan data**

The final solid fraction (or equivalently the part density) was calculated by taking the sum of the white pixels in the binary image, which gives the actual part volume accounting for the detected porosity, and dividing it by the sum of the “filled-in pores” image, which gives the ideal part volume assuming that there are no pores. The resulting fraction is the relative density of the scanned part. Because the part is represented by a 3D array, the sum for each image type is nested three times in order to capture the X, Y, and Z dimensions of the part. The slice density data was also used to produce a graph showing the density vs. distance in the X-direction.

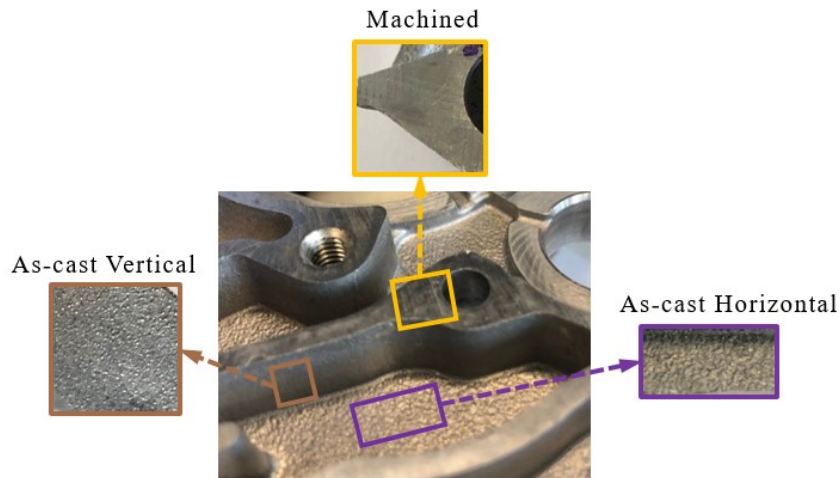
The binary images were also used to provide a visualization of the pore sizes and locations within the samples. This was done by using the MATLAB minimum intensity projection function to project all the zeros (black pores) from the 3D binary tiff-stack onto a single 2D image.

### **3.3.4 Surface Roughness**

The surface roughness was characterized by laser confocal microscopy (Keyence VK-X250). 3D imaging is performed by taking surface height measurements through the use of point illumination, where a laser beam is scanned across the sample in a regular raster pattern at incremental vertical displacements [105]. The vertical resolution is dependent on the aperture of the objective lens and should be carefully selected such that the finest features of the sample can be resolved across multiple “z-steps” of the laser scan. The surface height data is then processed by the Keyence Multi-file Analyzer software. Image processing may include surface shape correction for a planar tilt (for flat samples) or for a curved surface (cylindrical samples). The surface roughness value is then calculated using the “Sa” function, which averages the displacement of the height value from the reference plane for every measurement point within the selected area.

For the cast surfaces of the pump housing (Section 4.3.4), the surface roughness was measured with an objective lens of 20x magnification and a z-pitch of 0.50  $\mu\text{m}$ . The three surface types shown in Figure 3-6 were investigated, as well as one surface on the outside of the pump housing. A total area of 5.32

mm<sup>2</sup> was measured for the as-cast surfaces, and each surface type was measured on two different locations on the pump housing. For the machined surfaces, the objective lens magnification was increased to 50x and the z-pitch changed to 0.20 μm in order to provide better resolution, and a total area of 0.86 mm<sup>2</sup> was measured.

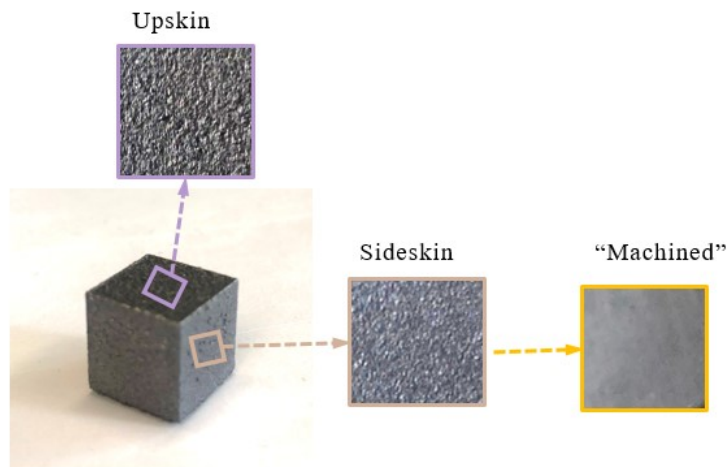


**Figure 3-6: Surface types on cast pump housing**

For the LPBF samples, the side surface roughness was measured for cylindrical samples in order to select suitable processing parameters for the part borders (Section 5.3.1). For these samples, the objective lens of 10x magnification and a z-pitch of 2 μm was used. Two images were taken per sample on the front-facing side (opposite from the powder spreading direction) and a total area of 3.08 mm<sup>2</sup> was measured.

After the selection of ideal printing parameters for the core and border, cubes and slot-shaped parts were manufactured and characterized for surface roughness (Section 6.2.2 and 6.2.3.2). For both sample geometries, the surface roughness was measured with an objective lens of 20x magnification and a z-pitch of 0.50 μm.

For the cube-shaped samples, three distinct surface types were investigated: the upskin, which is the top surface parallel to the build direction, the sideskin, which is perpendicular to the build direction, and a side surface that was lightly-polished in order to simulate the level of surface roughness that a machined part may exhibit. Figure 3-7 shows an example of each surface type on the cube. The “machined” surface was prepared by grinding the sample with SiC papers, as described in Section 3.3.2. A total area of 4.53 mm<sup>2</sup> was measured for each surface type, and was taken across three different specimens. For the polished surfaces, the z-pitch was decreased to 0.20 μm in order to provide better resolution.



**Figure 3-7: Surface types on cube manufactured by LPBF**

For the slot-shaped samples, the surface roughness was measured on the internal side wall (perpendicular to the build direction). A total area of 4.53 mm<sup>2</sup> was measured for each slot.

### **3.3.5 Hardness**

The Rockwell hardness test apparatus with a 1/16” diameter steel ball and 100 kg load was used for hardness measurements on the Rockwell B scale. The hardness of a sample is evaluated by measuring how far the indenter is able to penetrate into its surface under the given load.

For the cast pump housing, the hardness value was measured for 7 indentations per surface type and the average value was reported for each. The surfaces measured were the as-cast, outside surface of the pump, the as-cast, horizontal surface (inside), the machined surface, and the polished surface.

For the AM specimens, the hardness value was measured with 5 indentations on 2 samples for a total of 10 measurements per surface type, and the average value was reported for each. The surfaces measured were the upskin, the sideskin, and the polished surface for each.

### **3.3.6 Wear**

Wear testing was performed on a custom-built linear reciprocating wear apparatus (pin on disc), as shown in Figure 3-8. The linear pin on disc test is a bidirectional sliding wear test in which deformation and wear on the test sample is caused by mechanical movement of an abrasive pin. The samples were fixed to a stage and an Inconel 625 pin was moved in a linear motion along the sample surface with a 1 kg load applied. The frequency was approximately 1.5 cycles per second. The sliding distance was 6.75 mm in one direction (13.5 mm for a complete back and forth cycle) and the test was run for 10000



cycles for a total sliding distance of 135 m. Three surface types were tested for both the cast and the LPBF samples, as described in Section 3.3.4 (Figure 3-6 and Figure 3-7). Three replicates were performed for each surface type. For the cast surfaces of the pump housing, the irregular-shaped samples were hot-mounted in phenolic resin in order to ensure that the surface was flat and parallel to the sample stage. For the LPBF surfaces, cube shaped samples were printed with a side length of 10 mm using the process parameters selected in Section 5.3.3. Sample surfaces were cleaned with isopropanol prior to testing.

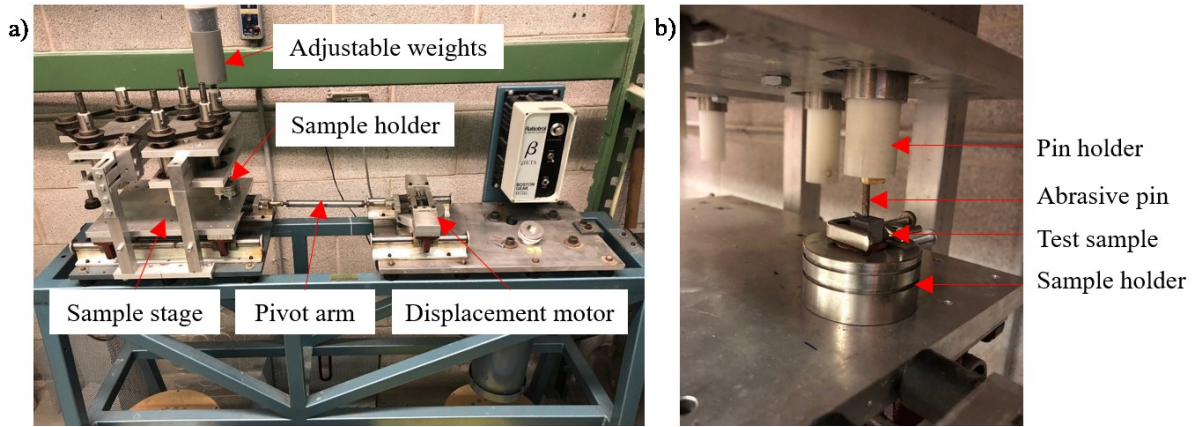


Figure 3-8: a) Linear wear test apparatus; and b) close-up view of the sample stage

### 3.3.6.1 Data Processing of Material Volume Loss

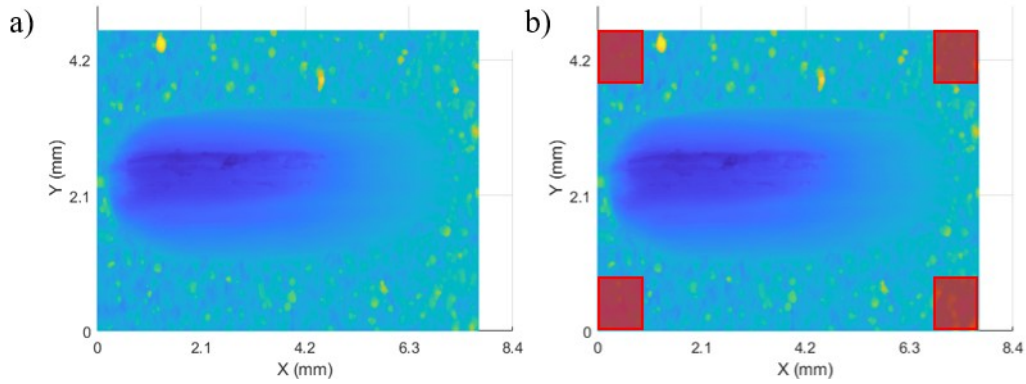
Laser confocal microscopy (Keyence VK-X250) was used to measure the wear track profiles. The surface height data for the entire wear track and surrounding surface was measured with an objective lens of 10x magnification and a z-pitch of 4  $\mu\text{m}$ . MATLAB (Version R2018b) was then used to determine the volume loss based on the geometric data of the wear track. Refer to Appendix D for the MATLAB code.

First, a plane was fit to the height data of the sample surface surrounding but not including the wear track. This was done by taking a sampling of data from the four corners surrounding the wear track when viewed from the top, as shown in Figure 3-9. The equation for a plane is shown below:

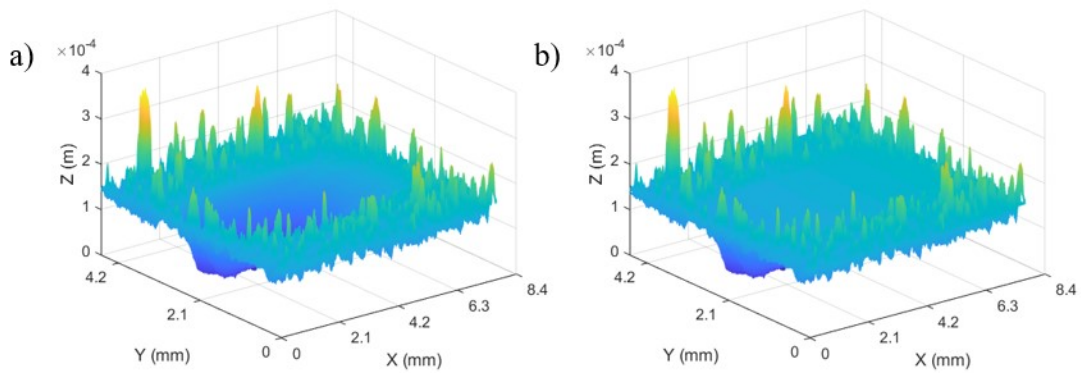
$$[A] \begin{bmatrix} a \\ b \\ c \end{bmatrix} = [B] \quad \text{Equation 4}$$

The X-Y data from each corner was saved in matrix A, the corresponding height data was saved in matrix B, and the coefficients [a b c] for the best-fitting plane were calculated by solving the system of

linear equations where  $fit = A \setminus B$ . Figure 3-10 shows an example of the height data with and without the plane fitted to the surface.



**Figure 3-9: Top view of wear track and surrounding surface height data (a), with corners used for best-fit plane highlighted (b)**



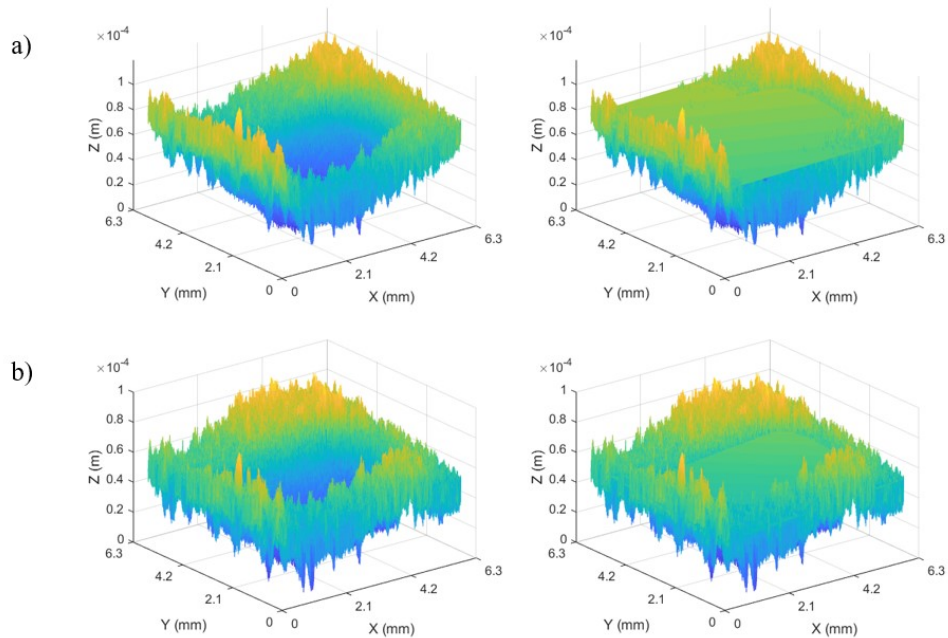
**Figure 3-10: Isometric view of height data (a), with surface best-fit plane overlaid (b)**

The plane represents the average surface of the peaks and valleys caused by the surface roughness of the original sample. To find the depth of the wear track, the difference between the plane and the experimental height data was taken in the area of the wear track. Each data point for the depth was multiplied by its area, which was found by checking the X-Y calibration of the Keyence measurement, in order to calculate the volume loss of the wear track. Equation 5 was then used to calculate the specific wear coefficient,  $k_w$ , in  $m^2/N$ , where  $V$  is the volume loss ( $m^3$ ),  $F$  is the applied load (N), and  $s$  is the sliding distance of the pin (m).

$$k_w = \frac{V}{F * s} \quad \text{Equation 5}$$

In the case of the as-cast, vertical sample, it was impossible to test a perfectly flat area due to the designed curve on the pump walls. As result, the cast-vertical samples required surface shape correction

in order to fit a flat plane to the curved surface without vastly overestimating the wear track depth due to empty space between the plane and the true surface, as shown in Figure 3-11. The surface shape correction was performed in the Keyence VK Analyzer software prior to importing the height data into MATLAB.



**Figure 3-11: a) As-cast vertical surface height data (left) and plane fit (right) before surface shape correction; and b) after surface shape correction for the curved surface**

### 3.3.7 Scanning Electron Microscopy and Energy Dispersive X-Ray Spectroscopy

Scanning electron microscopy (SEM) and energy dispersive x-ray spectroscopy (EDX) were performed on the cast and additive parts after wear testing. The SEM instrument uses a tungsten thermionic source to produce a beam of electrons which is focused on the sample. The incident beam interacts with the sample surface, resulting in backscattered electrons, secondary electrons, x-rays, and other emissions. Detectors convert the electrons into a signal that produces the final image. The emitted x-rays have different characteristic wavelengths depending on the specific atoms in the sample, so the EDX detector is able to identify the stoichiometry of the sample on a micro-scale.

SEM (TESCAN VEGA3) was used to examine the surface morphology of samples after wear testing to help in qualitatively identifying the wear mechanism. The equipment was set to secondary electron mode, the operating voltage was 20 kV, and the working distance ranged from 14.85 to 15.25 mm. Micrographs were taken at various locations inside the wear track and at magnifications ranging from 50x to 2000x.

EDX (TESCAN VEGA3) was used to determine the chemical composition of the wear sample surface and/or tribofilm present on the samples. EDX measurements were taken inside the wear track, outside the wear track, and at wear debris or particles present on the wear track.

SEM and EDX (Zeiss LEO FE-SEM 1530, Waterloo Advanced Technology Laboratory) were also used to examine the microstructure and chemical composition of the cast pump housing. The sample was prepared using the metallographic techniques described in Section 3.3.2. Secondary electron mode was used with a working distance of 11.5 mm and an operating voltage of 15 kV.

### 3.3.8 Corrosion

Electrochemical measurements were used to investigate the corrosion behaviour of the materials. An electrochemical cell consists of an anode, where an oxidation reaction results in the formation of oxides or other corrosion products, a cathode, where a reduction reaction occurs, and an electrolyte, which is required for electron movement. There also must be a return current path, which is often the underlying metal substrate connecting the anode and the cathode. Table 3-3 shows anodic and cathodic reactions that can occur for pure aluminum, depending on the environmental conditions. Figure 3-12 shows the simplified electrochemical potential/pH and Pourbaix diagrams for pure aluminum. The thermodynamically stable reaction product may be an oxide that forms a thin surface layer and reduces the rate of further corrosion through passivation, or a soluble ion that dissolves in the electrolyte causing active corrosion to occur.

**Table 3-3: Electrochemical reactions for pure aluminum**

Anodic Reactions	Cathodic Reactions
$Al = Al^{3+} + 3e^{-}$	$2H^{+} + 2e^{-} = H_2$
$2Al^{3+} + 3H_2O = Al_2O_3 + 6H^{+}$	$O_2 + 4H^{+} + 4e^{-} = 2H_2O$
$2Al + 3H_2O = Al_2O_3 + 6H^{+} + 6e^{-}$	$2H_2O + 2e^{-} = H_2 + 2(OH)^{-}$
$Al + 2H_2O = AlO_2^{-} + 4H^{+} + 3e^{-}$	$O_2 + 2H_2O + 4e^{-} = 4(OH)^{-}$
$Al_2O_3 + H_2O = 2AlO_2^{-} + 2H^{+}$	

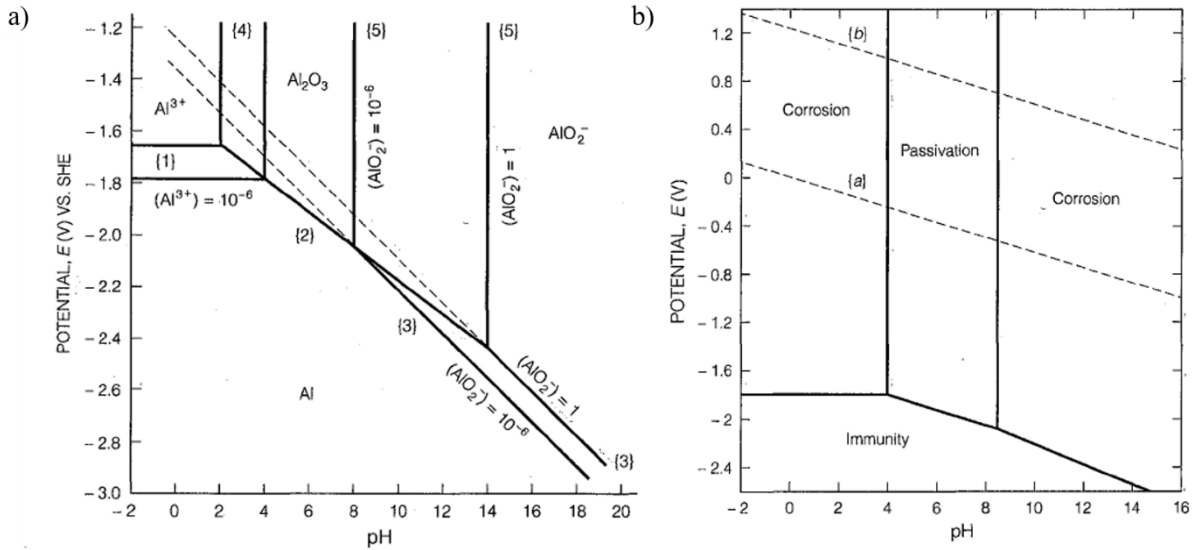


Figure 3-12: a) E/pH diagram, and b) Pourbaix diagram for pure aluminum in DI water [106]

Prior to selecting the electrolyte for the experiments, a preliminary test measurement was taken for the open circuit potential (OCP) of the aluminum alloy submerged in automatic transmission fluid (ATF L12108). The electrochemical potential could not be read, indicating that the electrolyte solution is non-conductive for the measurement of corrosion properties. To ensure measurable results for a comparative study, the subsequent experiments were carried out using deionized water and sodium chloride solutions of varying concentrations. The presence of chloride ions may promote the breakdown of passive films through mechanisms such as local thinning and stress-induced rupture, and can prevent repassivation by displacing the supply of hydroxide anions required for oxidation [107].

Electrochemical measurements were performed using test methods for cyclic polarization and linear polarization resistance. A three electrode polarization cell circuit was used with the test sample as the working electrode, a titanium mesh as the counter electrode, and a saturated calomel electrode (SCE) as the reference electrode. Three surface types were tested for both the cast and the LPBF samples, as described in Section 3.3.1 (Figure 3-6 and Figure 3-7). Samples were prepared by drilling a hole at 90° from the working surface so that electrical wire could be attached using a bolted terminal connection. The samples were then masked with non-conductive masking paint (Enplate stop-off no.1) so that only the working surface would be exposed to the electrolyte. The cast pump housing samples had flat surfaces of irregular shape with a surface area ranging from 62 to 284 mm<sup>2</sup>. The LPBF samples were cubes with a 10 mm side length and the working surface had an area of 100 mm<sup>2</sup>.

### ***Cyclic potentiodynamic polarization***

Prior to testing, each specimen was immersed and the OCP was measured for 1 hour to ensure an equilibrium corrosion potential ( $E_{corr}$ ) had been reached. Starting at the  $E_{corr}$ , the potential was scanned in the anodic direction using a scan rate of 0.1 mV/s and the resulting change in current was recorded. The potential was then either reversed in the cathodic direction at 0.5 V vs SCE or testing was stopped at a current limit of 5 mA. Three replicates of the cast and LPBF samples were tested in a 0.001M chloride solution, and one replicate was tested in a 0.1M chloride solution. LPBF samples were also tested in a 0.01M chloride solution. From the resulting E vs. log(i) plot, the Stern-Geary constant ( $B$ ) was calculated based on the anodic ( $\beta_a$ ) and cathodic ( $\beta_c$ ) Tafel slopes according to Equation 6.

$$B = \frac{\beta_a \beta_c}{2.3(\beta_a + \beta_c)} \quad \text{Equation 6}$$

### ***Potentiostatic linear polarization resistance***

The potentiostatic linear polarization resistance (LPR) technique consists of measurements taken close to the  $E_{corr}$ , where the relationship between potential and current is linear. A potential step of  $\pm 10$  mV was applied and the current response measured for 120 seconds per scan. The polarization resistance,  $R_p$ , can be determined by Equation 7. The corrosion current density,  $i_{corr}$ , can then be calculated according to Equation 8, where  $B$  is the Stern-Geary constant and  $A$  is the exposed area.

$$R_p = \frac{\Delta E}{\Delta i} \quad \text{Equation 7}$$

$$i_{corr} = \frac{B}{R_p A} \quad \text{Equation 8}$$

LPR testing was performed 10 times over a period of 38 days wherein the samples remained submerged in an electrolyte of deionized water or sodium chloride solution. The schedule of measurements and increases in sodium chloride concentration are shown in Table 3-4. Three replicates were tested for all three surface types of the cast and LPBF samples.

**Table 3-4: Schedule of LPR measurements**

Day	Electrolyte
1	DI H <sub>2</sub> O
7	
9	
11	0.01 M Cl <sup>-</sup> added
14	
20	
23	0.1 M Cl <sup>-</sup> added
30	
32	1 M Cl <sup>-</sup> added
38	

## 4 Benchmarking Performance in LPBF by Characterization of Cast Aluminum Pump Housing

### 4.1 Pump Housing Product Description

The selected fluid power application was an aluminum pump housing for use in automotive transmissions. The pump housing, traditionally manufactured by high-pressure die casting, was examined in order to determine benchmark specifications and develop design objectives for a similar part optimized for additive manufacturing. The selected cast aluminum pump was a dual stage, positive displacement gear pump from a 45RFE transmission, but may be considered representative of various other aluminum products used for similar applications and operating conditions. The pump assembly features a pump cover containing various torque converter control and pressure regulator valves (Figure 4-1-a) and a pump body containing one driver gear and two driven gears (Figure 4-1-b), separated by a spacer plate and fastened with screws when assembled (Figure 4-1-c). The pump would be connected to the transmission stator shaft and act as the main pressure source in the transmission, enabling circulation of oil through the transmission cooler and pressure in the valve body that controls the clutches. The service conditions may include operating temperatures from  $-30^{\circ}\text{C}$  to  $+120^{\circ}\text{C}$  and operating pressures up to 1.5 MPa. The service fluid may vary between different types of automatic transmission fluid.

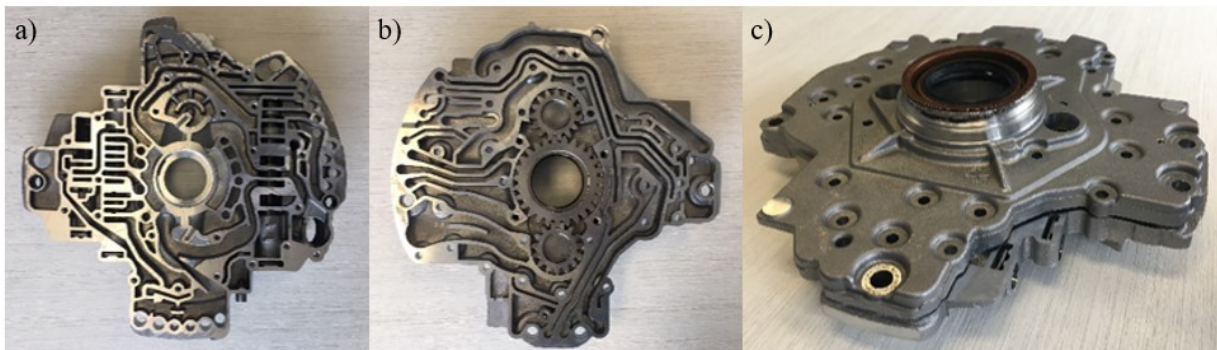


Figure 4-1: Cast aluminum pump product: a) pump cover; b) pump body; c) assembly

### 4.2 Methods for Cast Pump Housing Characterization

#### 4.2.1 Material Characterization

It is necessary to evaluate the mechanical and chemical properties to ensure that the additive manufacturing process can meet industrial manufacturing standards. In order to determine which

properties to investigate, the engineering requirements for the cast pump housing were considered. The general procedures for material characterization can be found in Section 3.3. Because the exact grade of aluminum was unknown, the chemical composition of the pump body was determined through x-ray fluorescence (Section 3.3.1) and energy dispersive x-ray (Section 3.3.7) spectroscopy. The microstructure was examined through both optical microscopy (Section 3.3.2) and scanning electron microscopy (Section 3.3.7). Achieving a highly dense part (greater than 99% relative density) is a key functional requirement for the pump housing application, not only to ensure a structurally sound product, but also to prevent the leakage of fluid from around gaskets or through thin walls. The density of the cast pump housing was characterized by x-ray computed tomography of dissections (Section 3.3.3) to provide target values for the LPBF process parameter selection. For the same purpose, the surface roughness of the various surface types that would be in contact with the working fluid in the pump were characterized using laser confocal microscopy (Section 3.3.4). Important geometric features of the pump housing were identified and measured in order to provide a guideline for the minimum feature size for the manufacturability requirement (Section 4.2.2). The durability was investigated through measurements of the hardness (Section 3.3.5), the dry sliding wear rate (Section 3.3.6), and the corrosion behaviour (Section 3.3.8).

#### 4.2.2 Geometric Feature Characterization

In order to investigate the manufacturability of the pump housing, the minimum geometry requirements for key features were measured using digital Vernier calipers. The features of interest were the inner and outer wall thicknesses, the slot width and depth of the internal channels, and the diameter of the circular holes. A total of 10 locations were measured for each feature, as shown in Figure 4-2.

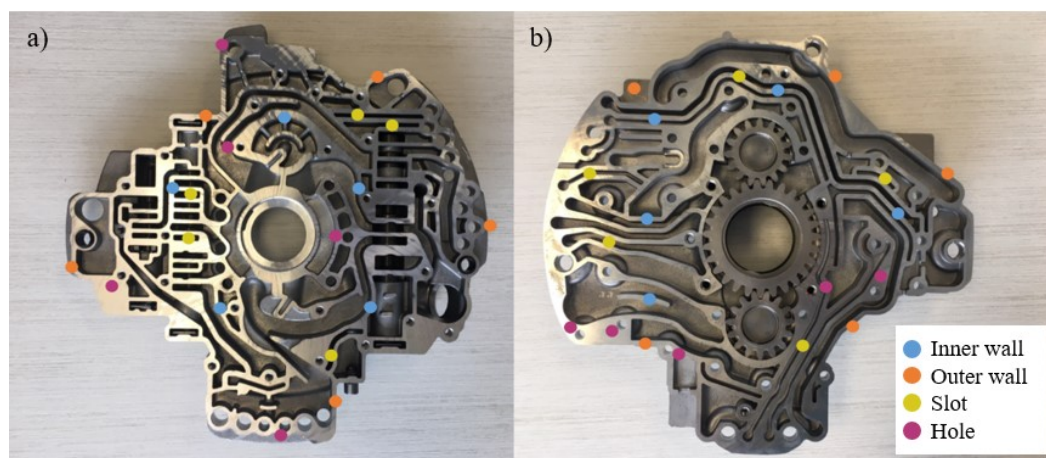
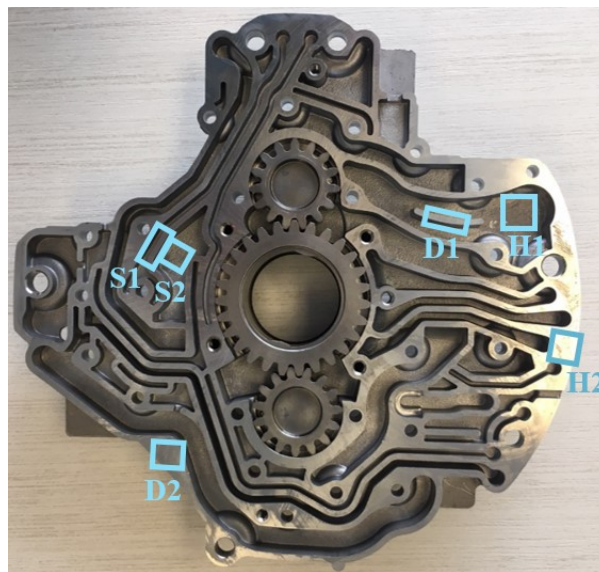


Figure 4-2: Measurement locations on the cast pump housing assembly:  
a) pump cover; and b) pump body



### 4.2.3 Pump Housing Sample Extraction

Test samples were extracted from the pump body through the use of a vertical band saw for large cuts and a precision saw for small cuts. Figure 4-3 shows the locations of the density, surface roughness, and hardness tests. The density measurements were made on one sample taken from the interior of the pump housing (D1) and one sample taken from the edge of the pump housing (D2). The surface roughness measurements were taken on both the as-cast and machined surfaces: location S1 was an interior thin wall with a machined surface on top and an as-cast, vertical surface on the side of the wall, and location S2 included the as-cast, horizontal surfaces on the inside and outside (reverse side – not pictured) of the pump. Additional surface roughness measurements were made at secondary locations for the three main surface types that would be in contact with the working fluid of the pump: as-cast, vertical; as-cast, horizontal; and the machined surface. Hardness testing was performed on the as-cast, horizontal surface (H1), the machined surface (H2), and the outside of the pump (H2 – reverse).



**Figure 4-3: Locations of surface roughness (S), density (D), and hardness (H) measurements on the cast pump housing**

The three main surface types on the cast pump housing were also characterized for wear and corrosion behaviour. These experiments required 9 samples per surface type to be cut from the pump housing with one flat surface of approximately 1 cm<sup>2</sup>. Figure 4-4 highlights the areas where the samples for each surface type were extracted.

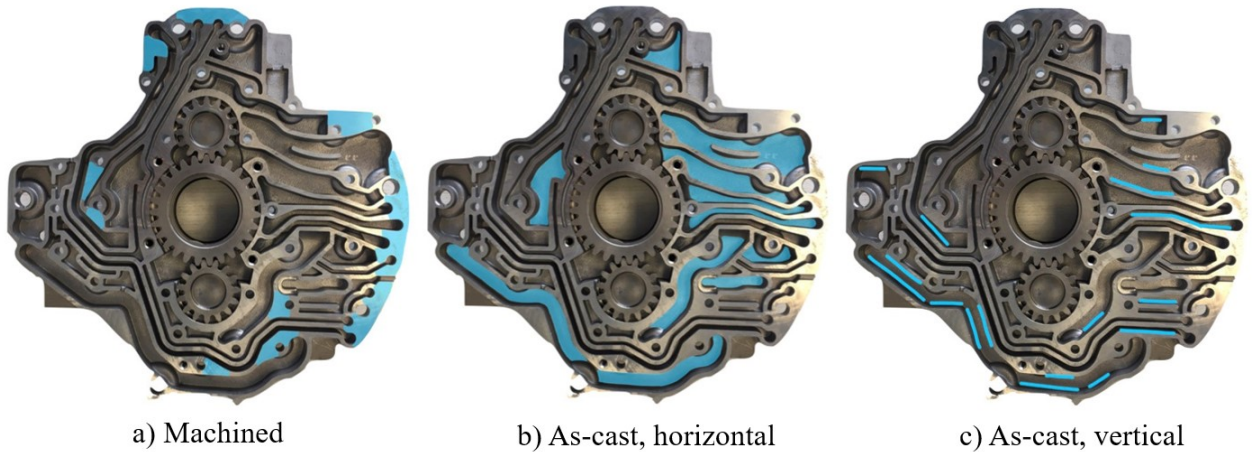


Figure 4-4: Locations of sample extraction for three surface types on the cast pump housing: a) machined; b) as-cast, horizontal; and c) as-cast, vertical

### 4.3 Results for Cast Pump Housing Characterization

#### 4.3.1 Chemical Composition

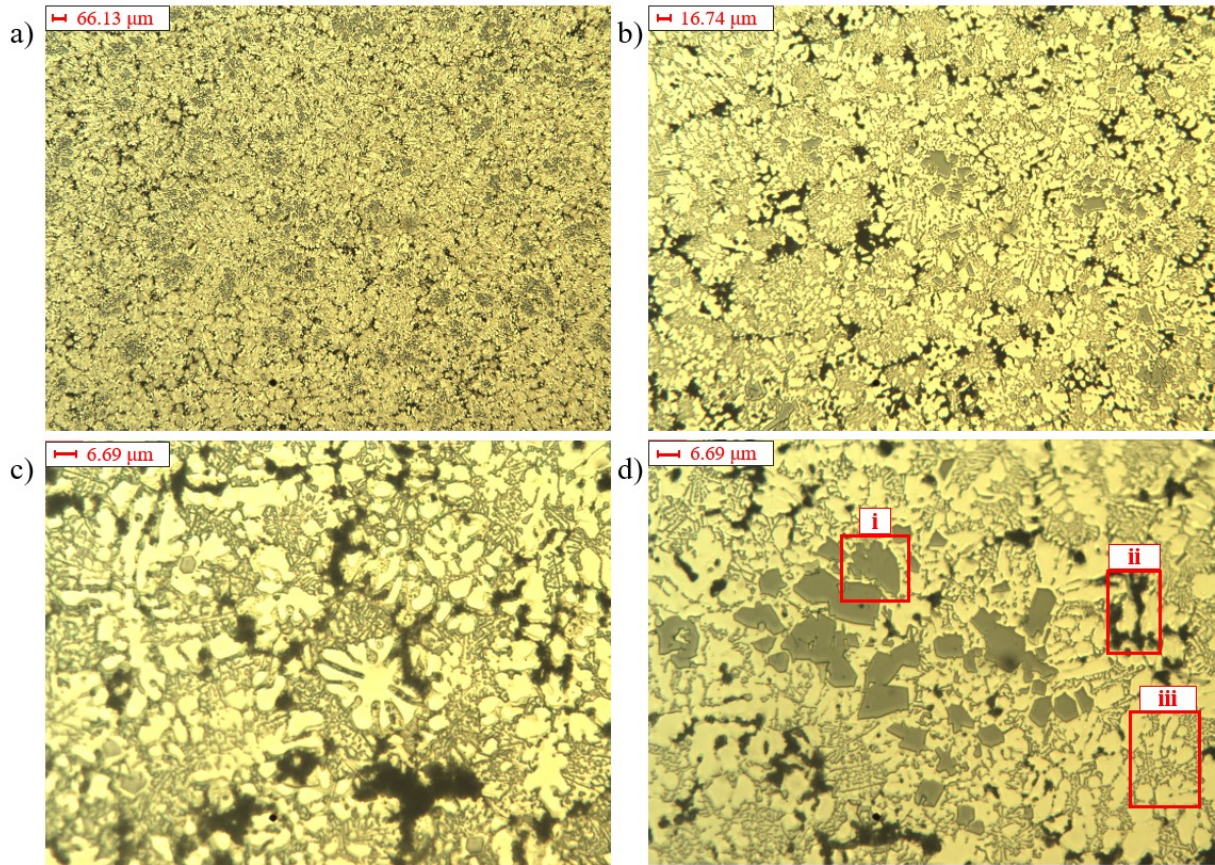
Table 4-1 shows the chemical composition results for the two halves of the cast aluminum pump assembly. The specifications provided by the OEM are also included for comparison. The pump cover was identified as aluminum alloy 383 with primary alloying elements Si, Cu, Fe, and Mg. The XRF measurement verified the presence and quantity of these constituents, with the exception of Mg, which was beyond the detection limit for the equipment. The pump body was analyzed by XRF and EDX spectroscopy, and it was found to also contain Si, Cu, and Fe as alloying elements. At over 20 wt%, the Si content was much higher in the pump body, exceeding even the OEM specification. This alloy may have been selected because higher Si content generally improves the wear resistance of the Al-alloy, and unlike the pump cover, the pump body is in direct contact with the moving gears. There was also a discrepancy between the XRF and EDX measurements of Cu, which was slightly above specification for the XRF surface measurements and slightly below for the EDX measurements. This may indicate that some level of solute macrosegregation occurred during the casting process.

**Table 4-1: XRF and EDX measurements compared with specifications (elemental weight %)**

Element	Pump Body			Pump Cover	
	Chrysler Spec. (Estimate)	XRF Results	EDX Results	Chrysler Spec. (AA 383)	XRF Results
Silicon	16.0-18.0	21.5	22.5	9.5-11.5	10.5
Iron	1.1	1.2	0.37	<=1.3	0.96
Copper	4.0-5.0	5.2	3.0	2.0-3.0	3.3
Magnesium	0.45-0.65	-	-	0.1	-
Manganese	0.1	0.26	-	0.5	0.24
Nickel	-	0.06	-	<=0.3	0.01
Zinc	0.1	1.4	-	3.0	2.8
Titanium	0.2	0.19	-	-	0.06
Other	0.2	0.28	-	0.5	0.29
Aluminum	balance	69.2	74.0	balance	81.8

### 4.3.2 Microstructure

Figure 4-5 shows the optical micrographs of the cast pump housing at various magnifications, taken at location H2 on the pump housing (shown in Figure 4-3). It features a dendritic matrix of Al (light) with three visible secondary phases (dark), likely composed of Si, Cu, and Fe –rich precipitates. The morphology of the secondary phases included coarse flakes (Figure 4-5-d – i), a broken network of discrete, coarse particles between dendrites (Figure 4-5-d – ii), and a fine, semi-continuous network of precipitates (Figure 4-5-d – iii).



**Figure 4-5: Optical micrographs of the cast pump housing at low magnifications (a and b) and high magnification (c and d)**

Scanning electron microscopy was also used to examine the microstructure, as shown in Figure 4-6. The sample was taken from location H2 on the pump housing (shown in Figure 4-3). In the SEM micrographs (secondary electron mode), the Al matrix appears as dark grey, while the secondary phases appear as light grey and white; features shown in the SEM micrographs are consistent with the observations captured in optical micrographs. EDX analysis was performed in order to identify the composition of the phases visible in the SEM images, and an example of the elemental mapping is shown in Figure 4-7. The coarse flakes and fine network of precipitates were found to primarily contain Si, while the larger distinct particles contained copper and oxygen. Iron was also detected in the form of needle-like precipitates and flakes.

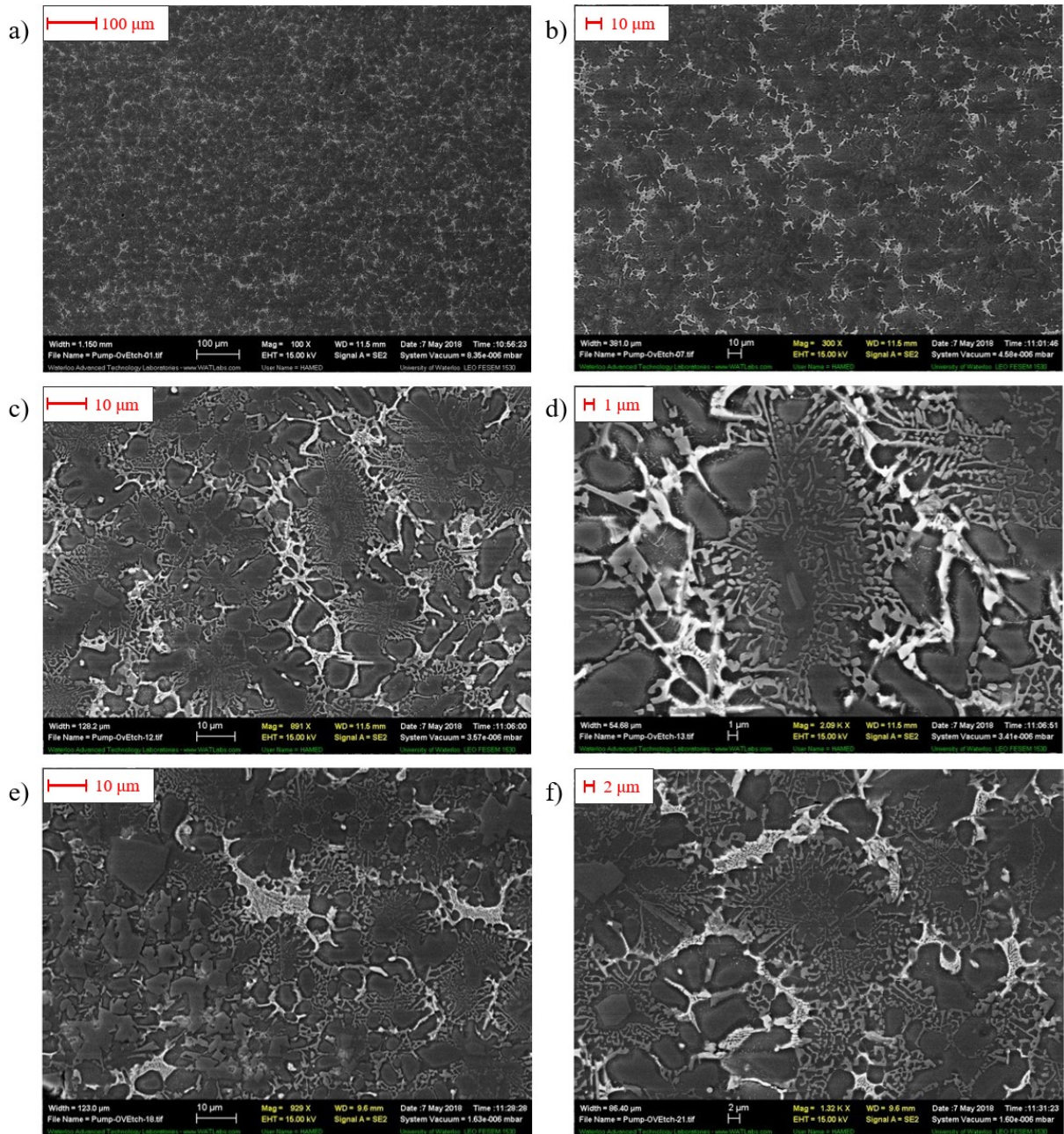


Figure 4-6: SEM images of the cast pump housing at various magnifications: a) 100x; b) 300 x; c) 891x; d) 2.09kx; e) 929x; f) 1.32kx

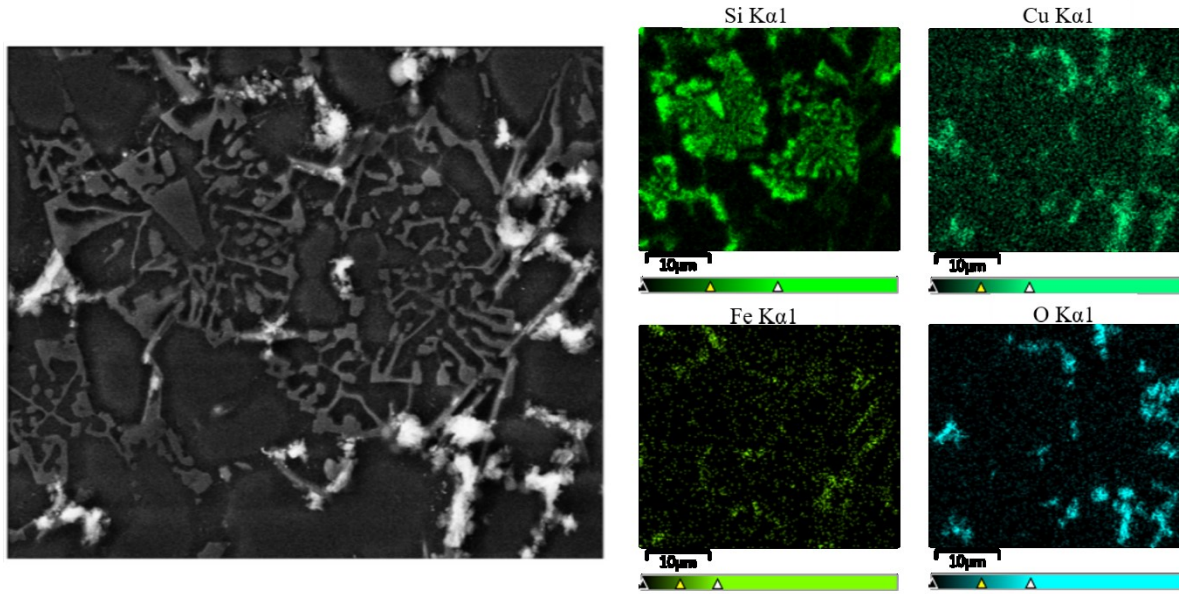


Figure 4-7: EDX element mapping of the cast pump housing microstructure

### 4.3.3 Density

Table 4-2 shows the estimated part density for two representative samples of the cast pump housing, as determined by CT scanning and image processing. The sample taken from the interior of the pump housing (D1) had an overall solid fraction or relative density of 99.97%, while the sample taken from near the exterior (D2) was approximately 99.15% dense. The average slice density for the X, Y, and Z dimensions was also reported and the data for the x-direction was used to create the density vs. distance graphs shown in Figure 4-8 and Figure 4-9. Porous defects are typical for all cast aluminum products, with two of the main causes being solidification shrinkage porosity resulting from an insufficient feeding of liquid metal, and gas porosity resulting from reduced solubility of dissolved hydrogen during solidification [108].

Table 4-2: Density measurements for cast pump housing

Sample	Density (%)	Ave. Slice Density – X (%)	Ave. Slice Density – Y (%)	Ave. Slice Density – Z (%)	Height - Z (mm)
D1	99.97	99.97 ± 0.037	99.98 ± 0.029	99.97 ± 0.036	2.56
D2	99.15	99.13 ± 0.45	99.24 ± 0.49	99.14 ± 0.61	3.51

Figure 4-8 and Figure 4-9 show the pore distributions for Sample D1 and D2, respectively. The slice density in the X-direction (relative density measured for y-z plane) was plotted as a function of X (Figure 4-8 a and Figure 4-9 a). The minimum intensity projections show all of the pores along the z-direction in each sample projected onto a 2-dimensional image in the x-y plane (Figure 4-8 b and Figure

4-9 b). Sample D1 was analyzed for 2.56 mm in the z-direction, and Sample D2 was analyzed for 3.51 mm. The binary images show the porosity in a single slice or random cross-section of the sample (Figure 4-8 c and Figure 4-9 c).

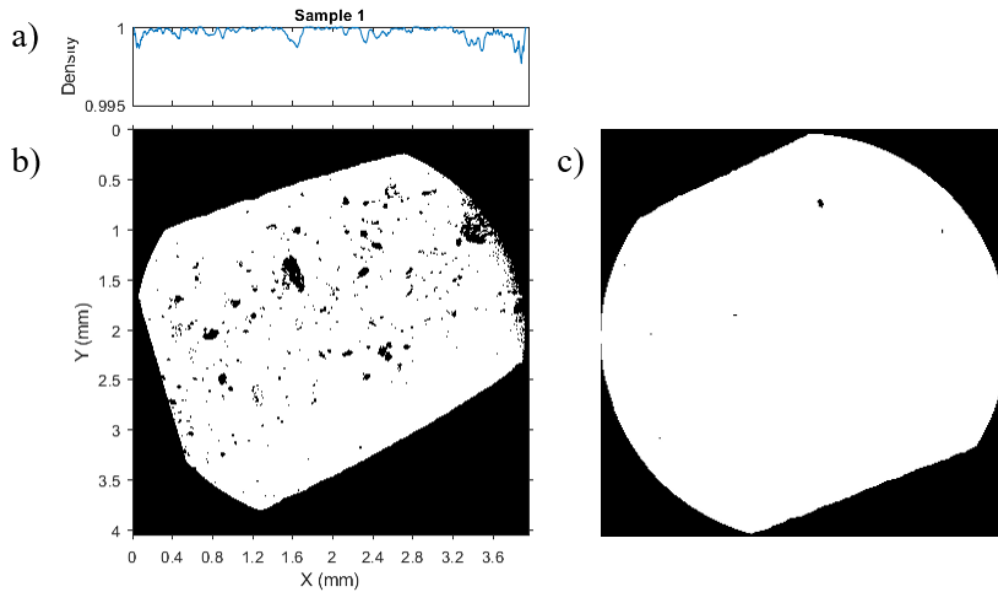


Figure 4-8: Cast pump housing sample D1: a) Density vs. distance graph; b) minimum intensity projection across 2.56 mm; c) binary image of single slice # 208/640 (0.832/2.56 mm)

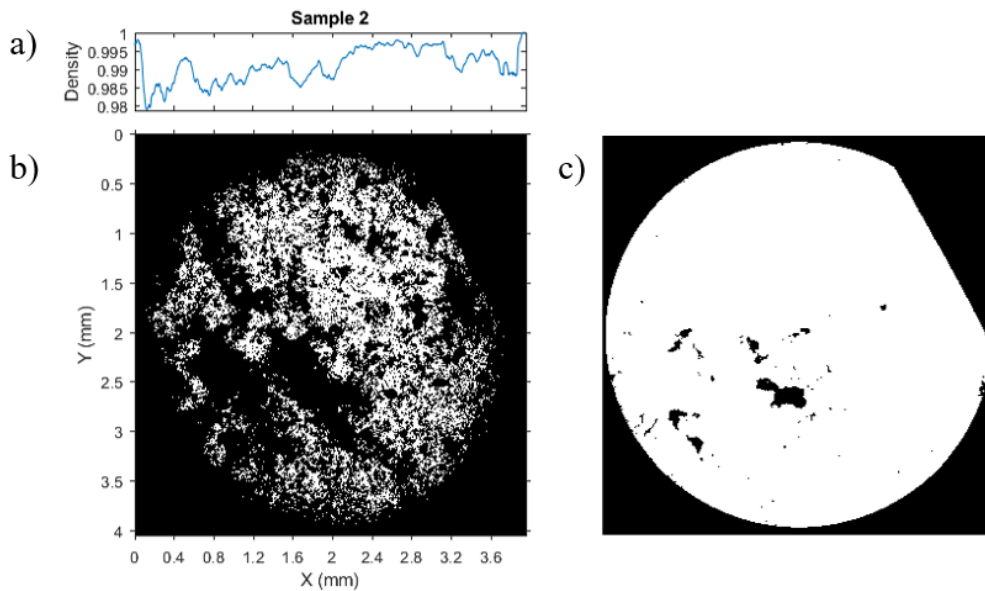
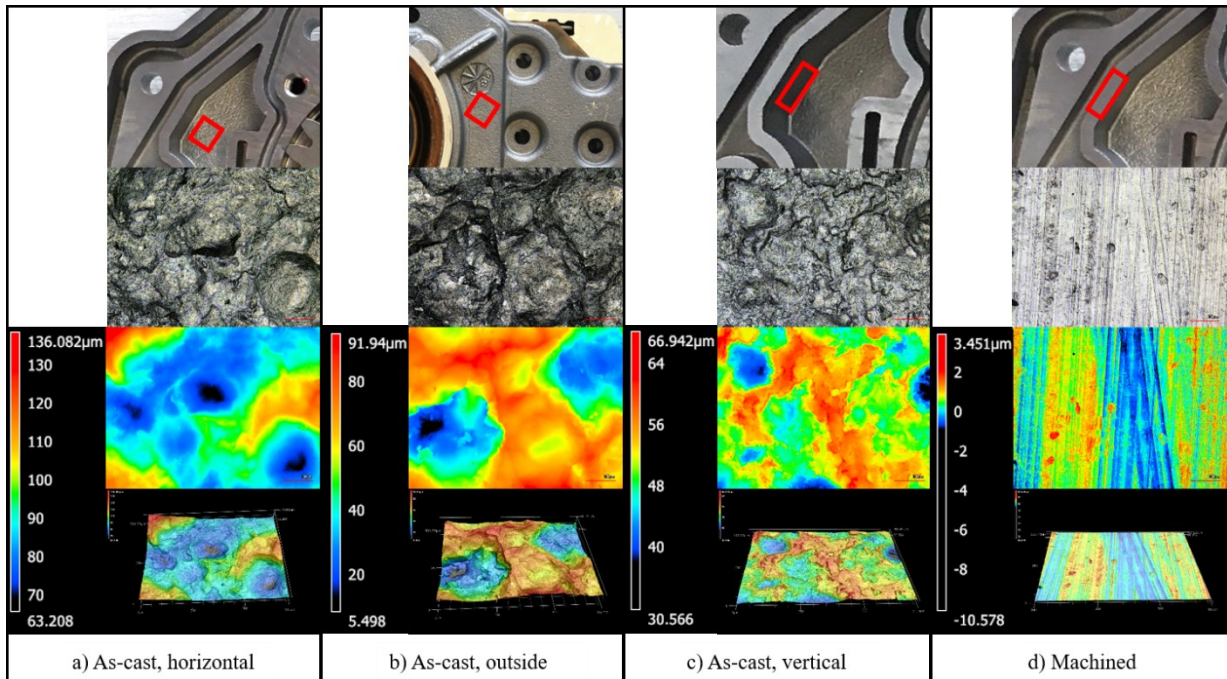


Figure 4-9: Cast pump housing sample D2: a) Density vs. distance graph; b) minimum intensity projection across 3.51 mm; c) binary image of single slice # 595/878 (2.38/3.51 mm)

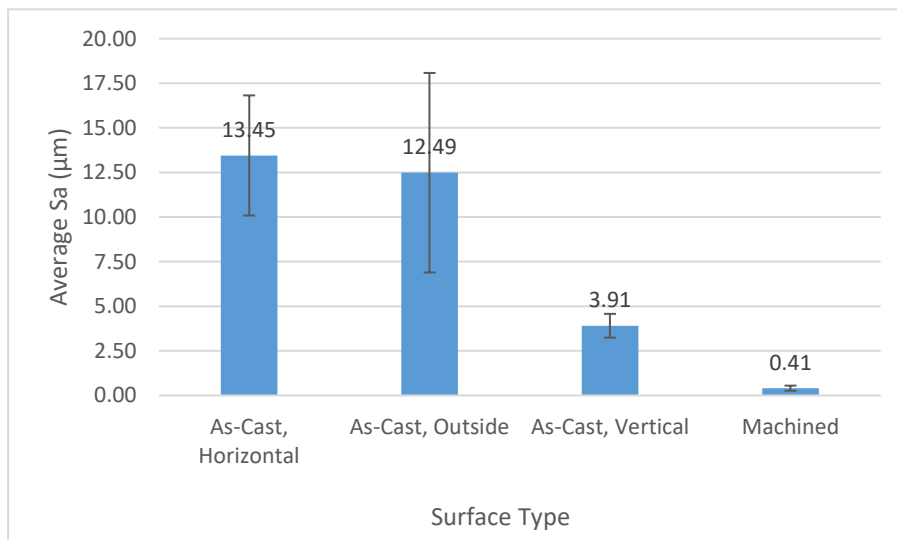
#### 4.3.4 Surface Roughness

The surface roughness was characterized for four surface types, as shown in Figure 4-10. The results are summarized in Figure 4-11. The outside of the pump housing and the as-cast, horizontal surface had

an average surface roughness of around 12.5 to 13.5  $\mu\text{m}$ . The outside of the pump had a larger standard deviation than the inner surfaces, perhaps due to less stringent tolerances and surface finish requirements for the non-functional surface of the pump housing. The as-cast, vertical surface had a lower surface roughness, averaging 3.91  $\mu\text{m}$ , which may be attributed to uneven wear on the die used for the casting process. As expected, the machined surface had the lowest surface roughness. These ranges were taken under consideration during the LPBF process parameter selection.



**Figure 4-10: Surface roughness measurement locations, optical micrographs, and height images for four surface types: a) as-cast, horizontal; b) as-cast, outside; c) as-cast, vertical; d) machined**



**Figure 4-11: Average surface roughness for cast pump housing**



### 4.3.5 Geometric Features

Table 4-3 shows the geometric feature size measurements for the cast pump housing, taken from various locations. Because the features throughout the pump housing are non-uniform by design, an average value is not reported for each feature. Instead, the minimum measurement is considered as the design requirement for geometric manufacturability. The minimum feature size requirement for the inner wall thickness, the slot width, and the hole diameter are listed in Table 4-4. The slot depth ranged from 4.75 to 22 mm. The outer wall thickness was larger than the inner wall thickness, so it was not considered.

**Table 4-3: Feature size measurements for cast pump housing; all dimensions in mm**

	#	Inner wall thickness	Outer wall thickness	Slot width	Slot depth	Hole diameter
Pump cover	1	2.55	3.15	2.75	11.95	8.75
	2	2.67	3.13	2.78	11.90	3.98
	3	2.64	3.26	4.56	18.20	6.80
	4	2.56	3.25	3.43	22.03	4.05
	5	2.50	3.13	2.86	12.34	6.91
Pump body	6	2.76	3.27	2.92	4.84	5.96
	7	2.73	3.04	2.74	4.75	5.90
	8	2.72	2.99	2.63	5.04	5.95
	9	2.76	4.07	4.17	10.63	4.97
	10	2.72	2.91	2.99	5.11	5.98

**Table 4-4: Minimum feature size requirements for cast pump housing; all dimensions in mm**

Inner Wall Thickness	Slot Width	Hole Diameter
2.50	2.63	3.98

### 4.3.6 Hardness

Figure 4-12 shows the hardness test results measured on the Rockwell B scale for three surface types on the pump housing. The average hardness of the as-cast, horizontal surface was  $72.8 \pm 2.9$  HRB, while the as-cast, outside and machined surfaces were slightly higher at  $84.8 \pm 3.3$  HRB and  $81.5 \pm 1.4$  HRB, respectively. The latter two surfaces were tested again after polishing the samples in order to account for any differences caused by surface irregularities. The average hardness values were close to the as-

received surfaces, while the standard deviation reduced to around 0.5 – 0.7 HRB. The hardness was likely also affected by work hardening caused by the machining and/or polishing procedures.

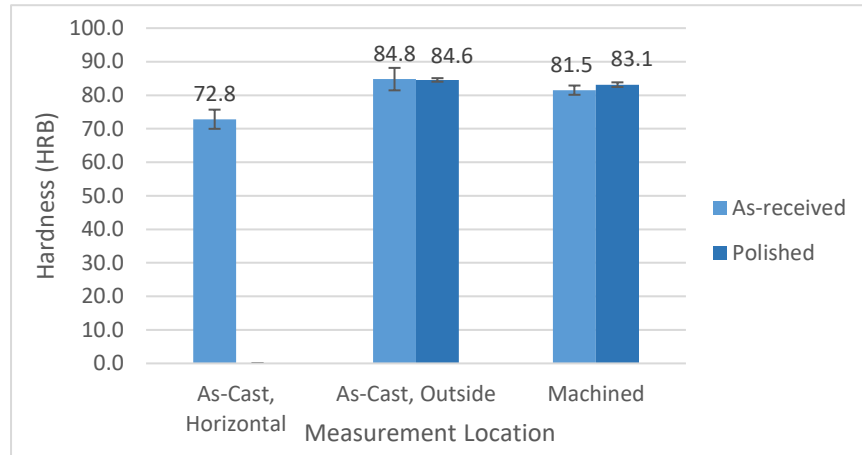


Figure 4-12: Rockwell B Hardness for cast pump housing

### 4.3.7 Wear

The specific wear rates for the cast pump surfaces, summarized in Figure 4-13, were calculated based on the material volume loss after the dry sliding wear test. Table 4-5 shows the specific wear rate for each trial. The average values were similar for all three surface types, ranging from  $2.50 \times 10^{-13}$  to  $2.55 \times 10^{-13} \text{ m}^2\text{N}^{-1}$ .

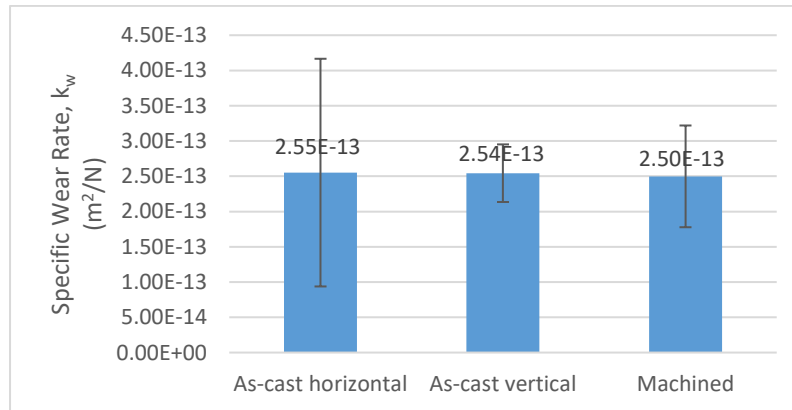


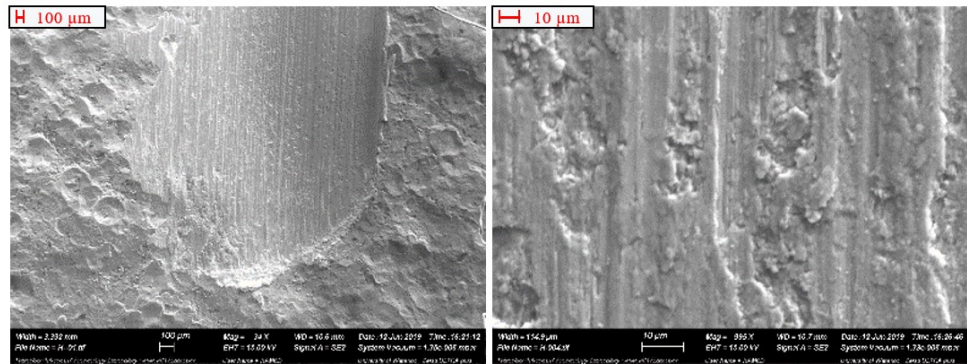
Figure 4-13: Average specific wear rate ( $k_w$ ) for cast pump housing surfaces

Table 4-5: Specific wear rate ( $k_w$ ) for cast pump housing surfaces, in units of  $\text{m}^2\text{N}^{-1}$

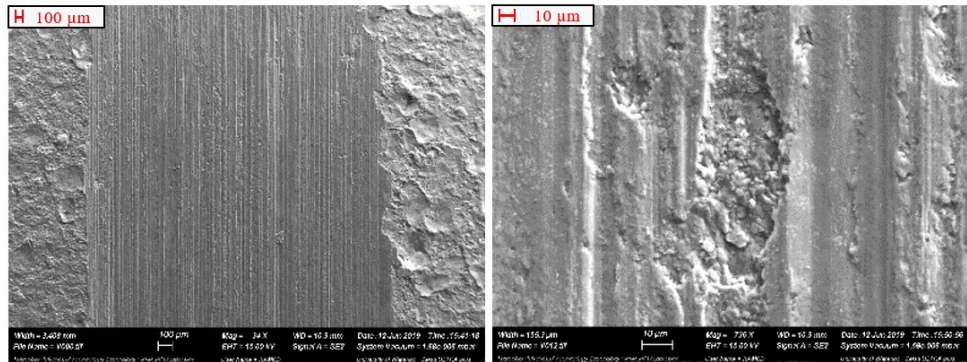
Surface type	Trial #			Average	St. Deviation
	1	2	3		
As-cast, horizontal	$3.12 \times 10^{-13}$	$1.09 \times 10^{-13}$	$4.57 \times 10^{-13}$	<b><math>2.55 \times 10^{-13}</math></b>	$1.61 \times 10^{-13}$
As-cast, vertical	$3.14 \times 10^{-13}$	$2.46 \times 10^{-13}$	$2.35 \times 10^{-13}$	<b><math>2.54 \times 10^{-13}</math></b>	$4.08 \times 10^{-14}$
Machined	$3.55 \times 10^{-13}$	$2.32 \times 10^{-13}$	$1.92 \times 10^{-13}$	<b><math>2.50 \times 10^{-13}</math></b>	$7.21 \times 10^{-14}$

Figure 4-14 shows representative SEM images for each surface type. In the low magnification image, a portion of the wear track or scar can be seen in the center of the image, while the unaltered sample surface is visible on either side. The high magnification images were taken inside each wear track to aid in the identification of the primary wear mechanisms. All three surface types exhibited features such as deep gouges and grooves parallel to the sliding direction and a high amount of loosened particles typical for two-body abrasive wear. The samples also showed signs of flaky wear debris, surface craters, and microcracks perpendicular to the sliding direction, shown in Figure 4-15.

a) As-cast, horizontal



b) As-cast, vertical



c) Machined

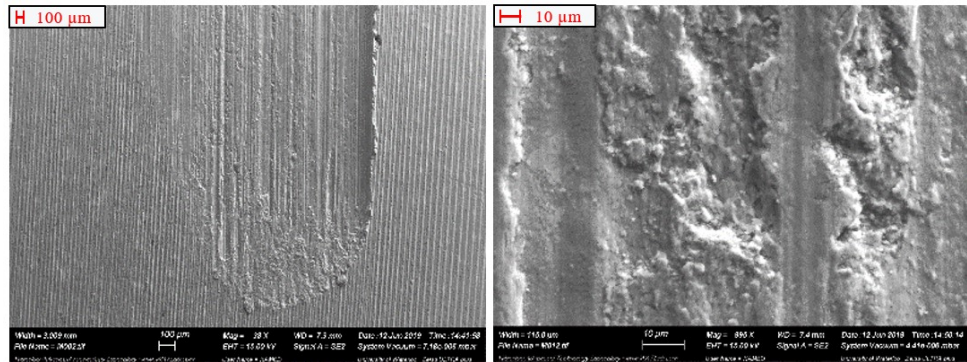
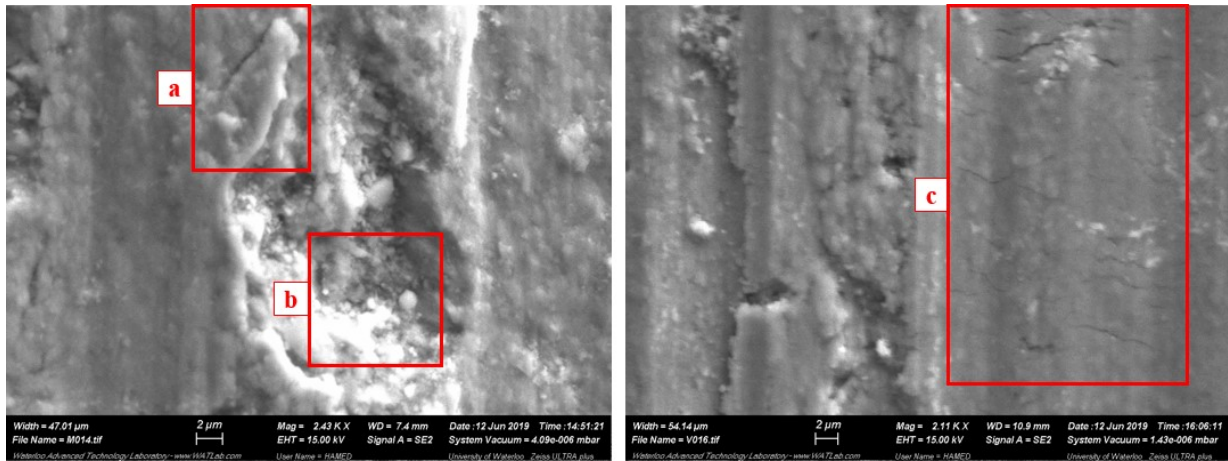
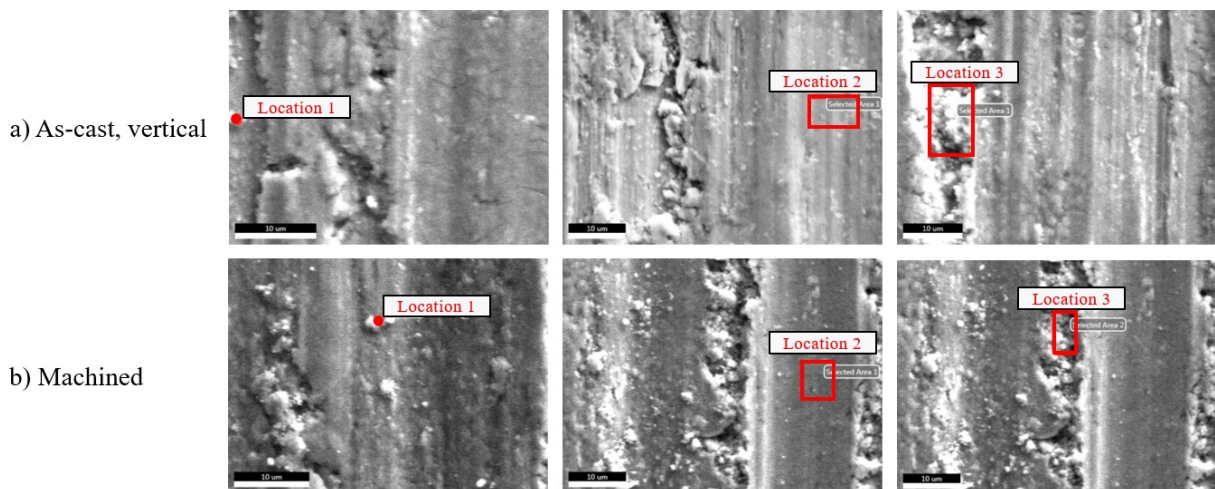


Figure 4-14: SEM images of the wear track for the cast surface types: a) as-cast, horizontal; b) as-cast, vertical; and c) machined, at low magnification (left) and high magnification (right)



**Figure 4-15: SEM images showing a) flaking of wear surface, b) crater containing wear debris, and c) transverse microcracks**

EDX analysis was performed in order to identify the chemical composition of the wear debris and the material at various locations inside the wear track. Figure 4-16 shows the measurement locations corresponding with the results in Table 4-6. The wear debris was measured at a single particle (location 1) and at an area containing flaking surface craters (location 3). Both locations had elevated oxygen levels when compared with the smooth gouges in the material (location 2), indicating that the wear debris was made up of oxide particles. It is likely that oxidative wear, which is distinguished by the growth of an oxide film that flakes off as it reaches a critical thickness, was acting in synergy with abrasive mechanical wear as the main wear mechanism.

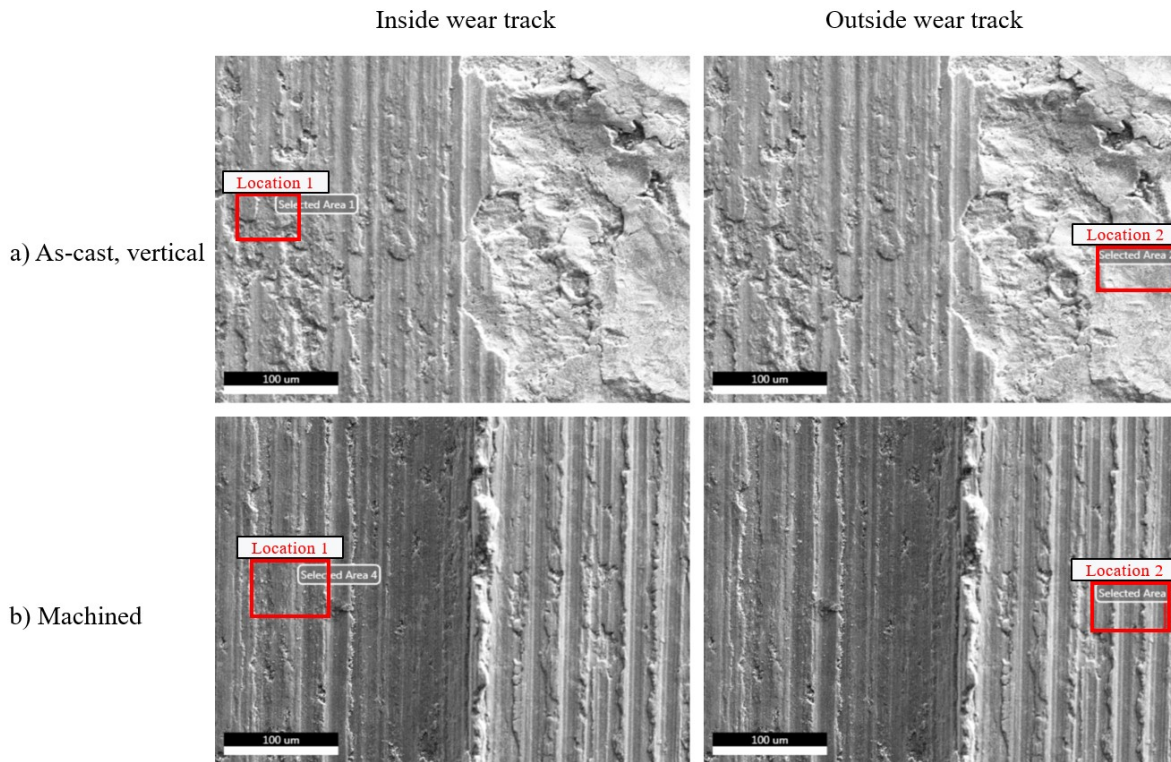


**Figure 4-16: EDX measurement locations within the wear track for a) the as-cast, vertical surface; and b) the machined surface**

**Table 4-6: EDX results for chemical composition at various locations within the wear track**

Surface Type	Measurement Location	Element (wt%)				
		O	Mg	Al	Si	Cu
As-cast, vertical	1	34.93	0.64	46.76	15.60	2.07
	2	15.92	1.01	65.21	14.05	3.81
	3	28.86	0.84	58.26	9.23	2.80
Machined	1	36.86	0.99	49.40	10.50	2.25
	2	12.33	0.60	56.67	28.78	1.61
	3	31.17	0.46	51.81	12.78	3.79

For comparison, EDX analysis was also performed outside the wear track on the untouched surface of the samples. Figure 4-17 shows the measurement locations corresponding with the results in Table 4-7. It was found that the inside of the wear track (location 1) contained 6 to 8 times the amount of oxygen (by weight %) when compared with the area outside of the wear track (location 2). This provides further evidence that oxidative wear has occurred, because if the oxygen was not already present in the material, the increase must have been the result of a reaction with oxygen from the environment.



**Figure 4-17: EDX measurement areas inside (location 1) and outside (location 2) the wear track, for a) the as-cast, vertical surface; and b) the machined surface**

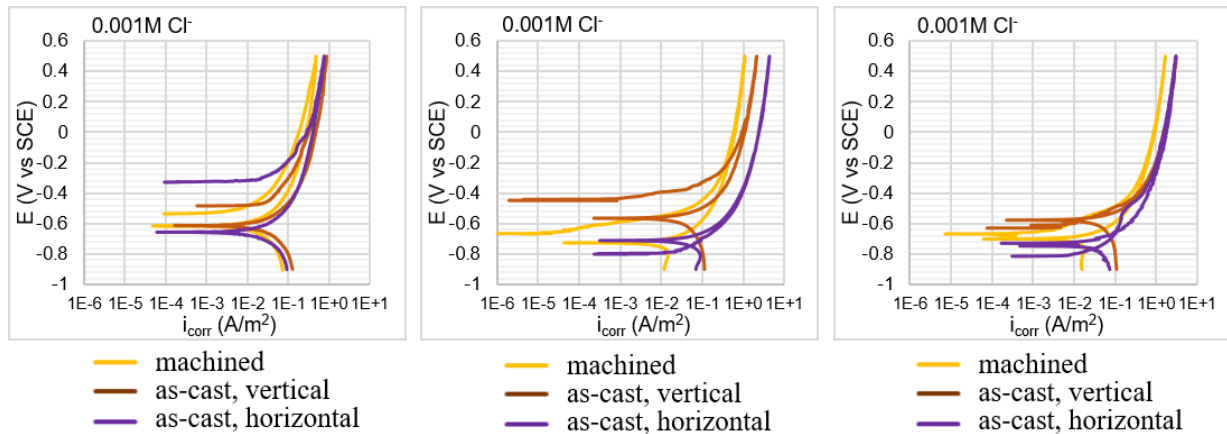
**Table 4-7: EDX results for chemical composition inside and outside the wear track**

Surface Type	Measurement Location	Element (wt%)				
		O	Mg	Al	Si	Cu
As-cast, vertical	Inside wear track	34.67	0.66	53.29	8.14	3.25
	Outside wear track	5.75	2.5	62.73	11.65	17.37
Machined	Inside wear track	21.81	0.74	59.78	14.18	3.5
	Outside wear track	2.52	0.75	71	22.79	2.93

### 4.3.8 Corrosion

#### *Cyclic potentiodynamic polarization*

Figure 4-18 shows the cyclic potentiodynamic curves for three replicates of the three cast pump housing surface types, which were all tested in a 0.001M chloride solution. The resulting anodic and cathodic corrosion potentials and anodic current density at 0.2V are listed in Table 4-8, and the average results for each surface type are listed in Table 4-9.

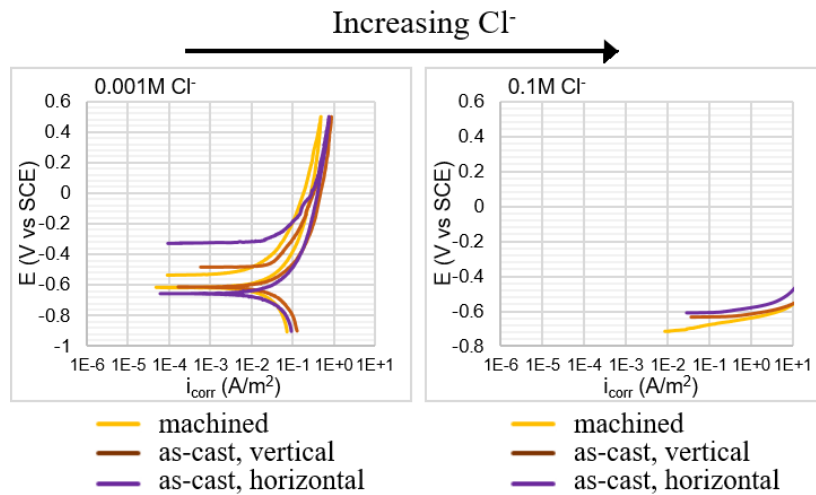


**Figure 4-18: Cyclic potentiodynamic polarization curves for three replicates of the cast pump housing surfaces**

For the three replicates of the cyclic polarization test, the anodic corrosion potentials ranged from -0.80 to -0.32 V (vs SCE). The anodic corrosion potentials for the three surface types were close in magnitude; however, the as-cast, horizontal surface had a larger variance. The cathodic corrosion potentials had less variance between replicates and surface types, ranging from -0.72 to -0.56 V (vs SCE). In this case, the machined and as-cast horizontal surfaces had similar potentials while the as-cast, vertical surface was typically more positive. The current density measured at 0.2 V was consistently the lowest for the machined surface, meaning that it would have the lowest corrosion rate. The as-cast

surfaces likely had higher current densities because of the increased surface roughness, which would result in more active sites for the electrochemical reactions since a rough surface is more prone to defects in the passive film and has a greater surface area. Despite normalizing the current with the sample surface area, the true surface area may have been higher than the apparent surface area because of the surface asperities.

Figure 4-19 shows a comparison of cyclic polarization curves that were generated by testing in either a 0.001M or 0.1M Cl<sup>-</sup> solution. The resulting anodic and cathodic corrosion potentials and anodic current density at 0.2V are listed in Table 4-8.



**Figure 4-19: Effect of increasing chloride concentration on cyclic polarization curves for the cast pump housing**

When the cyclic polarization test was performed in a solution with a higher concentration of chloride ions, the corrosion current density rapidly increased with the applied voltage, and the test was terminated at 5 mA. The samples immediately exhibited general corrosion. In contrast, at the lower chloride concentration the full test cycle was completed; however, the curves did not exhibit a change in slope or inflection point that is characteristic of the initiation of pitting corrosion. Instead, the initial pit formation likely occurred at the anodic corrosion potential, prior to starting the test.

**Table 4-8: Results for cyclic polarization testing of the cast pump housing**

Chloride Molarity	Surface Type	Anodic Corrosion Potential (V)	Anodic Current @ 0.2V (A/m <sup>2</sup> )	Cathodic Corrosion Potential (V)
0.001 M	Machined	-0.52	0.3	-0.61
	As-cast, vertical	-0.48	0.7	-0.61
	As-cast, horizontal	-0.32	0.6	-0.64
0.001 M	Machined	-0.67	0.9	-0.72
	As-cast, vertical	-0.50	1.18	-0.56
	As-cast, horizontal	-0.80	1.21	-0.70
0.001 M	Machined	-0.66	1.5	-0.70
	As-cast, vertical	-0.63	2.0	-0.59
	As-cast, horizontal	-0.80	2.0	-0.72
0.1 M	Machined	-0.72	Max (5mA)	N/A
	As-cast, vertical	-0.64	Max (5mA)	N/A
	As-cast, horizontal	-0.60	Max (5mA)	N/A

**Table 4-9: Average results for three replicates tested in the 0.001 M chloride solution**

Chloride Molarity	Surface Type	Anodic Corrosion Potential (V)	Anodic Current @ 0.2V (A/m <sup>2</sup> )	Cathodic Corrosion Potential (V)
0.001 M	Machined	-0.61 ± 0.084	0.90 ± 0.60	-0.68 ± 0.059
	As-cast, vertical	-0.54 ± 0.081	1.29 ± 0.66	-0.59 ± 0.025
	As-cast, horizontal	-0.64 ± 0.28	1.27 ± 0.70	-0.69 ± 0.042

**Calculation of Stern-Geary Coefficient**

The results from the first replicate of the cyclic polarization test were used to calculate the Stern-Geary coefficient for use in calculating the corrosion current density for the linear polarization resistance tests. Table 4-10 shows the results obtained by Tafel slope extrapolation of the polarization curves for the three surface types. The average of the calculated Stern-Geary coefficients,  $B = 0.0114$  V, was used for all LPR tests.

**Table 4-10: Corrosion properties for pump housing, from replicate 1 of cyclic polarization test**

Surface Type	Corrosion Current Density, $i_{\text{corr}}$ (A/m <sup>2</sup> )	Corrosion Potential, $E_{\text{corr}}$ vs. SCE (V)	Cathodic Tafel Constant, $\beta_c$ (V)	Anodic Tafel Constant, $\beta_a$ (V)	Stern-Geary Coefficient, B (V)
Machined	0.00549	-0.622	0.041	0.0472	0.00954
As-cast, vertical	0.00714	-0.613	0.05	0.0488	0.0107
As-cast, horizontal	0.0167	-0.660	0.068	0.0609	0.0140
<b>Average:</b>					<b>0.0114</b>



### Linear polarization resistance

Figure 4-20 shows the open circuit potential and corrosion current density over time, averaged for three replicates of each surface type of the cast pump housing. On day 11, the initial addition of chloride ions had a negative impact on the corrosion resistance, as demonstrated by the decrease in potential from between -400 and -500 mV to around -700 mV. The current density also increased by approximately two orders of magnitude, going from less than 0.001 A/m<sup>2</sup> to around 0.1 A/m<sup>2</sup>, meaning that the corrosion rate also increased. After that, further increases in chloride concentration had little effect on the severity of the corrosion, beyond the initial negative impact. After 38 days, the corrosion potentials for all three surface types were nearly the same, indicating that the thermodynamic likelihood of corrosion was equal. The corrosion current density fluctuated over time and with every addition of chloride ions (days 11, 23, and 32), showing that each of the three surface types had the highest corrosion rate at different points in time. At the conclusion of the testing, the as-cast, horizontal surface had the highest corrosion current density.

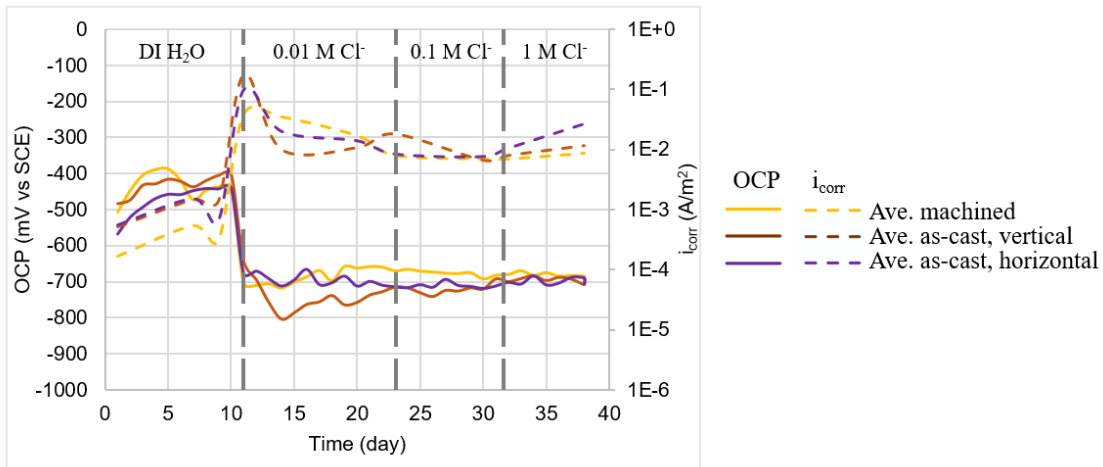


Figure 4-20: Open circuit potential (OCP) and corrosion current density ( $i_{\text{corr}}$ ) determined by LPR for the cast pump housing

## 4.4 Summary of Cast Pump Housing Characterization

The cast pump housing product demonstrator was characterized to provide benchmark values to help evaluate if the additive manufacturing process can meet industrial manufacturing standards. The main findings are as follows:

- Chemical analysis revealed over twice as much silicon and the presence of elements such as copper and iron, which are not present in the AlSi10Mg alloy
- Microstructure was a dendritic matrix of Al with precipitates in the form of coarse flakes, particles, and semi-continuous interdendritic network
- Relative density ranged from 99.15 to 99.97%
- Surface roughness ( $S_a$ ) of as-cast surfaces ranged from 3.91 to 13.45  $\mu\text{m}$ , while the machined surface was around 0.41  $\mu\text{m}$
- Minimum size requirements for key geometric features were identified: thin walls (min. thickness of 2.50 mm), slots (min. gap width of 2.63 mm), and holes (min. diameter of 3.98 mm)
- Hardness ranged from 72.8 to 84.8 HRB
- Specific wear rate ranged from  $2.50 \times 10^{-13}$  to  $2.55 \times 10^{-13} \text{ m}^2\text{N}^{-1}$
- Cyclic polarization curves measured in 0.001M  $\text{Cl}^-$  solution showed that general corrosion had occurred (no pitting potential observed), anodic corrosion potentials ranged from -0.80 to -0.32 V (vs SCE), cathodic corrosion potentials ranged from -0.72 to -0.56 V (vs SCE), and anodic current density (measured at 0.2 V vs SCE) ranged from 0.3 to 2.0  $\text{A}/\text{m}^2$
- Average Stern-Geary coefficient ( $B = 0.0114 \text{ V}$ ) was calculated for use in all LPR analysis
- During LPR testing, the addition of  $\text{Cl}^-$  caused a decrease in potential from between -400 and -500 mV to around -700 mV and an increase in corrosion current density from less than 0.001  $\text{A}/\text{m}^2$  to around 0.1  $\text{A}/\text{m}^2$

# 5 LPBF Process Parameter Mapping and Ideal Parameter Selection for Density and Surface Roughness

## 5.1 Powder Material Characterization

### 5.1.1 Powder Type Selected for Experiments

The AlSi10Mg powder material with the same chemistry was obtained from two suppliers. Supplier 1 was used in the first experiments for the purpose of creating an initial process map for the material using the Renishaw AM 400 machine. Due to material availability, the powder supplier was changed to Supplier 2 for the next set of experiments, which were used to further refine the process parameters in order to achieve a dense core and good surface quality. Finally, the powder supplier was changed back to Supplier 1 to verify that the selected ideal recipes could provide the desired part density and surface quality, and to print the final AM samples to use for characterizing the LPBF part performance. Table 5-1 identifies the powder supplier that was used for each Design of Experiment (DOE) that appears in the subsequent sections.

Each powder type was characterized according to the methods found in Section 3.1. The morphology of the powder was investigated through scanning electron microscopy (Section 3.1.1). The powder particle size distribution was determined using a dynamic image particle size / shape analyzer (Section 3.1.2).

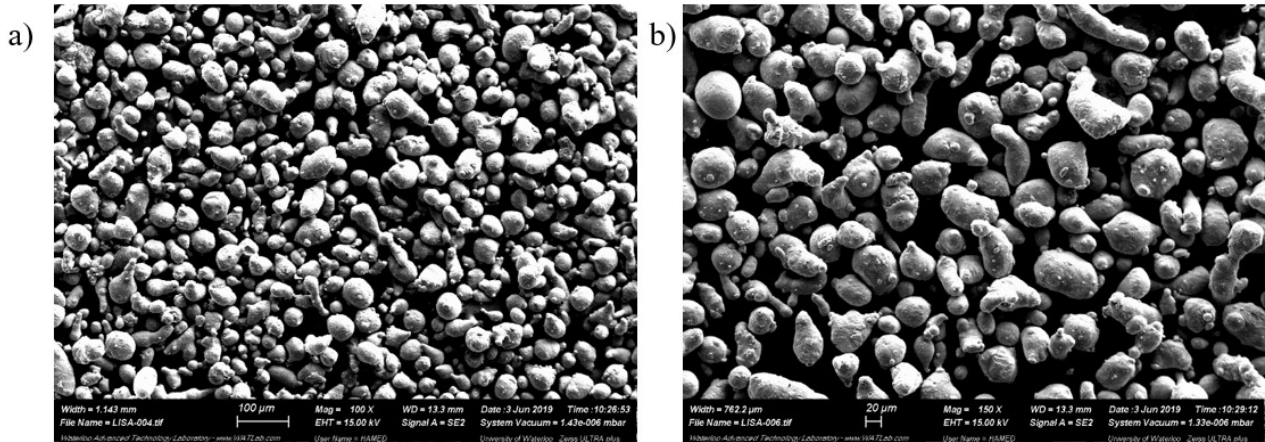
**Table 5-1: Powder type selected for each experiment**

Powder Type	Chapter	Experiment
Supplier 1	5.2.1 Initial Process Mapping with Low Cost Powder	DOE 2-1
		DOE 2-2
		DOE 2-3
		DOE 2-4
Supplier 2	5.2.2 Parameter Selection Using Thermal Modelling Tool 5.2.3 Selection of Ideal Recipes for Dense Core 5.2.4 Selection of Ideal Recipes for Surface Quality	DOE 3-1
		DOE 3-2
		DOE 3-3
		DOE 3-5 DOE 3-6
Supplier 1	5.2.3 Selection of Ideal Recipes for Dense Core 5.2.4 Selection of Ideal Recipes for Surface Quality 6.1.1 Manufacturing Strategy	DOE 3-6
		DOE 4-2

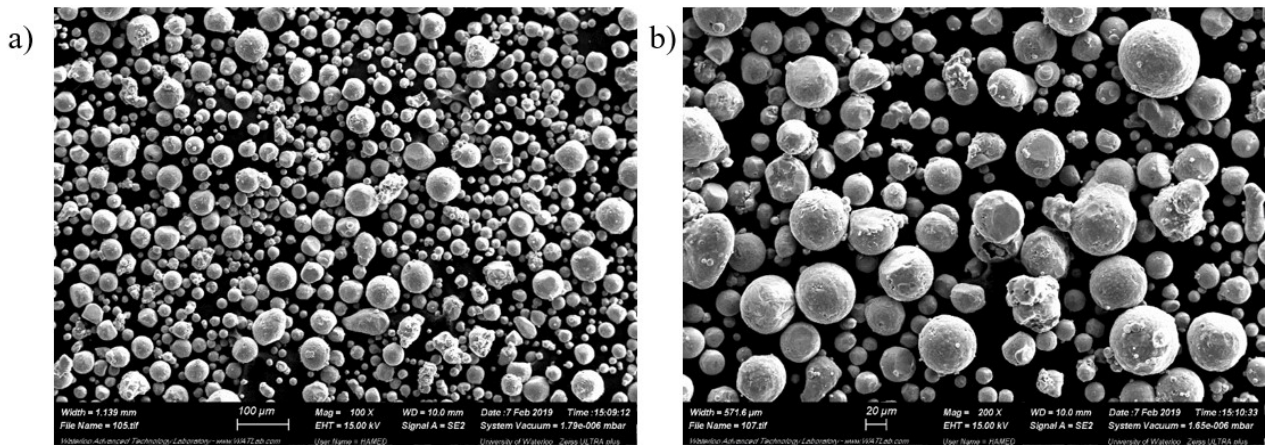
### 5.1.2 Scanning Electron Microscopy

Representative SEM images for the powder from Supplier 1 and Supplier 2 are shown in Figure 5-1 and Figure 5-2, respectively. The powder from Supplier 1 has an irregular morphology containing oblong

particles of varying aspect ratios. The powder from Supplier 2 features a more uniform morphology with near-spherical particles. These differences in morphology may impact the powder flowability and powder bed compaction as well as the material interaction with the laser due to discrepancies in the exposed surface area.



**Figure 5-1: SEM micrographs of the AlSi10Mg powder from Supplier 1: a) low magnification; b) high magnification**



**Figure 5-2: SEM micrographs of the AlSi10Mg powder from Supplier 2: a) low magnification; b) high magnification**

### 5.1.3 Particle Size Distribution

The particle size distributions for the two powder types are shown in Table 5-2. Refer to Appendix E for plots of the particle size versus the cumulative % passing (Q3). The Q3 value refers to the cumulative percentage of particles that measured below the specified size for the minimum chord length ( $X_{c,min}$ ). Accordingly, the  $D_{10}$  value corresponds with the size that 10% of the measured particles fall below, while 50% fall below the  $D_{50}$  and 90% fall below the  $D_{90}$ . The mean particle size of the powder from Supplier 1 was  $44.16 \pm 11.78 \mu\text{m}$ , and the mean for the powder from Supplier 2 was  $46.10 \pm 15.69$

$\mu\text{m}$ . The layer thickness for the LPBF process was set to 50, 35, or 30  $\mu\text{m}$  for the various experiments. The layer thickness setting may be smaller than the average particle size because in steady state, when the build platform is lowered by the layer thickness setting, the effective layer thickness is larger due to the melting of the previous layer.

**Table 5-2: Particle size values corresponding with 10%, 50%, and 90% cumulative passing**

Q3 (%)	Supplier 1 $X_{c,\min}$ ( $\mu\text{m}$ )	Supplier 2 $X_{c,\min}$ ( $\mu\text{m}$ )
D <sub>10</sub>	28.81 $\pm$ 0.38	25.81 $\pm$ 1.03
D <sub>50</sub>	44.04 $\pm$ 0.49	45.27 $\pm$ 0.46
D <sub>90</sub>	59.59 $\pm$ 1.10	67.60 $\pm$ 0.98
Mean	44.16 $\pm$ 11.78	46.10 $\pm$ 15.69

## 5.2 Process Parameter Selection for Core

### 5.2.1 Methods for Initial Process Mapping for Density

Cube-shaped artifacts with a side length of 10 mm were printed with the meander laser scan strategy and a 67° rotation between each layer. One border scan and one fill contour were used, with the default scan volume parameters. The upskin, downskin, and blocked path settings were turned off, and 5 mm tall cylindrical support structures were used. The process settings in Table 5-3 were also kept consistent throughout the experiments discussed in this section.

**Table 5-3: Controlled parameters for DOE 2-1 to 2-4**

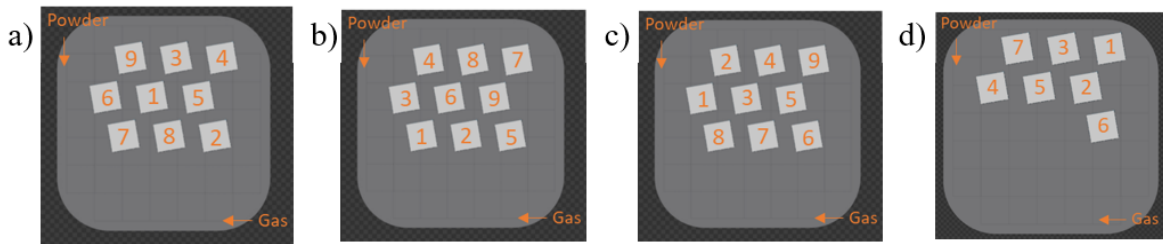
Powder type	Layer thickness ( $\mu\text{m}$ )	Hatch distance ( $\mu\text{m}$ )	Laser spot diameter ( $\mu\text{m}$ )
Supplier 1	50	100	70

In order to span the full process window, a variety of Volumetric Energy Densities were targeted by changing the set values for the laser power, point distance, and exposure time. A full 3<sup>3</sup> factorial experiment was run with a total of 27 samples that each received a different treatment, hereafter referred to as the manufacturing “recipe”. The levels for each factor are shown in Table 5-4. In addition, several samples were printed using a higher point distance (90  $\mu\text{m}$ ) and a lower exposure time (30  $\mu\text{s}$ ); however, based on the results of the first print, the levels were eliminated from the factorial experiment and replaced by 45  $\mu\text{m}$  and 75  $\mu\text{s}$ , respectively. Refer to Appendix F for the exact manufacturing recipes used for each print, and the calculated values for the effective scan speed and volumetric energy density for each recipe.

The samples were printed on the Renishaw Reduced Build Volume with up to 9 cubes per print, which were placed in a randomized order. A total of four prints were completed over a period of one month, and between each print the samples were analyzed and the machine was reset (which involved build plate removal/installation, powder supply restocking, cleaning and filter changes as necessary). Figure 5-3 shows the corresponding build plate layouts and the direction of powder spreading and gas flow. Sample analysis involved metallographic examination of the microstructure and porosity measurements as described in Section 3.3.2.

**Table 5-4: Levels used for 3<sup>3</sup> full factorial experiment – DOE 2-1 to 2-4**

Level	Power (W)	Point distance (μm)	Exposure time (μs)
-1	240 (DOE 2-3)	45	45
0	260 (DOE 2-2)	60	60
+1	280 (DOE 2-1, 2-4)	75	75



**Figure 5-3: Top view of the build plate layouts shown in QuantAM software for: a) DOE 2-1; b) DOE 2-2; c) DOE 2-3; d) DOE 2-4, where the label corresponds with the recipe number used for that sample.**

For the next set of experiments, the powder type was changed from the AlSi10Mg powder from Supplier 1 to the AlSi10Mg powder from Supplier 2. The other controlled parameters from Table 5-3 remained unchanged.

For DOE 3-1, the printing parameters from DOE 2-3 were repeated with the new powder in order to verify that the results and general trends observed with the original powder would still be applicable. On a separate build plate (DOE 3-2), 8 cylindrical samples were printed with a constant power of 200 W, and a constant point distance of 60 μm. This setting was selected based on the results of the 3<sup>3</sup> full factorial experiment, which indicated lower levels of porosity at a point distance of 60 μm. The microstructural analysis showed evidence of the “keyhole” melting regime, so a lower power level was selected in order to reduce the heat input during the process. Various exposure times ranging from 38 to 171 μs were used in order to span the possible processing window for the effective laser scan speed. Table 5-5 and Table 5-6 show the processing parameters for the two build plates printed using the powder from Supplier 2. The 9 cubes and 8 cylindrical samples were analyzed, again using the

techniques for metallographic examination of the microstructure and pore fraction measurements as described in Section 3.3.2.

**Table 5-5: Processing parameters for DOE 3-1**

Level	Power (W)	Point distance ( $\mu\text{m}$ )	Exposure time ( $\mu\text{s}$ )
-1	240	45	45
0		60	60
+1		75	75

**Table 5-6: Processing parameters for DOE 3-2**

Power (W)	Point distance ( $\mu\text{m}$ )	Exposure time ( $\mu\text{s}$ )
200	60	171, 119, 90, 72, 60, 50, 43, 38

## 5.2.2 Results for Initial Process Mapping for Density

### *DOE 2-1 to 2-4:*

Figure 5-4 shows the optical micrographs and estimated solid fraction for samples with various settings for the laser exposure time and point distance between exposures, and a constant power level of 280 W. The micrographs all contained large spherical pores typical for keyhole melting mode and indicative of excessive energy input during the LPBF process. Additional micrographs for samples processed at 280 W can be found in Appendix G. Figure 5-5 and Figure 5-6 show micrographs for samples with the same combinations of settings for exposure time and point distance, but the power level was reduced to 260 W and 240 W, respectively. At slower laser scan speeds, which occurred when the exposure time was long and/or when the point distance was close together (top row and left column of micrographs in each grid), keyhole porosity was observed. The size of those pores reduced as the laser power was reduced. Large, irregular pores occurred at faster laser scan speeds, especially when the combined parameters were the minimum exposure time and maximum point distance (bottom-right micrograph in each grid). This lack of fusion porosity is caused by insufficient melting, or too large a distance between melt pools for them to successfully weld together. As the power level decreased, the lack of fusion defects became more severe and more samples were affected. The process parameters and corresponding porosity levels (%) are visualized on a 3D bubble plot shown in Figure 5-7, where the bubble size indicates the estimated pore fraction for the sample.

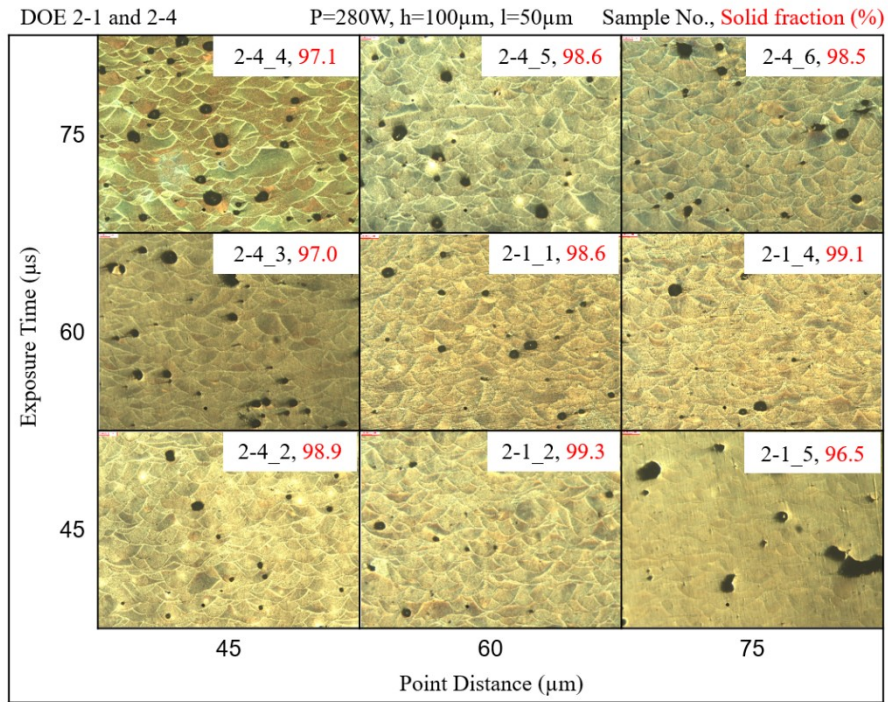


Figure 5-4: Optical micrographs for selected samples from DOE 2-1 and 2-4

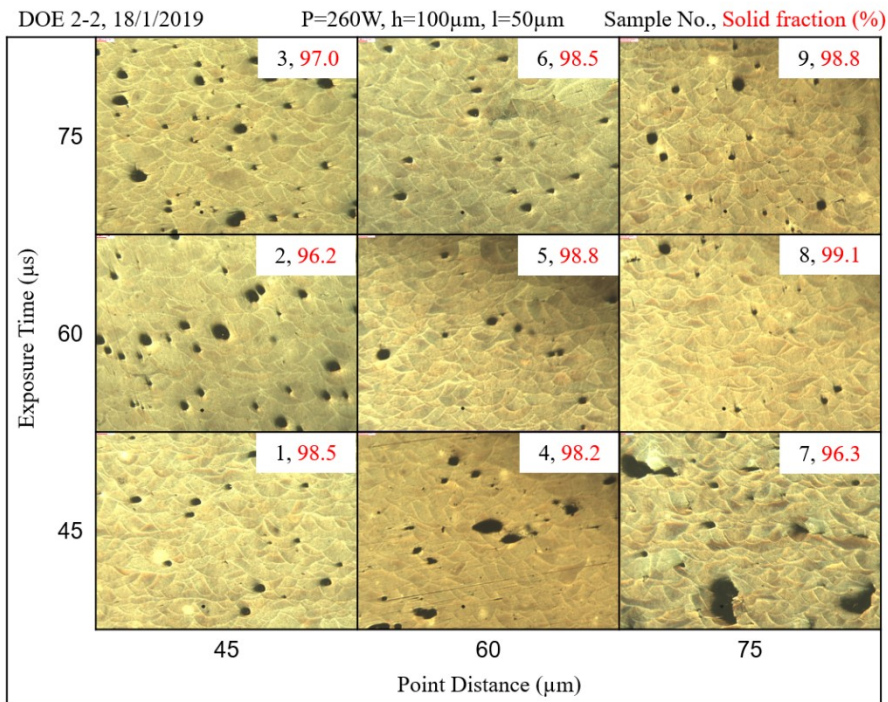


Figure 5-5: Optical micrographs for samples from DOE 2-2



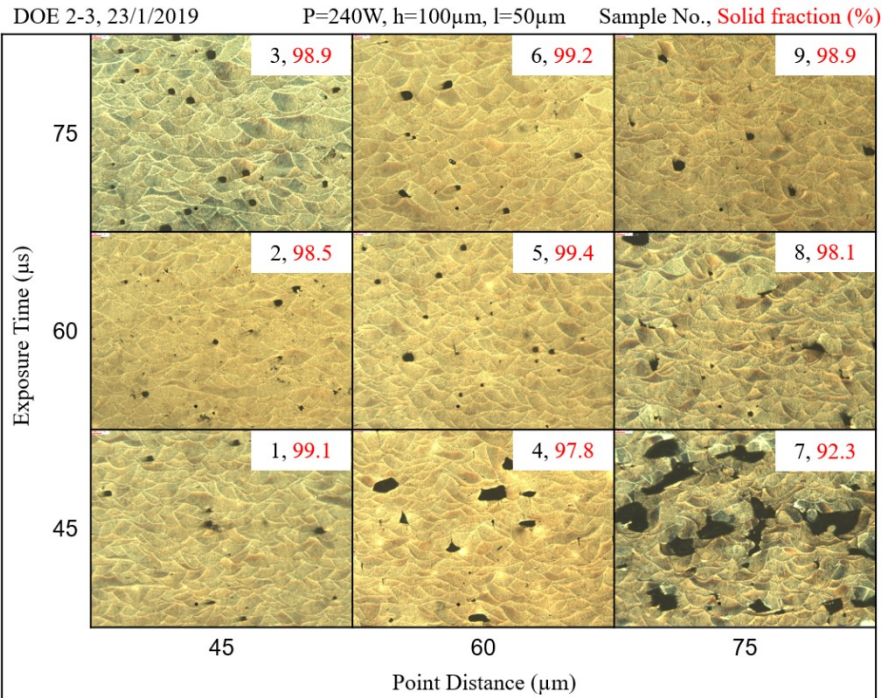


Figure 5-6: Optical micrographs for samples from DOE 2-3

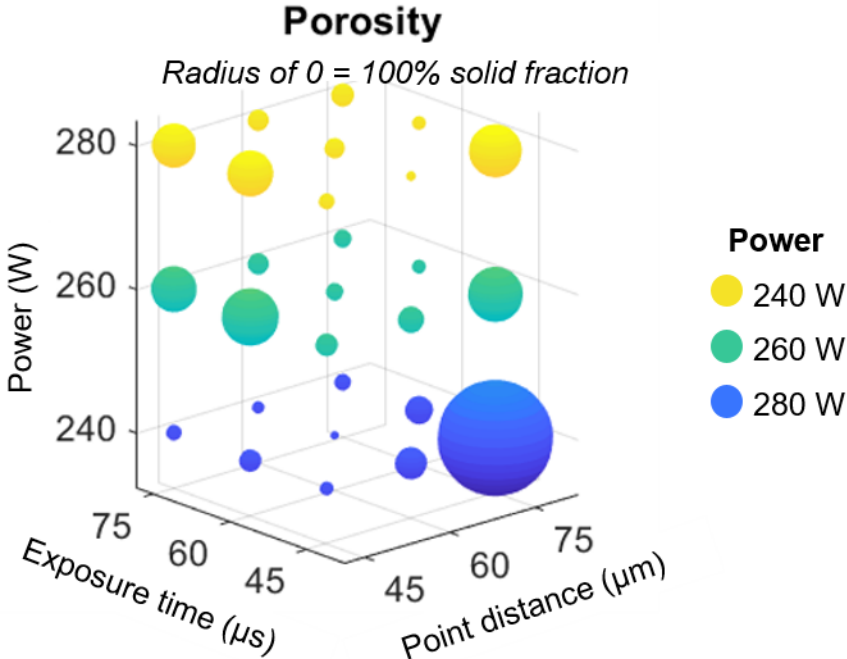
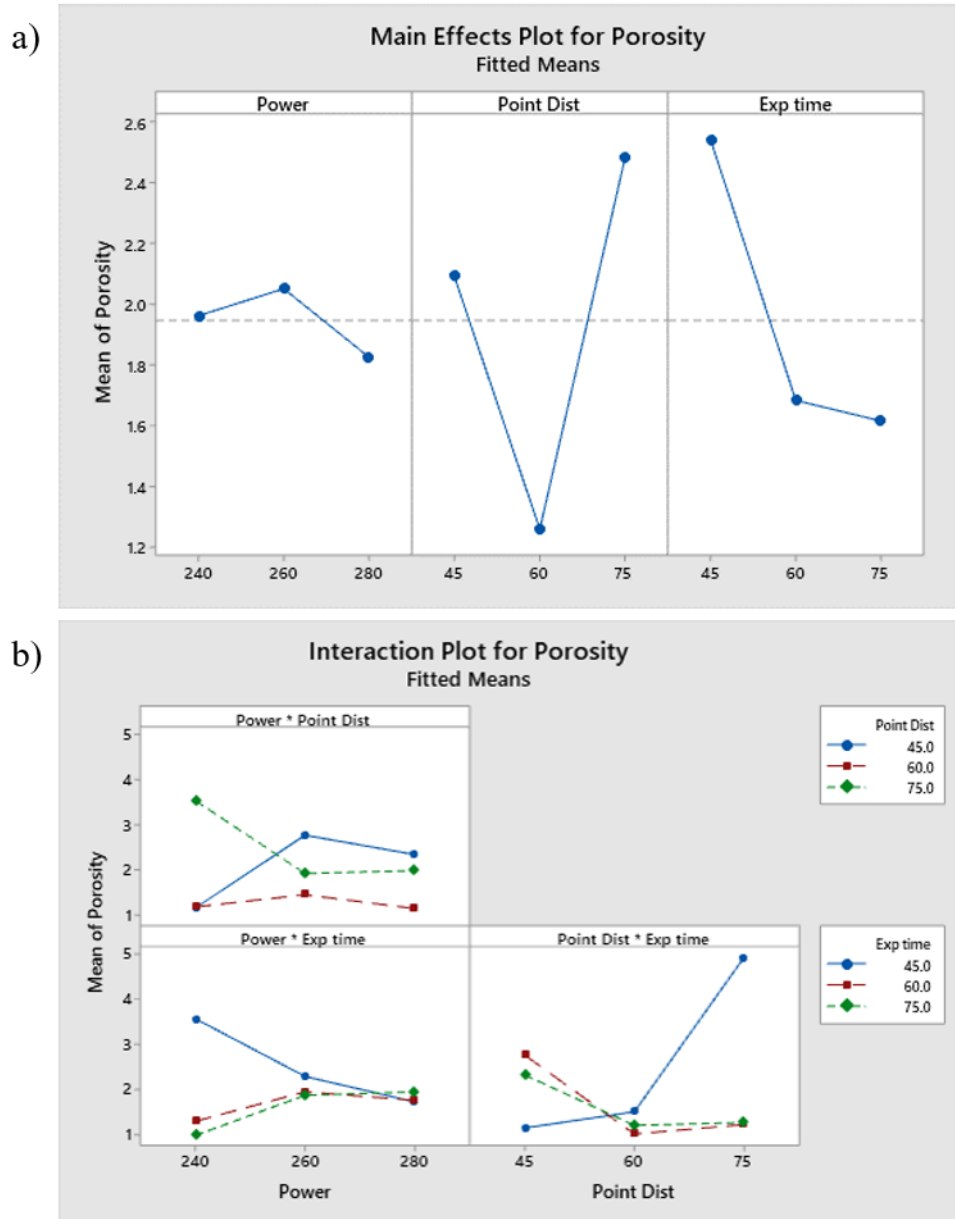


Figure 5-7: Bubble plot showing estimated porosity versus the process parameters for DOE 2-1 to 2-4

Collectively, DOE 2-1 to 2-4 contained all the treatments required for a 3<sup>3</sup> full factorial experimental design, so the results were used to perform a statistical analysis on the effect that changing the power, point distance, and exposure time had on the porosity level. Figure 5-8 shows the main effects and the interaction plots for the response of the sample porosity.



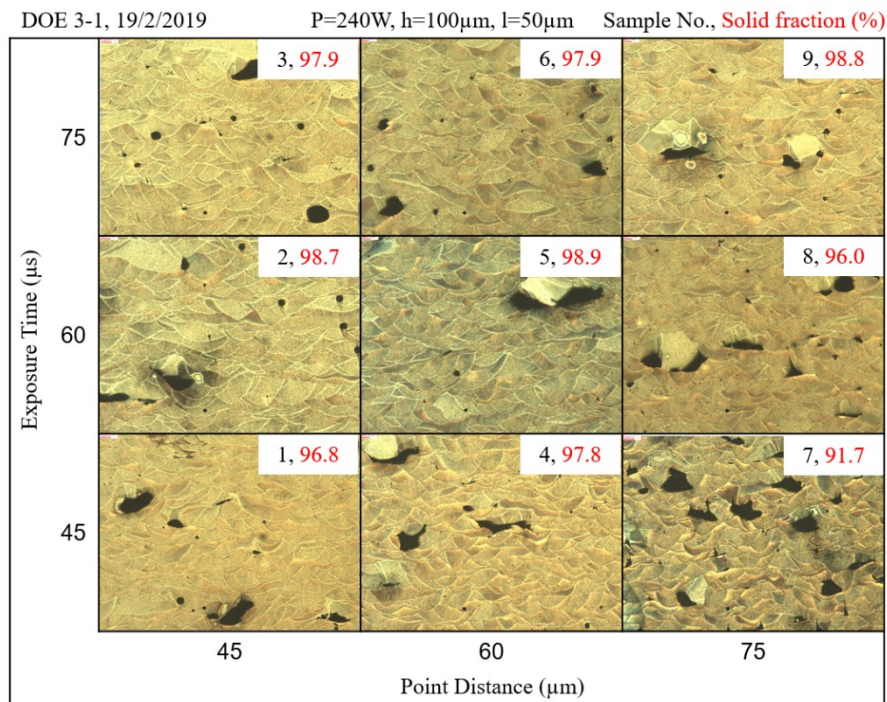
**Figure 5-8: a) Main effects and b) interaction plot for porosity**

The main effect of the power setting showed that the average porosity level was lowest at the highest power; however, the severe lack of fusion observed in some of the low-powered recipes may have skewed the result, and the interaction plots revealed that the highest power setting did not universally

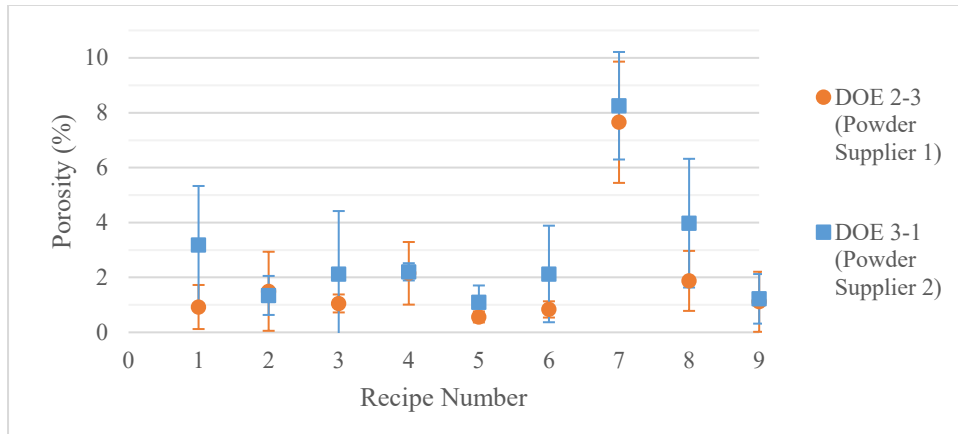
have the best outcomes. The intermediate point distance of 60  $\mu\text{m}$  consistently minimized the porosity level, even at varied powers and exposure times. The lowest exposure time generally had the worst porosity, but was largely dependent on the interaction with point distance.

**DOE 3-1:**

Figure 5-9 shows the optical micrographs and estimated solid fraction for samples from DOE 3-1, which repeated the same process parameters that were used for DOE 2-3, except the powder supplier was changed from Supplier 1 (irregular morphology) to Supplier 2 (spherical morphology). When compared with Figure 5-6, it can be seen that the samples manufactured with powder from Supplier 2 contained more numerous large, irregular pores, and the keyhole porosity was still present. The relative densities were lower due to the defects, but the general trends were consistent with the previous results and the intermediate point distance and exposure time again had the highest estimated density (recipe 5, center micrograph in grid). Figure 5-10 shows a direct comparison of the porosity for each recipe using the two different powder types.



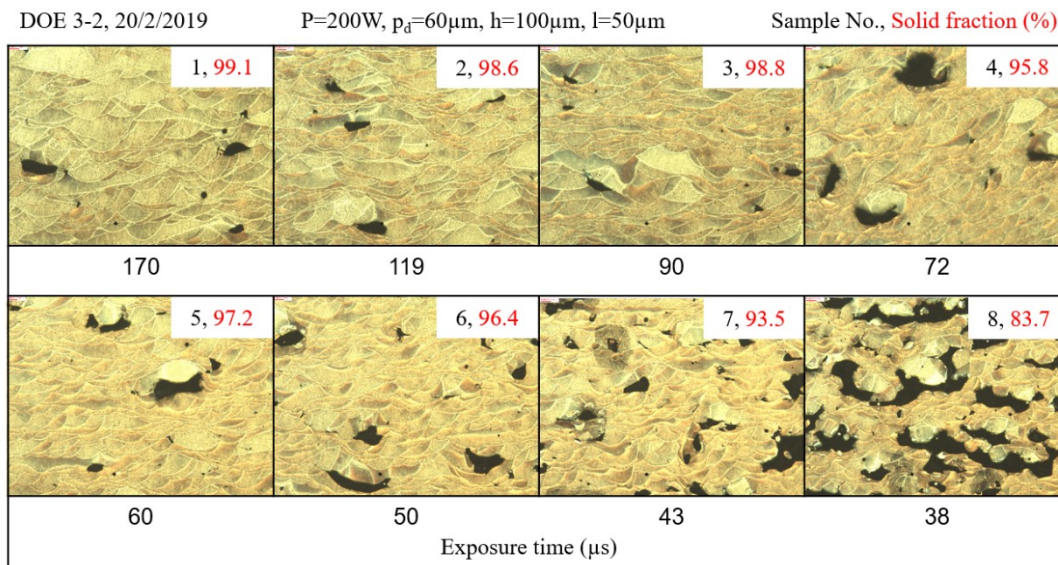
**Figure 5-9: Optical micrographs for samples from DOE 3-1**



**Figure 5-10: Mean pore fraction for 5 micrographs from each sample, which were manufactured with the same processing parameters but different powder suppliers**

**DOE 3-2:**

Figure 5-11 shows the optical micrographs and estimated solid fraction for samples from DOE 3-2, which were printed with a constant power of 200 W, a constant point distance of 60  $\mu\text{m}$ , and various settings for the exposure time that were selected to span the possible processing window for the effective laser scan speed. As the exposure time decreased, it was found that the relative density also decreased. Even the best sample (recipe 1, top-left in grid) exhibited both large, irregular-shaped pores and small spherical pores.



**Figure 5-11: Optical micrographs for samples from DOE 3-2**

**Summary:**

Figure 5-12 shows a 2D bubble plot summarizing all of the process parameters and corresponding porosity results presented in this section. The bubble size is commensurate with the estimated porosity percentage, while the x-axis is the non-dimensionalized laser scan speed ( $v^*$ ) and the y-axis is the non-dimensionalized laser power ( $P^*$ ). To help with the planning of future experiments, a region of low-porosity was identified as the area between the two dashed red lines. It was decided to permanently set the point distance to 60  $\mu\text{m}$  based on the findings from DOE 2-1 to 2-4. Because of the irregular pores and process instability still present in DOE 3-2, it was also decided to reduce the layer thickness from 50  $\mu\text{m}$  to 35  $\mu\text{m}$  for the next experiment.

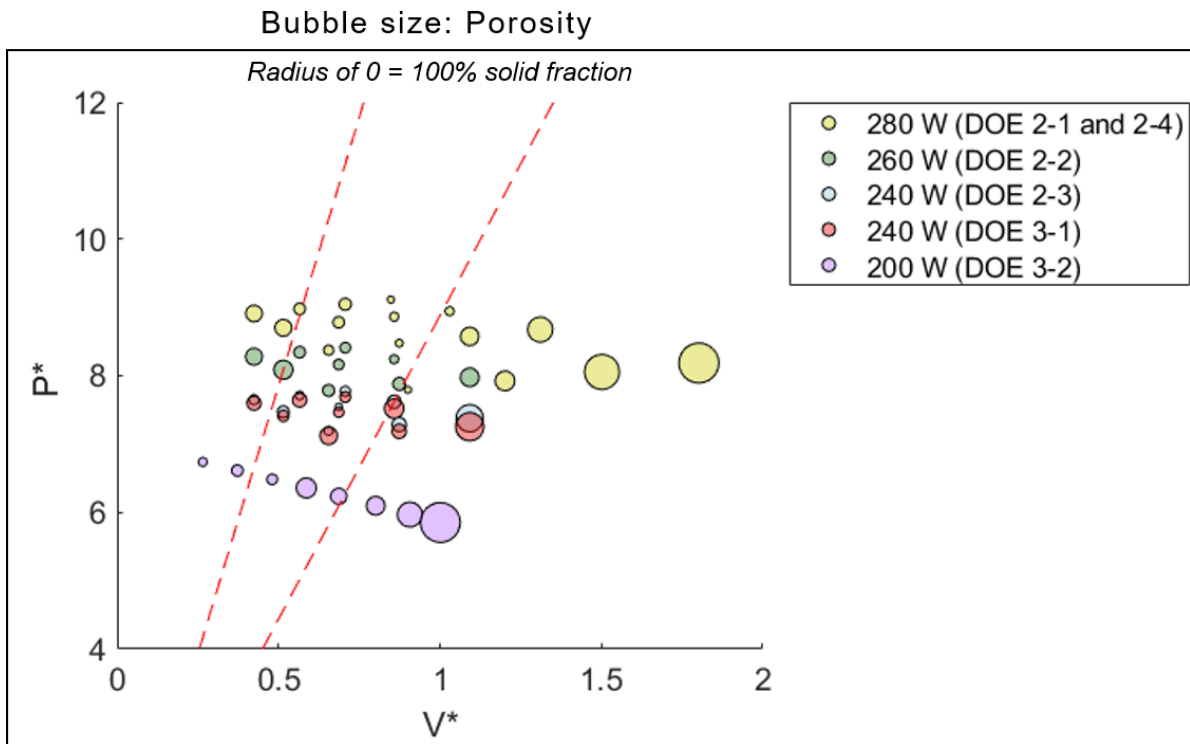


Figure 5-12: Bubble plot showing estimated porosity versus process parameters for DOE 2-1 to 3-2

### 5.2.3 Methods for Parameter Selection Using Thermophysical Modelling Tool

In this section, a thermophysical model was used to predict melt pool geometries based on the material properties and process parameter inputs. The material absorptivity was then calibrated based on empirical melt pool measurements so that the reverse-model could be used to calculate the required processing parameters for an ideal melt pool geometry. The thermophysical model was adapted for this use by Dr. Allan Rogalsky (Post-Doctoral Fellow, Multi-Scale Additive Manufacturing Laboratory),

who also provided the theoretical development in Sections 5.2.2.1 and 5.2.2.2. This theoretical development is part of ongoing scholarly publication efforts.

### 5.2.3.1 Thermophysical Model Suite

Melt pool temperatures and geometries were predicted using a modified version of the model developed by Rubenchik et al. [32], [109]. The core of this approach is an analytical solution for the temperature field of 3D Gaussian moving source on a semi-infinite plane (Equation 9, 10, 11). The origin of the coordinate system is at the point where the laser intersects the top surface of the work piece. The scanning direction is the (+x) coordinate vector, with y being perpendicular to the scanning direction and (-z) being in the layer direction. The x, y, z in this model are non-dimensionalized with respect to the spot radius r. Melt pool size is determined by solving for the coordinates when  $\frac{\Delta T}{\Delta T_m} = 1$ , where  $T_m$  is the melting temperature of the material and  $T_0$  is the ambient temperature (assumed to be 25°C).

$$\frac{\Delta T}{\Delta T_m} = \frac{T - T_0}{T_m - T_0} = B \cdot G(x^*, y^*, z^*, v^*) \quad \text{Equation 9}$$

$$G(x^*, y^*, z^*, v^*) = \int_0^\infty t^{-0.5} \left(4 \frac{t}{v^*} + 1\right)^{-1} \text{Exp} \left[ -\frac{z^{*2}}{4 \frac{t}{v^*}} - \frac{y^{*2} + (x^* - t)^2}{4 \frac{t}{v^*} + 1} \right] dt \quad \text{Equation 10}$$

$$x^* = \frac{x}{r}; \quad y^* = \frac{y}{r}; \quad z^* = \frac{z}{r} \quad \text{Equation 11}$$

While the functional form in Equations 9 – 11 is equivalent to that provided by Rubenchik & Wu [109], the following refinements were adopted: i) the non-dimensional scan speed  $v^*$  was substituted for  $p$  as described in Equation 12 for consistency with the laser welding literature [110], and ii) the  $z^*$  dependence on material properties has been adopted into  $G$  in the same manner as was done by [109] for the other two spatial dimensions.

$$v^* = \frac{v_{eff} r}{\alpha} = \frac{1}{p} \quad \text{Equation 12}$$

Based on a review of related modeling literature [32], [109], [111]–[114] the front factor was modified to the form presented in Equation 13. This is consistent with the thought experiment in [32] and, as such, represents an estimate of the maximum spot temperature over the melting temperature uncorrected for long range conduction effects. This only has a 5% discrepancy with the theoretically exact form from the 3D moving Gaussian model [111], [112], which is expected to be of negligible

importance at the level of uncertainty that the present model predicts the melt pool morphology. Material properties deployed for AlSi10Mg are as in Table 5-7; per [109] constant properties are used, with thermal absorptivity  $\beta$  evaluated at the melting temperature and all other properties approximated at room temperature.

$$B = \frac{\beta_{eff} P_{eff}}{\pi \rho C_p \Delta T_m \sqrt{\alpha v_{eff} r^3}} \quad \text{Equation 13}$$

To account for powder bed effects and provide a better estimate of the effective laser coupling, an effective absorptivity,  $\beta_{eff}$  (Equation 14) is used. This is calculated as the time weighted average between the melt absorptivity,  $\beta_{melt}$ , and the powder bed absorptivity,  $\beta_{powder}$ , estimated using [115].

$$\beta_{eff} = \frac{m_t}{t_{eff}} \beta_{powder} + \left(1 - \frac{m_t}{t_{eff}}\right) \beta_{melt} \quad \text{Equation 14}$$

$$t_{eff} = \frac{d}{p_d} (e_t + d_t) \quad \text{Equation 15}$$

Effective laser interaction time,  $t_{eff}$ , is as given in Equation 15. The average melting time,  $m_t$ , is estimated as the time required for the center of a particle of average diameter to reach the melting temperature when exposed uniformly over its surface to the average surface heat flux within the beam spot. Assuming constant material properties as found in Table 5-7 and neglecting the phase change and latent heat of fusion, this can be approximated by a sphere with constant surface heat flux [116].

**Table 5-7: Material properties used as inputs for thermal model**

Material Properties	
Material	AlSi10Mg
Thermal conductivity, k	113 W/m K
Thermal diffusivity, $\alpha$	4.37E-5 m <sup>2</sup> /s
Density, $\rho$	2685 kg/m <sup>3</sup>
Melting temperature, $T_m$	863 K
Thermal absorptivity, $\beta$	0.09 – 0.27
Specific heat capacity, $C_p$	963 J/kg K
Powder particle size $D_{50}$	45 $\mu$ m
Powder relative density	0.46

### 5.2.3.2 Combined Parameters for Experiment Planning

Four combined parameters are hypothesized to control the process space used for experiment planning, namely: i) material normalized energy density, as given by  $B$  in Equation 13; ii) non-dimensional scan

speed, as given by  $v^*$  in Equation 12; iii) non-dimensional laser power,  $P^*$ , as defined in Equation 16; and iv) the melt depth ratio (MDR) as defined in Equation 17.

$$P^* = B\sqrt{v^*} \quad \text{Equation 16}$$

$$MDR = \frac{d_{melt}}{l} \quad \text{Equation 17}$$

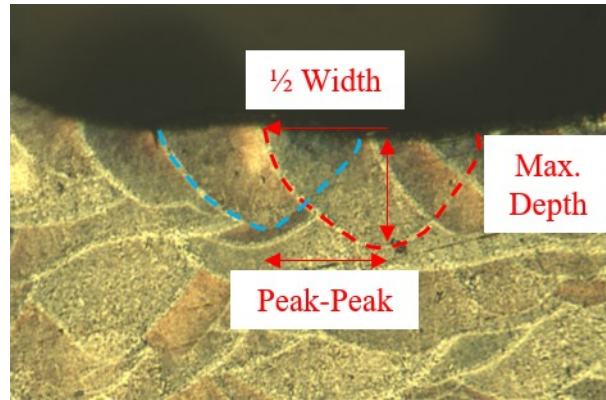
The most important of these parameters is MDR. Three authors are known to have defined a critical melt depth ratio (MDR) defined as the depth of melting,  $d_{melt}$ , over the layer thickness to quantify the probability of such defects [33], [117], [118]. Increasing this ratio reduces the probability of defects in the finished part by ensuring surface irregularities in previous layer are corrected during subsequent passes. The challenge is that it should be properly applied at the edge of the hatch spacing [33] meaning that the full 3D geometry of the melt pool needs to be empirically determined or modelled.

### 5.2.3.3 *Model Calibration of Absorptivity*

To compensate for a lack of data on the thermal absorptivity of powder materials, researchers may choose to instead use values that were determined for polished metal plates or rough oxidized surfaces [35]. However, it has been noted that the absorptivity of a powdered material may be up to 2 – 3 times higher [119], and the process parameters can also increase the absorptivity [49]. For AlSi10Mg, Li and Gu used an absorptivity of 0.09 for a parametric analysis of the thermal behaviour during LPBF [120]; for the purpose of this study, the absorptivity of AlSi10Mg powder was assumed to fall between 0.09 – 0.27.

To calibrate the absorptivity value, empirical melt pool measurements from experiments were used. Micrographs from the most successful (high relative density) recipes (DOE 3-1: Recipe 2, 5, 9; DOE 3-2: Recipe 1, 2, and 5) were selected for taking measurements of the melt pool dimensions at the final printed layer. Five adjacent melt pools from 11 different micrographs were measured using ImageJ software (Version 1.52i). The maximum depth, peak-to-peak distance, and half the width were measured as shown in Figure 5-13.





**Figure 5-13: Melt pool dimensional measurement locations**

Because the cutting plane of the cross-sectioned samples was not perpendicular with the laser raster pattern at the top layer of the part, the measured melt pool width may overestimate the true melt pool width. To correct for this effect, the offset angle ( $\theta$ ) was estimated by trigonometry and the assumption that if the cut was perpendicular to the laser scan track, the peak-to-peak distance between adjacent melt pools would be equal to the hatch distance, as shown in Equation 18. The corrected width ( $w'$ ) was then estimated by multiplying the measured width ( $w$ ) by the cosine of the offset angle, as in Equation 19.

$$\theta = \cos^{-1}\left(\frac{\text{hatch distance}}{\text{peak distance}}\right) \quad \text{Equation 18}$$

$$w' = w * \cos(\theta) \quad \text{Equation 19}$$

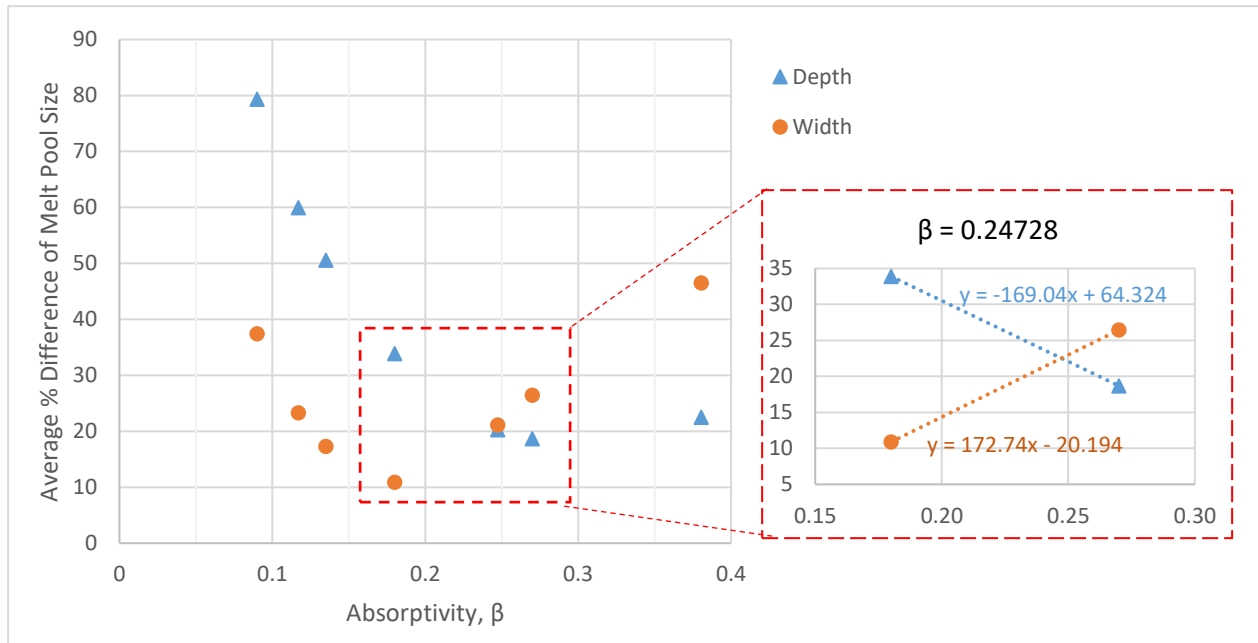
In addition to the material properties listed in Table 5-7, the processing parameters that are specified in Table 5-8 were used as inputs for the thermal model. The model was run 6 times, changing only the thermal absorptivity value ( $\beta = 0.09, 0.1169, 0.135, 0.18, 0.27, 0.38$ ).

**Table 5-8: Processing parameters used as inputs for thermal model**

Processing Parameters	
Power	
Point distance	
Exposure time	various manufacturing recipes
Hatch distance	
Laser spot diameter	
Layer thickness	

For each run, the predicted melt pool dimensions were compared to the actual melt pool dimensions corresponding with each manufacturing recipe that was investigated. Figure 5-14 shows the percent difference for the width and depth at each tested  $\beta$  value, averaged for all recipes. As the absorptivity

was increased from 0.09 to 0.27, the percent difference between the model and experimental dimensions was minimized to around 19% difference for the melt pool depth and 11% difference for the melt pool width. However, these minima did not occur at the same absorptivity level. Because both dimensions are critical for establishing the ideal melt pool geometry, it was desirable to select an intermediate absorptivity value that could provide reasonable estimates for both depth and width without favouring one over the other. For each melt pool dimension, a linear region was assumed between the  $\beta$  values corresponding with the two minima. The point of intersection,  $\beta = 0.2473$ , was selected as the optimal absorptivity to be used in the calibrated thermal model. The model was run again using this value, and Figure 5-15 shows the comparison between the empirical measurements (for image 1 and 2) and the dimensions predicted by the model. It can be seen that the model may tend to underestimate the maximum melt pool depth and overestimate the melt pool width; however, this effect was not observed for all processing parameters that were investigated, as illustrated in Figure 5-15.



**Figure 5-14: Average percent difference between the theoretical and experimental melt pool dimensions. Inset: optimal absorptivity value was selected at the point of intersection**

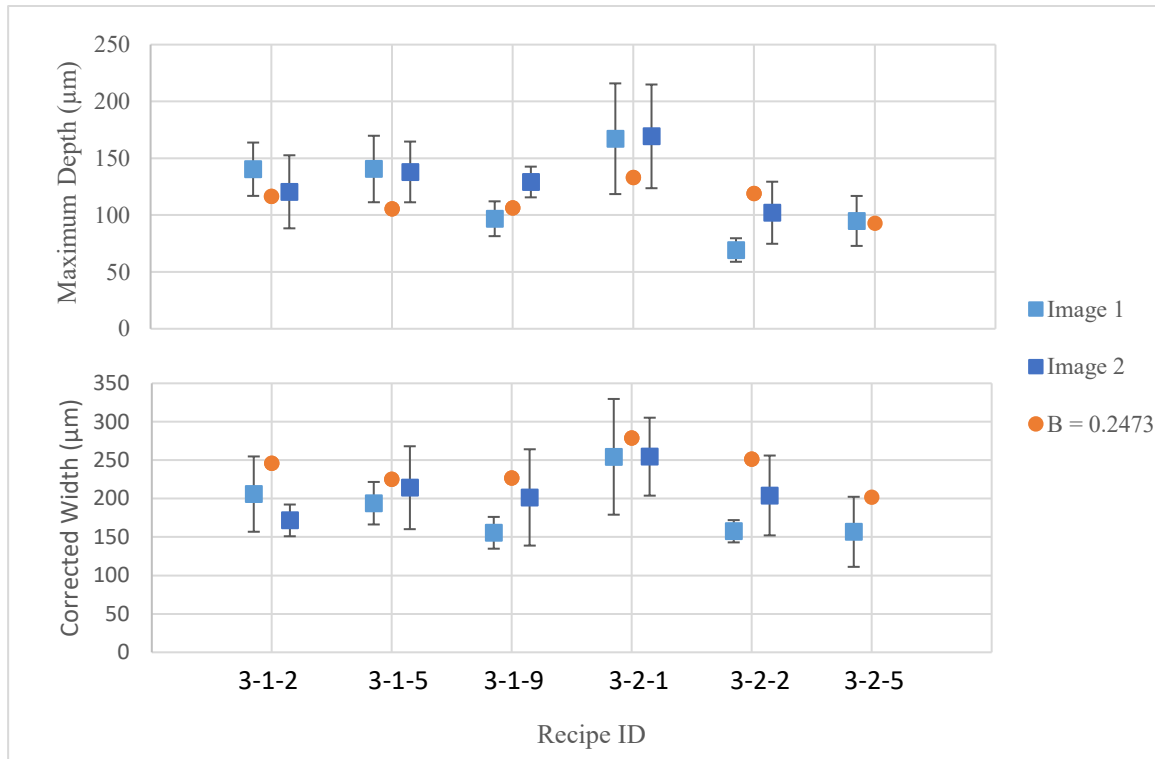


Figure 5-15: Comparison between experimental melt pool dimensions (for image 1 and image 2) and theoretical dimensions predicted using the calibrated absorptivity value ( $\beta = 0.2473$ )

#### 5.2.3.4 Manufacturing Strategy and Process Parameter Selection

After calibration of the absorptivity value for the thermophysical modelling of melt pool temperatures and geometries, the reverse-model was used to determine the required processing parameters to achieve an ideal melt pool geometry. Target melt depth ratios of 1.5, 2.0, and 2.5 were selected in order to obtain sufficient melting and re-melting between layers, as described in Section 5.2.3.2 (Equation 17 –  $MDR = \text{depth of melting/layer thickness}$ ). An example of a microstructure with an MDR equal to 2 is illustrated in Figure 5-16. The hatch spacing was selected such that the hatch spacing/laser spot diameter ratio was the same at the MDR. The point distance was kept constant at  $60 \mu\text{m}$ , while the exposure time was modified to control the effective laser scan speed. Six different scan speeds were selected based on the appropriate processing window that was identified in DOE 2-1 to 2-4, 3-1, and 3-2 (Section 5.2.1). Finally, the reverse-solver for the thermophysical model was used to calculate the laser power setting that would be necessary to achieve the targeted MDR at each of the selected scan speeds. Table 5-9 shows the processing parameters used for DOE 3-3. Figure 5-17 shows a visualization of the non-dimensionalized parameters  $P^*$  versus  $v^*$  for the new manufacturing recipes (DOE 3-3, shown in black), compared with the previous experiments (DOE 2-1 to 2-4, 3-1, and 3-2; shown in various colours, depending on laser power setting). The bubble size corresponds with the

estimated porosity level from the previous experiments, and the red dashed lines indicate the preferred processing window which the new experiment's  $v^*$  values were selected to span across.

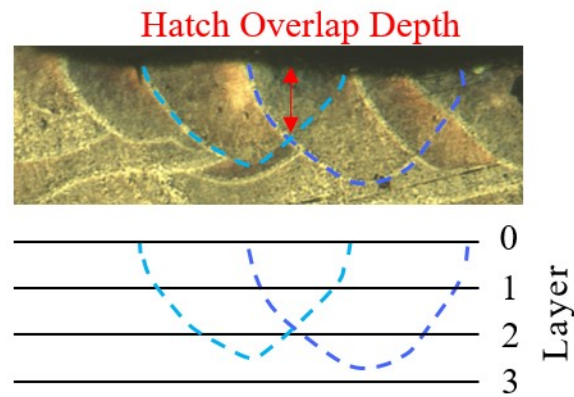
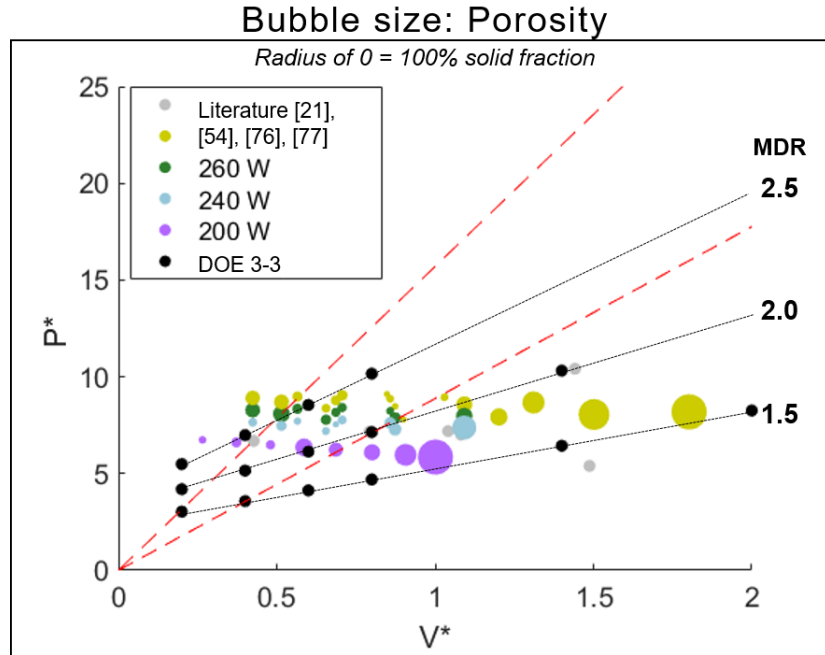


Figure 5-16: Schematic diagram showing a melt depth ratio = 2

Table 5-9: Processing parameters for DOE 3-3

Recipe #	Power (W)	Point distance ( $\mu\text{m}$ )	Exposure time ( $\mu\text{s}$ )	Hatch distance ( $\mu\text{m}$ )	MDR
1	88	60	230	105	1.5
2	108	60	110	105	1.5
3	129	60	70	105	1.5
4	152	60	50	105	1.5
5	240	60	24	105	1.5
6	366	60	14	105	1.5
7	123	60	230	140	2.0
8	156	60	110	140	2.0
9	193	60	70	140	2.0
10	234	60	50	140	2.0
11	390	60	24	140	2.0
12	161	60	230	175	2.5
13	212	60	110	175	2.5
14	270	60	70	175	2.5
15	334	60	50	175	2.5

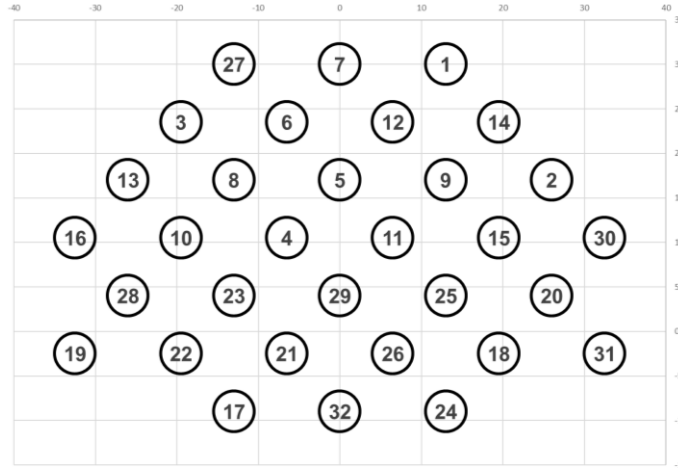


**Figure 5-17: Non-dimensionalized power ( $P^*$ ) and speed ( $v^*$ ) for DOE 3-3 (black) superimposed on porosity results for previous experiments and recipes from literature [21], [54], [76], [77]**

Cylindrical-shaped artifacts with a diameter of 6 mm were printed with the meander laser scan strategy and a  $67^\circ$  rotation between each layer. Two replicates for each recipe were printed on the Renishaw Reduced Build Volume. The part location on the build plate was randomized, as shown in Figure 5-18. One border scan and one fill contour were used, with the same processing parameters that were used for the core of the part (Table 5-9). The upskin, downskin, and blocked path settings were turned off, and no support structures were used. The process settings in Table 5-10 were kept consistent for all parts printed for DOE 3-3. The powder source was changed to Supplier 2 and the layer thickness was set to  $35 \mu\text{m}$  (half the laser spot diameter).

**Table 5-10: Controlled parameters for DOE 3-3**

Powder type	Layer thickness ( $\mu\text{m}$ )	Point distance ( $\mu\text{m}$ )	Laser spot diameter ( $\mu\text{m}$ )
Supplier 2	35	60	70



**Figure 5-18: Build plate layout for DOE 3-3, where the labels from 1 – 15 correspond with the recipe number used for that sample, and 17 – 31 correspond with the replicates**

The cylindrical samples were analyzed using the techniques for metallographic examination of the microstructure and porosity measurements as described in Section 3.3.2. The melt pool dimensions were measured as per Section 5.2.3.3 for comparison with the thermophysical model predictions. Surface roughness measurements were also obtained to aid in identifying ideal recipes for producing a good surface quality, and will be discussed further in Section 5.3.1.

## 5.2.4 Results for Thermophysical Model Parameters

### *DOE 3-3:*

Figure 5-19 shows the optical micrographs and estimated relative density for samples from DOE 3-3, which were printed using various laser powers and scan speeds in an effort to achieve specific melt pool dimensions that correspond with a melt depth ratio of 1.5, 2.0, or 2.5. The process parameters targeting an MDR of 1.5 (recipes 1 to 6) resulted in severe lack of fusion porosity, especially in samples with a high scan speed. Targeting the higher MDRs resulted in several samples with a high relative density, such as recipe 9, 10, 12, and 13. Out of these samples, recipe 9 was selected as the best because its microstructure was the most consistent in terms of melt pool size, as shown in Figure 5-20. The melt pools at the top layer of the part were uniform and even, and the part’s surface was relatively flat.

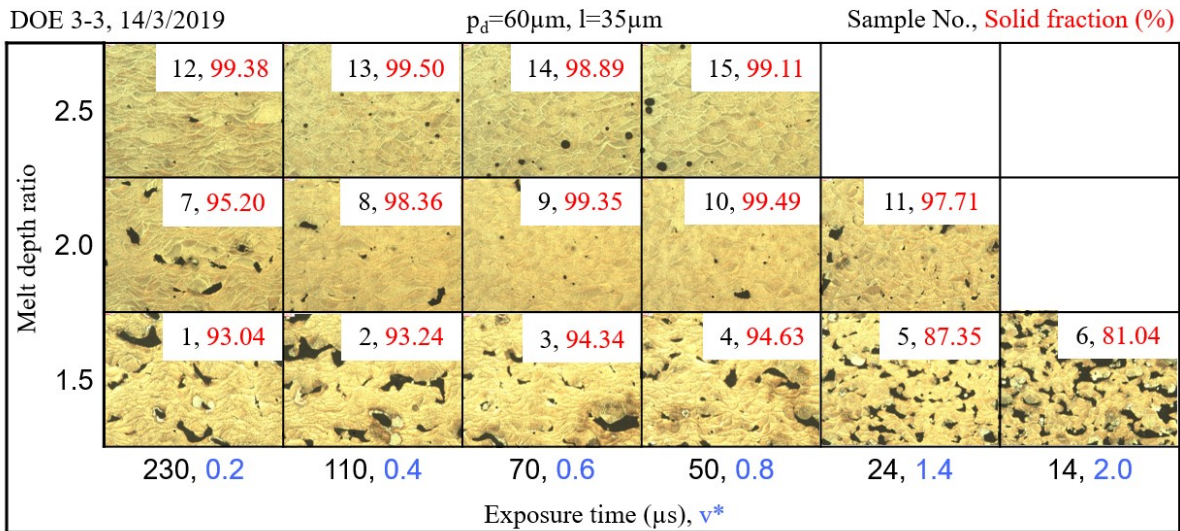


Figure 5-19: Optical micrographs for samples from DOE 3-3

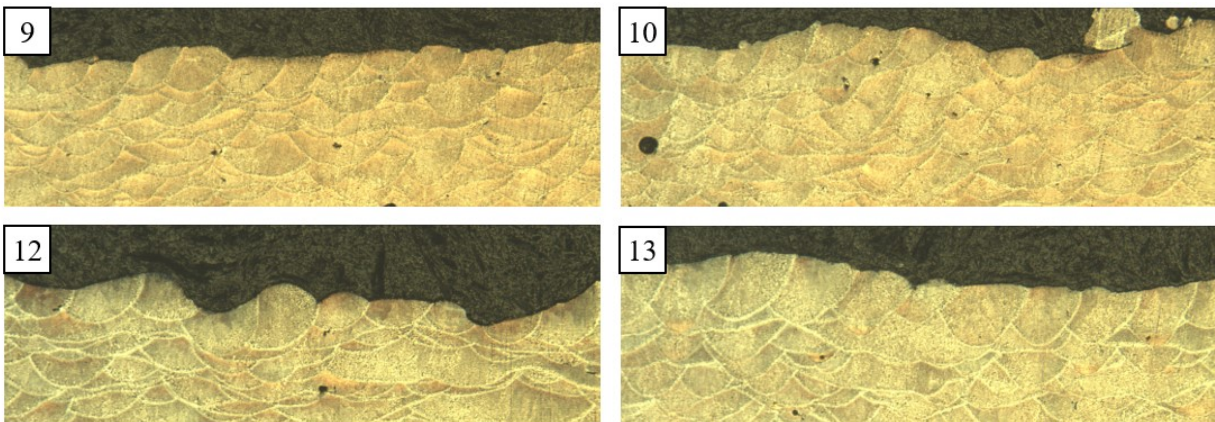


Figure 5-20: Optical micrographs of top layer for recipe 9, 10, 12, and 13 from DOE 3-3

The melt pool dimensions were measured and Figure 5-21 shows the MDR plotted against the temperature ratio,  $\frac{\Delta T_{max}}{\Delta T_m}$  (calculated by the thermophysical model). Note that the maximum temperature exceeded the boiling point for aluminum, so the physical interpretation of the model is limited and the temperature ratio is provided for comparative purposes only. Recipe 9 had the smallest variance for the measured MDR, and it also falls the closest to its targeted MDR of 2.0. Figure 5-22 shows the 2D bubble plot of the estimated porosity percentage and the corresponding non-dimensionalized process parameters  $v^*$  and  $P^*$ , and it can be seen that recipe 9 falls within the initial process window (red dashed lines) previously identified in Section 5.2.2.

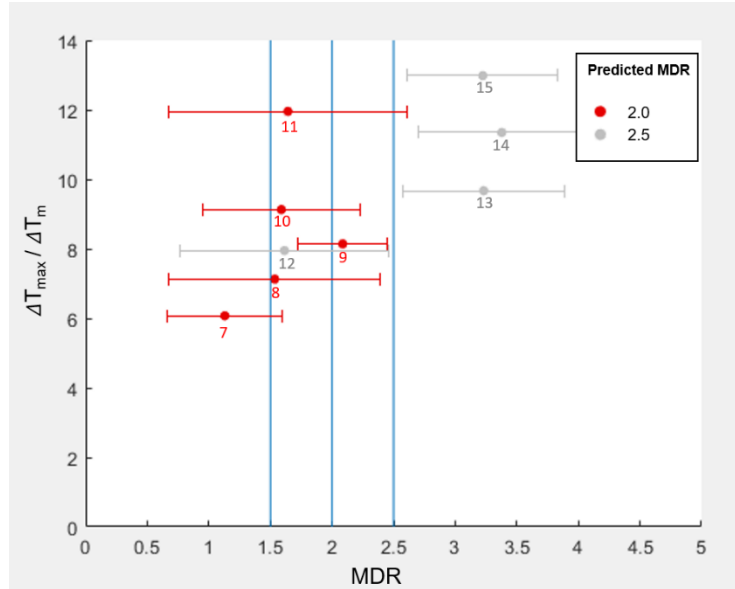


Figure 5-21: Melt pool temperature ratio ( $\Delta T_{max} / \Delta T_m$ ) vs. melt depth ratio for samples from DOE 3-3

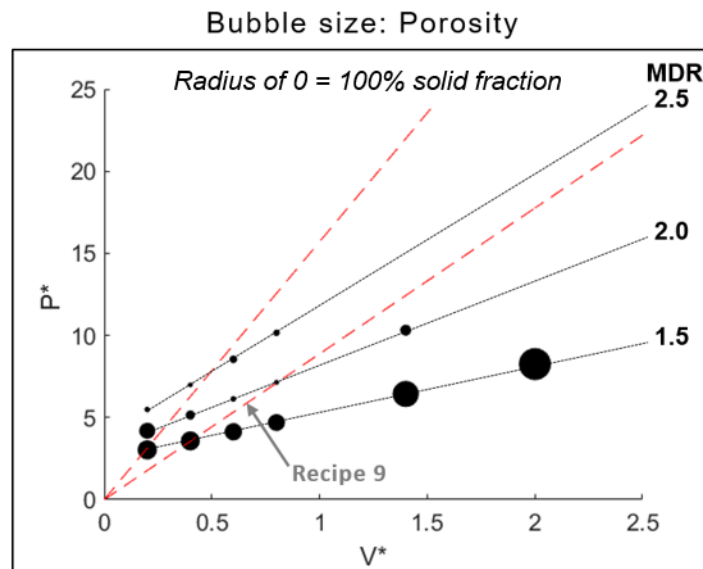


Figure 5-22: Bubble plot showing estimated porosity versus process parameters for DOE 3-3



### 5.2.5 Selection of Ideal Recipes for Dense Core

Based on the results of the experiment described in the previous section (DOE 3-3), four new sets of process parameter were generated in order to fine-tune the final core recipe for a highly dense part (DOE 3-5). Two preferred recipes were then selected and reprinted with the AlSi10Mg powder from both suppliers (DOE 3-6). For both experiments, cylindrical-shaped artifacts with a diameter of 6 mm were printed with the meander laser scan strategy and a 67° rotation between each layer. The upskin, downskin, and blocked path settings were turned off, and the laser spot diameter was kept at 70 μm.

For DOE 3-5, one of the most successful recipes from the previous experiment was reprinted (DOE 3-3, Recipe 9). For each of the three new core recipes used in DOE 3-5, linear regression was used to create an empirical model based on the melt pool dimensional measurements from DOE 3-3, which were taken for recipes with a MDR = 2.0 or 2.5. The factors used in the regression were the  $v^*$  and  $T/T_m$  values, and the response was either the melt pool width or maximum depth, as shown in Equation 20 and Equation 21.

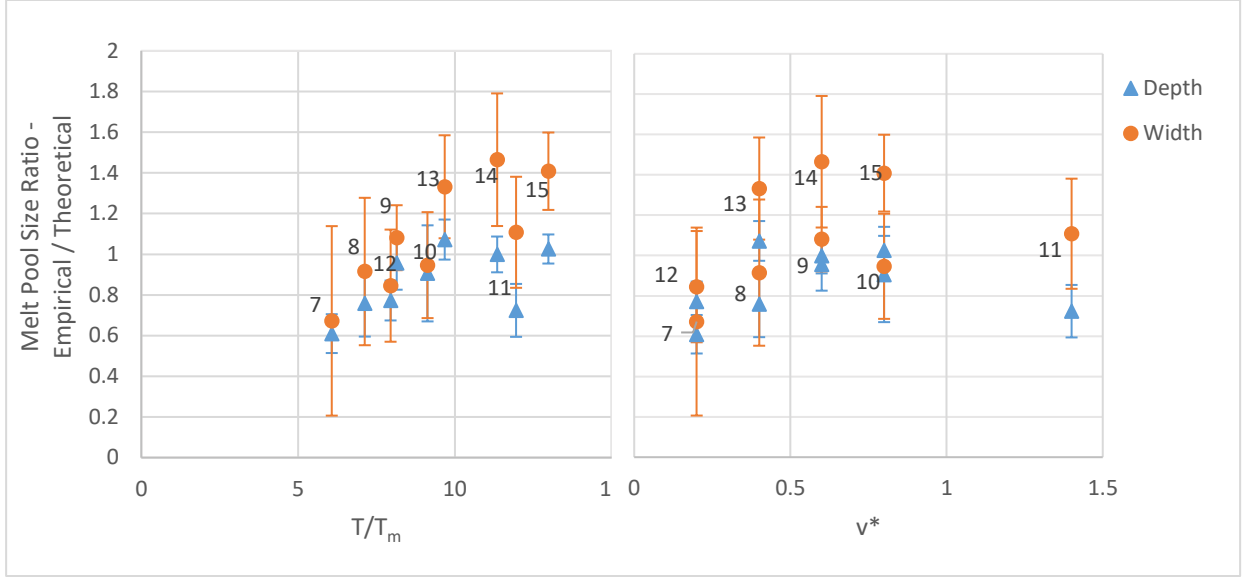
$$\text{Max. depth} = A_0 + A_1 \left( \frac{T}{T_m} \right) + A_2(v^*) \quad \text{Equation 20}$$

$$\text{Width} = B_0 + B_1 \left( \frac{T}{T_m} \right) + B_2(v^*) \quad \text{Equation 21}$$

Table 5-11 shows the regression coefficients that were fit based on data points from DOE 3-3. Different data points were selected to create unique regression models for each new recipe for DOE 3-5 based on the assumption that there is a region with a linear response close to each new targeted  $v^*$  value. Figure 5-23 shows the results for the melt pool depth and width (size ratio of empirical/theoretical) versus the ratio of the maximum melt pool temperature over the melting temperature ( $T/T_m$ ) or the dimensionless scan speed ( $v^*$ ) calculated by the thermophysical model, and was used to help identify the preferred data points to use.

**Table 5-11: DOE 3-3 data used for linear regression to generate each recipe for DOE 3-5**

DOE 3-5 Recipe #	Based on DOE 3-3 Recipe(s)	Depth – Regression coefficients			Width – Regression coefficients		
		A <sub>0</sub>	A <sub>1</sub>	A <sub>2</sub>	B <sub>0</sub>	B <sub>1</sub>	B <sub>2</sub>
1	7, 8, 9, 10, 12 13	-88.5	27.8	-76.4	-114.3	43.1	-94.7
2	9 (replicate)	-	-	-	-	-	-
3	10, 15	-98.8	20.7	-	13.8	19.0	-
4	10, 11, 13, 14, 15	-5.2	20.7	-102.6	159.2	17.5	-158.3



**Figure 5-23: Melt pool size ratio vs.  $T/T_m$  (left) or  $v^*$  (right) for DOE 3-3, Recipes 7 to 15**

The targeted  $v^*$  values were 0.4, 0.8, and 1.0 for new DOE 3-5 core recipes 1, 3, and 4, respectively. The regression models were used to generate melt pool dimensions for various  $T/T_m$  values ranging from 7.1 to 13. From those lists, melt pool geometries with a preferred aspect ratio were identified (depth of approx. 100  $\mu\text{m}$ , width of approx. 200  $\mu\text{m}$ ). The corresponding  $T/T_m$  value was then used to calculate the required laser power to achieve that geometry, based on the following equations:

$$P^* = \frac{\left(\frac{T}{T_m}\right) \sqrt{v^*}}{G^*} \quad \text{Equation 22}$$

$$P_{eff} = \frac{P^* r \pi \alpha \rho C_p (T_m - T_0)}{\beta} \quad \text{Equation 23}$$

$$P = P_{eff} \frac{t_e + t_d}{t_e} \quad \text{Equation 24}$$

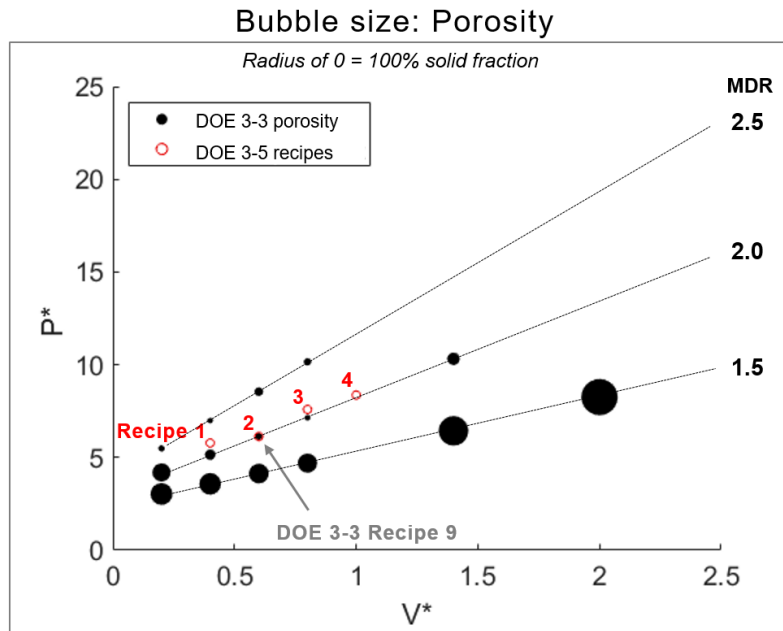
Finally, the required hatch spacing ( $h$ ) was calculated according to Equation 25, which was based on the criterion for full melting proposed by Tang et al. [33]. The geometry-based approach aims to prevent lack of fusion porosity by ensuring sufficient overlap between melt pools, and is dependent on melt pool width ( $w$ ), melt pool depth ( $d$ ), and the layer thickness ( $l$ ). In this work, the layer thickness was also multiplied by a target melt depth ratio of 2 in order to correspond with the desired depth for full melting to occur.

$$\left(\frac{h}{w}\right)^2 + \left(\frac{2l}{d}\right)^2 \leq 1 \quad \text{Equation 25}$$

Four samples were printed for each core recipe, each paired with a different border recipe (to be discussed in Section 5.3.1). Two replicates were printed for each treatment for a total of 32 samples on the Renishaw Reduced Build Volume with randomized locations on the build plate. Table 5-12 shows the processing parameters used for DOE 3-5. The powder was from Supplier 2 and the layer thickness was set at 35  $\mu\text{m}$ . Figure 5-24 shows a visualization of the non-dimensionalized parameters  $P^*$  versus  $v^*$  for the new manufacturing recipes (DOE 3-5, shown in red), compared with the previous experiment (DOE 3-3, shown in black). The bubble size corresponds with the estimated porosity level from the previous experiment. The samples were analyzed for porosity through metallographic examination of the microstructure as described in Section 3.3.2.

**Table 5-12: DOE 3-5 core recipes**

Powder type	Layer thickness ( $\mu\text{m}$ )	Core recipe #	Power (W)	Point distance ( $\mu\text{m}$ )	Exposure time ( $\mu\text{s}$ )	Hatch distance ( $\mu\text{m}$ )
Supplier 2	35	1	176.8	60	110.11	142
		2	192.8	60	70.08	140
		3	255.3	60	50.06	145
		4	287.0	60	38.05	132



**Figure 5-24: Non-dimensionalized power ( $P^*$ ) and speed ( $v^*$ ) for DOE 3-5 core recipes (red) superimposed on previous porosity results for DOE 3-3**

For DOE 3-6, two preferred parameter sets from DOE 3-5 (recipe 1 and 3) were selected and replicates of the test cylinders were reprinted using the AlSi10Mg powder from either Supplier 2 or Supplier 1. One border and one fill contour were used with the same manufacturing recipe for every part (to be discussed in Section 5.3.1). The powder from Supplier 2 was printed on the Renishaw Reduced Build Volume with a layer thickness of 35  $\mu\text{m}$  and no support structures. The powder from Supplier 1 was printed on the Renishaw full build environment with a layer thickness of 30  $\mu\text{m}$  and 5 mm tall support structures. These changes were due to equipment availability. All other processing parameters were kept consistent. Table 5-13 shows the processing parameters used for DOE 3-6. The samples were analyzed for porosity through metallographic examination of the microstructure as described in Section 3.3.2 and x-ray CT scanning as per Section 3.3.3.

**Table 5-13: DOE 3-6 core recipes**

Powder type	Layer thickness ( $\mu\text{m}$ )	Core recipe #	Power (W)	Point distance ( $\mu\text{m}$ )	Exposure time ( $\mu\text{s}$ )	Hatch distance ( $\mu\text{m}$ )
Supplier 2	35	1	176.8	60	110.11	142
		3	255.3	60	50.06	145
Supplier 1	30	1	176.8	60	110.11	142
		3	255.3	60	50.06	145

Finally, the two ideal core recipes were printed with the ideal border recipe for DOE 4-2. The final core recipes are the same as those used in DOE 3-6 and are listed above in Table 5-13. The powder was from Supplier 1 and the layer thickness was 30  $\mu\text{m}$ . The cylindrical samples were analyzed for porosity through optical microscopy (as per Section 3.3.2) and x-ray CT scanning (as per Section 3.3.3). Additional sample geometries were also printed and will be discussed in Chapter 6.

## 5.2.6 Outcomes for Ideal Core Recipes

### ***DOE 3-5:***

Figure 5-25 shows the optical micrographs and estimated relative density for samples from DOE 3-5. Four different core recipes were printed with varying power levels and laser scan speeds. Recipe 1, 3, and 4 were developed using linear regression to select parameters that correspond with ideal melt pool dimensions, and recipe 2 was a replicate of the best high-density recipe identified in Section 5.2.4 (DOE 3-3, recipe 9). Four samples were printed using each core recipe. It was found that recipe 4 (far-right column in the grid) had the lowest relative density, as the samples contained some lack of fusion porosity. Recipes 1 to 3 were considered successful in achieving a highly dense core, and each had a

relative density greater than 99.7% when estimated using the optical microscopy method. Table 5-14 shows the average density for each recipe.

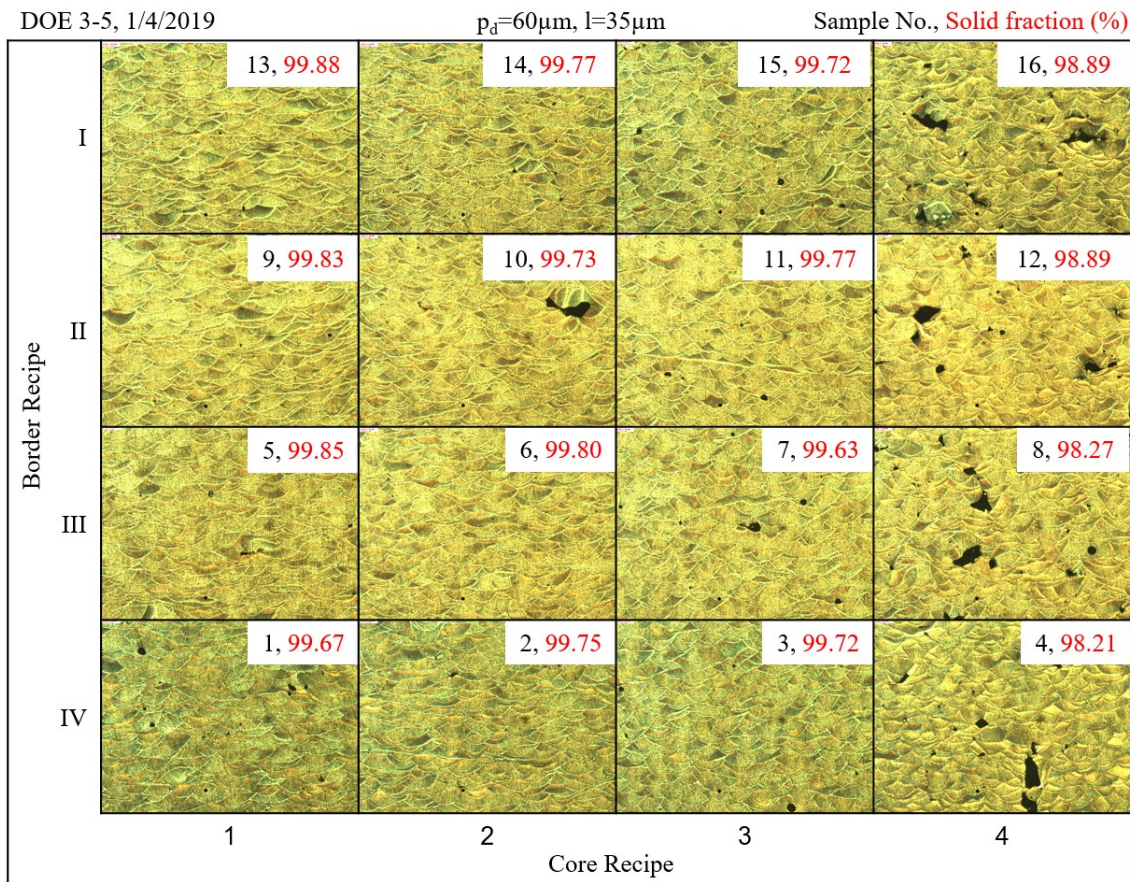


Figure 5-25: Optical micrographs for samples from DOE 3-5

Table 5-14: Average density measurements for each core recipe used in DOE 3-5, estimated using optical microscopy method

Core Recipe	Sample	Average Density – Optical (%)	St. Dev.
1	1, 5, 9, 13	99.81	0.15
2	2, 6, 10, 14	99.76	0.17
3	3, 7, 11, 15	99.71	0.13
4	4, 8, 12, 16	98.59	0.75

Two ideal recipes were selected for use in the LPBF of AlSi10Mg parts:

- High density option (Recipe 1): selected because it resulted in the highest relative density, and will likely produce high quality parts.
- High productivity option (Recipe 3): selected because it had the highest scan speed while still maintaining a high relative density, thus making it an economic choice for faster production.

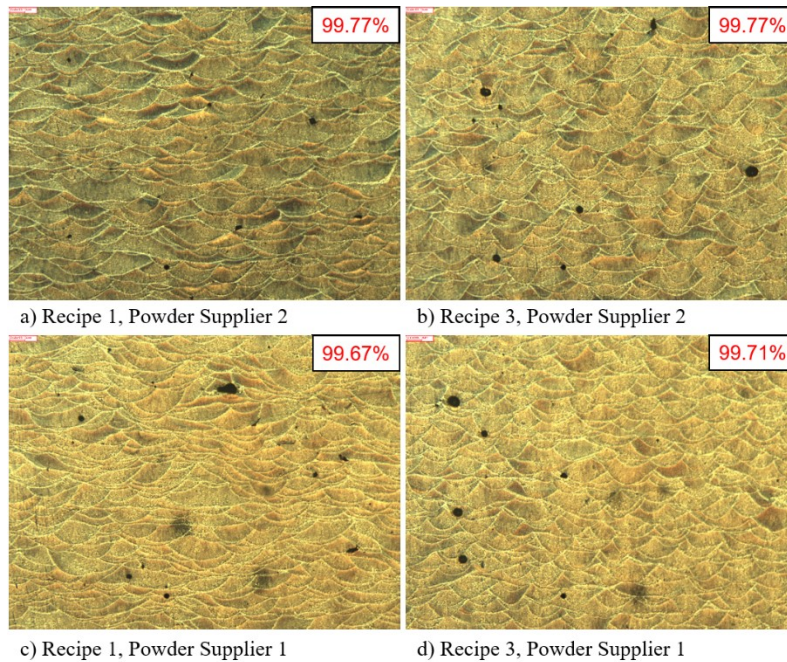
**DOE 3-6:**

In DOE 3-6, the two recipes selected in the previous section (DOE 3-5, recipe 1 and 3) were reprinted using AlSi10Mg powder from two different suppliers. Table 5-15 shows the average density results estimated using two methods: analysis of 2D optical micrographs, and 3D CT scan data. The CT scan method estimated a relative density greater than 99.82% for all samples, while the optical microscopy method resulted in slightly lower values ranging from 99.67 to 99.77%.

**Table 5-15: Average density measurements for DOE 3-6 samples estimated using optical microscopy and CT scan methods**

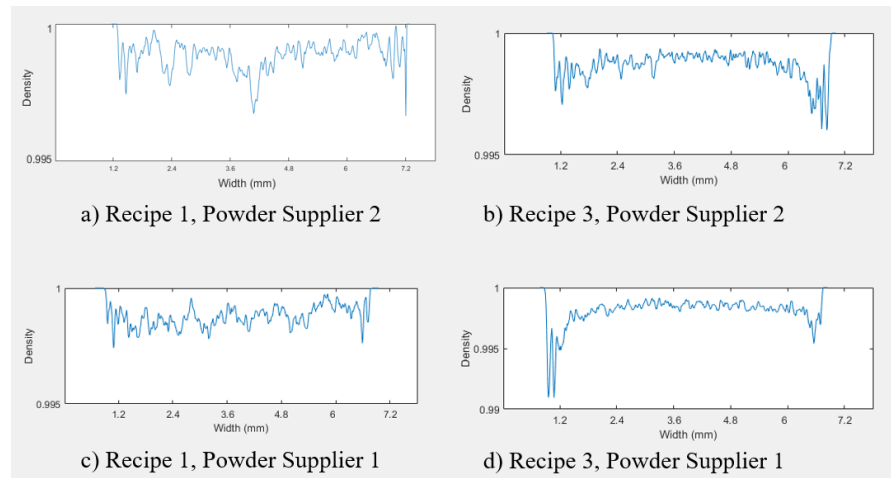
Core Recipe	Powder Type	Density – Optical (%)	St. Dev.	Density – CT scan (%)	Height - Z (mm)
1	Supplier 2	99.77	0.158	99.88	7.75
	Supplier 1	99.67	0.292	99.88	8.46
3	Supplier 2	99.77	0.111	99.88	7.76
	Supplier 1	99.71	0.100	99.82	8.04

Figure 5-26 shows the optical micrographs and estimated solid fraction for each sample. The solid fraction was slightly lower for powder Supplier 1; however, the average values fell within the ranges measured for Supplier 2, so the difference between powder types was not large. For both powder suppliers, the high productivity recipe (recipe 3) contained larger keyhole pores.

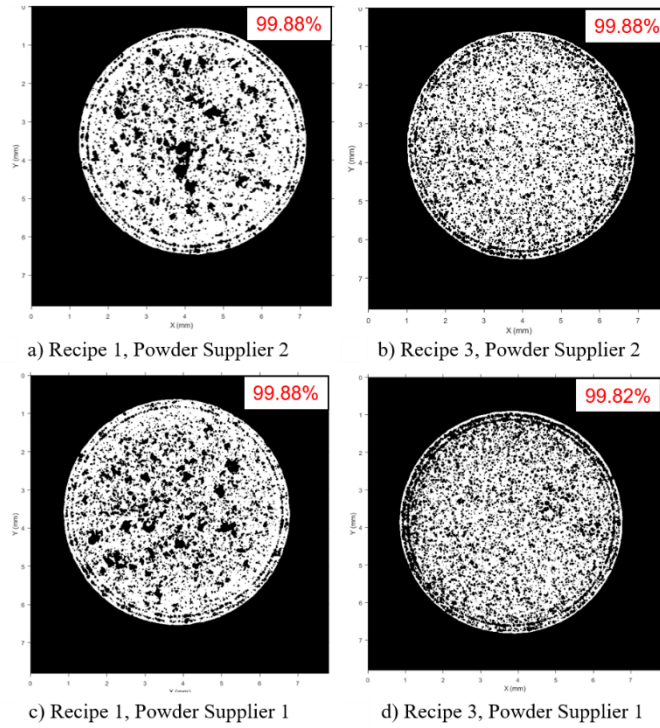


**Figure 5-26: Optical micrographs for samples from DOE 3-6, manufactured using: a) recipe 1, powder supplier 2; b) recipe 3, powder supplier 2; c) recipe 1, powder supplier 1; d) recipe 3, powder supplier 1**

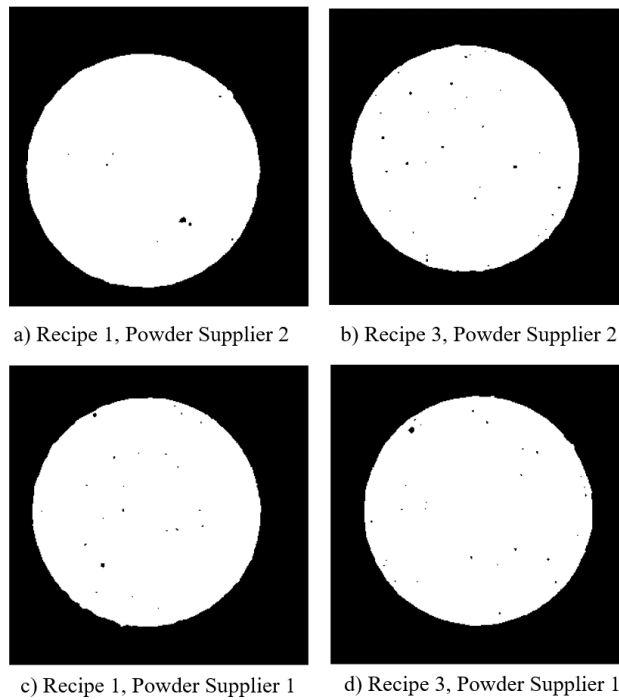
Figure 5-27 shows the slice density in the X-direction (relative density measured for y-z plane) plotted as a function of X. Figure 5-28 shows the minimum intensity projections of all the pores along the z-direction projected onto a 2-dimensional image in the x-y plane for each sample. The height (z-direction) analyzed for each sample is listed above in Table 5-15. Figure 5-29 shows a binary image for a single slice or random cross-section of each sample.



**Figure 5-27: Density vs. distance graph for samples from DOE 3-6 (Slice density in x-direction), manufactured using: a) recipe 1, powder supplier 2; b) recipe 3, powder supplier 2; c) recipe 1, powder supplier 1; d) recipe 3, powder supplier 1**



**Figure 5-28: Minimum intensity projections for samples from DOE 3-6, manufactured using: a) recipe 1, powder supplier 2; b) recipe 3, powder supplier 2; c) recipe 1, powder supplier 1; d) recipe 3, powder supplier 1**



**Figure 5-29: Binary image for single slice of samples from DOE 3-6, manufactured using: a) recipe 1, powder supplier 2 (slice # 583/646); b) recipe 3, powder supplier 2 (slice # 317/705); c) recipe 1, powder supplier 1 (slice # 434/647); d) recipe 3, powder supplier 1 (slice # 241/670)**



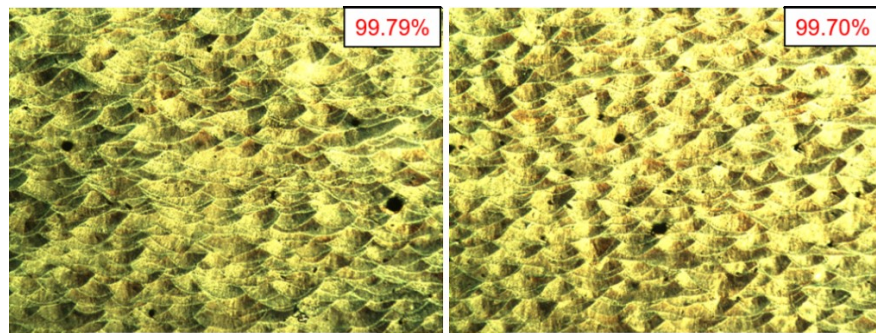
While the relative density was similar for all the samples, the distribution of the porosity was different for each recipe. Recipe 1 appeared to have some of the pores concentrated at different locations in X-Y space throughout the core of the sample, while recipe 3 had many evenly dispersed pores in the core. Both recipes had a high amount of porosity close to the edge of the samples, due to the high-powered border recipe that was used. This effect appeared to be more severe for recipe 3, since the density versus distance graphs showed much lower densities at the edges. This may have been an interaction effect between the core and border recipes due to higher amounts of residual heat from the hatch scan still remaining when the border and contour were scanned. Overall, it was decided that the powder supplier could be changed from Supplier 2 and back to Supplier 1 for the next set of experiments, with little effect on the resulting part density.

**DOE 4-2:**

In DOE 4-2, the two ideal core recipes were reprinted with the ideal border recipe (to be discussed in Section 5.3) and analyzed to determine the final part density. Table 5-16 shows the average density results estimated using two methods: analysis of 2D optical micrographs, and 3D CT scan data. Recipe 1 had the highest relative density by both methods, measuring 99.95% for the CT scan method and 99.79% for the optical microscopy method. Recipe 3 had an average relative density of 99.84% and 99.70% for each method. Figure 5-30 shows the optical micrographs and estimated relative density for each sample.

**Table 5-16: Average density measurements for DOE 4-2 samples estimated using optical microscopy and CT scan methods**

Core Recipe	Density – Optical (%)	St. Dev.	Density – CT scan (%)	St. Dev. – X (%)	Height - Z (mm)
1	99.79	0.06	99.95	0.23	9.0
3	99.70	0.14	99.84	0.18	8.9

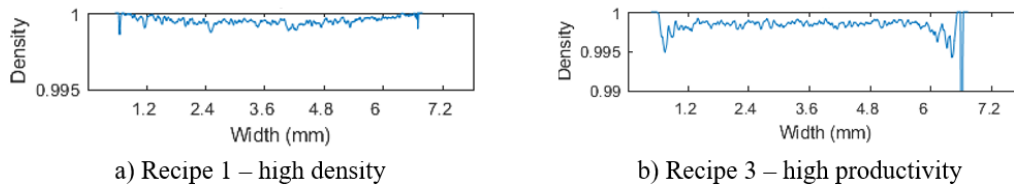


a) Recipe 1 – high density

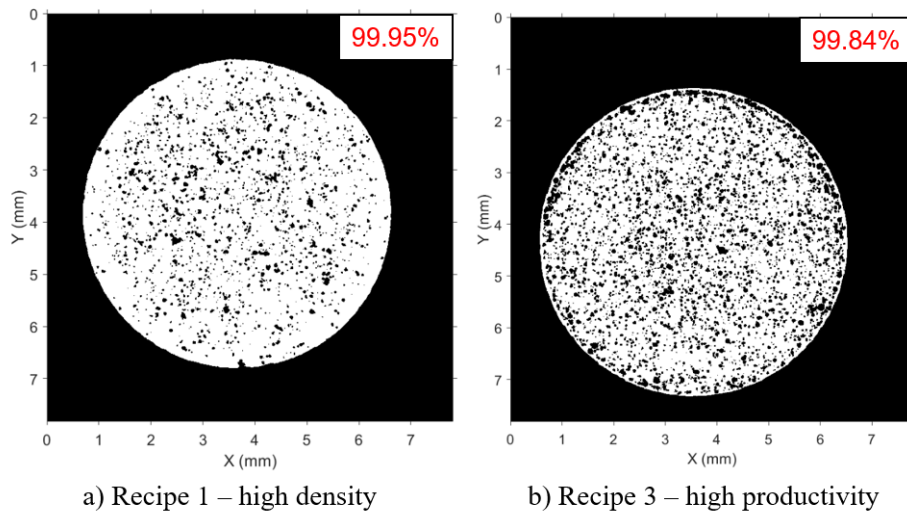
b) Recipe 3 – high productivity

**Figure 5-30: Optical micrographs for samples from DOE 4-2, manufactured using: a) recipe 1; b) recipe 3**

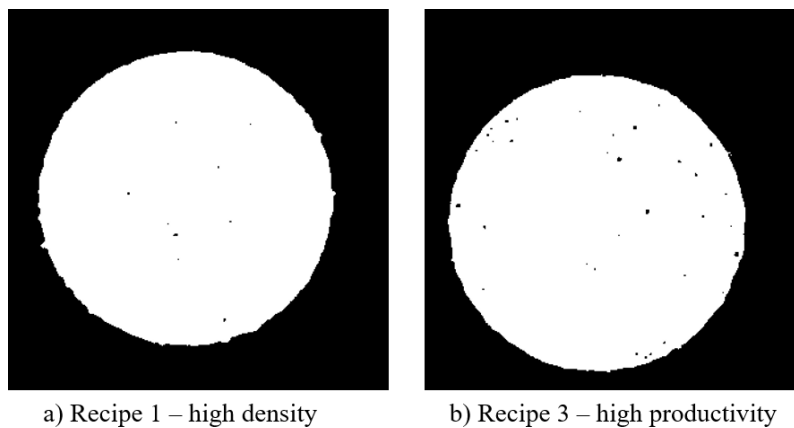
Figure 5-31 shows the slice density in the X-direction (relative density measured for y-z plane) plotted as a function of X. Figure 5-32 shows the minimum intensity projections of all the pores along the z-direction projected onto a 2-dimensional image in the x-y plane for each sample. The height (z-direction) analyzed for each sample is listed above in Table 5-16. Figure 5-33 shows a binary image for a single slice or random cross-section of each sample.



**Figure 5-31: Density vs. distance graph for samples from DOE 4-2 (Slice density in x-direction), manufactured using: a) recipe 1; b) recipe 3**



**Figure 5-32: Minimum intensity projections for samples from DOE 4-2, manufactured using: a) recipe 1; b) recipe 3**



**Figure 5-33: Binary image for single slice of samples from DOE 4-2, manufactured using: a) recipe 1 (slice # 419/750); b) recipe 3 (slice # 333/742)**

The porosity was randomly distributed throughout the cores of the samples for both recipes. When compared with DOE 3-6 (Figure 5-28 and Figure 5-27), the ring of porosity around the edge of the samples was reduced, and for Recipe 1 it was almost fully eliminated. This resulted in overall higher relative densities for the two combinations of ideal core recipes with the ideal border recipe, and fewer subsurface defects may result in better mechanical properties for the final parts.

### 5.3 Process Parameter Selection for Border

#### 5.3.1 Initial Process Mapping for Surface Roughness

The surface quality was controlled by changing the laser scan settings for the part border and fill contour (henceforth referred to as the “border recipe”). The scan order was set so that the hatch meander core was scanned first, followed by the border and then the contour. To obtain an initial process map for the surface quality, the border and fill contour for the cylinders printed in DOE 3-3 were manufactured using the same process parameters that were used for the hatch volume (core recipes listed previously in Table 5-9). The samples were analyzed for surface roughness according to Section 3.3.4, and the results are shown in Table 5-17.

**Table 5-17: Surface roughness results for samples from DOE 3-3**

Recipe	1	2	3	4	5	6	7	8	9	10	11	12	13	14	15
$S_a$ ( $\mu\text{m}$ )	55.2	46.2	36.0	29.9	18.4	20.4	64.6	38.8	38.6	27.2	20.0	39.6	28.6	12.6	17.0

Figure 5-34 shows the 2D bubble plot of the surface roughness and the corresponding non-dimensionalized process parameters  $v^*$  and  $P^*$ , where the bubble size corresponds with the average surface roughness. The surface roughness ranged from 12.6 to 64.6  $\mu\text{m}$ , and recipe 14 and 15 were identified as having the lowest surface roughness.

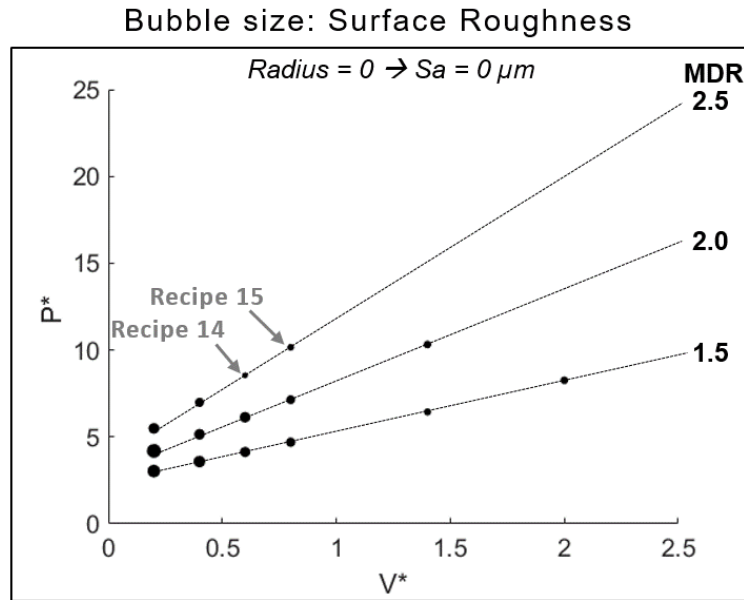


Figure 5-34: Bubble plot showing surface roughness versus process parameters for DOE 3-3

### 5.3.2 Selection of Ideal Recipes for Surface Quality

Based on the results for DOE 3-3, four new sets of process parameters were selected in order to fine-tune the final border recipe for a high surface quality (DOE 3-5). Table 5-18 shows the processing parameters used for DOE 3-5. The process parameters used for DOE 3-3: recipe 14 and 15 were repeated, while two new parameter sets were chosen with the same two values for  $v^*$  and a slightly higher or slightly lower  $P^*$  value, as visualized in Figure 5-35. The new parameters for DOE 3-5 are shown in red and compared with the previous experiment (DOE 3-3, shown in black). The bubble size for DOE 3-3 corresponds with the measured surface roughness.

Table 5-18: DOE 3-5 border recipes

Powder type	Layer thickness ( $\mu\text{m}$ )	Border Recipe #	Power (W)	Point distance ( $\mu\text{m}$ )	Exposure time ( $\mu\text{s}$ )	Contour distance ( $\mu\text{m}$ )
Supplier 2	35	I	270.0	60	70	140
		II	287.8	60	50	140
		III	325.5	60	70	140
		IV	334.0	60	50	140

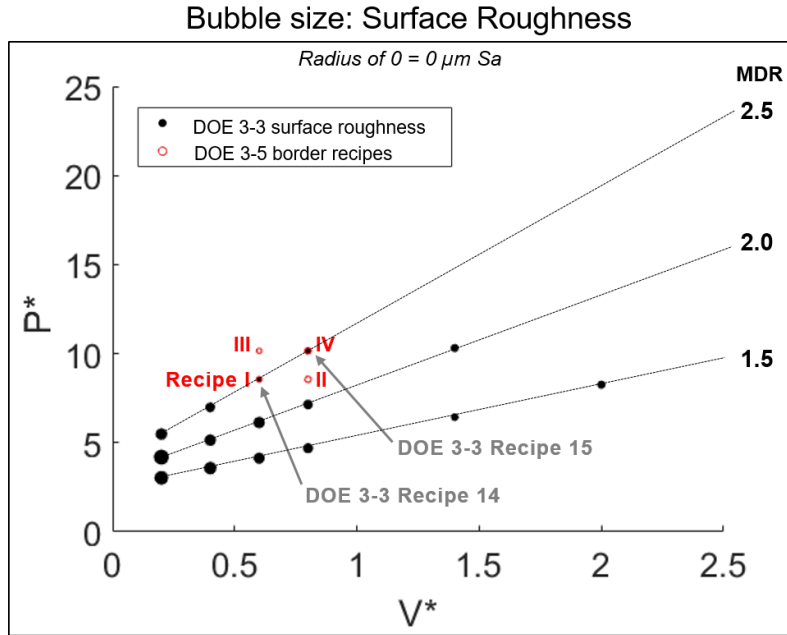


Figure 5-35: Non-dimensionalized power ( $P^*$ ) and speed ( $v^*$ ) for DOE 3-5 border recipes (red) superimposed on previous surface roughness results for DOE 3-3

The four selected border recipes were printed with each of the four different core recipes tested for DOE 3-5. The core recipes and manufacturing strategy for DOE 3-5 can be found in Section 5.2.4. Samples were analyzed for surface roughness according to Section 3.3.4 and the microstructure was examined at the edges of the parts according to Section 3.3.2.

For DOE 3-6, one border recipe was selected from DOE 3-5 to use for all of the parts, and is shown in Table 5-19. Cylindrical samples were built using the manufacturing strategy and core recipes for DOE 3-6 described in Section 5.2.4. The contour distance was changed from 140  $\mu\text{m}$  to match whichever hatch distance was used for the core recipe (either 142 or 145  $\mu\text{m}$ ). The samples were again analyzed for surface roughness (as per Section 3.3.4) and microstructure at the edges of the parts (as per Section 3.3.2).

Table 5-19: DOE 3-6 border recipe

Powder type	Layer thickness ( $\mu\text{m}$ )	Border Recipe #	Power (W)	Point distance ( $\mu\text{m}$ )	Exposure time ( $\mu\text{s}$ )	Contour distance ( $\mu\text{m}$ )
Supplier 2	35	I	270.0	60	70	142 or 145
Supplier 1	30					

The micrographs corresponding with DOE 3-6 revealed numerous large pores close to the edges of the part, likely caused by excessive energy input from the border recipes. To compensate for this effect, the

exposure time used for the border recipe was decreased from 70 to 50  $\mu\text{s}$  (thus increasing the effective scan speed from 749 to 999 mm/s). Table 5-20 shows the process parameters for the final new border recipe V, used for DOE 4-2. The corresponding core recipes are described in Section 5.2.4. The samples were analyzed for surface roughness (as per Section 3.3.4), microstructure (as per Section 3.3.2), and density (as per Section 3.3.3).

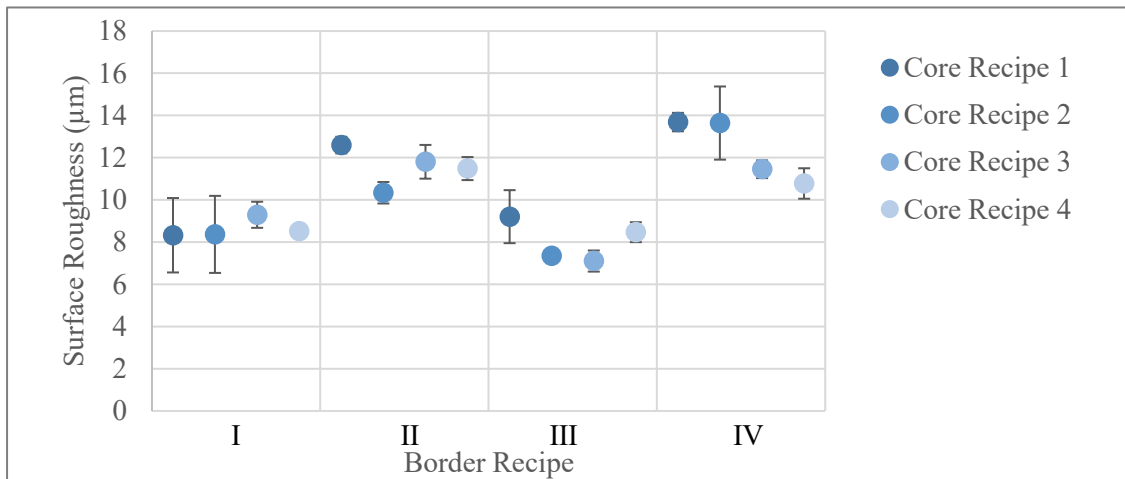
**Table 5-20: DOE 4-2 border recipe**

Powder type	Layer thickness ( $\mu\text{m}$ )	Border Recipe #	Power (W)	Point distance ( $\mu\text{m}$ )	Exposure time ( $\mu\text{s}$ )	Contour distance ( $\mu\text{m}$ )
Supplier 1	30	V	270.0	60	50	142 or 145

### 5.3.3 Outcomes for Ideal Border Recipes

#### DOE 3-5:

Figure 5-36 shows the surface roughness results for samples from DOE 3-5. Four different border recipes were each paired with four different core recipes. It was found that border recipe I and III had the lowest surface roughness, averaging 8.63 and 8.03  $\mu\text{m}$ , respectively. The core recipe did not have a large effect on the resulting surface roughness. The average surface roughness for each border recipe is listed in Table 5-21.

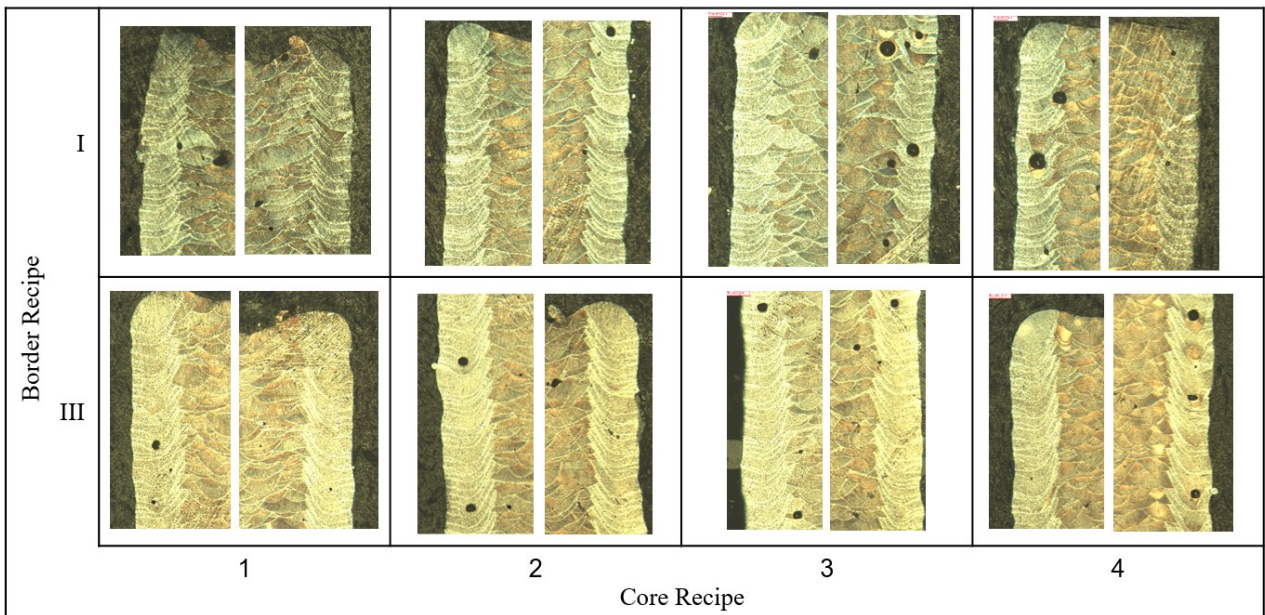


**Figure 5-36: Surface roughness results for samples from DOE 3-5**

**Table 5-21: Average surface roughness measurements for each border recipe used in DOE 3-5**

Border Recipe	Sample	Average Surface Roughness, Sa ( $\mu\text{m}$ )	St. Dev.
I	1, 2, 3, 4	8.63	1.08
II	5, 6, 7, 8	11.56	0.97
III	9, 10, 11, 12	8.03	1.06
IV	13, 14, 15, 16	12.39	1.57

Figure 5-37 shows optical micrographs of taken at the borders of all the samples that were printed using border recipe I and III. After etching, the melt pools at the part borders could be distinguished from the core of the part, and appeared to be wide and deep with each layer likely re-melting multiple times. Large, spherical pores typical for keyhole melting were present close to the borders. Border recipe I was selected for use in future experiments because it utilized a lower laser power setting, so the size and amount of keyhole porosity would likely be less severe.



**Figure 5-37: Optical micrographs taken at the edges of samples manufactured using border recipe I and III from DOE 3-5**

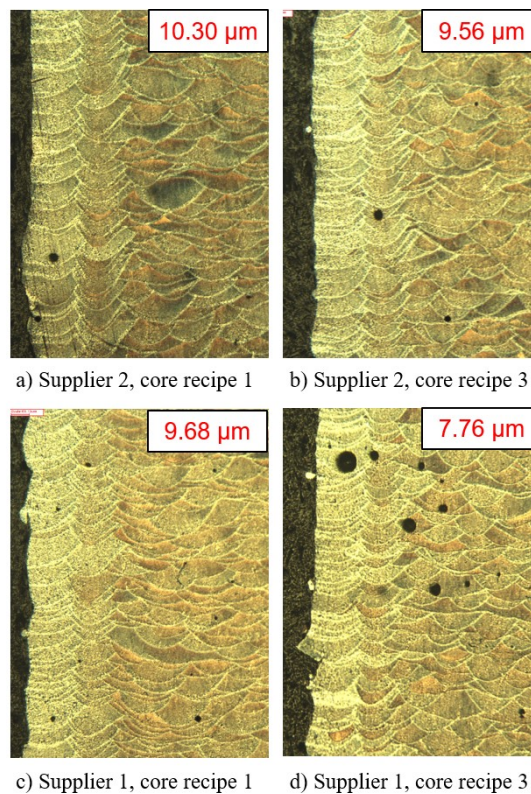
**DOE 3-6:**

In DOE 3-6, the border recipe selected in the previous section (DOE 3-5, border recipe I) was reprinted with two different core recipes and AlSi10Mg powder from two different suppliers. Table 5-22 shows the average surface roughness results for each sample. By switching to powder from Supplier 1, the surface roughness became slightly lower, averaging 9.68 and 7.76  $\mu\text{m}$  for the two core recipes that were

tested. Figure 5-38 shows the optical micrographs and surface roughness for each sample, which all contained spherical keyhole porosity near the borders.

**Table 5-22: Average surface roughness measurements for DOE 3-6**

Border Recipe	Core Recipe	Powder Type	Average Surface Roughness, Sa ( $\mu\text{m}$ )	St. Dev.
I	1	Supplier 2	10.30	2.04
		Supplier 1	9.68	2.31
I	3	Supplier 2	9.56	1.03
		Supplier 1	7.76	0.84

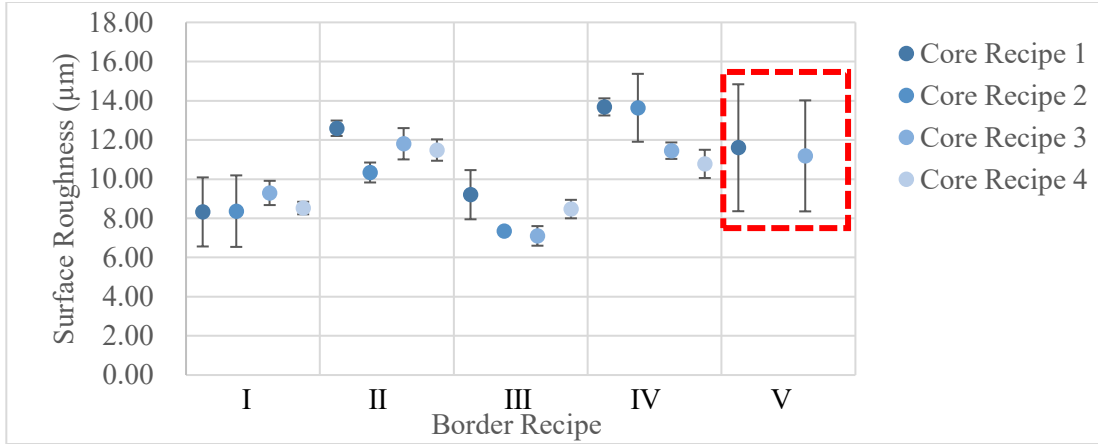


**Figure 5-38: Optical micrographs taken at the border of samples from DOE 3-6, manufactured using border recipe I and: a) powder supplier 2, core recipe 1; b) powder supplier 2, core recipe 3; c) powder supplier 1, core recipe 1; d) powder supplier 1, core recipe 3**

**DOE 4-2:**

In order to mitigate the effect of excessive energy input resulting in keyhole porosity at the borders, the exposure time used for the border recipe was decreased from 70 to 50  $\mu\text{s}$ . For DOE 4-2, the new recipe (border recipe V) was printed with the two ideal core recipes, and the parts were analyzed to determine the final part surface roughness. Border recipe V had an average surface roughness of 11.39  $\mu\text{m}$ .



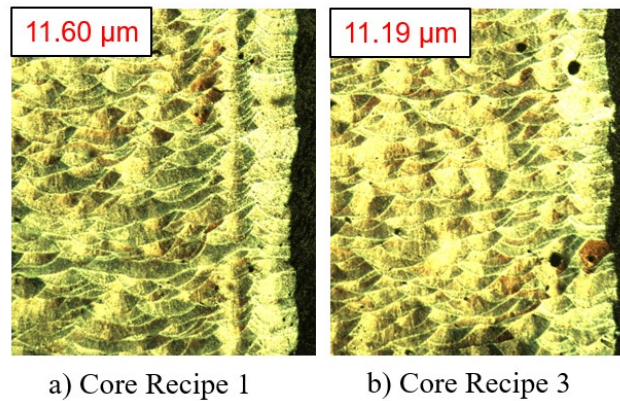


**Figure 5-39: Surface roughness results for samples from DOE4-2 (border recipe V), shown with DOE 3-5 results for comparison**

**Table 5-23: Average surface roughness measurement for DOE 4-2 (border recipe V), shown with DOE 3-5 results for comparison**

Border Recipe	Experiment	Average Surface Roughness (µm)	St. Dev.
I	DOE 3-5	8.63	1.08
II		11.56	0.97
III		8.03	1.06
IV		12.39	1.57
V	DOE 4-2	11.39	2.83

Figure 5-40 shows the optical micrographs and surface roughness for each sample. When border recipe V was paired with core recipe 1, very little porosity was observed at the edges of the sample. Core recipe 3 contained some small, spherical keyhole porosity near the borders. This result was confirmed by CT scan analysis of the part density and distribution of porosity, as discussed in Section 5.2.6.



**Figure 5-40: Optical micrographs taken at the edges of samples manufactured using border recipe V from DOE 4-2. The labels indicate the average Sa value.**

## 5.4 Summary of Selected Processing Parameters for AM Part Production

Two ideal recipes were selected for use in the LPBF of AlSi10Mg parts. The first recipe was the “high density” option and the relative density was estimated to be 99.95%. The second recipe was the “high productivity” option, which utilized a faster scan speed than the high density option while still achieving a high relative density of approximately 99.84%. Both recipes used identical processing parameters for the scan of the part border, with the exception of the contour distance, which was set to be equal to the hatch distance used for scanning the core of the part. The average surface roughness was 11.39  $\mu\text{m}$ . Table 5-24 shows the ideal processing parameters for the core and border, and Table 5-25 shows additional parameters that were kept constant for both core recipes.

**Table 5-24: Ideal processing parameters and resulting density and surface roughness**

Recipe	Scan Location	Power (W)	Point Distance ( $\mu\text{m}$ )	Exposure time ( $\mu\text{s}$ )	Eff. Scan Speed (mm/s)	Hatch or Contour Distance ( $\mu\text{m}$ )	Density (%) or Sa ( $\mu\text{m}$ )	St. Dev.
1	Core	176.8	60	110	500	142	99.95 %	0.23 %
3	Core	255.3	60	50	999	145	99.84 %	0.18 %
V	Border	270.0	60	50	999	142 or 145	11.39 $\mu\text{m}$	2.83 $\mu\text{m}$

**Table 5-25: Additional parameters for ideal manufacturing recipes**

Powder Type	Layer Thickness ( $\mu\text{m}$ )	Laser Spot Diameter ( $\mu\text{m}$ )	Scan Strategy
Supplier 1	30	70	meander

# **6 Performance of LPBF-Manufactured Components for Fluid Power Applications**

## **6.1 Methods for AM Part Characterization**

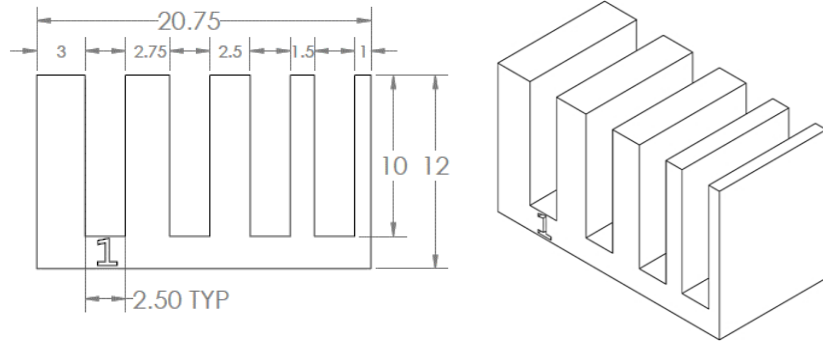
### **6.1.1 Characterization Approach**

In order to evaluate the performance of the LPBF-processed material for fluid power applications, various components were manufactured and characterized for a direct comparison with the cast pump housing performance benchmarks established in Chapter 4. Two different LPBF manufacturing recipes were investigated, as discussed in Section 6.1.3. The general procedures for material characterization can be found in Section 3.3. The density of the AM parts was characterized by x-ray computed tomography (Section 3.3.3). The surface roughness of the various surface types on the AM parts was characterized using laser confocal microscopy (Section 3.3.4). The manufacturability of the pump housing product was investigated through characterization of AM artifacts representative of key geometric features for quality in terms of density for thin walls, surface roughness for slots, and depowdering of circular channels (Section 6.1.2). The durability was investigated through measurements of the hardness (Section 3.3.5), the dry sliding wear rate (Section 3.3.6), and the corrosion behaviour (Section 3.3.8).

### **6.1.2 Geometric Feature Characterization**

Test artifacts representative of the pump housing's key features were designed in CAD software (Solidworks 2016), and were printed using the process parameters selected in Chapter 5, as summarized in Section 5.4. The artifacts were characterized for part quality in order to determine the feasibility of printing the pump housing product using LPBF.

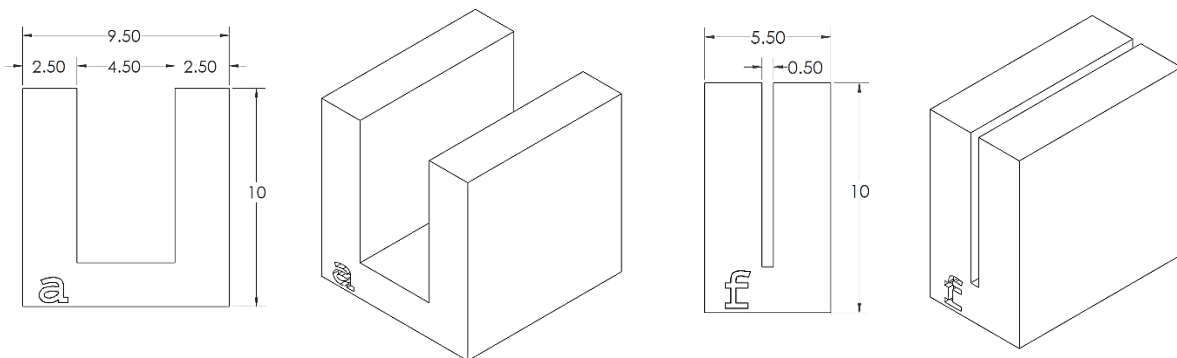
The thin wall artifact corresponds with the interior walls of the pump housing and was designed to have 5 evenly spaced vertical walls of varying thicknesses, as shown in Figure 6-1. The walls had a height and length of 10 mm, a thickness of 3.0, 2.75, 2.5, 1.5, or 1.0 mm, and were printed on a rectangular base with a 2.5 mm spacing between each wall. A sample label was printed on the front side of the base. Two replicates were printed for each manufacturing recipe.



**Figure 6-1: Thin wall artifact; all dimensions in mm.**

The thin wall artifacts were analyzed for porosity using the X-ray computed tomography method described in Section 3.3.3. The voxel size was  $7.91 \mu\text{m}$  and the detection was limited to pores with a minimum diameter of  $23.7 \mu\text{m}$ . Prior to CT scanning, a precision saw was used separate the thin walls from the base and also section them perpendicular to their length, resulting in individual walls with a height of 10 mm, length of 4 mm, and varying widths. Image analysis was performed using MATLAB in order to determine the density of each wall.

The slot artifacts correspond with the slot-shaped internal channels of the pump housing, and were designed to have equally sized parallel walls printed at a variety of separation distances. The slots each had two walls with a height of 8 mm, a length of 10 mm, a width of 2.5 mm, and the gap width between the walls was 4.5, 3.5, 2.5, 1.5, 1.0, or 0.5 mm. A sample label was printed on the front side of the slot. Figure 6-2 shows the CAD drawings for the largest and smallest slots, and the intermediate slots can be found in Appendix H.



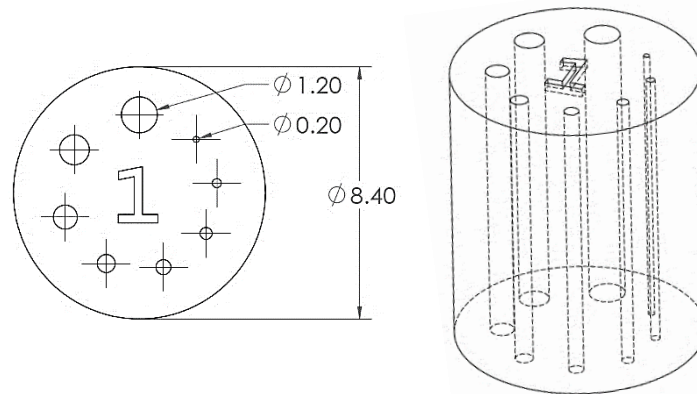
**Figure 6-2: Largest (left) and smallest (right) slot artifacts; all dimensions in mm.**

The slot artifacts were analyzed for surface roughness using the laser confocal microscopy method described in Section 3.3.1. The analyzed surfaces were the vertical internal walls of the slot. Prior to

scanning, a precision saw was used to cut each slot in half, separating the two parallel walls and exposing the surfaces of interest. The surface roughness was measured with an objective lens of 20x magnification and a z-pitch of 0.50  $\mu\text{m}$ . A total area of 3.02  $\text{mm}^2$  was measured for each slot.

The circular channel artifact was designed with smaller hole diameters than the pump housing, in order to determine the minimum resolution possible for manufacturing by LPBF. The channels were printed vertically through a cylindrical base with a height of either 10 or 20 mm. Two replicates were printed for each height and manufacturing recipe.

The channels were situated in a circular array and arranged counterclockwise from the largest to the smallest diameter: 1.2, 1.0, 0.8, 0.6, 0.5, 0.4, 0.3, and 0.2 mm, as shown in Figure 6-3. The sample label was printed in the center.



**Figure 6-3: Circular channel artifact; all dimensions in mm.**

The circular channel artifacts were tested for manufacturability through analysis of the ability to fully clear the powder out of the channel after printing. After removal from the build plate and support structures, the bottom of each sample was polished with 600 grit sandpaper to ensure that the end of the channel was not obstructed by cutting burrs. The samples were placed in an ultrasonic cleaning bath with isopropanol for 30 minutes to facilitate the removal of powder. Powder removal was tested by placing the bottom of the sample on an illuminated screen and visually checking for light continuity at the top of the channel. A low-powered microscope (Dino-Lite DinoCapture 2.0) was used to image each sample. X-ray computed tomography was also performed on one sample per recipe, as described in Section 3.3.3. The voxel size was 12  $\mu\text{m}$  and the detection was limited to pores with a minimum diameter of 36  $\mu\text{m}$ . Image analysis was performed using MATLAB in order to check for the presence of powder inside each channel.

### 6.1.3 Manufacturing Strategy

The processing parameters used for AM part production are shown in Table 6-1 and Table 6-2. The parameters were selected in Chapter 5, in which ideal manufacturing recipes were developed in order to manufacture parts with a high density and low surface roughness. Two different core recipes were investigated to compare the resulting part performance with each other and with the cast pump housing benchmark:

- **Recipe 1: High density option**, selected because it resulted in the highest relative density, and will likely produce high quality parts.
- **Recipe 3: High productivity option**, selected because it had the highest scan speed while still maintaining a high relative density, thus making it an economic choice for faster production.

The same border recipe was paired with both of the core recipes, and was used for one part border and one fill contour. The scan order was set so that the hatch volume (core) was scanned first, followed by the border and then the contour. The meander scan strategy was used with a 67° rotation between each layer. The powder source was Supplier 1 and the layer thickness was set to 30 μm.

**Table 6-1: Processing parameters for LPBF part production**

Recipe	Scan Location	Power (W)	Point Distance (μm)	Exposure time (μs)	Eff. Scan Speed (mm/s)	Hatch or Contour Distance (μm)
1	Core	176.8	60	110	500	142
3	Core	255.3	60	50	999	145
V	Border	270.0	60	50	999	142 or 145

**Table 6-2: Additional parameters for LPBF part production**

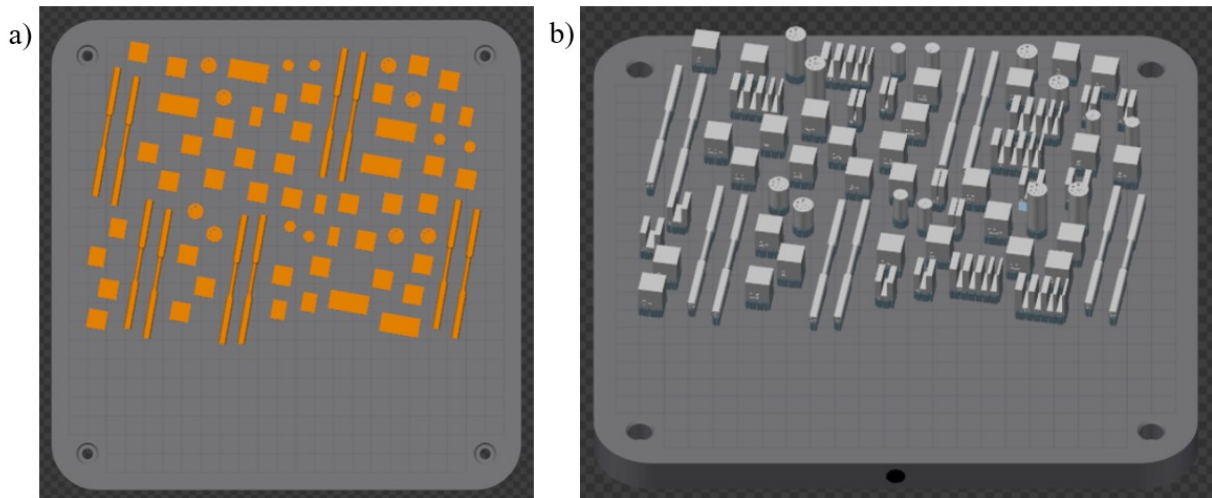
Powder Type	Layer Thickness (μm)	Laser Spot Diameter (μm)	Scan Strategy
Supplier 1	30	70	meander

In addition to the geometric feature artifacts described in Section 6.1.2, other part geometries such as cylinders and cubes were printed for characterization. Table 6-3 lists the artifact geometries and amount that were printed for each characterization type. The cubes printed for corrosion testing were also characterized for surface roughness and hardness. Images of each artifact type can be found in Appendix H.

**Table 6-3: Artifact type and quantity**

Artifact Type	Characterization Type(s)	Quantity
Cylinder	Density	6
Cube	Wear	6
	Corrosion	18
	Surface Roughness	-
	Hardness	-
Thin Walls	Density	6
Slots	Surface Roughness	12
Channels	Depowdering	8

Artifacts were printed in the Renishaw Full Build Environment with 5 mm tall cylindrical support structures. The part location on the build plate was semi-randomized, as shown in Figure 6-4. Parts with the same geometry were placed in pairs so that recipe 1 and 2 could be printed in close proximity, and replicates were randomly distributed across the build plate.



**Figure 6-4: a) Top view and b) isometric view of the build plate layout shown in QuantAM**

## 6.2 Results for AM Part Characterization

### 6.2.1 Density

Figure 6-5 shows the estimated part density for cylindrical AM artifacts manufactured using the two recipe options compared with two representative samples of the cast pump housing. The relative density was determined by CT scanning and image processing. Both of the AM recipes fell within the range of densities measured for the cast pump housing. Recipe 1, the high density option, was just below the maximum cast density at 99.95%. This recipe was also on-par with the best recipe found in literature, which reported a maximum relative density of 99.94% [54]. Recipe 3, the high productivity option, had a relative density of 99.84% and was also well above the minimum density measured for the cast pump housing.

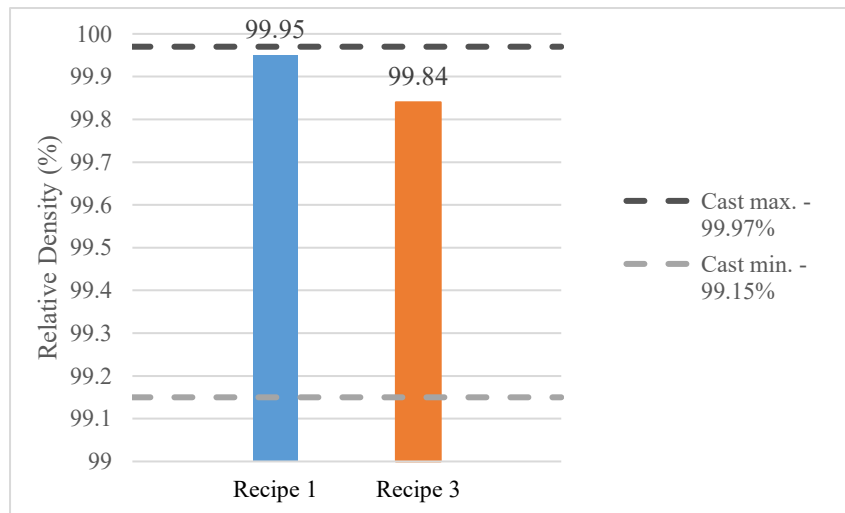
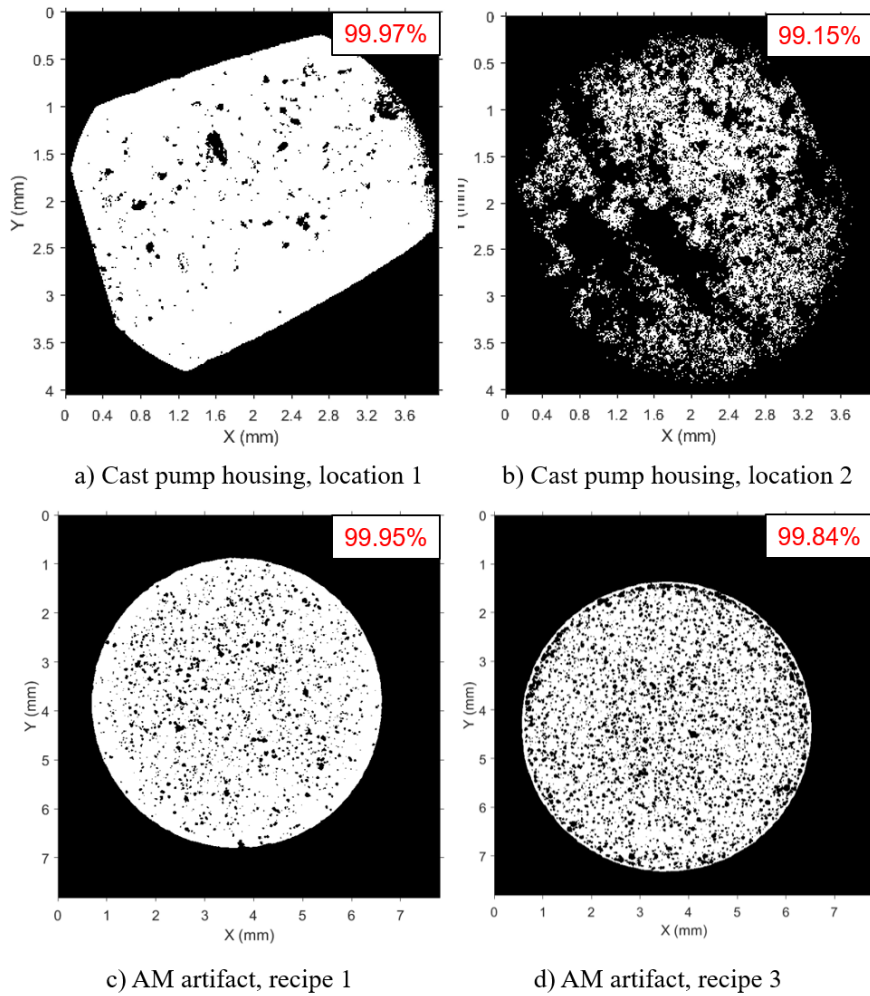


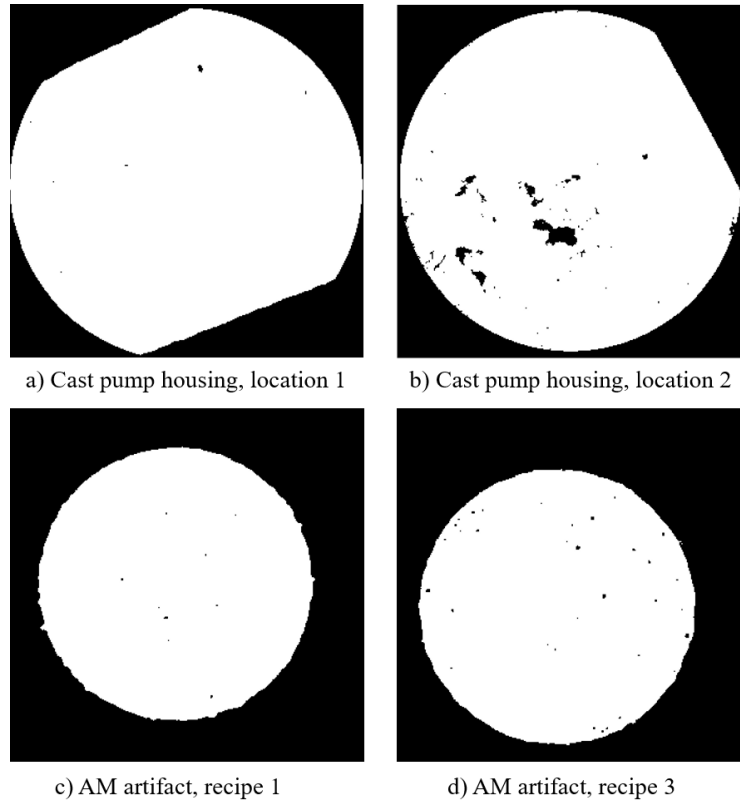
Figure 6-5: Density measurements for AM artifacts and cast pump housing

Figure 6-6 shows the minimum intensity projections of all the pores in each sample projected onto a 2-dimensional image. The cast samples were analyzed for 2.56 and 3.51 mm in the z-direction, and the AM samples were analyzed for 4.0 mm. The size and distribution of the pores was similar for the high density samples (Figure 6-6 – a and c). The lower density samples (Figure 6-6 – b and d) exhibited more pores near the edges of the parts, and the cast sample had several concentrated areas of high porosity, which contained a higher amount and/or larger sized pores. Figure 6-7 shows a binary image for a single slice or random cross-section of each sample. Note that the binary images for the cast pump housing are not set to the same scale as the AM samples.





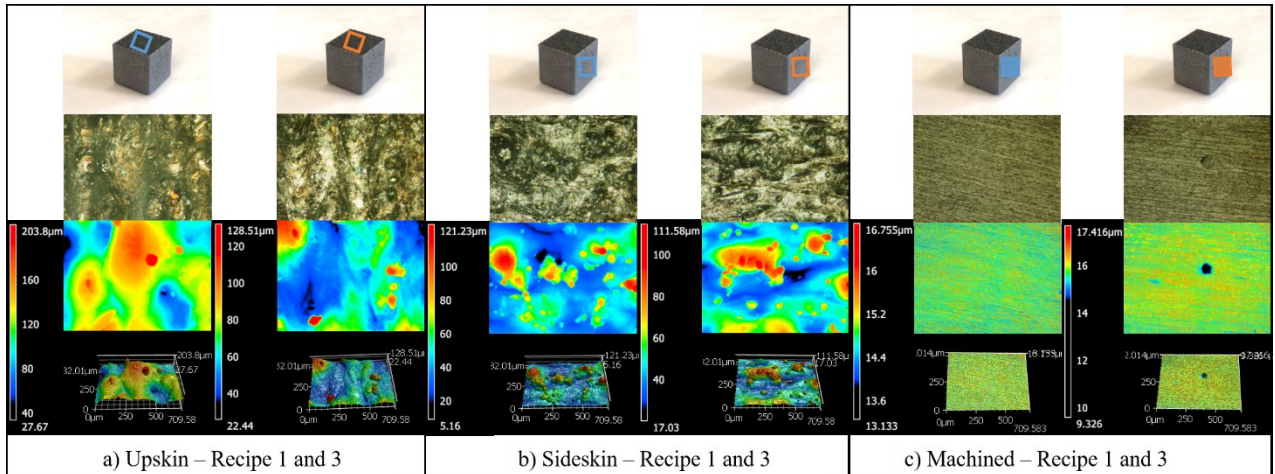
**Figure 6-6: Minimum intensity projections of pores for samples: a) cast pump housing, location 1; b) cast pump housing, location 2; c) AM artifact manufactured with Recipe 1; and d) AM artifact manufactured using Recipe 3**



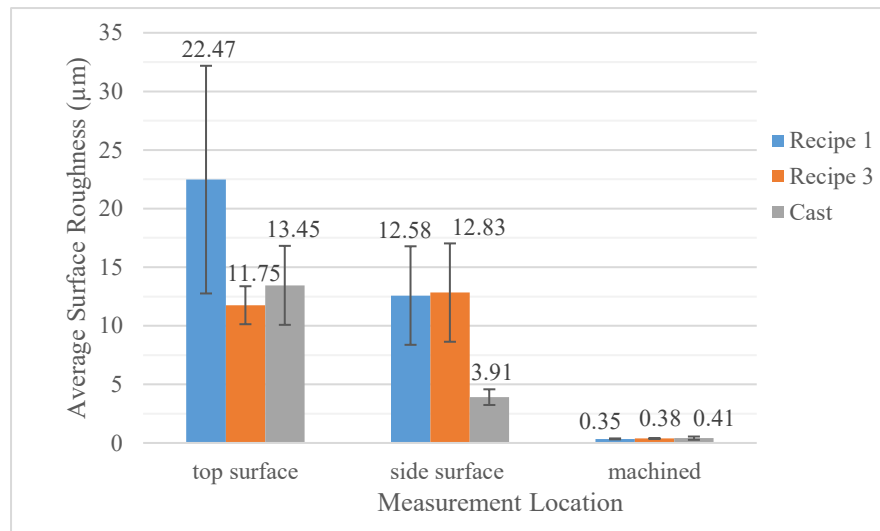
**Figure 6-7: Binary image for single slice of samples from: a) cast pump housing, location 1 (slice # 208/640); b) cast pump housing, location 2 (slice # 595/878); c) AM artifact manufactured with Recipe 1 (slice # 419/750); and d) AM artifact manufactured using Recipe 3 (slice # 333/742)**

### 6.2.2 Surface Roughness

The surface roughness was characterized for three surface types on the AM cube-shaped artifacts that were manufactured using the two recipe options, as shown in Figure 6-8. The average surface roughness results are summarized in Figure 6-9, which also includes the cast pump housing for comparison. The top surface corresponds with the AM upskin and the as-cast, horizontal surfaces; the side surface corresponds with the AM sideskin and the as-cast, vertical surfaces; and the machined surface refers to the machined surfaces on the cast pump housing and the AM samples that were polished in order to achieve a similar surface roughness.



**Figure 6-8: Surface roughness measurement locations, optical micrographs, and height images for AM Recipe 1 (left-hand columns) and Recipe 3 (right-hand columns)**



**Figure 6-9: Average surface roughness for AM artifacts and cast pump housing**

On the upskin surfaces, laser weld lines were visible in the optical micrograph, and the surface shape was wavy with some small adhered particles. Recipe 3, the high productivity option, had an average surface roughness of 11.75  $\mu\text{m}$ , which was similar to the as-cast, horizontal surface. Recipe 1, the high density option, had a higher average surface roughness of 22.47  $\mu\text{m}$ , which was more than 60% larger than that of the cast surface. Recipe 1 had a wavier surface than Recipe 3, likely because the higher energy density and lower laser scan speed resulted in melt pool instability during material solidification.

On the sideskin surfaces, periodic roughness due to the layer-by-layer manufacturing could not be discerned, so much of the surface roughness was attributed to small particles that were adhered to the surface. The average surface roughness was similar for both Recipe 1 and Recipe 3, likely because the same manufacturing parameters for the borders were used, and was measured to be around 12.58 to

12.83  $\mu\text{m}$ . This was more than 3 times higher than the average surface roughness of the as-cast, vertical surface, but was still lower than the as-cast, horizontal surface. It was also within the same range as the sideskin of the cylindrical AM artifacts, which measured  $11.39 \pm 2.83 \mu\text{m}$  (Section 5.4).

The machined surfaces were lightly ground with SiC papers in order to achieve a target surface roughness close to that of the machined surfaces on the cast pump housing, which was 0.41  $\mu\text{m}$ . This was done so that three different surface types could be compared for durability by investigating the hardness, dry sliding wear rate, and corrosion behaviour.

### 6.2.3 Geometric Features

#### 6.2.3.1 Thin Walls

Thin walls were printed with varying thicknesses from 1.0 to 3.0 mm, as shown in Figure 6-10. X-ray computed tomography was used to scan the samples for internal porosities.

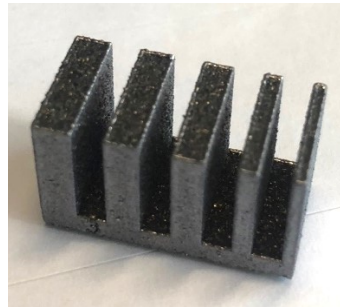


Figure 6-10: Example of thin wall artifact printed using Recipe 1

Table 6-4 shows the average relative density results for varying wall thicknesses printed using Recipe 1 or 3. Figure 6-11 shows a visualization of the results, with the density of the cast pump housing samples shown for comparison. All of the estimated densities fell within the same range measured for the cast pump housing, with the minimum relative density for the thin wall artifacts measuring 99.77%. As expected, samples manufactured using Recipe 1 had higher densities than Recipe 3, the high productivity option. The wall thickness did not have a large effect on the part density; however, for both recipes the 2.5 mm wall had the highest density.

Table 6-4: Relative density (%) results for thin wall artifacts

Recipe	Wall thickness (mm)					Average	St. Deviation
	1.0	1.5	2.5	2.75	3.0		
1	99.91	99.93	99.95	99.92	99.94	<b>99.93</b>	0.016
3	99.77	99.88	99.92	99.82	99.81	<b>99.84</b>	0.060

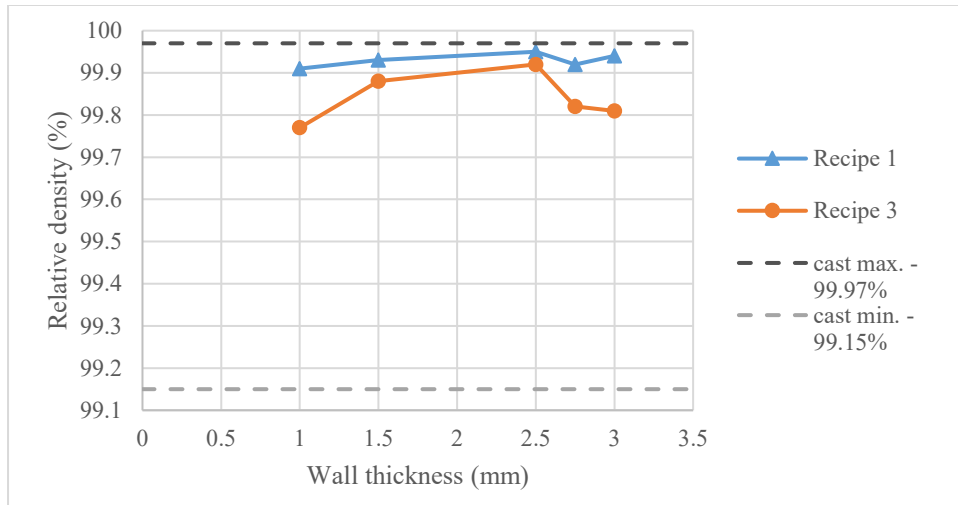


Figure 6-11: Density for AM thin wall artifacts of varying thicknesses and cast pump housing

Figure 6-12 shows the minimum intensity projections of all the pores in each sample projected onto a 2-dimensional image. The thin wall artifacts were analyzed for 4.0 mm in the z-direction.

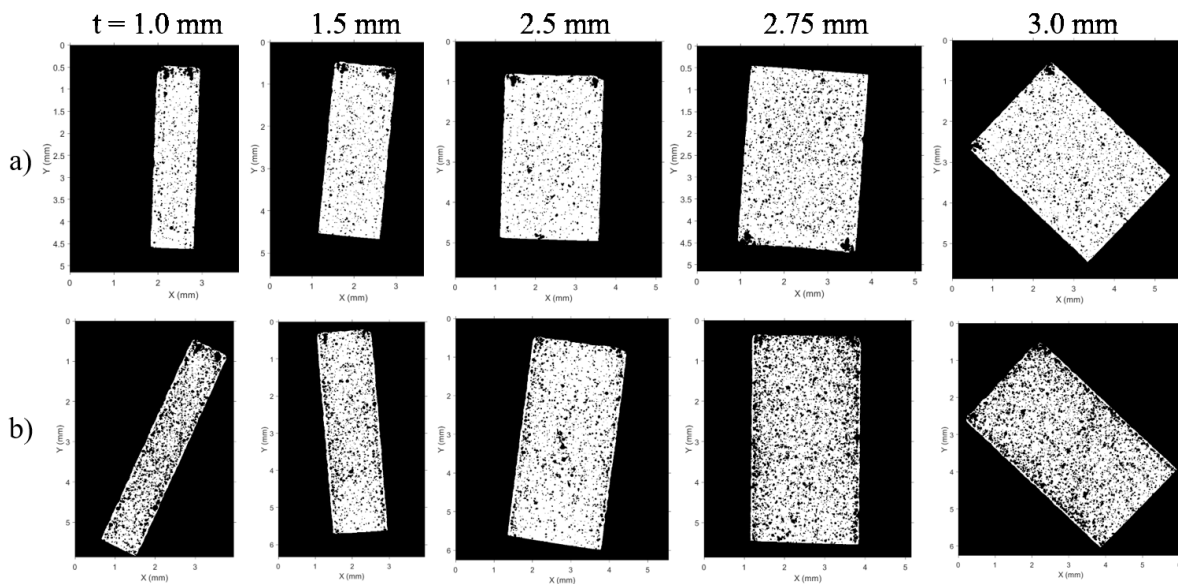


Figure 6-12: Minimum intensity projections across 4mm in Z-direction showing porosity for thin wall artifacts of varying thickness, manufactured using a) Recipe 1, high density option; or b) Recipe 3, high productivity option

In the minimum intensity projections, it can be seen that the pore distribution is mostly random, except there is a high amount of porosity in the two “as-printed” corners. The opposite two corners for each wall do not show this problem because the walls were sectioned prior to CT scanning, so the apparent corners are not the true as-printed corners of the artifacts. This localized porosity may be reduced by modifying the laser scan strategy.

In addition, the average densities for the thin walls printed using Recipe 1 (99.93%) and Recipe 3 (99.84%) were very close to the densities of the cylindrical artifacts reported in Section 6.2.1, which were 99.95% for Recipe 1 and 99.84% for Recipe 3. This suggests that the manufacturing recipes are robust and suitable for achieving high density parts with various thin wall geometries, within the bounds of the experiment at hand.

### 6.2.3.2 Slots

Slot artifacts were printed with varying gap widths ranging from 0.5 to 4.5 mm, as shown in Figure 6-13. The surface roughness was analyzed for the interior vertical walls.



**Figure 6-13: Examples of slot artifacts printed using Recipe 1**

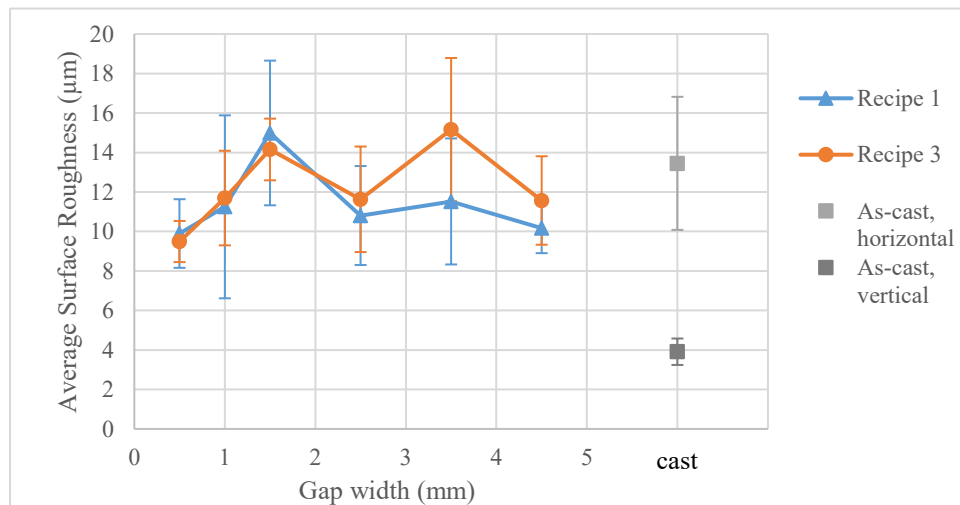
Table 6-5 shows the average relative surface roughness results for the slot artifacts printed using Recipe 1 or 3. Figure 6-14 shows a visualization of the results, with the surface roughness for two of the cast pump housing surfaces shown for comparison. The average surface roughness ranged from 9.49 to 15.16  $\mu\text{m}$ , and was similar to the as-cast, horizontal surface which had a surface roughness of  $13.45 \pm 3.37 \mu\text{m}$ . Generally, artifacts manufactured using Recipe 3 had a higher surface roughness than Recipe 1, but this trend did not hold true for every gap width. Furthermore, increasing the gap width did not have a large effect on the surface roughness, but the surface quality for the smallest and largest gap widths was marginally better. The smallest slot artifact, with a gap width of 0.5 mm, had the lowest surface roughness for both manufacturing recipes. As the slot size increased, fluctuations in surface roughness were observed, with similar trends for both Recipe 1 and Recipe 3. This may have been related to artifact position on the build plate, as slots of equal size were printed side by side for each recipe, so any influence of particle spatter and gas flow on the surface roughness would be similar for both artifacts.

In addition, the average surface roughness for the slot artifacts printed using Recipe 1 ( $11.44 \pm 1.85 \mu\text{m}$ ) and Recipe 3 ( $12.28 \pm 2.04 \mu\text{m}$ ) were similar (less than one standard deviation) to the values for the sideskin of the cube artifacts (Section 6.2.2), which measured 12.58  $\mu\text{m}$  for Recipe 1 and 12.83  $\mu\text{m}$  for Recipe 3, and the cylindrical artifacts (Section 5.3.3), which averaged 11.39  $\mu\text{m}$  for both recipes. The

consistent results show that a similar side surface roughness can be expected despite variations in gap width or flatness of the vertical surface. Moreover, it is possible that if the walls of the slot are close together (0.5 mm) or far apart (4.5 mm), the particle ejections could miss the border of the adjacent thin wall, thus resulting in a better surface quality. Other contributions from neighbouring parts and powder recoating may also contribute to the variability in surface roughness.

**Table 6-5: Average surface roughness ( $\mu\text{m}$ ) results for slot artifacts**

Recipe	Gap width (mm)						Average	St. Deviation
	0.5	1.0	1.5	2.5	3.5	4.5		
1	9.90	11.25	14.99	10.81	11.52	10.18	<b>11.44</b>	1.85
3	9.49	11.69	14.15	11.63	15.16	11.57	<b>12.28</b>	2.04



**Figure 6-14: Average surface roughness for AM slot artifacts with varying gap width and cast pump housing**

### 6.2.3.3 Channels

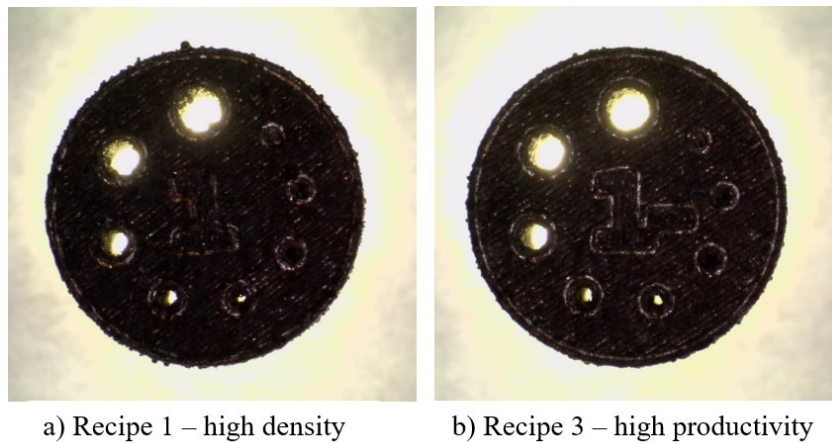
Straight circular channels were printed with hole diameters ranging from 0.2 to 1.2 mm, and with a height of 10 or 20 mm, as shown in Figure 6-15.



**Figure 6-15: Examples of circular channel artifacts printed using Recipe 1**

Powder removal was evaluated by a pass/fail criterion based on whether visible light could show through the channel when magnified with a low-power optical microscope. The channels were not evaluated for circularity or internal surface roughness.

A total of four artifacts were examined per recipe. Figure 6-16 shows an example of one artifact per recipe viewed under the microscope. Table 6-6 shows the results for the visible light test. The minimum channel size that could be fully cleared of all unmelted powder had a diameter 0.5 mm. The result was independent of channel length. Artifacts printed with Recipe 1 consistently cleared the powder for all channels up to 0.5 mm, and Recipe 3 had three out of four channels clear for that size.



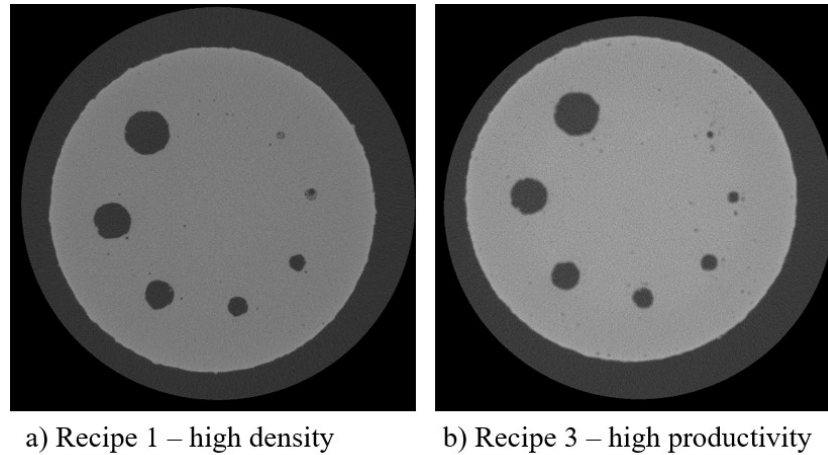
**Figure 6-16: Examples of circular channels printed with a) Recipe 1 and b) Recipe 3, viewed through optical microscope for the visible light test**

**Table 6-6: Visible light test results for channels of varying length and diameter**

Length (mm)	Recipe 1				Recipe 3			
	10	10	20	20	10	10	20	20
Diameter (mm)	Visible light? Yes / No				Visible light? Yes / No			
1.2	yes	yes	yes	yes	yes	yes	yes	yes
1.0	yes	yes	yes	yes	yes	yes	yes	yes
0.8	yes	yes	yes	yes	yes	yes	yes	yes
0.6	yes	yes	yes	yes	yes	yes	yes	yes
0.5	yes	yes	yes	yes	yes	no	yes	yes
0.4	no	no	no	no	no	no	no	no
0.3	no	no	no	no	no	no	no	no
0.2	no	no	no	no	no	no	no	no



Visible light could not be observed through any channels below 0.5 mm in diameter, but it is possible that the smaller channels were only partially obstructed with powder. One artifact per recipe was CT scanned in order to further investigate the presence of powder in the channels, as shown in Figure 6-17.



**Figure 6-17: Cross sectional image of circular channels printed with a) Recipe 1 and b) Recipe 3, examined through CT scanning**

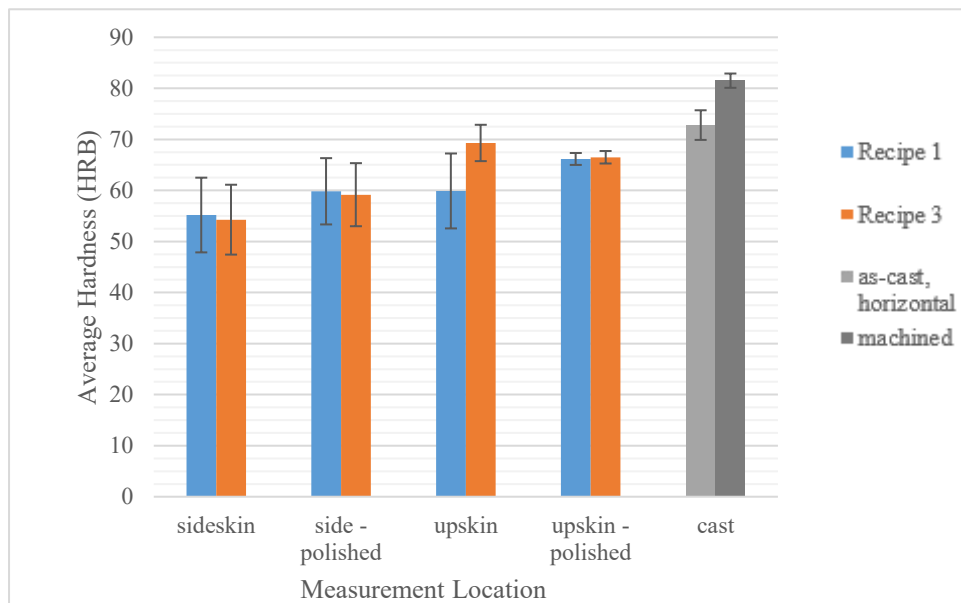
For both recipes, only 7 of the 8 channels were visible through CT scanning. This confirms that the smallest channel, with a diameter of 0.2 mm, was too small to even be successfully printed. The 0.3 and 0.4 mm channels were printed, but powder could not be cleared from the entire length of the channels.

#### **6.2.4 Hardness**

Table 6-7 shows the average Rockwell hardness test results measured on different surface types of the AM cube artifacts and the cast pump housing. Figure 6-18 shows a visualization of the results. The cast pump housing had a higher hardness, ranging from 72.8 to 81.5 HRB depending on the surface, while the AM artifacts ranged from 54.3 to 69.3 HRB. This was likely due to differences in heat treatments and alloy composition, as the cast pump housing contained copper and higher silicon content. The AM artifacts were not heat treated, but it has been shown in literature that the hardness of LPBF-manufactured AlSi10Mg can be increased by using an aging heat treatment [36]. Conversely, heat treatments that include solutionizing typically result in a lower hardness than the as-built part [121]–[123].

**Table 6-7: Average hardness (HRB) for AM artifacts and cast pump housing**

Sample Type	Surface type	Average	St. Deviation
Cast	As-cast, horizontal	<b>72.8</b>	2.9
	Machined	<b>81.5</b>	1.4
AM Recipe 1	Upskin	<b>59.9</b>	7.3
	Upskin – polished	<b>66.2</b>	1.2
	Sideskin	<b>55.2</b>	7.3
	Side – polished (machined)	<b>59.8</b>	6.5
AM Recipe 3	Upskin	<b>69.3</b>	3.6
	Upskin – polished	<b>66.5</b>	1.2
	Sideskin	<b>54.3</b>	6.8
	Side – polished (machined)	<b>59.2</b>	6.2



**Figure 6-18: Average hardness (HRB) for AM artifacts and cast pump housing**

The manufacturing recipe did not have a large effect on the hardness of the side surface and polished surface since the contribution from the skin recipe was dominant; however, the average hardness for the upskin of the as-printed samples was lower for Recipe 1, where the core recipe is probed for hardness. This was attributed to variations in surface quality and core recipe strategy, as Recipe 1 had a top surface roughness almost twice that of Recipe 3. The difference in hardness values was reduced when the upskin surface was polished prior to testing. In addition, the upskin surfaces had a higher average hardness than the sideskin and the polished side surfaces (which were representative of the “machined” surface type for the AM samples). It is not unusual for LPBF parts to exhibit anisotropic mechanical properties due to the layer-by-layer processing.

### 6.2.5 Wear

Figure 6-19 shows the specific wear rates for three different surface types on the AM artifacts and cast pump housing. The top surface corresponds with the AM upskin and the as-cast, horizontal surfaces; the side surface corresponds with the AM sideskin and the as-cast, vertical surfaces; and the machined surface refers to the machined surfaces on the cast pump housing and the AM samples that were polished in order to achieve a similar surface roughness.

Table 6-8 shows the specific wear rate for each trial. The cast pump housing exhibited a better wear resistance for all surface types, with the average specific wear rate ranging from  $2.50 \times 10^{-13}$  to  $2.55 \times 10^{-13} \text{ m}^2\text{N}^{-1}$ . The AM artifacts had higher specific wear rates, with average values ranging from  $3.92 \times 10^{-13}$  to  $6.04 \times 10^{-13} \text{ m}^2\text{N}^{-1}$ . Recipe 1 had a worse wear resistance than Recipe 3 for the upskin surface, but the wear rates for the sideskin and machined surface were similar for both recipes. This may have been related to the high surface roughness, as the decreased contact area between the surface and the abrasive pin would result in a higher localized pressure until the surface has been worn down. This could also explain why the machined surface exhibited a lower specific wear rate, despite having a similar hardness value.

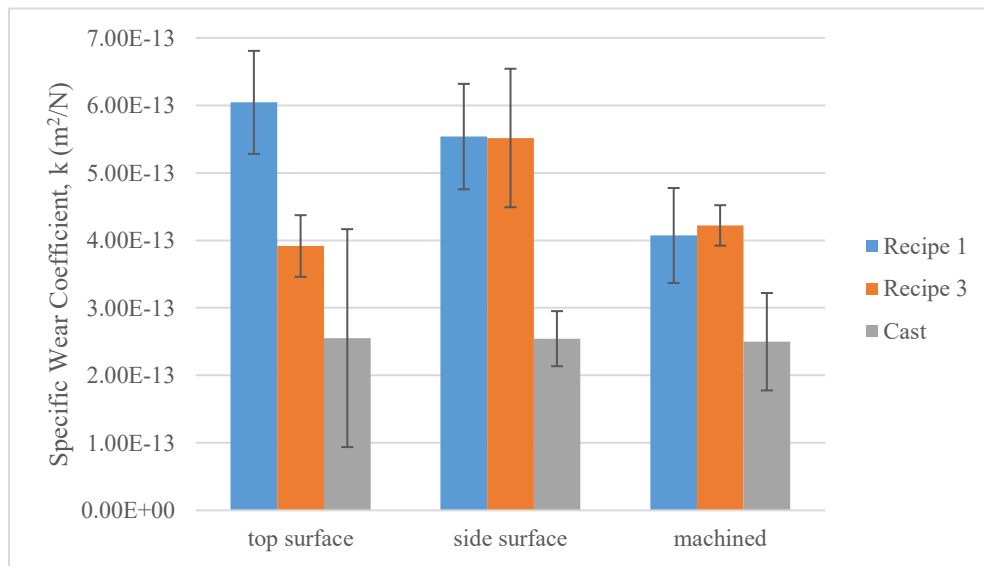
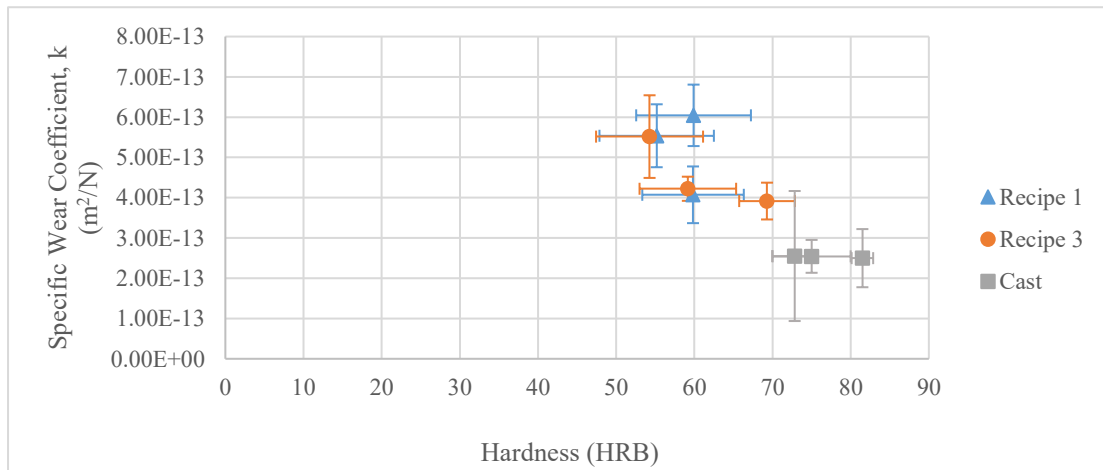


Figure 6-19: Average specific wear rate ( $k_w$ ) for AM artifacts and cast pump housing

**Table 6-8: Specific wear rate ( $k_w$ ) for AM artifacts and cast pump housing, in units of  $m^2N^{-1}$**

Sample Type	Surface type	Trial #			Average	St. Deviation
		1	2	3		
Cast	As-cast, horizontal	3.12E-13	1.09E-13	4.57E-13	<b>2.55E-13</b>	1.61E-13
	As-cast, vertical	3.14E-13	2.46E-13	2.35E-13	<b>2.54E-13</b>	4.08E-14
	Machined	3.55E-13	2.32E-13	1.92E-13	<b>2.50E-13</b>	7.21E-14
AM Recipe 1	Upskin	6.11E-13	6.77E-13	5.25E-13	<b>6.04E-13</b>	7.63E-14
	Sideskin	4.85E-13	6.39E-13	5.37E-13	<b>5.54E-13</b>	7.81E-14
	Machined	4.76E-13	4.09E-13	3.36E-13	<b>4.07E-13</b>	7.04E-14
AM Recipe 3	Upskin	3.40E-13	4.26E-13	4.09E-13	<b>3.92E-13</b>	4.57E-14
	Sideskin	4.33E-13	6.09E-13	6.13E-13	<b>5.52E-13</b>	1.03E-13
	Machined	3.88E-13	4.42E-13	4.36E-13	<b>4.22E-13</b>	3.00E-14

Generally, the wear resistance of a material increases as the hardness increases [35], [60], [61]. Figure 6-20 shows the specific wear rate versus the hardness measurements for all three surface types. Overall, it was found that the wear resistance increases as the hardness increases, especially for Recipe 3 and the cast pump housing. However, the trend is not as strong for Recipe 1, which may have been due to the large variations in surface roughness.



**Figure 6-20: Specific wear rate ( $k_w$ ) versus hardness for AM artifacts and cast pump housing**

Figure 6-21 shows representative SEM images of the wear tracks for each surface type and recipe. In the low magnification image, a portion of the wear track or scar can be seen in the center of the image, while the unaltered sample surface is visible above, below, and to the left side of it. The high magnification images were taken inside each wear track. All six sample types had features such as deep gouges and grooves parallel to the sliding direction, and flaky wear debris.

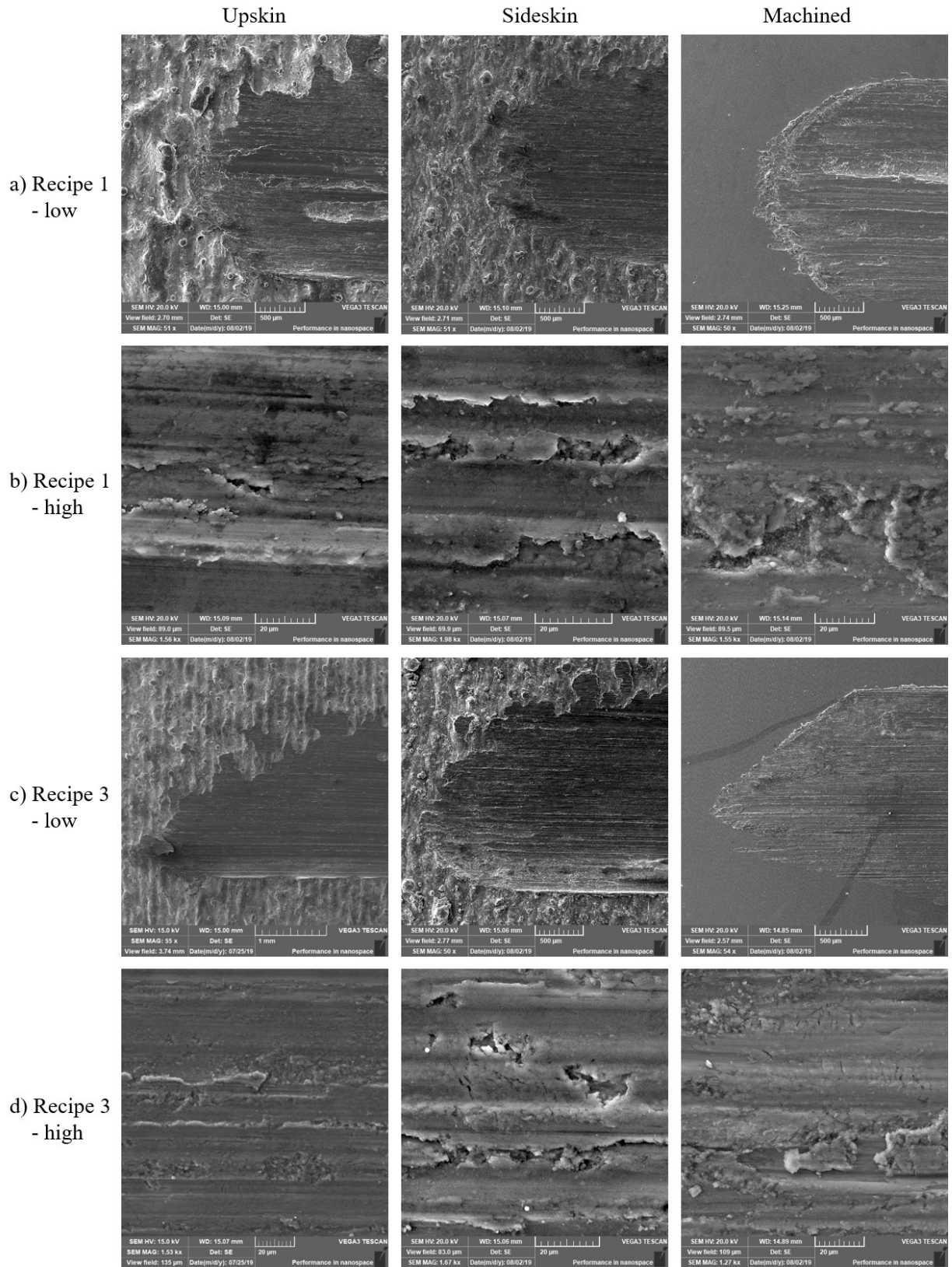
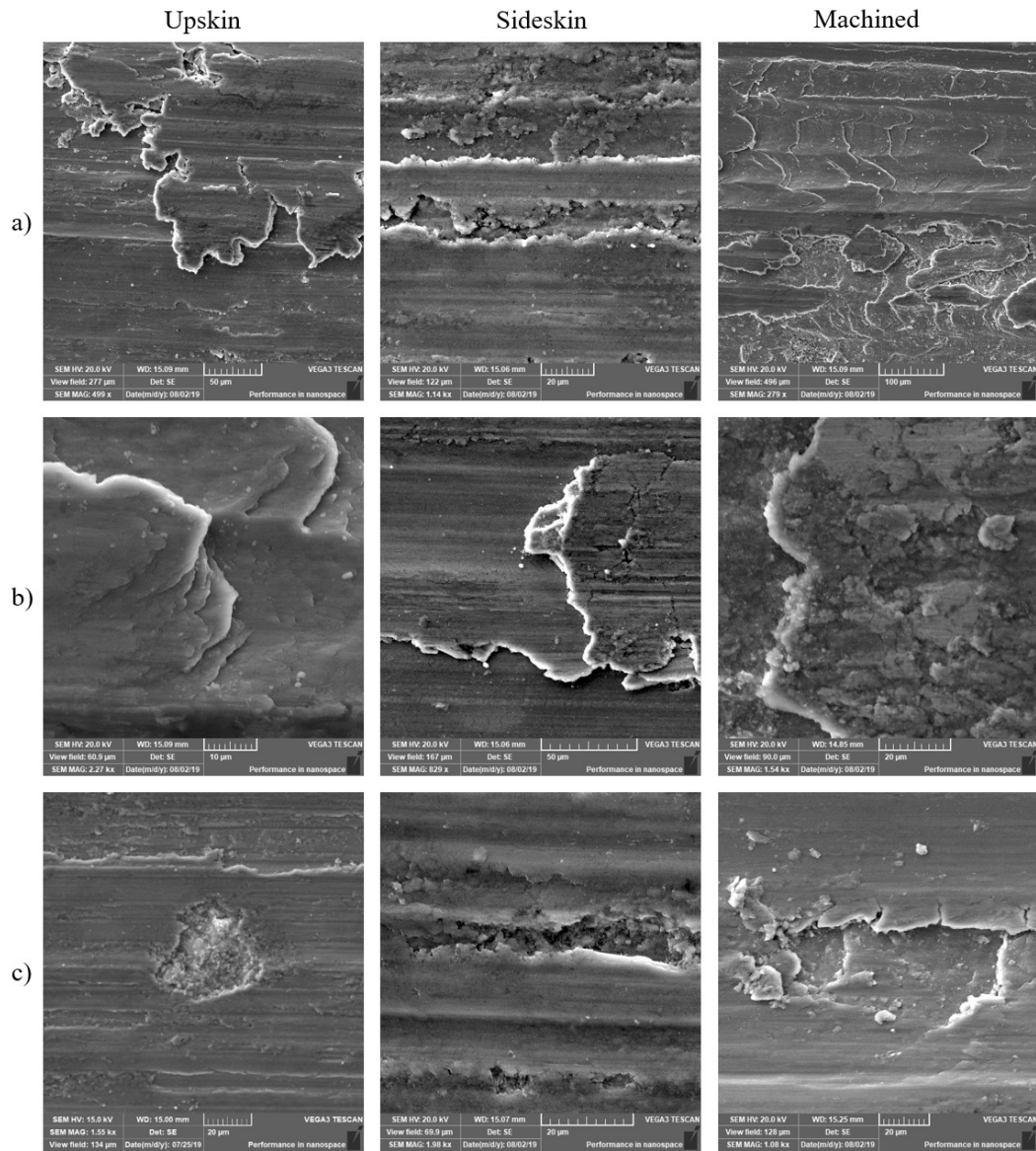


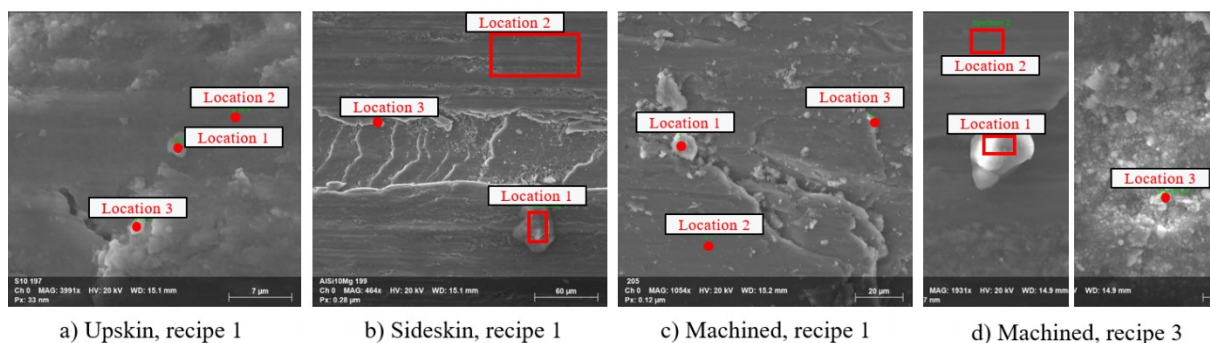
Figure 6-21: Low and high magnification SEM images of the wear track for the AM samples manufactured with Recipe 1 (a and b) and Recipe 3 (c and d)

Transverse and longitudinal ridges with a smooth, wavy morphology were observed on the surface of the samples, as shown in Figure 6-22–a and b. This is indicative of plastic deformation causing the sample surface and/or loosened wear debris to flatten with the continued relative motion of the pin. These smooth ridges were not observed on the cast pump housing samples, which mainly featured flaky wear debris, rough gouges and grooves, surface craters, and microcracks perpendicular to the sliding direction. Flaky wear debris and surface craters with sharp edges were also observed on the AM samples, as shown in Figure 6-22–c. It is likely that oxidative wear accompanied the mechanical wear of the samples.



**Figure 6-22: SEM images from three surface types showing a) and b) ridges; and c) craters with flaky wear debris**

Figure 6-23 shows EDX measurement locations for the three surface types manufactured using Recipe 1, and corresponds with the results in Table 6-9. Similar locations were analyzed for the machined surface manufactured with Recipe 3 (not pictured). The chemical composition of the wear debris was measured for distinct particles as well as rough areas on the wear surface, and consistently contained elevated oxygen levels. Smooth areas in the wear track had considerably less oxygen content. In addition, for the sideskin and machined surfaces of Recipe 1, EDX analysis was performed on the rough edges of a gouge and a ridge. These locations had a higher oxygen content than the smooth areas, but much lower than the wear debris particles and rough areas. This indicates that the gouges or ridges were caused by a mechanical wear mechanism, rather than breakage of the oxide layer resulting from oxidative wear. In comparison to the cast pump housing, the AM material exhibited more evidence of mechanical wear in addition to the oxidative wear, therefore leading to the increase in specific wear rate.



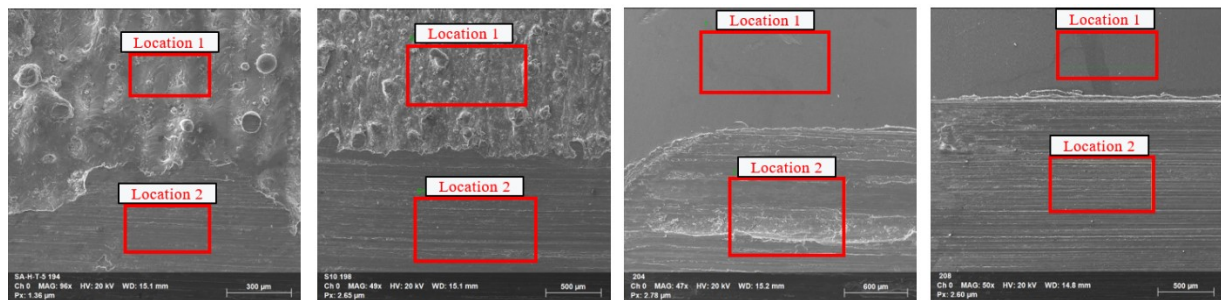
**Figure 6-23: EDX measurement locations within the wear track for a) the upskin surface; b) the sideskin surface; and c) the machined surface, for samples manufactured using recipe 1, and d) the machined surface for sample manufactured using recipe 2**

**Table 6-9: EDX results for chemical composition at various locations within the wear track on the AM artifacts**

Recipe	Surface Type	Measurement Location	Element (wt%)				
			O	Mg	Al	Si	Ni
1	Upskin	1. particle	32.6	0.26	49.8	6.3	0.45
		2. smooth	10.1	-	81.5	8.5	-
		3. rough	45.1	0.29	46.9	7.0	0.79
1	Sideskin	1. particle	20.6	-	12.1	1.1	-
		2. smooth	29.5	-	61.4	6.8	-
		3. gouge	13.1	-	75.3	7.8	-

1	Machined	1. particle	15.0	-	72.1	8.1	-
		2. smooth	1.70	-	86.4	8.5	-
		3. ridge	12.0	-	71.4	9.5	-
3	Machined	1. particle	41.5	-	3.0	-	-
		2. smooth	1.39	-	82.0	10.2	-
		3. rough	40.0	-	43.0	5.0	0.38

EDX analysis was also performed inside and outside the wear track on the untouched surface of the samples for the three surface types. Figure 6-24 shows the measurement locations corresponding with the results in Table 6-10. The machined surface of the artifact manufactured using Recipe 3 was also analyzed in similar locations (not pictured). It was found that the inside of the wear track (location 2) contained 1.5 to 6 times the amount of oxygen (by weight %) when compared with the area outside of the wear track (location 1). This provides confirmation that oxidative wear has occurred, because if the oxygen was not already present in the material, the increase must have been the result of a reaction with oxygen from the environment. Additionally, trace amounts of nickel were present within the wear track on the upskin surface, revealing that the abrasive pin (IN625) also generated wear particles, likely by adhesion since the pin is harder than the samples and unlikely to experience abrasive wear.



a) Upskin, recipe 1      b) Sideskin, recipe 1      c) Machined, recipe 1      d) Machined, recipe 3

**Figure 6-24: EDX measurement areas outside (location 1) and inside (location 2) the wear track, for the upskin (a), sideskin (b), and machined surfaces (c and d)**

**Table 6-10: EDX results for chemical composition inside and outside the wear track on the AM artifacts**

Recipe	Surface Type	Measurement Location	Element (wt%)				
			O	Mg	Al	Si	Ni
1	Upskin	1. Outside track	14.1	1.35	69.2	6.6	-
		2. Inside track	22.3	-	64.8	6.8	0.12
1	Sideskin	1. Outside track	4.6	0.41	84.2	10.8	-
		2. Inside track	27.4	0.13	64.9	7.53	-



1	Machined	1. Outside track	3.6	-	81.4	10.4	-
		2. Inside track	13.5	-	73.2	8.4	-
3	Machined	1. Outside track	5.2	-	79.6	9.6	-
		2. Inside track	28.3	-	58.3	6.8	-

## 6.2.6 Corrosion

### *Cyclic potentiodynamic polarization*

Figure 6-25 shows the cyclic potentiodynamic curves for one replicate of the cast and AM surfaces, which were tested in a 0.001M chloride solution. Table 6-11 shows the average results for anodic and cathodic corrosion potentials, pitting potential, and anodic current density at 0.2V. Refer to Appendix I for the polarization curves and tabulated results of all three replicates.

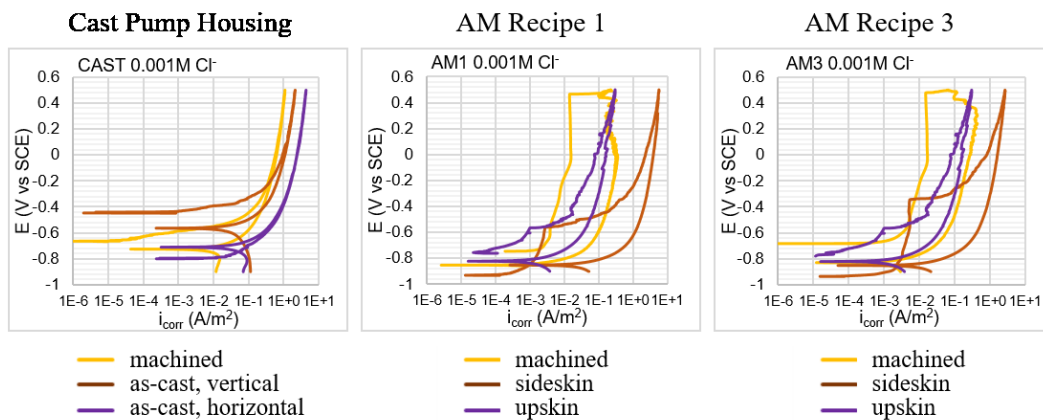


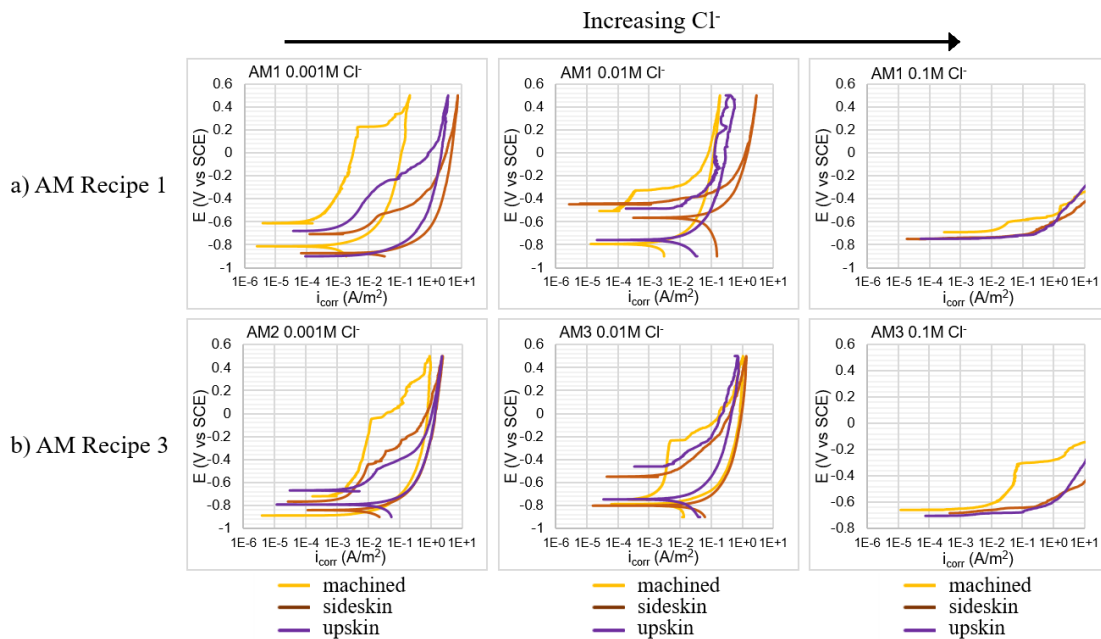
Figure 6-25: Cyclic polarization curves for one replicate of the cast and AM surfaces

Table 6-11: Average results for three replicates of cyclic polarization testing of the cast pump housing and AM artifacts

Chloride Molarity	Sample Type	Surface Type	Anodic Corrosion Potential (V)	Pitting Potential (V)	Anodic Current @ 0.2V (A/m <sup>2</sup> )	Cathodic Corrosion Potential (V)
0.001 M	Cast	Machined	-0.61 ± 0.084	General corr.	0.90 ± 0.60	-0.68 ± 0.059
		Vertical	-0.54 ± 0.081	General corr.	1.29 ± 0.66	-0.59 ± 0.025
		Horizontal	-0.64 ± 0.28	General corr.	1.27 ± 0.70	-0.69 ± 0.042
	AM Recipe 1	“Machined”	-0.68 ± 0.074	0.39 ± 0.15	0.010 ± 0.006	-0.84 ± 0.023
		Sideskin	-0.75 ± 0.16	-0.53 ± 0.036	2.97 ± 2.05	-0.84 ± 0.036
		Upskin	-0.64 ± 0.14	-0.39 ± 0.095	0.79 ± 0.56	-0.87 ± 0.053
	AM Recipe 3	“Machined”	-0.69 ± 0.023	0.27 ± 0.28	0.089 ± 0.067	-0.84 ± 0.051
		Sideskin	-0.76 ± 0.16	-0.34 ± 0.24	0.97 ± 0.55	-0.83 ± 0.026
		Upskin	-0.67 ± 0.12	-0.29 ± 0.40	0.50 ± 0.56	-0.81 ± 0.012

For the cast pump housing, the average anodic corrosion potentials ranged from -0.64 to -0.54 V vs SCE, while the AM artifacts ranged from -0.76 to -0.64 V vs SCE. The anodic corrosion potential of the sideskin surface was generally more negative than the upskin or machined surfaces. The average cathodic potentials had less variance and ranged from -0.69 to -0.59 V vs SCE for the cast pump housing and -0.87 to -0.81 V vs SCE for the AM artifacts. Based on corrosion potential alone, it would appear that the AM artifacts had a worse corrosion resistance than the cast pump housing; however, the shape of the cyclic polarization curves showed that the AM artifacts had a much higher pitting potential than the cast samples. For the cast samples, no pitting potential was observed, meaning that pitting had already started at the anodic corrosion potential (thus allowing general corrosion to occur). The average pitting potential for AM recipe 1 was around 0.39 V vs SCE for the machined surface, -0.53 V vs SCE for the sideskin surface, and -0.39 V vs SCE for the upskin surface. The average results for AM recipe 3 were similar; however, the variance for all three surface types was larger. The machined surfaces likely had a greater resistance to pitting because the lower surface roughness would allow for a more uniform passive film to form on the surface of the metal. The corrosion currents measured at 0.2V were lowest for the machined and upskin surfaces of the AM artifacts, and highest for the sideskin surface. The current density for the cast pump housing typically fell somewhere in between.

Figure 6-26 shows a comparison of cyclic polarization curves that were generated by testing in either a 0.001M or 0.1M Cl<sup>-</sup> solution. The resulting anodic and cathodic corrosion potentials, pitting potential, and anodic current density at 0.2V are listed in Table 6-12.



**Figure 6-26: Effect of increasing chloride concentration on cyclic polarization curves for the AM artifacts manufactured using a) Recipe 1 and b) Recipe 3**

With increasing chloride concentration, the pitting potential of the AM artifacts decreased, and in some cases only general corrosion was observed. AM recipe 3 had a better resistance to pitting than AM recipe 1 in the solutions with elevated chloride concentrations; however, only one replicate was performed.

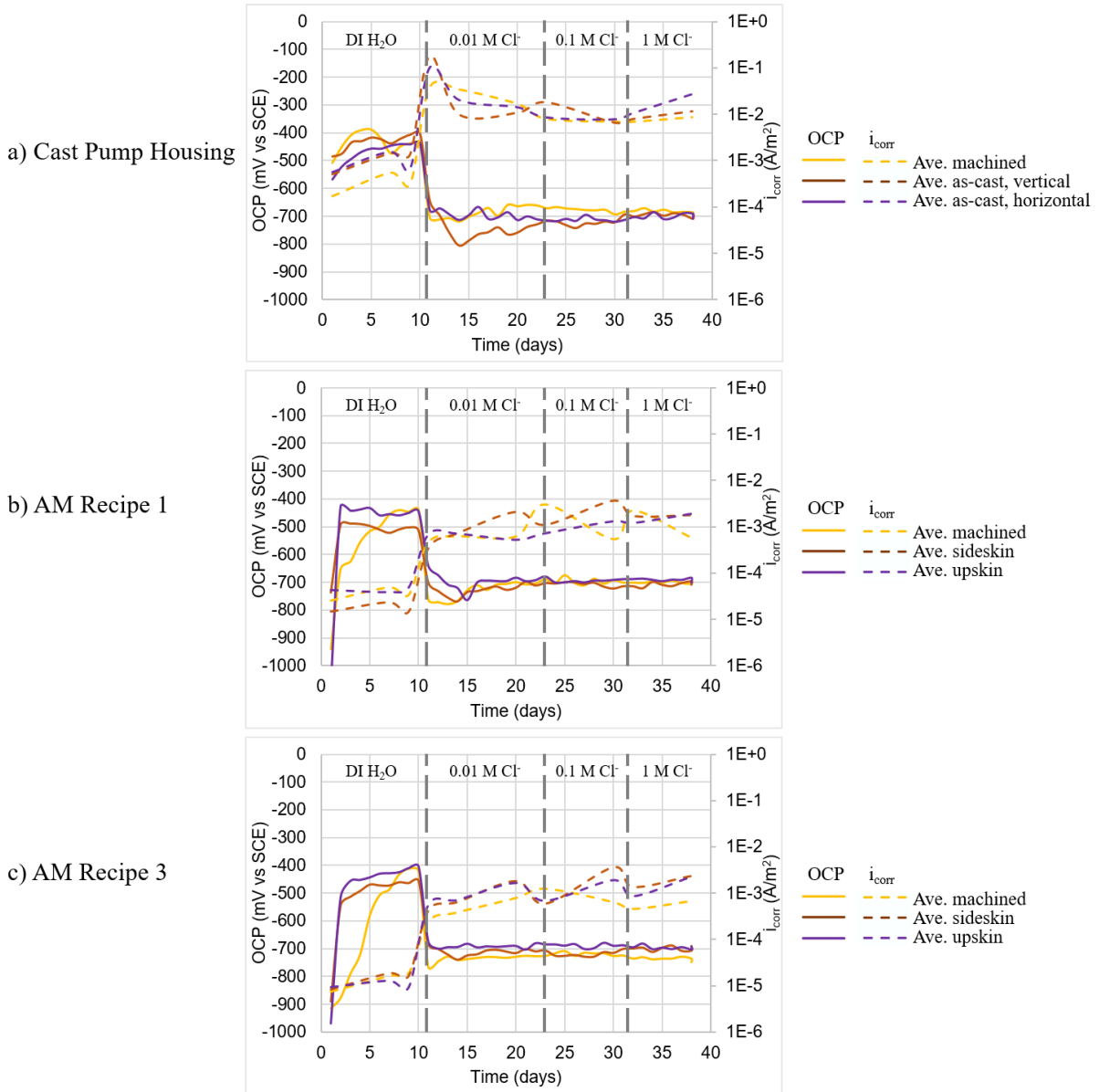
**Table 6-12: Results for cyclic polarization testing of the cast pump housing and AM artifacts at varying chloride concentrations**

Chloride Molarity	Sample Type	Surface Type	Anodic Corrosion Potential (V)	Pitting Potential (V)	Anodic Current @ 0.2V (A/m <sup>2</sup> )	Cathodic Corrosion Potential (V)
0.001 M	Cast	Machined	-0.67	General corr.	0.9	-0.72
		Vertical	-0.50	General corr.	1.18	-0.56
		Horizontal	-0.80	General corr.	1.21	-0.70
	AM Recipe 1	“Machined”	-0.74	0.47	0.013	-0.85
		Sideskin	-0.92	-0.57	3.0	-0.85
		Upskin	-0.75	-0.57	0.16	-0.82
	AM Recipe 3	“Machined”	-0.68	0.48	0.018	-0.83
		Sideskin	-0.92	-0.34	1.5	-0.85
		Upskin	-0.78	-0.57	0.16	-0.82
0.01 M	Cast	Machined	<i>No data</i>			
		Vertical				
		Horizontal				
	AM Recipe 1	“Machined”	-0.50	-0.32	0.11	-0.80
		Sideskin	-0.44	-0.40/Gen. corr.	2.0	-0.57
		Upskin	-0.47	-0.40/Gen. corr.	0.2	-0.75
	AM Recipe 3	“Machined”	-0.75	-0.23	0.6	-0.80
		Sideskin	-0.54	Gen. corr.	0.7	-0.80
		Upskin	-0.46	Gen. corr.	0.3	-0.75
0.1 M	Cast	Machined	-0.72	General corr.	Max (5mA)	N/A
		Vertical	-0.64	General corr.	Max (5mA)	N/A
		Horizontal	-0.60	General corr.	Max (5mA)	N/A
	AM Recipe 1	“Machined”	-0.70	-0.60	Max (5mA)	N/A
		Sideskin	-0.75	General corr.	Max (5mA)	N/A
		Upskin	-0.75	General corr.	Max (5mA)	N/A
	AM Recipe 3	“Machined”	-0.65	-0.30	Max (5mA)	N/A
		Sideskin	-0.68	General corr.	Max (5mA)	N/A
		Upskin	-0.70	General corr.	Max (5mA)	N/A

### ***Linear polarization resistance***

Figure 6-27 shows the open circuit potential and corrosion current density over time, averaged for three replicates of each surface type of the cast pump housing and AM artifacts. The open circuit potential was around the same for all sample types, but the corrosion current was much lower for the AM artifacts when compared with the cast pump housing. The addition of chlorides on day 11 had a negative impact on the corrosion resistance of the AM artifacts, but the reduction in potential and increase in corrosion current were not as severe as the responses for the cast pump housing samples.

Further increases in chloride concentration (day 23 and 32) did not have a significant impact on the results, as the initial concentration of chlorides was enough to cause changes in the corrosion behaviour by breaking down the oxide film at the surface of the metal and blocking repassivation. For the AM artifacts, the machined surface had the best corrosion resistance, while the sideskin was the worst. These results were consistent with the observations from the cyclic polarization testing.



**Figure 6-27: Open circuit potential (OCP) and corrosion current density ( $i_{corr}$ ) determined by LPR for the cast pump housing and AM artifacts**

Overall, the corrosion resistance of the LPBF-processed samples was better than that of the cast samples. In the literature, it has been shown that the melt pool borders are subject to selective attack due to microgalvanic corrosion caused by the potential difference between the Si-particles and the Al matrix [71]. The samples from the cast pump housing may have suffered from a similar occurrence due to the potential difference between the Al matrix and the numerous precipitates rich in Si, Cu, and Fe. In addition, it has been noted that the corrosion resistance of aluminum casting alloys generally decreases as the copper content increases [43].

## 7 Summary, Conclusions, and Future Work

In this thesis, process parameter selection for the LPBF of AlSi10Mg on a modulated laser system was addressed in the context of evaluating the technology and material system for deployment in fluid power applications. Ideal manufacturing recipes were identified for the production of parts with a near fully dense core, high processing speed, and good surface quality. The key findings are as follows:

- High density core recipe (**99.95 ± 0.23%** dense) used a power of 176.8 W, effective scan speed of 500 mm/s (exposure time of 110 μs and point distance of 60 μm), hatch distance of 142 μm, layer thickness of 30 μm, laser spot diameter of 70 μm, and a meander scan strategy
- High productivity core recipe (**99.84 ± 0.18%** dense) used a power of 255.3 W, effective scan speed of 999 mm/s (exposure time of 50 μs and point distance of 60 μm), hatch distance of 145 μm, layer thickness of 30 μm, laser spot diameter of 70 μm, and a meander scan strategy
- Low surface roughness border recipe (**11.39 ± 2.83 μm Sa**) used a power of 270.0 W, effective scan speed of 999 mm/s (exposure time of 50 μs and point distance of 60 μm), contour offset distance of 142 or 145 μm, layer thickness of 30 μm, and laser spot diameter of 70 μm
- Parts manufactured with powder from two different suppliers had similar porosity and surface roughness results for the ideal recipes, with mean values falling within one standard deviation

The ideal process parameters were used to manufacture parts that were characterized for density, surface roughness, and durability based on the hardness, wear resistance, and corrosion resistance for three surface types. The material performance was evaluated by comparison with benchmark values for a cast aluminum pump housing. The surface roughness and durability were tested for three different surface types for the AM artifacts (upskin, sideskin, and polished) and cast pump housing (as-cast, horizontal; as-cast, vertical; and machined). The manufacturability of design features such as thin walls, slots, and channels was also investigated. The key findings are as follows:

- Relative density of cylindrical AM artifacts printed with Recipe 1 ( $99.84 \pm 0.18\%$  dense) and Recipe 3 ( $99.95 \pm 0.23\%$  dense) exceeded the minimum benchmark from the cast pump housing ( $99.13 \pm 0.45\%$  to  $99.97 \pm 0.037\%$  dense)
- Surface roughness of cube-shaped AM artifacts printed with Recipe 1 (12.58 to 22.47 μm Sa) and Recipe 3 (11.75 to 12.83 μm Sa) were similar to the as-cast, horizontal benchmark ( $12.83 \pm 3.38$  μm Sa)
- Hardness of AM artifacts (54.3 to 69.3 HRB) was lower than the cast pump housing (72.8 to 81.5 HRB)

- Specific wear rate of AM artifacts ( $3.92 \times 10^{-13}$  to  $6.04 \times 10^{-13} \text{ m}^2\text{N}^{-1}$ ) was higher than the cast pump housing ( $2.50 \times 10^{-13}$  to  $2.55 \times 10^{-13} \text{ m}^2\text{N}^{-1}$ ), indicating a lower wear resistance
- Cyclic polarization testing revealed that the corrosion resistance and pitting potential were better for the AM artifacts (-0.57 to 0.48 V vs SCE in 0.001M Cl<sup>-</sup>) than the cast pump housing, which exhibited general corrosion
- Linear polarization resistance tests also suggested a better corrosion resistance for the AM artifacts, as the corrosion current density was lower
- Thickness of thin wall artifacts ranging from 1.0 to 3.0 mm did not have a large effect on the part density, which averaged 99.93% and 99.84% dense for each of the two manufacturing recipes
- Gap width of slot artifacts ranging from 0.5 to 4.5 mm did not have a large effect on the surface roughness of the interior vertical walls, which ranged from 9.49 to 14.99  $\mu\text{m}$  across both manufacturing recipes
- Straight circular channels with hole diameters ranging from 0.2 to 1.2 mm, and with a height of 10 or 20 mm were manufactured, and powder was successfully removed from channels with a minimum diameter of 0.5 mm

The recipe development and selection of ideal process parameters focussed mainly on achieving parts with a high relative density and low surface roughness. To do so, the macrostructure of the LPBF samples was examined for melt pool size and the amount of porosity. In future work, it would be beneficial to also investigate the microstructure in order to determine the effect of changing the process parameters and to clarify the cause of the variations in material and mechanical properties. Scanning electron microscopy and EDX analysis could be used to identify the morphology, size, distribution, and chemical composition of secondary phases, which may help determine the material strengthening mechanisms and therefore explain the hardness and wear behaviour. Examining samples after corrosion testing could also prove or disprove the presence of microgalvanic corrosion causing selective attack.

Future work may also include further development of the design constraints for LPBF of AlSi10Mg. This would enable designers to leverage the full potential of the technology to make performance enhancements for the product while still ensuring manufacturability. The current work has successfully manufactured different geometries such as near fully dense thin walls (minimum thickness of 1.0 mm), slots with a high surface quality (minimum gap width of 0.5 mm), and vertical channels that were not blocked by unmelted powder (minimum diameter of 0.5 mm). It would be interesting to quantify the ability to remove powder from non-uniform channels with varying geometries and build orientations

using electropolishing or chemical polishing. This would give designers of fluid power components more freedom in creating custom networks of fluid delivery channels. For the application of the transmission pump, this could also enable the injection of air at different locations inside the pump to test the effects of oil aeration, or the integration of fluid diagnostic sensors to help prevent unexpected reductions in hydraulic efficiency and premature wear.



## References

- [1] M. Tang and P. C. Pistorius, "Oxides, porosity and fatigue performance of AlSi10Mg parts produced by selective laser melting," *Int. J. Fatigue*, vol. 94, pp. 192–201, Jan. 2017.
- [2] C. Leinenbach, "Selective Laser Melting (SLM)," *Empa - Coating Competence Center*. [Online]. Available: <https://www.empa.ch/web/coating-competence-center/selective-laser-melting>. [Accessed: 27-Sep-2019].
- [3] J. Algardh *et al.*, "State-of-the-art for Additive Manufacturing of Metals," Vinnova - SIP Metallic Materials, Sweden, 2016–03898, Jun. 2017.
- [4] Y. Zhang *et al.*, "Additive Manufacturing of Metallic Materials: A Review," *J. Mater. Eng. Perform.*, vol. 27, no. 1, pp. 1–13, Jan. 2018.
- [5] F. Kim, H. Villarraga-Gómez, and S. Moylan, "Inspection of Embedded Internal Features in Additive Manufactured Metal Parts Using Metrological X-ray Computed Tomography," in *American Society for Precision Engineering 2016 Summer Topical Meeting*, 2016, vol. 64, pp. 191–195.
- [6] J. Mingear, B. Zhang, D. Hartl, and A. Elwany, "Effect of process parameters and electropolishing on the surface roughness of interior channels in additively manufactured nickel-titanium shape memory alloy actuators," *Addit. Manuf.*, vol. 27, pp. 565–575, May 2019.
- [7] A. Salmi, F. Calignano, M. Galati, and E. Atzeni, "An integrated design methodology for components produced by laser powder bed fusion (L-PBF) process," *Virtual Phys. Prototyp.*, vol. 13, no. 3, pp. 191–202, Jul. 2018.
- [8] S. N. Reddy K., V. Maranan, T. W. Simpson, T. Palmer, and C. J. Dickman, "Application of Topology Optimization and Design for Additive Manufacturing Guidelines on an Automotive Component," in *Volume 2A: 42nd Design Automation Conference*, Charlotte, North Carolina, USA, 2016.
- [9] J. Parthasarathy, B. Starly, and S. Raman, "A design for the additive manufacture of functionally graded porous structures with tailored mechanical properties for biomedical applications," *J. Manuf. Process.*, vol. 13, no. 2, pp. 160–170, Aug. 2011.
- [10] C. Yan, L. Hao, A. Hussein, S. L. Bubb, P. Young, and D. Raymont, "Evaluation of light-weight AlSi10Mg periodic cellular lattice structures fabricated via direct metal laser sintering," *J. Mater. Process. Technol.*, vol. 214, no. 4, pp. 856–864, Apr. 2014.
- [11] F. Calignano *et al.*, "Investigation of accuracy and dimensional limits of part produced in aluminum alloy by selective laser melting," *Int. J. Adv. Manuf. Technol.*, vol. 88, no. 1–4, pp. 451–458, Jan. 2017.
- [12] T. Peng, K. Kellens, R. Tang, C. Chen, and G. Chen, "Sustainability of additive manufacturing: An overview on its energy demand and environmental impact," *Addit. Manuf.*, vol. 21, pp. 694–704, May 2018.

- [13] P. C. Priarone, V. Lunetto, E. Atzeni, and A. Salmi, "Laser powder bed fusion (L-PBF) additive manufacturing: On the correlation between design choices and process sustainability," *Procedia CIRP*, vol. 78, pp. 85–90, Jan. 2018.
- [14] D. Buchbinder, H. Schleifenbaum, S. Heidrich, W. Meiners, and J. Bültmann, "High Power Selective Laser Melting (HP SLM) of Aluminum Parts," *Phys. Procedia*, vol. 12, pp. 271–278, Jan. 2011.
- [15] H. Asgari, C. Baxter, K. Hosseinkhani, and M. Mohammadi, "On microstructure and mechanical properties of additively manufactured AlSi10Mg\_200C using recycled powder," *Mater. Sci. Eng. A*, vol. 707, pp. 148–158, Nov. 2017.
- [16] F. Del Re *et al.*, "Statistical approach for assessing the effect of powder reuse on the final quality of AlSi10Mg parts produced by laser powder bed fusion additive manufacturing," *Int. J. Adv. Manuf. Technol.*, vol. 97, no. 5, pp. 2231–2240, Jul. 2018.
- [17] A. Hadadzadeh, C. Baxter, B. S. Amirkhiz, and M. Mohammadi, "Strengthening mechanisms in direct metal laser sintered AlSi10Mg: Comparison between virgin and recycled powders," *Addit. Manuf.*, vol. 23, pp. 108–120, Oct. 2018.
- [18] H. Qin, V. Fallah, Q. Dong, M. Brochu, M. R. Daymond, and M. Gallerneault, "Solidification pattern, microstructure and texture development in Laser Powder Bed Fusion (LPBF) of Al10SiMg alloy," *Mater. Charact.*, vol. 145, pp. 29–38, Nov. 2018.
- [19] L. Thijs, K. Kempen, J.-P. Kruth, and J. Van Humbeeck, "Fine-structured aluminium products with controllable texture by selective laser melting of pre-alloyed AlSi10Mg powder," *Acta Mater.*, vol. 61, no. 5, pp. 1809–1819, Mar. 2013.
- [20] B. K. Panda and S. Sahoo, "Thermo-mechanical modeling and validation of stress field during laser powder bed fusion of AlSi10Mg built part," *Results Phys.*, Jan. 2019.
- [21] L. Wang, S. Wang, and J. Wu, "Experimental investigation on densification behavior and surface roughness of AlSi10Mg powders produced by selective laser melting," *Opt. Laser Technol.*, vol. 96, pp. 88–96, Nov. 2017.
- [22] W. H. Kan, Y. Nadot, M. Foley, L. Ridosz, G. Proust, and J. M. Cairney, "Factors that affect the properties of additively-manufactured AlSi10Mg: porosity versus microstructure," *Addit. Manuf.*, p. 100805, Jul. 2019.
- [23] I. Rosenthal, A. Stern, and N. Frage, "Microstructure and Mechanical Properties of AlSi10Mg Parts Produced by the Laser Beam Additive Manufacturing (AM) Technology," *Metallogr. Microstruct. Anal.*, vol. 3, no. 6, pp. 448–453, Dec. 2014.
- [24] N. T. Aboulkhair, N. M. Everitt, I. Ashcroft, and C. Tuck, "Reducing porosity in AlSi10Mg parts processed by selective laser melting," *Addit. Manuf.*, vol. 1–4, pp. 77–86, Oct. 2014.
- [25] E. O. Olakanmi, R. F. Cochrane, and K. W. Dalgarno, "A review on selective laser sintering/melting (SLS/SLM) of aluminium alloy powders: Processing, microstructure, and properties," *Prog. Mater. Sci.*, vol. 74, pp. 401–477, Oct. 2015.

- [26] F42 Committee, “Standard for Additive Manufacturing — Finished Part Properties — Specification for AlSi10Mg with Powder Bed Fusion — Laser Beam,” ASTM International, F3318-18.
- [27] S. Yang and J. R. G. Evans, “Metering and dispensing of powder; the quest for new solid freeforming techniques,” *Powder Technol.*, vol. 178, no. 1, pp. 56–72, Sep. 2007.
- [28] M. J. Matthews, G. Guss, S. A. Khairallah, A. M. Rubenchik, P. J. Depond, and W. E. King, “Denudation of metal powder layers in laser powder bed fusion processes,” *Acta Mater.*, vol. 114, pp. 33–42, Aug. 2016.
- [29] V. Gunenthiram *et al.*, “Experimental analysis of spatter generation and melt-pool behavior during the powder bed laser beam melting process,” *J. Mater. Process. Technol.*, vol. 251, pp. 376–386, Jan. 2018.
- [30] S. Ly, A. M. Rubenchik, S. A. Khairallah, G. Guss, and M. J. Matthews, “Metal vapor micro-jet controls material redistribution in laser powder bed fusion additive manufacturing,” *Sci. Rep.*, vol. 7, no. 1, pp. 1–12, Jun. 2017.
- [31] Renishaw plc., “Renishaw QuantAM Build Preparation Software User Guide.” Dec-2015.
- [32] W. E. King *et al.*, “Observation of keyhole-mode laser melting in laser powder-bed fusion additive manufacturing,” *J. Mater. Process. Technol.*, vol. 214, no. 12, pp. 2915–2925, Dec. 2014.
- [33] M. Tang, P. C. Pistorius, and J. L. Beuth, “Prediction of lack-of-fusion porosity for powder bed fusion,” *Addit. Manuf.*, vol. 14, pp. 39–48, Mar. 2017.
- [34] N. T. Aboulkhair, “Additive manufacture of an aluminium alloy: processing, microstructure, and mechanical properties,” University of Nottingham, Nottingham, United Kingdom, 2015.
- [35] N. T. Aboulkhair, M. Simonelli, L. Parry, I. Ashcroft, C. Tuck, and R. Hague, “3D printing of Aluminium alloys: Additive Manufacturing of Aluminium alloys using selective laser melting,” *Prog. Mater. Sci.*, vol. 106, p. 100578, Dec. 2019.
- [36] K. Kempen, L. Thijs, J. Van Humbeeck, and J.-P. Kruth, “Processing AlSi10Mg by selective laser melting: parameter optimisation and material characterisation,” *Mater. Sci. Technol.*, vol. 31, no. 8, pp. 917–923, Jun. 2015.
- [37] M. Krishnan *et al.*, “On the effect of process parameters on properties of AlSi10Mg parts produced by DMLS,” *Rapid Prototyp. J.*, vol. 20, no. 6, pp. 449–458, Oct. 2014.
- [38] E. O. Olakanmi, “Selective laser sintering/melting (SLS/SLM) of pure Al, Al–Mg, and Al–Si powders: Effect of processing conditions and powder properties,” *J. Mater. Process. Technol.*, vol. 213, no. 8, pp. 1387–1405, Aug. 2013.
- [39] P. Wei *et al.*, “The AlSi10Mg samples produced by selective laser melting: single track, densification, microstructure and mechanical behavior,” *Appl. Surf. Sci.*, vol. 408, pp. 38–50, Jun. 2017.

- [40] U. Scipioni Bertoli, A. J. Wolfer, M. J. Matthews, J.-P. R. Delplanque, and J. M. Schoenung, "On the limitations of Volumetric Energy Density as a design parameter for Selective Laser Melting," *Mater. Des.*, vol. 113, pp. 331–340, Jan. 2017.
- [41] F. Calignano, G. Cattano, and D. Manfredi, "Manufacturing of thin wall structures in AlSi10Mg alloy by laser powder bed fusion through process parameters," *J. Mater. Process. Technol.*, vol. 255, pp. 773–783, May 2018.
- [42] A. T. Sutton, C. S. Kriewall, M. C. Leu, and J. W. Newkirk, "Powder characterisation techniques and effects of powder characteristics on part properties in powder-bed fusion processes," *Virtual Phys. Prototyp.*, vol. 12, no. 1, pp. 3–29, Jan. 2017.
- [43] F. C. Campbell, *Elements of Metallurgy and Engineering Alloys*. ASM International, 2008.
- [44] J. R. Davis, "Aluminum and Aluminum Alloys," in *Alloying: Understanding the Basics*, ASM International, 2001, pp. 351–416.
- [45] Renishaw plc., "AlSi10Mg-0403 400W material data sheet." Jul-2015.
- [46] J. R. Davis, Ed., "Aluminum Foundry Products," in *Metals Handbook Desk Edition*, ASM International, 1998, pp. 484–489.
- [47] "Aluminum (AlSi10Mg)," *Proto3000*. [Online]. Available: <https://proto3000.com/materials/dmls-aluminum-2/>. [Accessed: 02-Oct-2019].
- [48] K. Kempen, L. Thijs, M. Badrossamay, W. Verheecke, and J.-P. Kruth, "Process optimization and microstructural analysis for selective laser melting of AlSi10Mg," presented at the Solid Freeform Fabrication (SFF) Symposium, Austin, TX, 2011.
- [49] J. Trapp, A. M. Rubenchik, G. Guss, and M. J. Matthews, "In situ absorptivity measurements of metallic powders during laser powder-bed fusion additive manufacturing," *Appl. Mater. Today*, vol. 9, pp. 341–349, Dec. 2017.
- [50] C. A. Biffi, J. Fiochi, and A. Tuissi, "Selective laser melting of AlSi10 Mg: Influence of process parameters on Mg<sub>2</sub>Si precipitation and Si spheroidization," *J. Alloys Compd.*, vol. 755, pp. 100–107, Jul. 2018.
- [51] Y. Li and D. Gu, "Parametric analysis of thermal behavior during selective laser melting additive manufacturing of aluminum alloy powder," *Mater. Des.*, vol. 63, pp. 856–867, Nov. 2014.
- [52] N. Read, W. Wang, K. Essa, and M. M. Attallah, "Selective laser melting of AlSi10Mg alloy: Process optimisation and mechanical properties development," *Mater. Des. 1980-2015*, vol. 65, pp. 417–424, Jan. 2015.
- [53] D. Manfredi, F. Calignano, M. Krishnan, R. Canali, E. Ambrosio, and E. Atzeni, "From Powders to Dense Metal Parts: Characterization of a Commercial AlSiMg Alloy Processed through Direct Metal Laser Sintering," *Materials*, vol. 6, no. 3, pp. 856–869, Mar. 2013.

- [54] N. T. Aboulkhair, I. Maskery, C. Tuck, I. Ashcroft, and N. M. Everitt, "The microstructure and mechanical properties of selectively laser melted AlSi10Mg: The effect of a conventional T6-like heat treatment," *Mater. Sci. Eng. A*, vol. 667, pp. 139–146, Jun. 2016.
- [55] F. Calignano, D. Manfredi, E. P. Ambrosio, L. Iuliano, and P. Fino, "Influence of process parameters on surface roughness of aluminum parts produced by DMLS," *Int. J. Adv. Manuf. Technol.*, vol. 67, no. 9–12, pp. 2743–2751, Aug. 2013.
- [56] A. Boschetto, L. Bottini, and F. Veniali, "Roughness modeling of AlSi10Mg parts fabricated by selective laser melting," *J. Mater. Process. Technol.*, vol. 241, pp. 154–163, Mar. 2017.
- [57] D. Buchbinder, H. Schleifenbaum, S. Heidrich, W. Meiners, and J. Bültmann, "High Power Selective Laser Melting (HP SLM) of Aluminum Parts," *Phys. Procedia*, vol. 12, pp. 271–278, Jan. 2011.
- [58] B. Sagbas, "Post-Processing Effects on Surface Properties of Direct Metal Laser Sintered AlSi10Mg Parts," *Met. Mater. Int.*, Jul. 2019.
- [59] N. T. Aboulkhair, I. Maskery, C. Tuck, I. Ashcroft, and N. M. Everitt, "On the formation of AlSi10Mg single tracks and layers in selective laser melting: Microstructure and nano-mechanical properties," *J. Mater. Process. Technol.*, vol. 230, pp. 88–98, Apr. 2016.
- [60] Y. J. Liu, Z. Liu, Y. Jiang, G. W. Wang, Y. Yang, and L. C. Zhang, "Gradient in microstructure and mechanical property of selective laser melted AlSi10Mg," *J. Alloys Compd.*, vol. 735, pp. 1414–1421, Feb. 2018.
- [61] N. Kang, P. Coddet, H. Liao, T. Baur, and C. Coddet, "Wear behavior and microstructure of hypereutectic Al-Si alloys prepared by selective laser melting," *Appl. Surf. Sci.*, vol. 378, pp. 142–149, Aug. 2016.
- [62] N. Kang, P. Coddet, C. Chen, Y. Wang, H. Liao, and C. Coddet, "Microstructure and wear behavior of in-situ hypereutectic Al-high Si alloys produced by selective laser melting," *Mater. Des.*, vol. 99, pp. 120–126, Jun. 2016.
- [63] K. G. Prashanth *et al.*, "Tribological and corrosion properties of Al–12Si produced by selective laser melting," *J. Mater. Res.*, vol. 29, no. 17, pp. 2044–2054, Sep. 2014.
- [64] Md. A. Islam and Z. N. Farhat, "Effect of porosity on dry sliding wear of Al–Si alloys," *Tribol. Int.*, vol. 44, no. 4, pp. 498–504, Apr. 2011.
- [65] Y. Liu, R. Asthana, and P. Rohatgi, "A map for wear mechanisms in aluminium alloys," *J. Mater. Sci.*, vol. 26, no. 1, pp. 99–102, Jan. 1991.
- [66] A. Leon, A. Shirizly, and E. Aghion, "Corrosion Behavior of AlSi10Mg Alloy Produced by Additive Manufacturing (AM) vs. Its Counterpart Gravity Cast Alloy," *Metals*, vol. 6, no. 7, p. 148, Jun. 2016.
- [67] A. Leon and E. Aghion, "Effect of surface roughness on corrosion fatigue performance of AlSi10Mg alloy produced by Selective Laser Melting (SLM)," *Mater. Charact.*, vol. 131, pp. 188–194, Sep. 2017.

- [68] M. Cabrini *et al.*, “Corrosion resistance of direct metal laser sintering AlSiMg alloy,” *Surf. Interface Anal.*, vol. 48, no. 8, pp. 818–826, Aug. 2016.
- [69] M. Cabrini *et al.*, “Effect of heat treatment on corrosion resistance of DMLS AlSi10Mg alloy,” *Electrochimica Acta*, vol. 206, pp. 346–355, Jul. 2016.
- [70] M. Cabrini *et al.*, “Evaluation of corrosion resistance of Al–10Si–Mg alloy obtained by means of Direct Metal Laser Sintering,” *J. Mater. Process. Technol.*, vol. 231, pp. 326–335, May 2016.
- [71] M. Cabrini *et al.*, “Corrosion behavior of AlSi10Mg alloy produced by laser powder bed fusion under chloride exposure,” *Corros. Sci.*, Mar. 2019.
- [72] T. Duchardt, G. Andersohn, and M. Oechsner, “Corrosion behavior of EN AC-AlSi10Mg in boiling coolant with various average flow temperatures,” *Mater. Corros.*, vol. 66, no. 9, pp. 931–939, Sep. 2015.
- [73] L. Girelli, M. Tocci, L. Montesano, M. Gelfi, and A. Pola, “Investigation of cavitation erosion resistance of AlSi10Mg alloy for additive manufacturing,” *Wear*, vol. 402–403, pp. 124–136, May 2018.
- [74] J. Zou, Y. Zhu, M. Pan, T. Xie, X. Chen, and H. Yang, “A study on cavitation erosion behavior of AlSi10Mg fabricated by selective laser melting (SLM),” *Wear*, vol. 376–377, pp. 496–506, Apr. 2017.
- [75] Y. Zhu, J. Zou, W. L. Zhao, X. B. Chen, and H. Y. Yang, “A study on surface topography in cavitation erosion tests of AlSi10Mg,” *Tribol. Int.*, vol. 102, pp. 419–428, Oct. 2016.
- [76] Renishaw plc., “QuantAM Material Editor.” .
- [77] J. Fiochi, A. Tuissi, P. Bassani, and C. A. Biffi, “Low temperature annealing dedicated to AlSi10Mg selective laser melting products,” *J. Alloys Compd.*, vol. 695, pp. 3402–3409, Feb. 2017.
- [78] R. Casati, M. Nasab, and M. Vedani, “Effect of Different Heat Treatment Routes on Microstructure and Mechanical Properties of AlSi7Mg, AlSi10Mg and Al-Mg-Zr-Sc Alloys Produced by Selective Laser Melting,” presented at the Euro PM2018, 2018, p. 7.
- [79] C. A. Biffi *et al.*, “Microstructure and preliminary fatigue analysis on AlSi10Mg samples manufactured by SLM,” *Procedia Struct. Integr.*, vol. 7, pp. 50–57, Jan. 2017.
- [80] D. Herzog, V. Seyda, E. Wycisk, and C. Emmelmann, “Additive manufacturing of metals,” *Acta Mater.*, vol. 117, pp. 371–392, Sep. 2016.
- [81] U. Tradowsky, J. White, R. M. Ward, N. Read, W. Reimers, and M. M. Attallah, “Selective laser melting of AlSi10Mg: Influence of post-processing on the microstructural and tensile properties development,” *Mater. Des.*, vol. 105, pp. 212–222, Sep. 2016.
- [82] S. Romano, A. Brückner-Foit, A. Brandão, J. Gumpinger, T. Ghidini, and S. Beretta, “Fatigue properties of AlSi10Mg obtained by additive manufacturing: Defect-based modelling and prediction of fatigue strength,” *Eng. Fract. Mech.*, Nov. 2017.

- [83] M. Tang and P. C. Pistorius, "Oxides, porosity and fatigue performance of AlSi10Mg parts produced by selective laser melting," *Int. J. Fatigue*, vol. 94, pp. 192–201, Jan. 2017.
- [84] C. A. Biffi *et al.*, "Microstructure and preliminary fatigue analysis on AlSi10Mg samples manufactured by SLM," *Procedia Struct. Integr.*, vol. 7, pp. 50–57, Jan. 2017.
- [85] E. Brandl, U. Heckenberger, V. Holzinger, and D. Buchbinder, "Additive manufactured AlSi10Mg samples using Selective Laser Melting (SLM): Microstructure, high cycle fatigue, and fracture behavior," *Mater. Des.*, vol. 34, pp. 159–169, Feb. 2012.
- [86] D. Herzog, V. Seyda, E. Wycisk, and C. Emmelmann, "Additive manufacturing of metals," *Acta Mater.*, vol. 117, pp. 371–392, Sep. 2016.
- [87] S. Romano, A. Brückner-Foit, A. Brandão, J. Gumpinger, T. Ghidini, and S. Beretta, "Fatigue properties of AlSi10Mg obtained by additive manufacturing: Defect-based modelling and prediction of fatigue strength," *Eng. Fract. Mech.*, Nov. 2017.
- [88] K. Kempen, L. Thijs, J. Van Humbeeck, and J.-P. Kruth, "Mechanical Properties of AlSi10Mg Produced by Selective Laser Melting," *Phys. Procedia*, vol. 39, pp. 439–446, 2012.
- [89] C. Silbernagel, I. Ashcroft, P. Dickens, and M. Galea, "Electrical resistivity of additively manufactured AlSi10Mg for use in electric motors," *Addit. Manuf.*, vol. 21, pp. 395–403, May 2018.
- [90] H. Jee, Y. Lu, and P. Witherell, "Design rules with modularity for additive manufacturing," presented at the Solid Freeform Fabrication Symposium, Austin, TX, 2015, pp. 1450–1462.
- [91] M. Mani, P. Witherell, and H. Jee, "Design Rules for Additive Manufacturing: A Categorization," in *Volume 1: 37th Computers and Information in Engineering Conference*, Cleveland, Ohio, USA, 2017.
- [92] M. Saunders, "Design for metal AM - a beginner's guide," Renishaw plc., Gloucestershire, U.K., 2017.
- [93] Q. Han, H. Gu, S. Soe, R. Setchi, F. Lacan, and J. Hill, "Manufacturability of AlSi10Mg overhang structures fabricated by laser powder bed fusion," *Mater. Des.*, vol. 160, pp. 1080–1095, Dec. 2018.
- [94] F. Calignano, "Design optimization of supports for overhanging structures in aluminum and titanium alloys by selective laser melting," *Mater. Des.*, vol. 64, pp. 203–213, Dec. 2014.
- [95] E. Atzeni and A. Salmi, "Study on unsupported overhangs of AlSi10Mg parts processed by Direct Metal Laser Sintering (DMLS)," *J. Manuf. Process.*, vol. 20, pp. 500–506, Oct. 2015.
- [96] T. Kolb, A. Mahr, F. Huber, J. Tremel, and M. Schmidt, "Qualification of channels produced by laser powder bed fusion: Analysis of cleaning methods, flow rate and melt pool monitoring data," *Addit. Manuf.*, vol. 25, pp. 430–436, Jan. 2019.
- [97] R. B. Lippert and R. Lachmayer, "A Design Method for SLM-Parts Using Internal Structures in an Extended Design Space," in *Industrializing Additive Manufacturing - Proceedings of Additive Manufacturing in Products and Applications - AMPA2017*, 2018, pp. 14–23.

- [98] Z. Yousif and L. Roland, “Additive Repair Design Approach: Case Study of Transverse Loading of Aluminum Beams,” in *Industrializing Additive Manufacturing - Proceedings of Additive Manufacturing in Products and Applications - AMPA2017*, 2018, pp. 169–177.
- [99] F. Calignano, G. Cattano, L. Iuliano, and D. Manfredi, “Controlled Porosity Structures in Aluminum and Titanium Alloys by Selective Laser Melting,” in *Industrializing Additive Manufacturing - Proceedings of Additive Manufacturing in Products and Applications - AMPA2017*, 2018, pp. 181–190.
- [100] M. Huber *et al.*, “Process Setup for Manufacturing of a Pump Impeller by Selective Laser Melting,” in *Industrializing Additive Manufacturing - Proceedings of Additive Manufacturing in Products and Applications - AMPA2017*, 2018, pp. 252–263.
- [101] A. Kirchheim, H.-J. Dennig, and L. Zumofen, “Why Education and Training in the Field of Additive Manufacturing is a Necessity,” in *Industrializing Additive Manufacturing - Proceedings of Additive Manufacturing in Products and Applications - AMPA2017*, 2018, pp. 329–336.
- [102] EOS GmbH - Electro Optical Systems, “EOS Aluminium AlSi10Mg.” May-2014.
- [103] Renishaw plc., “H-5800-0704-05-B\_EN - User Guide - AM250-AM 400.” 2016.
- [104] N. Otsu, “A Threshold Selection Method from Gray-Level Histograms,” *IEEE Trans. Syst. Man Cybern.*, vol. 9, no. 1, pp. 62–66, Jan. 1979.
- [105] Keyence Corporation, “VK-H1XV2E VK-H1XJE Reference Manual.” 2014.
- [106] D. A. Jones, *Principles and Prevention of Corrosion*. Prentice Hall, 1996.
- [107] P. Marcus, V. Maurice, and H.-H. Strehblow, “Localized corrosion (pitting): A model of passivity breakdown including the role of the oxide layer nanostructure,” *Corros. Sci.*, vol. 50, no. 9, pp. 2698–2704, Sep. 2008.
- [108] P. D. Lee, R. C. Atwood, R. J. Dashwood, and H. Nagaumi, “Modeling of porosity formation in direct chill cast aluminum–magnesium alloys,” *Mater. Sci. Eng. A*, vol. 328, no. 1, pp. 213–222, May 2002.
- [109] A. M. Rubenchik, W. E. King, and S. S. Wu, “Scaling laws for the additive manufacturing,” *J. Mater. Process. Technol.*, vol. 257, pp. 234–243, Jul. 2018.
- [110] J. C. Ion, H. R. Shercliff, and M. F. Ashby, “Diagrams for laser materials processing,” *Acta Metall. Mater.*, vol. 40, no. 7, pp. 1539–1551, Jul. 1992.
- [111] T. W. Eagar, “Temperature Fields Produced by Traveling Distributed Heat Sources,” presented at the 64th Annual AWS Convention, Philadelphia, Pennsylvania, 1983.
- [112] G. G. Gladush and I. Smurov, *Physics of laser materials processing: theory and experiment*. Berlin ; New York: Springer, 2011.
- [113] W. E. King *et al.*, “Laser powder bed fusion additive manufacturing of metals; physics, computational, and materials challenges,” *Appl. Phys. Rev.*, p. 55, Sep. 2015.



- [114] J. Metelkova, Y. Kinds, K. Kempen, C. de Formanoir, A. Witvrouw, and B. Van Hooreweder, “On the influence of laser defocusing in Selective Laser Melting of 316L,” *Addit. Manuf.*, vol. 23, pp. 161–169, Oct. 2018.
- [115] A. V. Gusarov, I. Yadroitsev, Ph. Bertrand, and I. Smurov, “Model of Radiation and Heat Transfer in Laser-Powder Interaction Zone at Selective Laser Melting,” *J. Heat Transf.*, vol. 131, no. 7, Jul. 2009.
- [116] J. H. VanSant, “Conduction Heat Transfer Solutions.” Lawrence Livermore National Laboratory, Mar-1980.
- [117] T. Mukherjee and T. DebRoy, “Mitigation of lack of fusion defects in powder bed fusion additive manufacturing,” *J. Manuf. Process.*, vol. 36, pp. 442–449, Dec. 2018.
- [118] K. Darvish, Z. W. Chen, and T. Pasang, “Reducing lack of fusion during selective laser melting of CoCrMo alloy: Effect of laser power on geometrical features of tracks,” *Mater. Des.*, vol. 112, pp. 357–366, Dec. 2016.
- [119] W. Pei, W. Zhengying, C. Zhen, L. Junfeng, Z. Shuzhe, and D. Jun, “Numerical simulation and parametric analysis of selective laser melting process of AlSi10Mg powder,” *Appl. Phys. A*, vol. 123, no. 8, p. 540, Jul. 2017.
- [120] Y. Li and D. Gu, “Parametric analysis of thermal behavior during selective laser melting additive manufacturing of aluminum alloy powder,” *Mater. Des.*, vol. 63, pp. 856–867, Nov. 2014.
- [121] J. S. Zuback and T. DebRoy, “The Hardness of Additively Manufactured Alloys,” *Materials*, vol. 11, no. 11, p. 2070, Oct. 2018.
- [122] W. Li *et al.*, “Effect of heat treatment on AlSi10Mg alloy fabricated by selective laser melting: Microstructure evolution, mechanical properties and fracture mechanism,” *Mater. Sci. Eng. A*, vol. 663, pp. 116–125, Apr. 2016.
- [123] N. T. Aboulkhair, C. Tuck, I. Ashcroft, I. Maskery, and N. M. Everitt, “On the Precipitation Hardening of Selective Laser Melted AlSi10Mg,” *Metall. Mater. Trans. A*, vol. 46, no. 8, pp. 3337–3341, Aug. 2015.
- [124] D. Bradley and G. Roth, “Adaptive Thresholding using the Integral Image,” *J. Graph. Tools*, vol. 12, no. 2, pp. 13–21, Jan. 2007.

## Appendix A – LPBF Process Parameters

Table A-1 lists the process parameters that can be edited for the Renishaw AM400. Refer to the Renishaw QuantAM Build Preparation Software User Guide for the full description of each parameter [31].

**Table A-1: Process parameters for the Renishaw AM400 [31]**

Category	Description	Parameters
General	Spatial information for part(s) that will be printed	Layer thickness Position X Position Y Layers count
Strategy	Hatch pattern strategy for how the laser scan will fill in the part's cross-section	Hatch pattern strategy Field size Field offset Minimal field size Stripe size Stripe offset Merge vector length Merge vector Block sort/sort optimized
Control	Control (on/off setting) if hatches are used for the interior part volume, and if unique settings for the fill contours, upskin, or downskin of the part are used	Total fill Volume fill contours Volume hatch Volume jump optimisation Upskin Downskin Upskin border Blocked path
Order	The order that the different hatch types will be scanned	Scan order (1 to 9) Volume border in/out Volume fill contour in/out
Volume	Spatial information for how the hatch pattern, border(s), and fill contour(s) will be implemented	Beam compensation Border count Border distance Fill contour offset Number of fill contours Fill contour distance Hatch distance Hatch offset Hatch start angle Hatch increment angle Filter length Blocked path resolution Blocked path trim distance Blocked path filter length
Upskin / Downskin	Spatial information for how the hatch pattern, border(s), and fill contour(s) will be implemented for the upskin and downskin	Use start angle Keep additional borders (upskin) Border offset (upskin) Number of exposures Number of layers

Appendix A – LPBF Process Parameters

		Skin area tolerance Hatch offset Hatch distance Filter length Rotation increment angle Rotation start angle Offset volume area (downskin)
Scan Volume / Scan Upskin / Scan Downskin	The laser power and exposure settings for the border(s), hatches, fill contour(s)	Border power Border focus Border point distance Border exposure time Hatches power Hatches focus Hatches point distance Hatches exposure time Fill contours power Fill contours focus Fill contours point distance Fill contours exposure time Additional border power Additional border focus Additional border point distance Additional border exposure time

## Appendix B – MATLAB Code for CT Scan Data Processing

```

%MATLAB R2018b
%CT scan image processing written by Henry Ma, 2017
%Edited by Martin Ethier, 03/2018
%Edited by Lisa Brock, 08/2018

%script to folder containing CT scan .tif images
PathFolder = uigetdir;
srcfiles = dir(strcat(PathFolder, '\', '*.*tif*'));

%Height of the stack
stackheight = size(srcfiles,1);

%Filepath of all images
InfoImage = imfinfo(strcat(PathFolder, '\', srcfiles(1).name));
mImage = InfoImage.Width; %Width of images, in pixels
nImage = InfoImage.Height; %Height of images, in pixels

%Initializing the MATLAB Variable that stores the images
tifstack = uint16(zeros(nImage, mImage, stackheight));

%Importing the .TIFF files to MATLAB
for i = 1:stackheight
    tifstack(:, :, i) = imread(strcat(PathFolder, '\', srcfiles(i).name), 'Info', InfoImage);
end
clear srcfiles; clear InfoImage;

%%%%%%%%%%%%%%
%run this to find cropping values
imshow3D(tifstack)
axis on

cropped = tifstack(200:900, 250:750, 1:17:888); %edit cropping values
imshow3D(cropped)
axis on

%%%%%%%%Image filtering
U = cropped;
clear cropped, clear tifstack;
counter0 = 1;
filtered = uint16(zeros(size(U)));
for nt = 1:length(U(1,1,:))
    filtered(:, :, nt) = imbilatfilt(U(:, :, nt));
    counter0 = counter0 + 1
end
clear U;
figure, imshow3D(filtered);
axis on;

```

## Appendix B – CT Scan Data Processing in MATLAB

```

%%imbinarize using LOCAL threshold
V = filtered(:,:,);
counter1=1;
solidPart = zeros(size(V));
bw2 = zeros(size(V));
mask = true(size(V(:,:,1)));
nSize = 2*floor(size(V(:,:,1))/20)+1;
binary = zeros(size(V));

for nt = 1:length(V(1,1,:))
    bw2(:,:,nt) = activecontour(V(:,:,nt),mask,1200, 'Chan-Vese');
    solidPart(:,:,nt) = bwareaopen(bw2(:,:,nt),200);
    %%adaptive local
    aThresh =
        adaptthresh(V(:,:,nt),0.4,'ForegroundPolarity','dark','NeighborhoodSize',nSize,'Statistic','mean');
    bw1(:,:,nt) = imbinarize(V(:,:,nt),aThresh);
    %%binary image
    binary(:,:,nt) = and(solidPart(:,:,nt), bw1(:,:,nt));
    counter1 = counter1+1
end
figure, imshow3D(binary)
axis on

%%imbinarize using OTSU threshold

%%first get rid of white dots
%%use value between 27000 (if dark) and 45000 (if bright)
V = filtered;
for nt = 1:length(V(1,1,:))
    for p = 1:length(V(:,1,1))
        for q = 1:length(V(1,:,1))
            if V(p,q,nt) > 37000
                V(p,q,nt) = 37000;
            end
        end
    end
end
figure, imshow3D(V)

counter1=1;
binary = zeros(size(V));
OtsuEM = zeros(length(V(1,1,:)),1);
threshTemp = zeros(length(V(1,1,:)),1);

for nt = 1:length(V(1,1,:))
    [thresh1, metric] = multithresh(V(:,:,nt),3);
    valuesMax = [thresh1 max(V(:))];
    thresh = double(thresh1(3))/65535 ; %%normalized
    thresh2 = double(thresh1(2));
    threshTemp(nt) = thresh;
    OtsuEM(nt) = metric; %%Effectiveness metric
    binary(:,:,counter1) = imbinarize(V(:,:,nt),thresh); %%use with normalized thresh
    counter1 = counter1+1
end
clear V;

```

## Appendix B – CT Scan Data Processing in MATLAB

```
figure, imshow3D(binary)
axis on
%Crop if necessary
binary = binary(:,:,1:755);

%%%%%%%%%%%%%%%%%%%%%%%%%%%%%%%%%%%%%%%%%%%%%%%%%%%%%%%%%%%%%%%%%%%%%%%%
%%%%%%%%%%%%%%%%%%%%%%%%%%%%%%%%%%%%%%%%%%%%%%%%%%%%%%%%%%%%%%%%%%%%%%%%
%%%Following code is to align part along Z axis%%%
%loop through stack and get centroid of largest CC of each slice
truecenter = zeros(length(binary(1,1,:)),3);
for ii = 1:length(binary(1,1,:))
    stats = regionprops(binary(:,:,ii),'Area','Centroid');
    areas = sort([stats(:).Area],'descend');
    %get index of the second largest component (first largest being the
    %background)
    idx = [stats.Area] == areas(1);
    %get the center coordinates of the notch
    center = stats(idx).Centroid;

    truecenter(ii,1) = center(1);
    truecenter(ii,2) = center(2);
    truecenter(ii,3) = ii;
end

%%% Following code copied and edited from Rotation function %%%
alignROW = flipud(robustfit(truecenter(:,3),truecenter(:,2),'bisquare'));
alignCOL = flipud(robustfit(truecenter(:,3),truecenter(:,1),'bisquare'));

%The angle is defined by the inverse tangent of the slope
angleROW = rad2deg(atan(alignROW(1)));
angleCOL = rad2deg(atan(alignCOL(1)));

%aligning part about y
%yzslice = permute(cropped,[3 1 2]); %Same as 'left slice' in ImageJ
%%original
yzslice = permute(binary,[3 1 2]); %Same as 'left slice' in ImageJ
yzslice = imrotate(yzslice,-angleROW,'crop'); %Counter-clockwise is positive

%aligning part about x
xzslice = permute(yzslice,[3 1 2]); %Same as 'left slice' in ImageJ
xzslice = imrotate(xzslice,angleCOL,'crop');

aligned = permute(xzslice, [3 1 2]);
clear binary;

%%%%%%%%%%%%%%%%%%%%%%%%%%%%%%%%%%%%%%%%%%%%%%%%%%%%%%%%%%%%%%%%%%%%%%%%
%%%%%%%%%%%%%%%%%%%%%%%%%%%%%%%%%%%%%%%%%%%%%%%%%%%%%%%%%%%%%%%%%%%%%%%%
figure, imshow3D(aligned)
axis on
%crop out black images at start and end of aligned
binary1 = zeros(1012, 988, 877);
binary1 = aligned(:,:,16:760);
clear aligned;
```

## Appendix B – CT Scan Data Processing in MATLAB

```
%%%%%%%%%%%%%%%%%%%%%%%%%%%%%%%%%%%%%%%%%%%%%%%%%%%%%%%%%%%%%%%%%%%%%%%%%
%%%%%%%%%%%%%%%%%%%%%%%%%%%%%%%%%%%%%%%%%%%%%%%%%%%%%%%%%%%%%%%%%%%%%%%%%
%%%%%%%%%%%%%%%%%%%%%%%%%%%%%%%%%%%%%%%%%%%%%%%%%%%%%%%%%%%%%%%%%%%%%%%%% Isolate pores and calculate relative density %%%%%%%%%%

%V2 = binary1;
counter3=1;
filled_BG = zeros(size(binary1));
for nt = 1:length(binary1(1,1,:))
    V2nt = logical(binary1(:,nt));
    filled_BG(:,counter3) = imfill(V2nt,[1 1], 8);
    counter3 = counter3+1
end

%check that background filled correctly
figure
imshow3D(filled_BG)
axis on

filled_BG = filled_BG(1:645,5:224,:); %use to crop edge if bad

%calculate density by comparing images before and after filling in pores
background = logical(filled_BG - binary1);
clear filled_BG;

background_fill = zeros( size(background));
background_fill = imfill(background,'holes');
clear background;
SE = strel('sphere',1);
bw_dilated = zeros( size(background_fill));
bw_dilated = imdilate(background_fill,SE);
background_filled = zeros( size(bw_dilated));
background_filled = imerode(bw_dilated,SE);
clear bw_dilated;
clear background_fill;

bw = zeros( size(binary1));
bw = binary1-background_filled;

idx = bw == 1;
bw_final = zeros( size(idx) );
ind2d = find(idx);
bw_final( ind2d ) = bw( ind2d );
clear bw;
bw_final = logical(bw_final);

total_density = sum(sum(sum(bw_final)))/sum(sum(sum(~background_filled)));

%%Calculate slice density
slice_dens = zeros(1,length(bw_final(1,1,:)));
for i=1:length(binary1(1,1,:))
    slice_dens(i) = sum(sum(bw_final(:,i)))/sum(sum(~background_filled(:,i)));
end
```

## Appendix B – CT Scan Data Processing in MATLAB

```

%%other direction
slice_dens2 = zeros(1,length(bw_final(:,1,1)));
for i=1:length(binary1(:,1,1))
    slice_dens2(i) = sum(sum(bw_final(i,:,:)))/sum(sum(~background_filled(i,:,:)));
end

%%last direction
slice_dens3 = zeros(1,length(bw_final(1,:,1)));
for i=1:length(binary1(1,:,1))
    slice_dens3(i) = sum(sum(bw_final(:,i,:)))/sum(sum(~background_filled(:,i,:)));
end

%%average slide densities for each direction
st_dev_x = nanstd(slice_dens3);
st_dev_y = nanstd(slice_dens2);
st_dev_z = nanstd(slice_dens);
aveslice_x = nanmean(slice_dens3);
aveslice_y = nanmean(slice_dens2);
aveslice_z = nanmean(slice_dens);

%%save both density vectors to a .mat file (choose directory and filenames)
savedLength = length(binary1(1,1,:));
savedLength2 = length(binary1(:,1,1));
savedLength3 = length(binary1(1,:,1));
save('C:\directory\dataFilename.mat','OtsuEM','slice_dens','total_density','slice_dens2','slice_dens3','savedLength',
'savedLength2','savedLength3','st_dev_x','st_dev_y','st_dev_z','aveslice_x','aveslice_y','aveslice_z')
save('C:\directory\workspaceFilename.mat','background_filled','binary1','bw_final','-v7.3');

%%plot slice densities
figure('rend','painters','pos',[100 100 461 529])
subplot('Position',[0.1440 0.8 0.7 0.12])
density_plot = plot(1:savedLength3,slice_dens3);
title('Sample 1','FontSize',10)
xlabel('Distance (mm)', 'FontSize',10);
ylabel('Density', 'FontSize',10);
xlim([1 savedLength3])

hold on
set(gca, 'FontSize', 10);
xticks(0:100:1000);
aD = ancestor(density_plot,'axes');
x = get(aD,'XTick');
new_x = x.*0.012;    %%convert pixels to mm
set(aD,'XTickLabel', new_x);
%set(aD,'XTickLabel', []);
ylim([0.99 1]);
yticks(0:0.005:1);
xlabel('Width (mm)');

%%%%%%%%%%%%%% BINARY Minimum Intensity Projections %%%%%%%%%%%%%%%
%%crop binary1 to control the distance projected for MinIPs
MinIP_Z = squeeze(min(permute(binary1(:,:,:), [3 1 2])));
MinIP_X = squeeze(min(permute(binary1(:, :, :), [2 3 1])));
MinIP_Y = squeeze(min(permute(binary1(:, :, :), [1 3 2])));

```



## Appendix B – CT Scan Data Processing in MATLAB

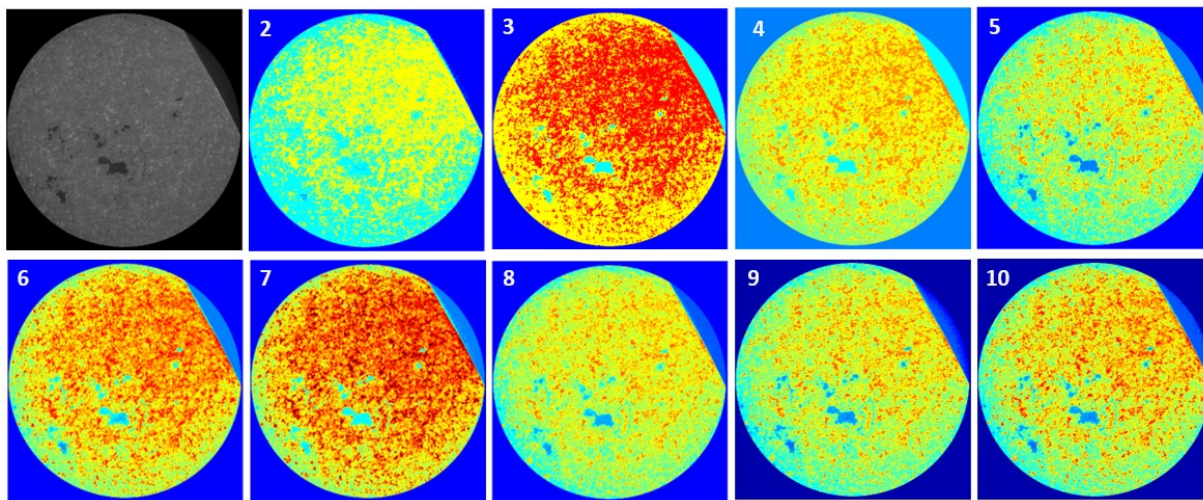
```
%save MinIP
imwrite(MinIP_Z, strcat('C:\directory\filename.tiff'), 'Compression', 'none');

%%Add to figure under density graph
flipX = permute(MinIP_Z, [2 1]);
maxY = 741 * 0.012; %%pixels * conversion to mm
maxX = 651 * 0.012;
RI = imref2d(size(flipX));
RI.XWorldLimits = [0 maxX];
RI.YWorldLimits = [0 maxY];
subplot(2,1,2), imshow(flipX,RI);
xlabel('X (mm)');
subplot(2,1,2), ylabel('Y (mm)');
set(gca, 'FontSize', 18)
```

## Appendix C – Selection of Threshold for Image Segmentation

When generating the binary image from the greyscale image, it is critical to select an appropriate threshold for the greyscale intensity level so that the image is accurately segmented into pores (black) and solid part (white). If the threshold is too low, not all of the pores will be captured and the relative part density will be overestimated. Similarly, if the threshold is too high, some portions of the solid part may be erroneously identified as pores and the relative part density will be underestimated.

In order to automatically process the CT scan data, which was in the form of hundreds of greyscale images each representing a “slice” of the three-dimensional part, the threshold was calculated for each individual image using the built-in image threshold functions in MATLAB. The selected function for analysis was Otsu’s multi-threshold method. However, the method required user input to select the best level of binning, which is the number of subdivisions the greyscale intensity values are divided into (and relates to the number of thresholds calculated), and to select the best threshold for segmentation, as the binary image only requires division into two bins. Figure C-1 illustrates the effect of changing the binning level, and Figure C-2 shows an example of segmentation by selecting different thresholds that were generated using ten bins. Additionally, it was observed that Otsu’s method occasionally resulted in noise that was difficult to eliminate. Figure C-3 shows two examples of the random noise appearing as false porosity.



**Figure C-1: Effect of changing binning level of the Otsu multi-threshold in order to accurately highlight the size, shape, and amount of pores present in the greyscale image**

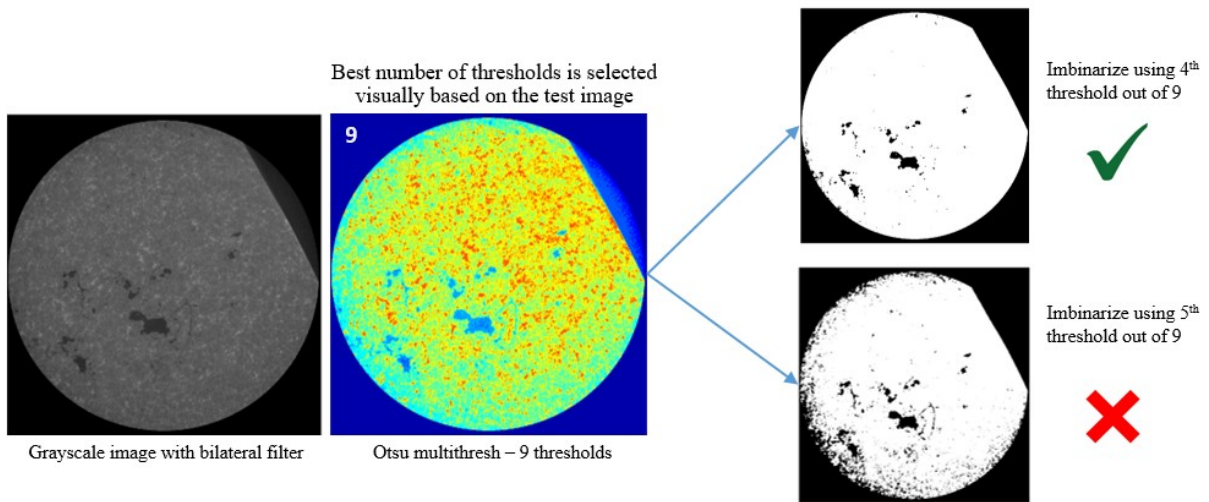


Figure C-2: Effect of changing the threshold selection on the binary segmentation

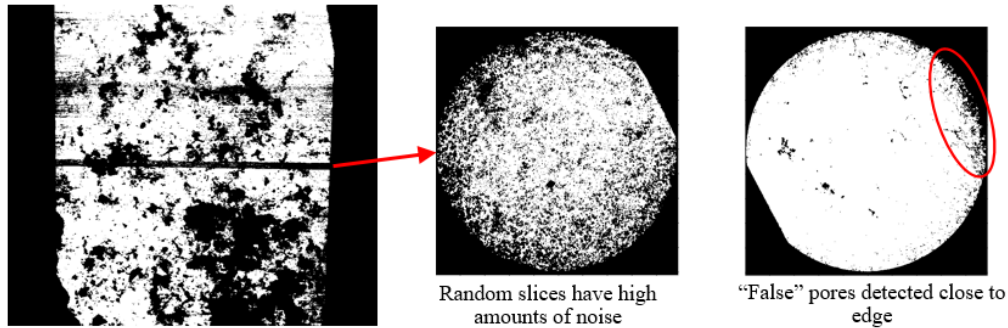
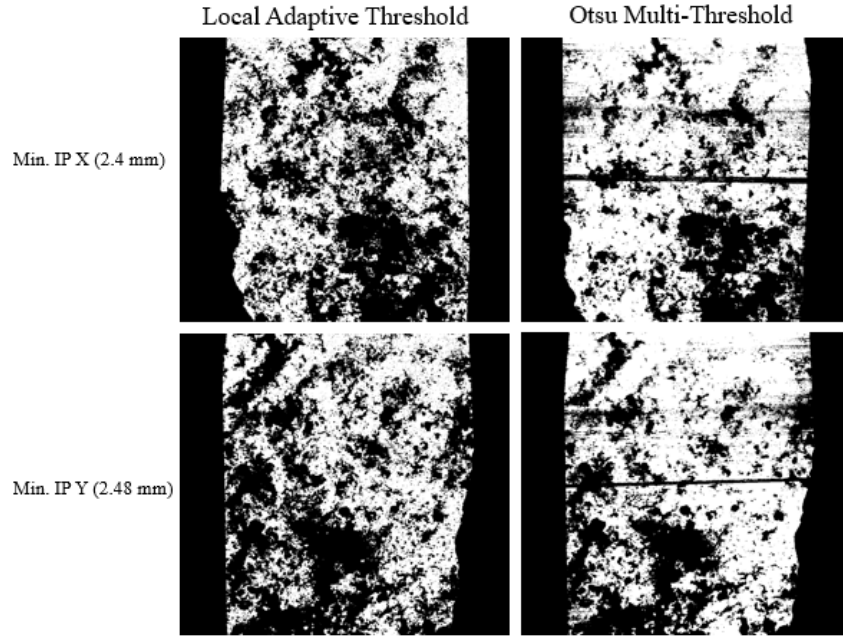


Figure C-3: Minimum intensity projection showing bands of slices with high noise (left), and false porosity present near the edge of the part (right)

For comparison, an alternative method of image segmentation using a locally adaptive threshold was performed for the cast parts only. The locally adaptive threshold, based on [124], uses first-order statistics to choose the threshold for each pixel in the image by calculating the mean intensity of the neighbouring pixels and applying a sensitivity multiplier. The local threshold may account for non-uniform illumination on the grayscale image, unlike the Otsu method which selects a global threshold for the entire image. The local threshold was found to successfully eliminate the bands of high noise, as shown in Figure C-4. However, it is likely that the local threshold would have underestimated the porosity close to the edges of the part, because the black surroundings were included in the mean of the surrounding neighbourhood for those pixels.

Appendix C – Image Segmentation



**Figure C-4: Minimum intensity projections in the X and Y directions for binary images generated using the local adaptive threshold and the Otsu multi-threshold method**

Table C-1 shows the results for the estimated part density for the two samples of the cast pump housing, as determined by the local threshold method and the Otsu threshold method. Figure C-5 and Figure C-6 show the density versus distance graphs and minimum intensity projections for the two samples of the cast pump housing, as determined by the local threshold method and the Otsu threshold method. It was found that both threshold methods resulted in similar levels of porosity, with the local threshold estimating a slightly lower relative density than the Otsu threshold. The results were also consistent for the comparison between samples, with cast sample D1 having a higher relative density than cast sample D2. Overall, the Otsu threshold was selected as the primary analysis method because it had a much faster computation time.

**Table C-1: Porosity measurements for cast pump housing**

Sample	Threshold method	Density (%)	Ave. Slice Density – X (%)	Ave. Slice Density – Y (%)	Ave. Slice Density – Z (%)	Height - Z (mm)
D1	Local	99.95	99.95 ±0.038	99.96 ±0.041	99.95 ±0.048	2.56
	Otsu	99.97	99.97 ±0.037	99.98 ±0.029	99.97 ±0.036	2.56
D2	Local	99.12	99.19 ±0.51	99.26 ±0.58	99.12 ±0.51	3.48
	Otsu	99.15	99.13 ±0.45	99.24 ±0.49	99.14 ±0.61	3.51

Appendix C – Image Segmentation

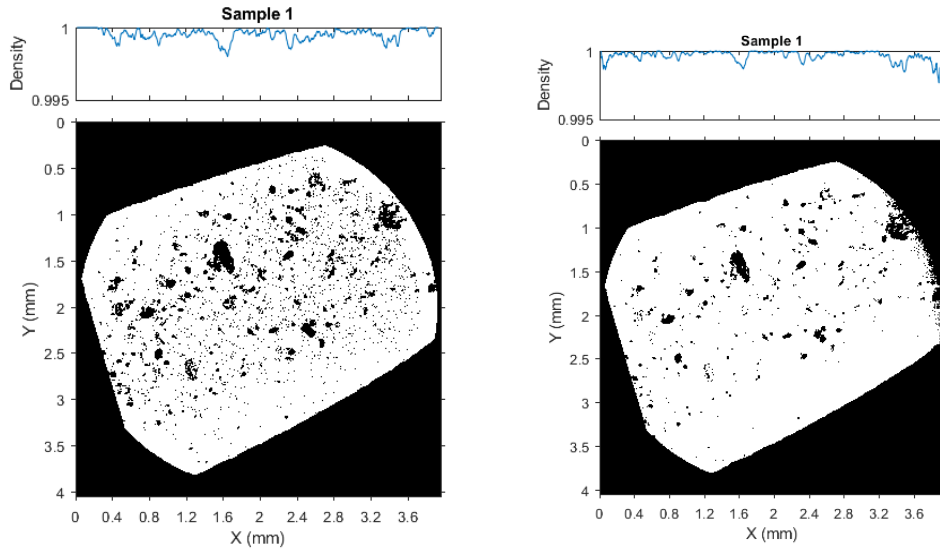


Figure C-5: Density vs. distance graph and minimum intensity projection for Sample D1.

Left: Local threshold (99.95% density) Right: Otsu threshold (99.97% density)

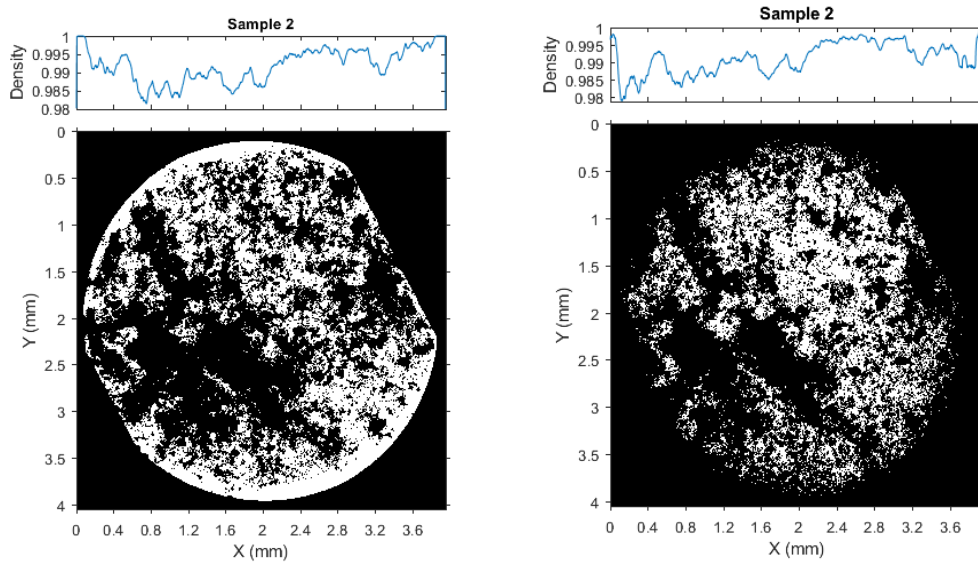


Figure C-6: Density vs. distance graph and minimum intensity projection for Sample D2.

Left: Local threshold (99.12% density) Right: Otsu threshold (99.15% density)

## Appendix D – MATLAB Code for Wear Rate Calculation

```

%MATLAB R2018b
%Wear rate calculation written by Pablo Enrique, 24/03/2019
%Edited by Lisa Brock, 03/05/2019

format long
dx= 4.198074e-6 ; %m/px scale to convert from pixels to meters (Depends on Keyence XY calibration – use
4.198074e-6 for AM, 2.798716e-6 for cast)

%Import the csv file
M=csvread('S12_machined_height_input_Sept24.csv');

%Rescale the height data based on information in the csv file
zdist = 0.1; %conversion factor 0.1nm per digit
M2=M*zdist*1e-9; %height in m

[a,b]=size(M); %Determine the size of the height map
k=1; %Index variable

%The individual formulas for the equation of a plane are built here.
%Data from the four corners of the height map are chosen (using the i and j values).
%Default 4 corners: [i=200:400, j=200:400] [i=a-200:a, j=200:400]
%[i=200:400, j=b-200:b] [i=a-200:a, j=b-200:b]
%They are then arranged into A and B matrix/array.
mesh(M); %check corner locations; adjust if necessary

for i=1:200
    for j=1:200
        A(k,:)=[(i-1)*dx (j-1)*dx 1];
        B(k,1)=M(i,j);
        k=k+1;
    end
end
k %Display to show that the code is progressing
for i=a-200:a
    for j=1:200
        A(k,:)=[(i-1)*dx (j-1)*dx 1];
        B(k,1)=M(i,j);
        k=k+1;
    end
end
k
for i=1:200
    for j=b-200:b
        A(k,:)=[(i-1)*dx (j-1)*dx 1];
        B(k,1)=M(i,j);
        k=k+1;
    end
end
k
for i=a-200:a
    for j=b-200:b
        A(k,:)=[(i-1)*dx (j-1)*dx 1];

```

## Appendix D – Wear Rate Calculation in MATLAB

```
B(k,1)=M(i,j);
k=k+1;
end
end
k
fit=A\B; %Do back division to find the best fits (in the format [a b c]')

%Using the best fit values, create a matrix z that has height values for the plane.
z=ones(a,b);
for i=1:1:a
    for j=1:1:b
        z(i,j)=(i-1)*dx*fit(1)+(j-1)*dx*fit(2)+fit(3);
    end
end

%Plot the experimental (M) and best fit plane (z) height data on the same graph (use M2 and z2 to get plot with z-
axis in meters)
mesh(M)
hold on
mesh(z)

z2 = z*zdist*1e-9; %convert plane height data to meters

%Take the difference between the plane and the height data to find the depth of the wear track. Add up all the
heights and multiply by their areas (dx by dx) to give the volume loss in m^3
V=sum(sum((z2(140:760,:)-M2(140:760,:))))*dx^2;

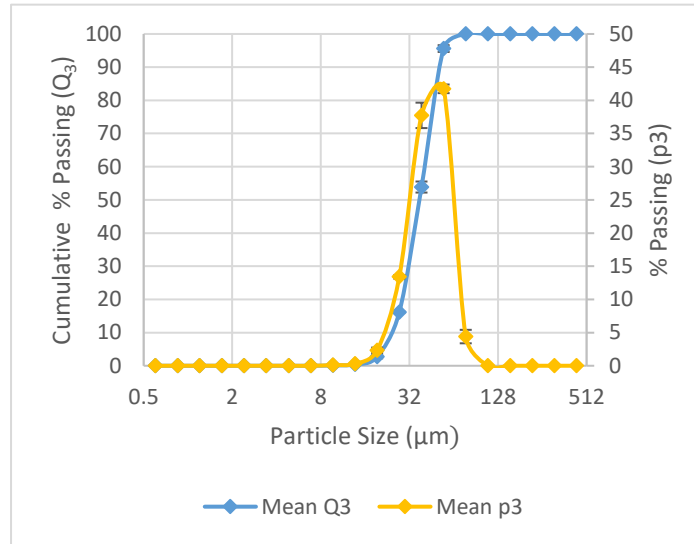
%Sliding distance is 135 meters (use 1609 pixels for AM, 2410 for cast – depends on XY calibration of Keyence
data)
s=1609*dx*10000*2;

%Loading force in N
F=0.923146*9.81;

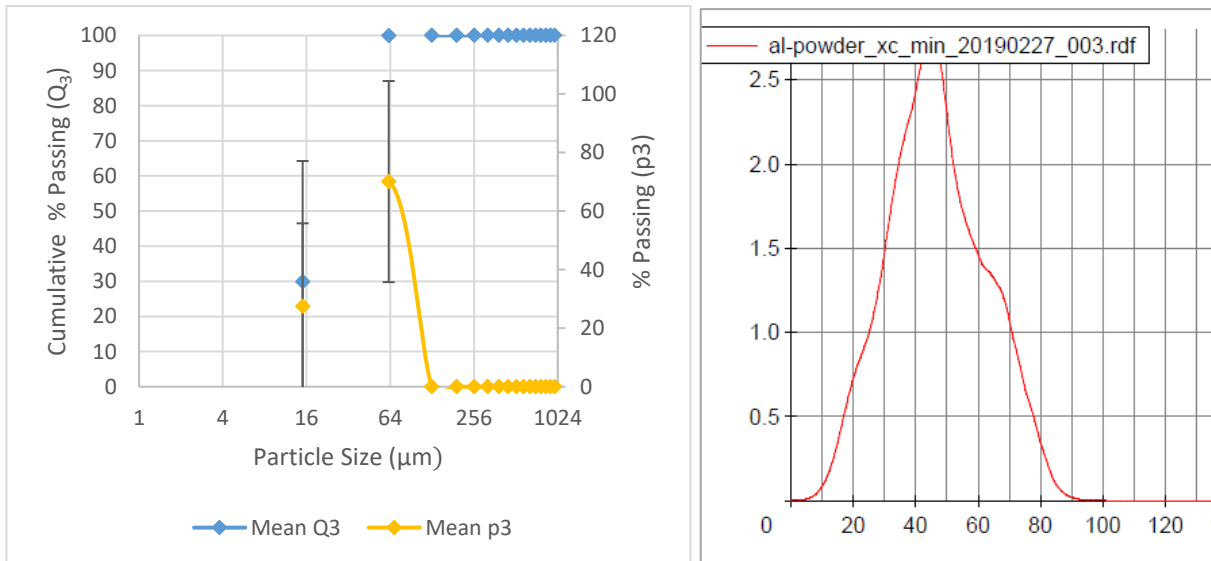
%specific wear rate in m^2/N
K=V/(F*s)
```

## Appendix E – Powder Particle Size Distribution

The particle size distribution for the two powder types are shown in Figure E-1 and Figure E-2. The P3 value, shown on the right hand y-axis, refers to the percentage of particles that measured a specified size for the minimum chord length ( $X_{c,min}$ ). The mean Q3 value, shown on the left hand y-axis, refers to the cumulative percentage of particles that measured below the specified size.



**Figure E-1: Particle size distribution for AlSi10Mg powder from Supplier 1**



**Figure E-2: Particle size distribution for the AlSi10Mg powder from Supplier 2**

**Left: Average results for 3 tests; Right: Result for single replicate**



## Appendix F – LPBF Manufacturing Parameters

Table F-1: Processing parameters for DOE 2-1 to 2-4

DOE #	Recipe #	Power (W)	Point distance (μm)	Exposure time (μs)	Effective scan speed (mm/s)	VED (J/mm <sup>3</sup> )
2-1	1	280	60	60	857	93.3
	2	280	60	45	1091	73.3
	3	280	60	30	1500	53.3
	4	280	75	60	1071	74.7
	5	280	75	45	1364	58.7
	6	280	75	30	1875	42.7
	7	280	90	60	1286	62.2
	8	280	90	45	1636	48.9
	9	280	90	30	2250	35.6
2-2	1	260	45	45	818	90.8
	2	260	45	60	643	115.6
	3	260	45	75	529	140.3
	4	260	60	45	1091	68.1
	5	260	60	60	875	86.7
	6	260	60	75	706	105.2
	7	260	75	45	1364	54.5
	8	260	75	60	1071	69.3
	9	260	75	75	882	84.2
2-3	1	240	45	45	818	83.8
	2	240	45	60	643	106.7
	3	240	45	75	529	129.5
	4	240	60	45	1091	62.9
	5	240	60	60	875	80.0
	6	240	60	75	706	97.1
	7	240	75	45	1364	50.3
	8	240	75	60	1071	64.0
	9	240	75	75	882	77.7
2-4	1	280	45	30	1125	71.1
	2	280	45	45	818	97.8
	3	280	45	60	643	124.4
	4	280	45	75	529	151.1
	5	280	60	75	706	113.3
	6	280	75	75	882	90.7
	7	280	90	75	1059	75.6

Appendix F – LPBF Manufacturing Parameters

**Table F-2: Processing parameters for DOE 3-1 and 3-2**

DOE #	Recipe #	Power (W)	Point distance (μm)	Exposure time (μs)	Effective scan speed (mm/s)	VED (J/mm <sup>3</sup> )
3-1	1	240	45	45	818	83.8
	2	240	45	60	643	106.7
	3	240	45	75	529	129.5
	4	240	60	45	1091	62.9
	5	240	60	60	875	80.0
	6	240	60	75	706	97.1
	7	240	75	45	1364	50.3
	8	240	75	60	1071	64.0
	9	240	75	75	882	77.7
3-2	1	200	60	171	332	90.8
	2	200	60	119	465	115.6
	3	200	60	90	598	140.3
	4	200	60	72	730	68.1
	5	200	60	60	863	86.7
	6	200	60	50	996	105.2
	7	200	60	43	1129	54.5
	8	200	60	38	1262	69.3

**Table F-3: Processing parameters for DOE 3-3**

Recipe #	Power (W)	Point distance (μm)	Exposure time (μs)	Hatch distance (μm)	Effective scan speed (mm/s)	MDR
1	88	60	230	105	250	1.5
2	108	60	110	105	500	1.5
3	129	60	70	105	749	1.5
4	152	60	50	105	999	1.5
5	240	60	24	105	1748	1.5
6	366	60	14	105	2498	1.5
7	123	60	230	140	250	2.0
8	156	60	110	140	500	2.0
9	193	60	70	140	749	2.0
10	234	60	50	140	999	2.0
11	390	60	24	140	1748	2.0
12	161	60	230	175	250	2.5
13	212	60	110	175	500	2.5
14	270	60	70	175	749	2.5
15	334	60	50	175	999	2.5

## Appendix G – Micrographs

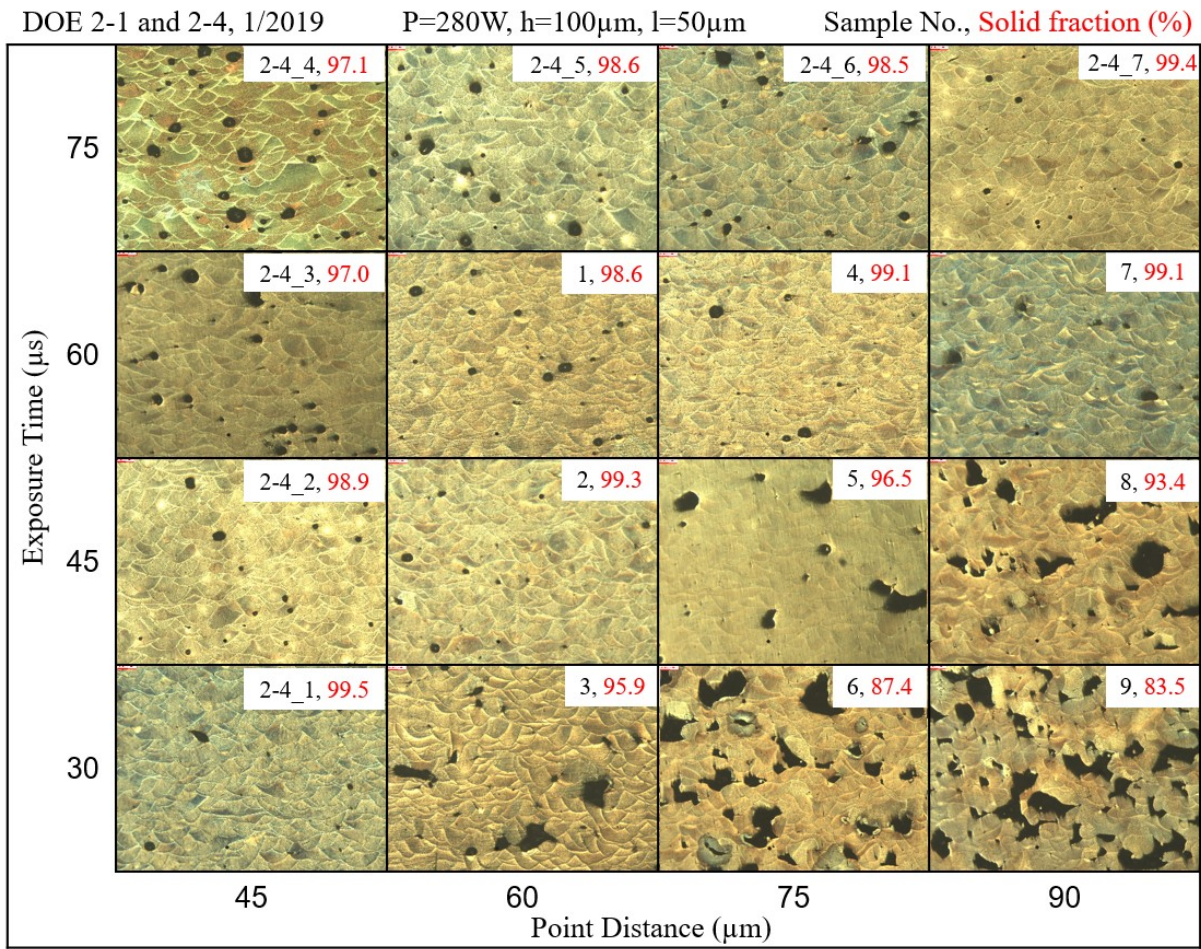
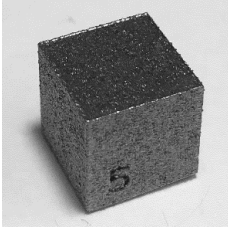
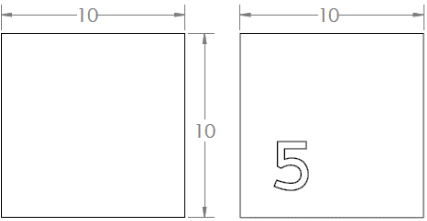
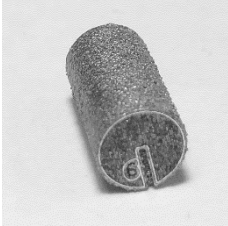
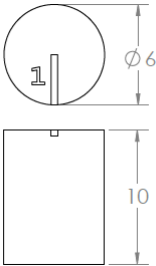

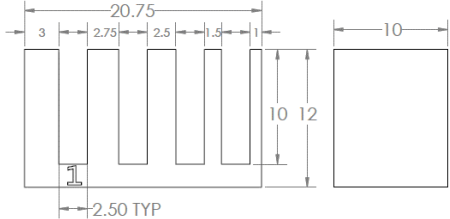
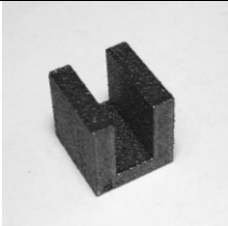
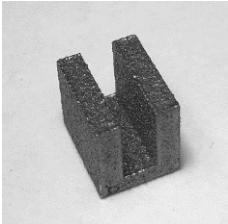
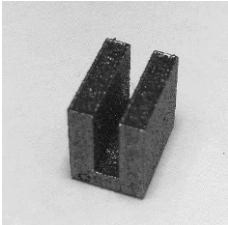
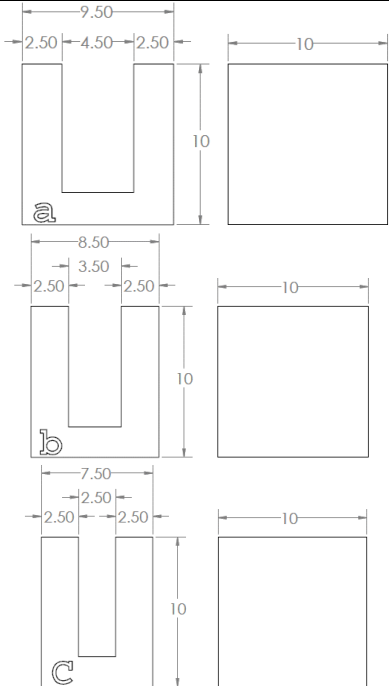
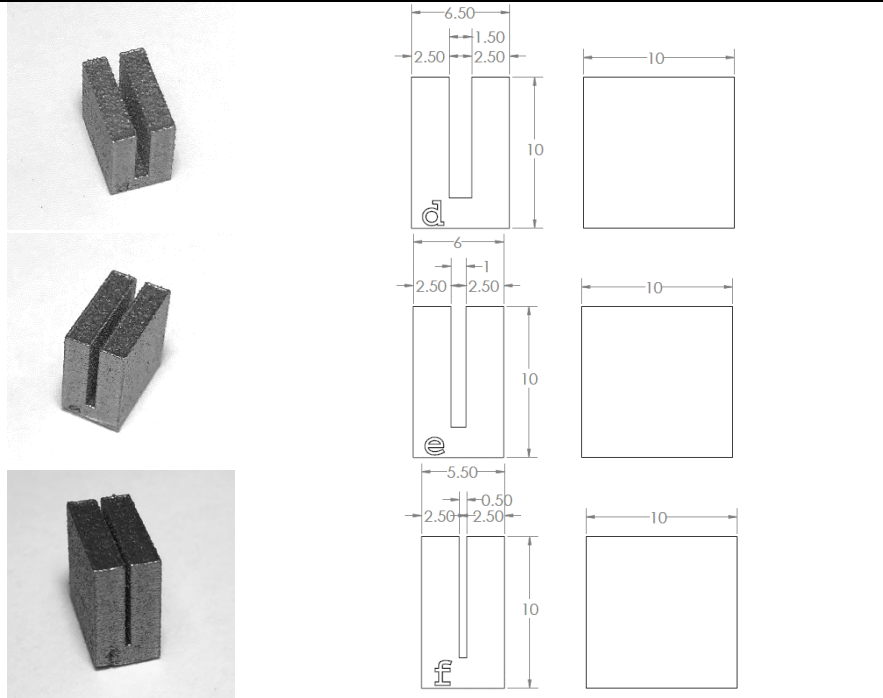


Figure G-1: Optical micrographs for all samples from DOE 2-1 and 2-4

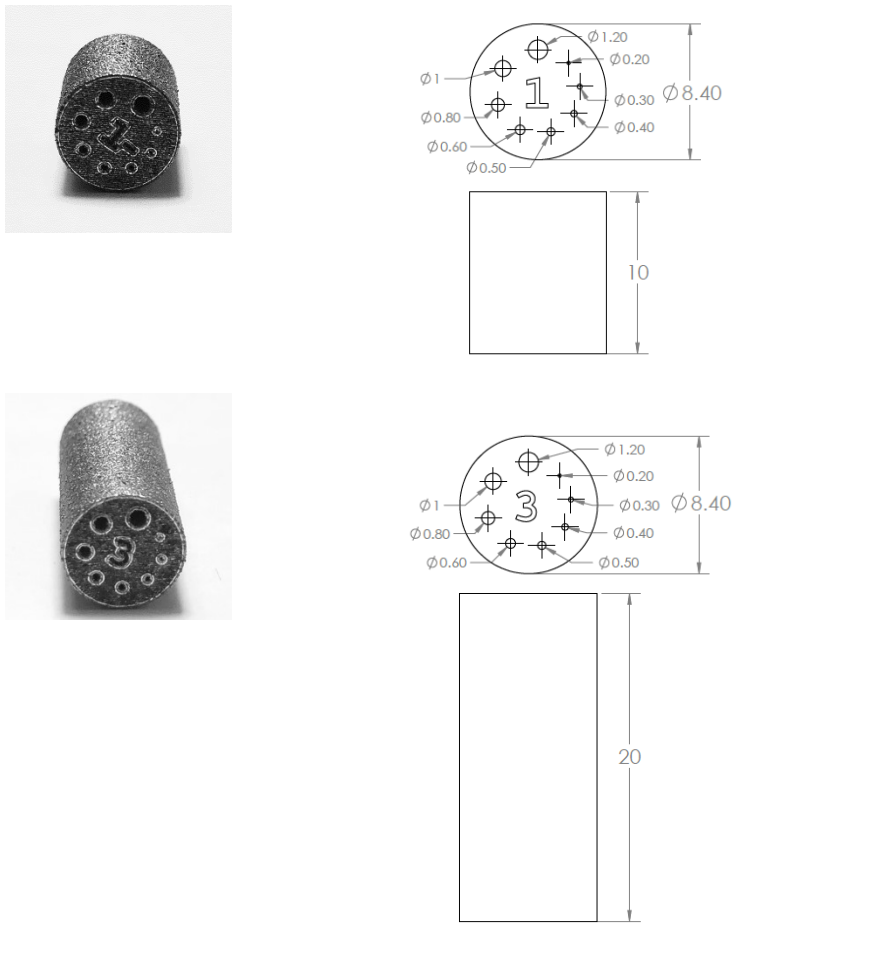
## Appendix H – LPBF Design Artifacts

**Table H-1: LPBF design artifacts; all dimensions in mm.**

Artifact	Experiment (DOE)	Photo(s)	CAD drawing(s)
Cube	2-1 2-2 2-3 2-4 3-1 4-2		
Cylinder	3-2 3-3 3-5 3-6 4-2		
Thin Walls	4-2		
Slots	4-2	  	



Channels 4-2



## Appendix I – Electrochemical Results

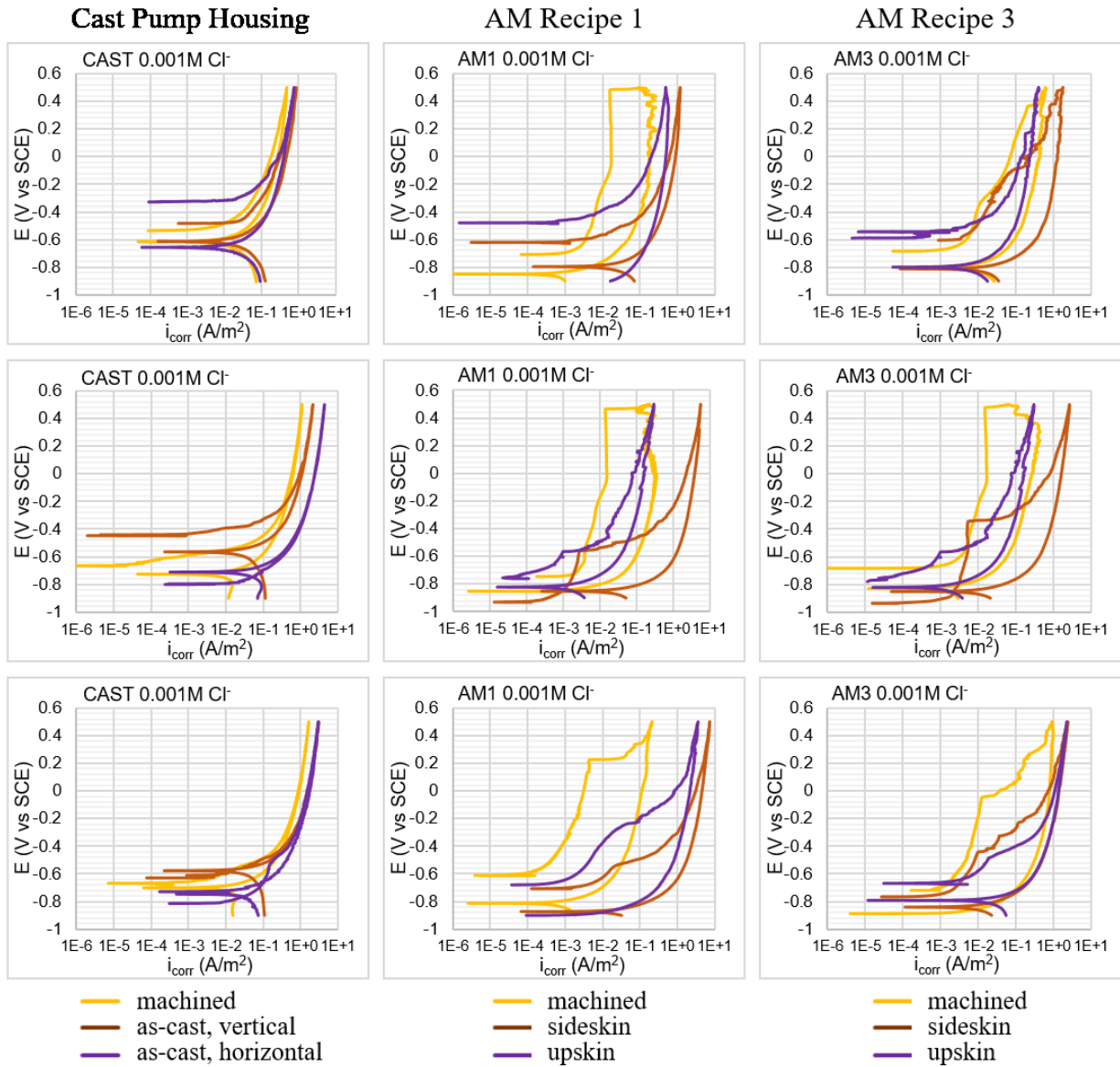


Figure I-1: Cyclic potentiodynamic polarization curves for three replicates of the cast and AM surfaces

Appendix I – Electrochemical Results

**Table I-1: Results for cyclic polarization testing of the cast pump housing and AM artifacts**

Chloride Molarity	Sample Type	Surface Type	Anodic Corrosion Potential (V)	Pitting Potential (V)	Anodic Current @ 0.2V (A/m <sup>2</sup> )	Cathodic Corrosion Potential (V)
0.001 M	Cast	Machined	-0.52	General corr.	0.3	-0.61
		Vertical	-0.48	General corr.	0.7	-0.61
		Horizontal	-0.32	General corr.	0.6	-0.64
	AM Recipe 1	“Machined”	-0.71	0.48	0.015	-0.85
		Sideskin	-0.62	-0.50/Gen. corr.	0.9	-0.80
		Upskin	-0.48	-0.38/Gen. corr.	0.2	-0.90
	AM Recipe 3	“Machined”	-0.68	0.37	0.1	-0.80
		Sideskin	-0.60	-0.1	0.4	-0.80
		Upskin	-0.54	0.17	0.2	-0.80
0.001 M	Cast	Machined	-0.67	General corr.	0.9	-0.72
		Vertical	-0.50	General corr.	1.18	-0.56
		Horizontal	-0.80	General corr.	1.21	-0.70
	AM Recipe 1	“Machined”	-0.74	0.47	0.013	-0.85
		Sideskin	-0.92	-0.57	3.0	-0.85
		Upskin	-0.75	-0.57	0.16	-0.82
	AM Recipe 3	“Machined”	-0.68	0.48	0.018	-0.83
		Sideskin	-0.92	-0.34	1.5	-0.85
		Upskin	-0.78	-0.57	0.16	-0.82
0.001 M	Cast	Machined	-0.66	General corr.	1.5	-0.70
		Vertical	-0.63	General corr.	2.0	-0.59
		Horizontal	-0.80	General corr.	2.0	-0.72
	AM Recipe 1	“Machined”	-0.60	0.22	0.003	-0.81
		Sideskin	-0.70	-0.52	5.0	-0.87
		Upskin	-0.68	-0.22	2.0	-0.90
	AM Recipe 3	“Machined”	-0.72	-0.05	0.15	-0.90
		Sideskin	-0.77	-0.57	1.0	-0.84
		Upskin	-0.68	-0.48	1.15	-0.80
0.01 M	Cast	Machined				
		Vertical	<i>No data</i>			
		Horizontal				
	AM Recipe 1	“Machined”	-0.50	-0.32	0.11	-0.80
		Sideskin	-0.44	-0.40/Gen. corr.	2.0	-0.57
		Upskin	-0.47	-0.40/Gen. corr.	0.2	-0.75
	AM Recipe 3	“Machined”	-0.75	-0.23	0.6	-0.80
		Sideskin	-0.54	Gen. corr.	0.7	-0.80
		Upskin	-0.46	Gen. corr.	0.3	-0.75
0.1 M	Cast	Machined	-0.72	General corr.	Max (5mA)	N/A
		Vertical	-0.64	General corr.	Max (5mA)	N/A
		Horizontal	-0.60	General corr.	Max (5mA)	N/A
	AM Recipe 1	“Machined”	-0.70	-0.60	Max (5mA)	N/A
		Sideskin	-0.75	General corr.	Max (5mA)	N/A
		Upskin	-0.75	General corr.	Max (5mA)	N/A
	AM Recipe 3	“Machined”	-0.65	-0.30	Max (5mA)	N/A
		Sideskin	-0.68	General corr.	Max (5mA)	N/A
		Upskin	-0.70	General corr.	Max (5mA)	N/A